Probing the Effects of Nano-Domains on the Redox Products in Molecular Solvents-RTILs Mixtures

Abderrahman Atifi
Marquette University

Recommended Citation

Atifi, Abderrahman, "Probing the Effects of Nano-Domains on the Redox Products in Molecular Solvents-RTILs Mixtures" (2016). *Dissertations (2009 -)*. 665.
https://epublications.marquette.edu/dissertations_mu/665

Probing the Effects of Nano-Domains on the Redox Products in Molecular Solvents-RTILs Mixtures

By

Abderrahman Atifi

A Dissertation submitted to the Faculty of the Graduate School, Marquette University, in Partial Fulfillment of the Requirements for the Degree of Doctor of Philosophy

Milwaukee, Wisconsin

August 2016

Abstract

Probing the Effects of Nano-Domains on the Redox Products in Molecular Solvents-RTILs Mixtures

Abderrahman Atifi

Marquette University, 2016

Room temperature ionic liquids (RTIL) have been very attractive as replacements for molecular solvents (MS) in many areas in chemistry. The use of the RTIL in mixture with MS as reaction media will reduce the cost and viscosity of RTILs. The formation of RTIL nano-domains (nano-structures) in the mixture may lead to partitioning of solutes between the MS and the RTIL phase, where the properties and reactivity would be more like those in pure ionic liquids. In the present work, analytical approaches have been employed to probe the presence and effects of RTIL nano-domains on redox processes in the mixture. A focus was on substrates that undergo multi-electron reductions/oxidations, such as: dinitrobenzene, fullerene and metalloporphyrins.

Throughout our investigation, there was strong evidence of the presence of RTIL and MS domains in the mixture system. Correlation of the potential shifts with acceptor properties of the mixture enabled to evaluate the extent of ion paring interactions within the molecular and RTIL domains. Influence of RTIL domains on the transport properties of the solution was evaluated versus the change in the viscosity of the mixture. The impact of RTIL domains on the electronic structures of redox products was examined using several spectroscopic methods, including UV-visible, infrared and NMR spectroscopy. Computational tools such as chemometrics, voltammetric simulations and DFT calculations were used to complement the experimental analysis.

Acknowledgements

I would like to express my sincere gratitude to my supervisor, Dr. Michael D. Ryan, whose expertise, guidance, understanding and encouragement added considerably to my journey at Marquette University. I would like to thank the other members of my research committee, Dr. J. Kincaid, Dr. Q. Timerghazin and Dr. R Rathore for their valuable suggestions in the preparation of this dissertation. My gratitude goes also to Schmitt foundation for supporting my research work during the academic year 2014-2015.

I am especially grateful for the loving support of my parents and brothers, my wife "Maryem" and my little daughter "Reem", my in-laws and my friends.

A.A

Table of Contents

List of Tables

List of Figures

Chapter 1 Introduction

The need for using solvents in the synthesis and analysis of compounds places them at the core of many chemical applications. In general, the choice of the type of solvent, often based on its solvation ability, is crucial for a reaction to take place. For electrochemical applications, factors other than the solvation and the chemical stability are important, including the electrochemical stability of the solvent. The use of an electrolyte (salt), as a second component to assure the conductivity of the solvent system, is generally required. Until lately, most of solvents that have been employed in electrochemical applications were molecular solvents. In addition to their toxicity, these liquids suffer from high volatility, making them a potential source of environmental problems. As a result, extensive efforts have been directed during the last decades toward the development of alternatives to the conventional solvents.

Room Temperature Ionic Liquids (RTILs) have attracted considerable attention from chemists due to their potential as a replacement for molecular solvents in a wide range of electrochemical applications.[1–9] Their valuable properties include low-volatility, high physical and chemical stability, wide electrochemical windows, intrinsic conductivity, wide liquid range, high polarity and the ability to dissolve a wide range of compounds. Defined as salts that melt below 100 ^{0}C, RTILs are composed of a bulky organic cation paired with an inorganic/organic anion. The structures of some common cations and anions are shown in *Figure 1*.

1-Alkyl-3-MethylImidazolium [C_nMIm^+] **Tetraalkylammonium [Am^+ or $N_{a,b,c,d}^+$]**

Pyrrolidinium [C_nMPyrr^+] **Tetraalkylphosphonium [$P_{a,b,c,d}^+$]**

Hexafluorophosphate [PF_6^-] **Tetrafluoroborate [BF_4^-]**

Trifluoromethylsulfonate [OTF^-] **Bis(trifluoromethylsulfonyl)imide [NTF_2^-]**

Figure 1: Chemical structures of common cations and anions in RTILs

A review of the relevant proprieties of RTIL will be presented in this introduction, along with studies on electron transfer processes in RTILs and literature background on redox systems that will be investigated in this work. The introduction will include four major parts:

- ✓ Properties of RTILs
- ✓ Electron transfer in RTILs
- ✓ Redox systems
- ✓ Objectives

1.1 Properties of RTILs

1.1.1 Viscosity & Conductivity

The first physical property to consider when dealing with ionic liquids is viscosity. RTILs are viscous liquids and their viscosity is 1 to 3 orders of magnitude higher than those of conventional solvents.[10,11] This high viscosity has a strong effect on electrochemical processes like mass transport and conductivity. Values of viscosity for some common RTILs are shown in *Table 1*.

Table 1: Viscosities of some common RTILs[10,11]

Cation	**Anion**	**Viscosity**
BMIm$^+$	PF$_6^-$	308
	BF$_4^-$	154
	NTF$_2^-$	52
HexMIm$^+$	PF$_6^-$	690
	BF$_4^-$	314
	NTF$_2^-$	87
OctMIm$^+$	PF$_6^-$	861
	BF$_4^-$	135
	NTF$_2^-$	119
N$_{1123}^+$		83

For comparison, the viscosity of water is 1cP.

There are different interactions that determine this physicochemical property in RTILs.[12] For a given cation, the viscosity is lowest for larger anions NTF_2^-, while it's higher for non-planar symmetric anions like PF_6^- or BF_4^-. The relative basicity of the anions and their ability to form hydrogen bonds or van der Waals attractions have been shown to have a pronounced effect on viscosity. For a given anion, increasing the length of the alkyl substituents of the cation results in an increase in the viscosity because of stronger van der Waals interactions between larger and bulky cations. Ion association results in more order within the ionic liquid, which increases the viscosity. A significant decrease in viscosity is generally observed in ionic liquids as the temperature increases.

The second physical characteristic of RTILs is their intrinsic conductivity. Although they are conductive media for electrochemical purpose, RTILs exhibit lower conductivities than aqueous electrolytes. In general, the conductivity is inversely related to the viscosity. Ion pairing has been shown to cause a lower conductivity, because ion pairs neutralize the charge, which reduces the conductivity. The extent of ion pairing could be measured by comparing the experimental conductivity (Λ_{exp}) with calculated conductivity (Λ_{calc}), based on diffusion coefficients.[13] The ratio $\Lambda_{exp}/\Lambda_{calc}$ gives information about the ionic association and/or the degree of ionicity of the ionic liquids. Ratios of 0.6 to 0.8 were assigned to highly charged ionic liquids, resulting in higher conductivities. However, the lower viscosity of NTF_2^- ionic liquids over the BF_4^- RTILs was not reflected in its conductivity. It was suggested that strong interactions raise the extent of neutral ion pairs, lowering both the conductivity and viscosity of NTF_2^- RTIL.

In another report, molar conductivities of imidazolium-based ionic liquids were measured in acetonitrile solution.[14] All the binary systems exhibited maximum conductivities between 10 and 20% of RTILs. Above these maxima, the average interionic distances decreased to 600–800 pm, forming ionic pairs and decreasing the conductivity of the mixture. Similar variations of the conductivity in mixture of imidazolium liquid and propylene carbonate solvents have been reported by Shi et al.[15] In this system, a maximal conductivity was found at about 50%RTIL, before dropping at higher concentrations of the ionic liquid (Figure 2). It is worth noting that these observations are quite consistent with structural ordering of RTIL in mixture with molecular solvent. This feature is described in more details in the following discussion.

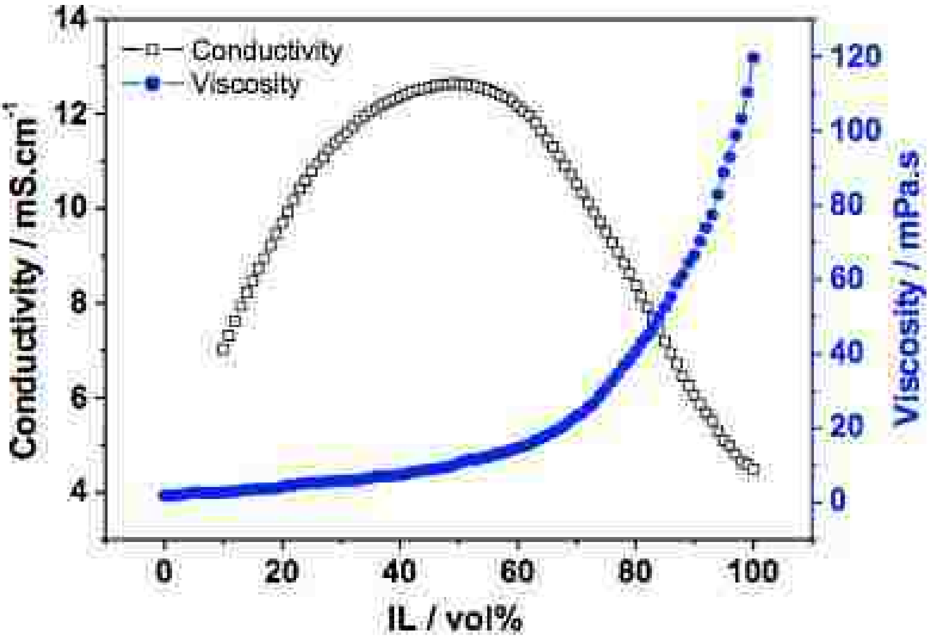

Figure 2*: The viscosity and the electrical conductivity of the BMImOTF/propylene carbonate solution as a function of the RTIL volume fraction.*[15]

1.1.2 RTIL nano-structures

From a structural perspective, RTILs are not simple fluids: they are generally highly asymmetric, with components having large differences in molecular size and shape. Due to these differences, the coulombic attractions are weakened, preventing the formation of solids at room temperature. As a result, RTILs can be considered as nano-structured, nano-segregated liquids.[16]

1.1.2.1 Nano-structures in neat RTIL

In pure RTILs, theses structural features were analyzed by molecular dynamics simulation by Padua et al.[17] Nano-aggregation of the imidazolium cation side chains, when going from C_2 to C_8, results in formation of nonpolar domains, while polar domains are mainly formed by aggregation of the ionic parts, the cation ring and the anion. Early experimental evidence of nanostructures in neat RTIL has been reported by Triolo et al.[18] In their work, X-Ray diffraction was used to probe heterogeneities in imidazolium RTILs. Although X-ray diffraction is not a common method for liquid analysis, significant evidence of nano-aggregation was found in liquid salts at room temperature. In supercooled RTILs, the structural organizations were found to be of the order of a few nanometers, where the size was temperature dependent and proportional to the alkyl chain length of the imidazolium cation. It is noteworthy to mention that the nomenclature “nano-domains”, adopted in the present work, has been already used in this study, in describing the nano-aggregation in RTILs.

Further experimental evidence of nano-aggregation in neat RTILs was reported, using mass spectrometry. Electrospray ionization has been employed as a soft ionization technique for mass spectroscopy, allowing the analysis of weakly bound species in RTIL solutions. Using ESI-MS, aggregates or clusters of the constituent ions of aprotic ILs have been observed.[19–22] In their work on 1-butyl-3-methylimidazolium salts, Kennedy and Drummond reported large aggregated parent ions, $C_8A_7^+$ (with C: cation and A: anion) within some protic ionic liquids.[23] The formation of these aggregates was mostly attributed to hydrogen bonding between the anions and cations. The nitrate (small and highly charged) anion was found to form the largest aggregates, upon forming a network of hydrogen bonds with protic RTIL cations. Licence and co-workers have introduced an NMR based method to investigate partitioning of solutes between the polar and non-polar domain in neat $BMImNTF_2$ RTIL.[24] Based on volume integral of cross peaks of 2D-NMR, Domain Preference Integral Ratio (DPIR) was defined as the solubility ratio of methyl methacrylate (MMA) oligomers between non-polar and polar domains. Increase of DPIR with increased molecular size (from MMA to MMA_5) indicated partitioning into the non-polar domain of the ionic liquid as the polymerization progresses. These results implied a possible use of RTIL nano-domains in shaping the conformation of the polymer backbone chain by introducing functional groups (polar/non-polar). The solvation of non-polar solutes by non-polar domain of RTIL was also reported by Dong et al.[25] Based on intermolecular vibrational motions, the authors suggested that at 5 mol % of CS_2 in $PMImNTF_2$, the non-polar molecules were confined in the nonpolar domains of the RTIL.

In more recent work, the effect of these nano-structures on spin dynamics of the photo-excited zinc tetraphenylporphyrin (ZnTPP) was investigated in imidazolium RTILs.[26] Based on time resolved EPR analysis, two different spin relaxation rates were observed, corresponding to two different solvation environments. The two domains were mostly characterized by different micro-viscosities within the RTIL, leading to a fast relaxation (as seen in molecular solvents) and slow relaxation signals (Figure 3). It was suggested that such increase of polarization lifetime in frozen RTILs could be used to investigate inaccessible short-lived intermediates.

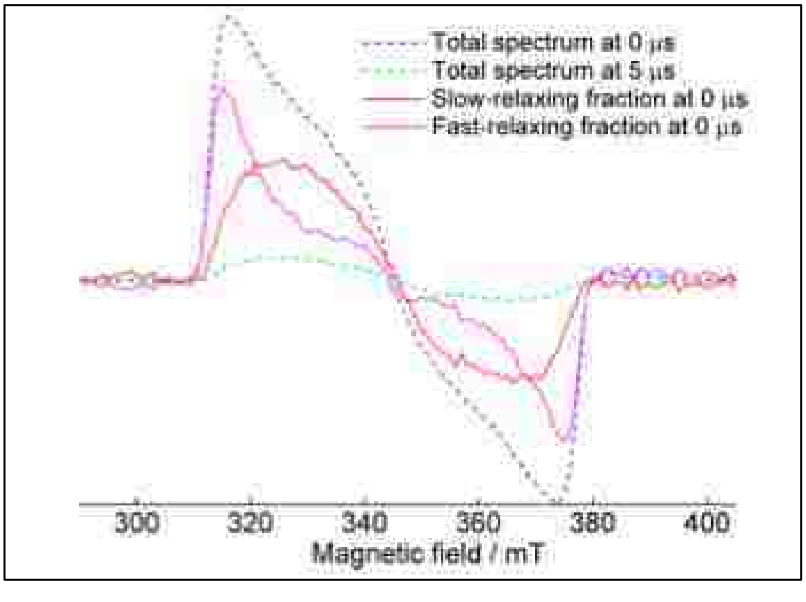

Figure 3: *Decomposition of TR-EPR spectrum of ZnTPP in BmimPF$_6$ at 200 K into two contributions of slow-relaxing and fast-relaxing fractions.*[26]

1.1.2.2 Nano-structures in the mixture

The structure of RTIL in the presence of molecular solvents has been also examined in the work of Padua et al., using molecular dynamics.[17,27] Mixtures of RTILs with acetonitrile led to four recognized regimes, depending on the ratio of RTIL/molecular solvent (Figure 4). At low concentrations of the RTIL, they behave as an electrolyte in solution. As the concentration of RTIL increases, aggregates (nano-domains) form. In RTIL-rich mixtures, the molecular solvents will become a dilute solute, interacting with the RTIL domains, breaking up the ionic network. The fourth regime is the neat RTIL.

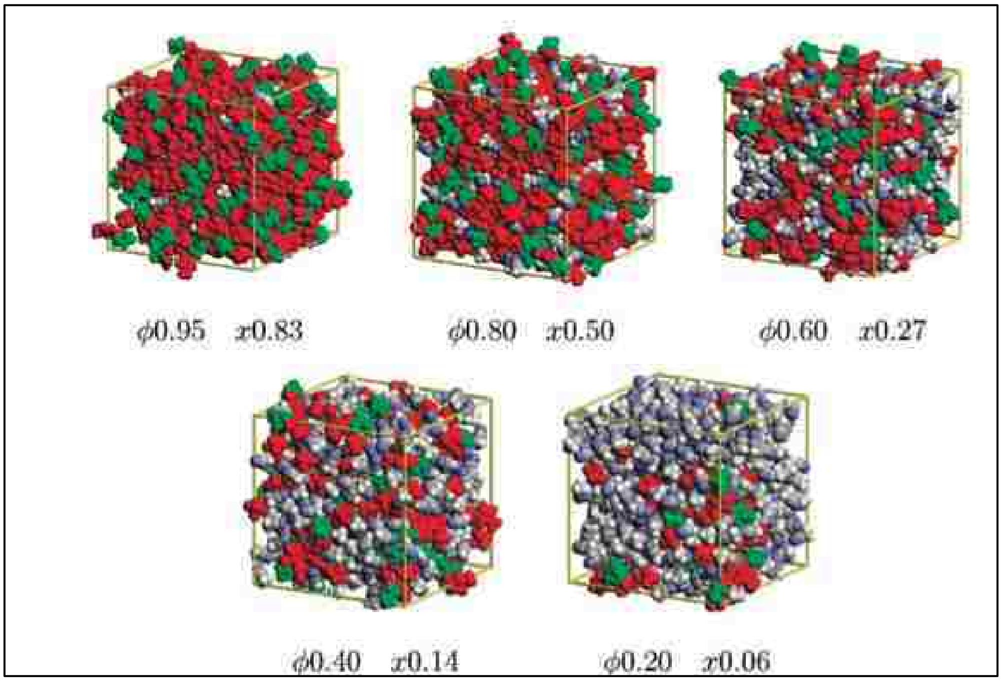

Figure 4*: Mixture of BMImPF$_6$ with acetonitrile at different compositions, identified by the volume fraction (Ø) and the mole fraction (x) of ionic liquid. Because the ionic liquid and the molecular compound have very different molecular sizes and weights, the volume fraction is for many purposes a convenient quantity to express composition.*[27]

Unlike surfactants, molecular dynamics showed that the RTIL nano-domains in RTIL/molecular solvent mixtures have a filamentous structure along with isolated ions in the aggregate regime. The formation of these aggregates can occur at relatively low mole fractions (0.06) of RTIL. In similar studies, water was shown to induce the formation of RTIL nanostructures in the mixture with imidazolium nitrate ionic liquids.[28] In these mixtures, polar, water and micelles networks could be visualized by molecular dynamics simulations. Hydrogen bonding interactions of the RTIL the anion with water could lead to highly ordered structures.

Significant experimental work has also been dedicated to investigate the nano-structures in mixed RTIL/molecular solvents. Early investigations on imidazolium RTILs in mixture with molecular solvents showed formation of hydrogen-bonding networks, based on NMR and conductivity measurements.[29] In mixtures with non-polar solvents, the non-conducting stacking imidazolium cations could lead to a quasi-molecular solution. Based on NMR analysis, Dupont et al. reported similar observations on pi-interactions of imidazolium RTIL in mixtures with $CHCl_3$ and DMSO.[30] Increasing the ionic liquid concentration in the chloroform mixture led to formation of hydrogen-bonded aggregates of the RTIL. In their work on imidazolium RTILs, Consorti et al. reported the presence of RTIL supramolecular aggregate in mixtures, using NMR and conductivity measurements.[31] In solution, this supramolecular structural organization could be maintained to a significant extent, indicating that mixtures of imidazolium ionic liquids with other molecules can be considered as nanostructured materials. At low concentrations, the anions and cations of the RTIL species were solvated mostly as ionic species. As the concentration of the RTIL increases, tight ion pairs and triplet or higher aggregates are formed. The formation of nano-structures was enhanced in mixtures with solvent of low dielectric constant (chloroform) compared to a high dielectric constant solvent (acetonitrile). Combining NMR spectroscopy and molecular dynamics, Remsing et al. demonstrated the aggregation of BMImCl in water and DMSO solutions.[32] Formation of clusters at low fractions (10%) of RTIL in DMSO and high concentrations (75%) in water, illustrated the ability of protic and aprotic solvents to disrupt RTIL clustering. Based on conductivity and molar volume measurements, Qingqin et al. evaluated the critical aggregation concentration (CAC) of imidazolium RTIL in molecular solvents (Figure 5).[33] It was found that CAC values of C_{12}MImBr increased in the sequence: H_2O<DMSO<ACN<DMF. The extent of aggregation was attributed to the solvophobic interactions of the cation alkyl chain with the solvent and the hydrogen-bonding interactions of the IL anions with the solvents. In more recent work, Zheng et al. investigated the presence of nano-clusters in RTIL-acetonitrile mixtures, using spectroscopic methods.[34] From ATR-FTIR and ^{1}H-NMR analysis, the results showed that these clusters were hydrogen bonding based networks. The downfield chemical shifts of RTIL cation hydrogen atoms in mixtures were indicative of the breaking apart of the ion clusters by acetonitrile molecules during the dilution process.

Using N,N-dimethyl-4-nitroaniline as a probe, Wenjing et al. studied the aggregation of imidazolium RTIL in molecular solvents, based on UV-visible and conductivity analysis.[35] It was shown that RTIL aggregates could form at lower concentrations of the RTIL in small dielectric constant solvents (like THF), where the probe could partition into the ionic liquid droplets. There was no obvious aggregation in acetonitrile mixtures, indicating that the two solvents were miscible at the molecular level.

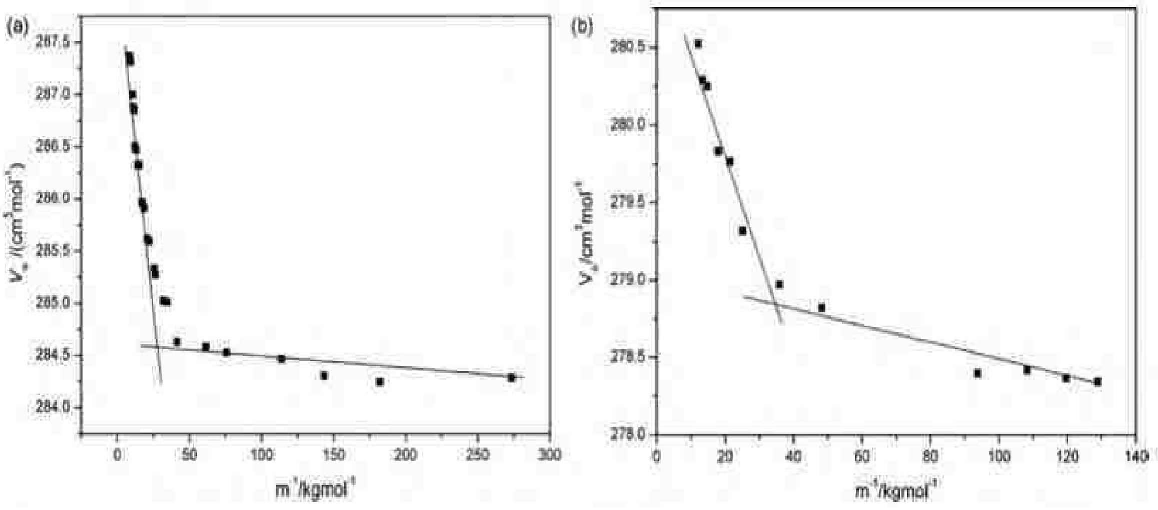

Figure 5*: Variation of the apparent molar volumes of C_{12}MImBr with the reciprocal of molality in (a) DMF and (b) ACN. CAC is the concentration at which the two straight lines intersect.*[33]

1.1.3 Impurities

One of the important issues when dealing with RTILs is their purity. Electrochemical analysis is usually very sensitive to impurities compared to other methods, such as spectroscopic techniques. Water has been shown to decrease the viscosity, increase the conductivity and modify the diffusion rates of species dissolved in RTILs. Moreover, water has been shown to shrink significantly the electrochemical window. The addition of 4% of water to $BMImBF_4$ and $BMImPF_6$ was enough to reduce the electrochemical window from 4 to 2.5 V. The processes responsible for the narrowing of the potential window are likely to be associated with water electrolysis.[36] Recently, an in situ method was suggested to determine water content, based on electro-oxidation of a gold electrode in RTILs to form gold oxide in the presence of water.[37] The reduction of the gold oxide back to gold gives rise to a cathodic stripping peak with a current that is proportional to the water concentration present in the RTIL (Figure 6).

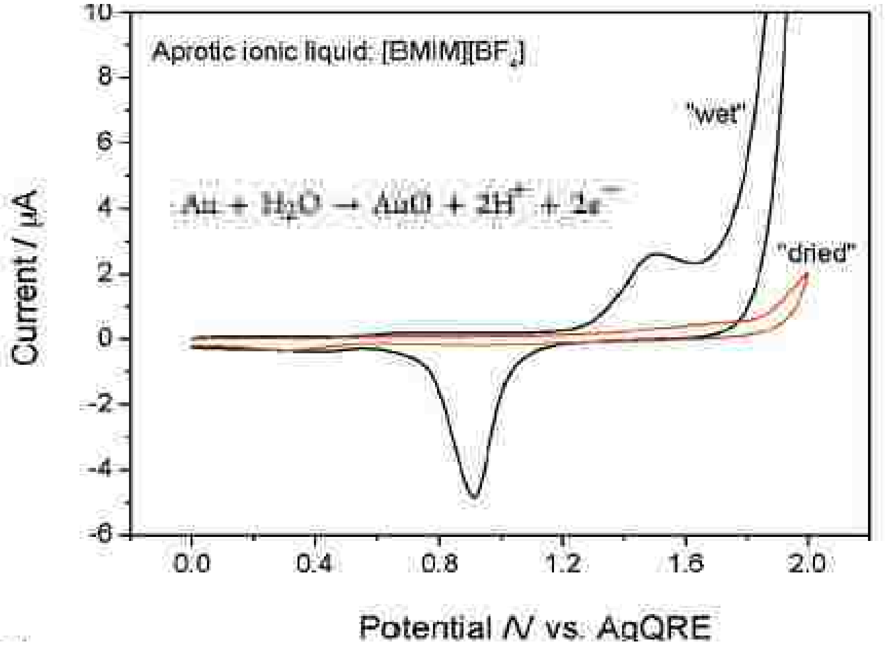

Figure 6*: Determination of water in RTIL by electro-oxidation of gold electrode.*[37]

Quantitative methods for the determination of unreacted and residual contaminants in imidazolium RTIL have been reported by Sark et al.[38] Impurities like 1-methylimidazole, imidazole and pyridine were analyzed using chromatographic methods. The presence of trace amounts of imidazole derivative impurities in BMImNTF$_2$ has been shown to stabilize gold nanoparticles.[39] In that work, the concentration of 1-methylimidazole in the RTIL was determined using proton NMR, at a detection limit of 1mM.

Oxygen, an electroactive molecule, is also easily dissolved in the RTILs from air and often accompanies water. Its removal is required before any electrochemical measurements and can be accomplished with extensive argon bubbling.[40] Halide impurities are also of concern when interpreting voltammetric responses. These impurities are generally introduced during the preparation of the RTILs, which commonly involves a halide precursor, mainly a chloride or a bromide salt.[41–43]

1.2 Electron transfer in RTILs

Several investigations have been dedicated to study how electrochemical processes are modified by the ionic liquids. These investigations have addressed changes on the thermodynamics (potential shifts), the electron transfer kinetics (apparent heterogeneous rate constants) and solution mass transport (diffusion coefficients).[44]

Electron transfer kinetics of ferrocene (Fc/Fc^+), as a standard reversible system, has been studied in several RTILs.[45–50]. However, the electrochemical characteristics remained controversial, producing widely different results depending to a large extent on the concentration of ferrocene, measurement technique, electrode material and surface. This discrepancy made some investigators report quasi-reversible behavior for the Fc/Fc^+ reaction, whereas other groups, working in the same ionic liquids, found a reversible electron transfer. Using electrochemical impedance spectroscopy (EIS) the electron transfer kinetics of the Fc/Fc^+ was investigated in NTF_2-based ionic liquids.[51] The estimated kinetic values in these ionic liquids corresponded to fast electron transfers and highly depended on the solution viscosity. *Table 1* summarizes kinetic values of Fc/Fc^+ obtained in RTILs.

Electron transfer of nitro compounds was studied both in acetonitrile and in NTF_2-based ionic liquids using cyclic voltammetry.[52] For all the compounds studied, the rate constants were lower in ionic liquids than in acetonitrile. Smaller changes in the kinetics were observed with more steric hindrance around the NO_2. An interpretation of this change was based on the contributions of outer and inner reorganization energies. The outer sphere contribution involves the interaction between the cation of the RTIL and the radical anion of the molecule, while the inner sphere contribution reflects the turning of the nitro group out of the plane of the ring. It was suggested that the passage from ACN to the RTILs increased the outer sphere contribution, but this effect was partially compensated by a diminution of the inner sphere reorganization. Similar to molecular solvents, reduction potentials became more negative in RTIL, when donor groups were introduced on the aromatic ring. The potentials were always less negative in ionic liquids than in acetonitrile, due to the higher stabilization of the electrogenerated radical anion by the cation of the ionic liquid, through ion-pairing associations. The higher stabilization in imidazolium RTIL was attributed to the planar geometry of the imidazolium cation and to its ability to form hydrogen bonds.

Table 2: List of reported values of k^0 of Fc/Fc^+ in RTILs.

RTIL	***k^0(cm/s)*** ^{Ref}
$EMImNTF_2$	0.15-0.2 [45]
	0.21 [46]
$BMImPF_6$	2.5×10^{-3} [47]
	2.3×10^{-4} [48]
HMe_3NNTF_2	0.2 [49]
$BMPyrNTF_2$	4.3×10^{-3} [50]
$EtMeImNTF_2$	> 0.18 [51]
$BuMePyrNTF_2$	> 0.12 [51]
$Bu_3MeAmNTF_2$	> 0.049 [51]

In their work on the oxidation of organic molecules in RTILs, Lagrost et al. reported no impact of RTIL on the electrochemical process, compared to molecular solvents.[45] Although no significant shifts in oxidation potentials were observed in RTILs, small variations of 10-20 mV to more positive values could be seen from *Table 3*. This result indicated a weak interaction and solvation of cation radicals by RTIL anions. Decreases in diffusion coefficients and electron-transfer kinetics were mainly due to higher viscosity in RTILs.

Table 3: Electrochemical characteristics for anthracene oxidation in RTILs[45]

Solvent	**$E_{1/2}$ (V/SCE)**	**D (cm^2/s)**	**k_s (cm/s)**
$BMImNTF_2$	1.27	2.8 10^{-7}	0.1 – 0.2
$EMImNTF_2$	1.27	5.3 x 10^{-7}	0.6 – 0.7
$(C_8H_{17})_3NCH_3NTF_2$	1.26	-	-
$BMImPF_6$	1.27	5.6 x 10^{-7}	0.2 – 0.3
Acetonitrile	1.25	2.5 x 10^{-5}	3 - 5

One electron oxidation and reduction of 2,2-diphenyl-1-picrylhydrazyl (DPPH) have been studied in RTILs by Taylor and al.[53] Variation in the potential differences (ΔE) between the two processes in several ionic liquids showed dependence upon the RTIL anion. In contrast to molecular solvents, attempts to correlate the changes in ΔE with RTILs Gutmann DN and Lewis basicity were not satisfactory, demonstrating complex solvation modes in these media. Although not much effort was dedicated to investigate variation of ΔE in mixtures RTIL-molecular solvent, the authors presumed partitioning of solutes into RTIL domain even at low fractions of the ionic liquid.

There has been significant work dedicated on the evaluation of diffusion in RTIL solutions. Diffusion coefficients values were generally found about 2 orders of magnitude lower in RTILs than molecular solvents, mainly due to the high viscosity in the former media.[54–56] Diffusion of electroactive materials in RTILs and molecular solvents has been observed to follow the Stokes-Einstein relationship:

$$D = \frac{k_B T}{6\pi\eta r}$$

Where k_B is the Boltzmann constant, T is the temperature, η is the viscosity, and r is the hydrodynamic radius of the diffusing species. This equation worked reasonably well for large changes in viscosity, as was seen for ferrocene in acetonitrile (0.34 cP) and $BMImPF_6$ (308 cP).[57]

In addition to slower diffusions, unequal diffusion coefficients of redox species have been observed in RTILs. The most significant difference was observed in the reduction of oxygen to superoxide in two NTF_2 ionic liquids, resulting in changes of the diffusion regime (*Table 4*).[58] While the diffusion of oxygen to the electrode was mostly spherical (sigmoidal shaped), diffusion of superoxide appeared to be planar (peak shaped) (*Figure 7*).

Table 4: Diffusion coefficients of Oxygen and superoxide in NTF RTILs[58]

RTIL	**D O_2 (m^2/s)**	**D $O_2^{\cdot-}$ (m^2/s)**
$EMImNTF_2$	7.3×10^{-10}	2.7×10^{-10}
$N_{6222}NTF_2$	1.48×10^{-10}	4.66×10^{-12}

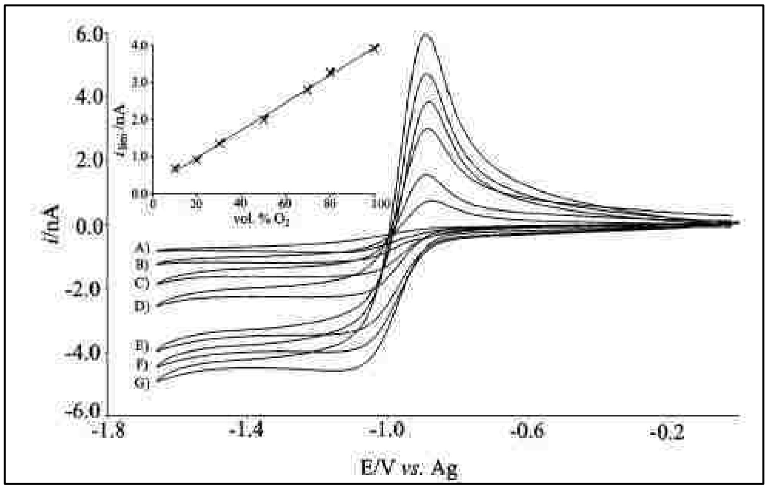

Figure 7: Reduction of O_2 in $N_{6222}NTF_2$, 1V/s, 10.8 μm Au, at varying O_2 volume.[58]

The higher viscosity of $N_{6222}NTF_2$ compared to $EMImNTF_2$ increased the ratio of diffusion coefficients between oxygen and superoxide to a factor of 30. The ratio of both diffusion coefficients was found to follow the change of the viscosity upon addition of DMF to ammonium-based RTIL.[59] Strong interactions of the superoxide with the RTIL resulted in larger change of its diffusion coefficient by the mixture composition. Smaller differences in diffusion coefficients between neutral ($4.81x10^{-11}$ m^2/s) and anion ($1.70x10^{-11}$ m^2/s) were observed for the reduction of benzoquinone in $EMImNTF_2$.[60] One major consequence in changes of the diffusion regime to non-steady state conditions in RTILs consisted in the difficulty in accurately measuring the diffusion coefficients. In highly viscous media, the transient currents are more subjected to Ohmic drop problems, making modeling analysis difficult. By semi-integrating transient voltammograms obtained at macro disk electrode, Bentley et al. could accurately evaluate the diffusion coefficient of $[Co(Cp)_2]^+$ in imidazolium RTIL at 9.4×10^{-9} cm^2 s^{-1} versus 1.6×10^{-5} cm^2 s^{-1} in acetonitrile.[61]

The two-electron reduction of benzaldehyde in pyrrolidinium and imidazolium NTF_2-based ionic liquids was investigated by Brooks and Doherty.[62] Although both media exhibited similar bulk viscosities, large discrepancies were found when comparing the voltammetry in these media. The two-electron reduction was unaffected in pyrrolidinium-based ionic liquids as compared to molecular solvents. A high stabilization of more than a 0.5V for the second reduction together with a 1 order of magnitude decrease of the electron-transfer kinetics, were observed in the imidazolium RTIL. Since NTF_2 was a common anion between both RTILs, this higher stabilization was attributed to π-π interaction that occurs between imidazolium cation and the aromatic dianion.

The two reductions of trans-stilbene have been studied by cyclic voltammetry in the molecular solvent, acetonitrile, and in three NTF_2-based ionic liquids, by Abdul-Rahim and al.[63] The irreversibility of the second reduction in acetonitrile at high concentrations of solute indicated that the solvent protonated the very basic dianion. In RTILs, significant reversibility was achieved when the solute concentration exceeded the water content in these media. The potentials of the two electron oxidation of bisferrocene (BF) were evaluated versus decamethylferrocene (DmFc) in RTILs.[64] While linear dependence was observed for the first oxidation potential with RTIL anion volume, the second oxidation showed no correlation. This was attributed to poor solvation of the dication by larger RTIL anions. Of note, due to complex interactions in RTILs, a better evaluation of these trends could have been achieved if a larger data set (more than three points) of anions was considered.

Few computational works have been devoted to evaluate electrochemical processes of organic molecules in RTILs. Nikitina et al. reported redox potentials of quinone (Q) compounds in RTILs and molecular solvents, using DFT methods.[65] Values for chloranile, as a model compound for quinone compounds are shown in *Table 5*. While polarized continuum model (PCM) gave a good correlation of Q/Q•- potentials with experimental values, the calculated $Q^{\bullet-}/Q^{2-}$ potentials did not correlate well. A better correlation could be achieved using microscopic treatment, involving RTIL-quinone clusters. Where the full solvation energy was calculated as the sum of electrostatic component and estimated in terms of the PCM formalism and the ion-pairs energies ΔG_{chem}:

$$-FE = \Delta G_{gas} + \Delta G_{Sol} = \Delta G_{gas} + \Delta G_{PCM} + \Delta G_{chem}$$

With F is the faraday constant and E is the electrode potential

Strong interactions between the dianion and the RTIL cation, mainly through hydrogen bonding, resulted in shifting the potentials to more positive values. However, this approach overestimated the potentials shifts in the RTIL, leading to difference potentials of 200 mV compared to experimental value of 500mV. The magnitude of these specific ion-ion interactions for highly charged species of polytungstates with RTIL cation was emphasized in a more recent work of the same authors.[66] These results suggested that specific solvation models, like molecular dynamics (MD), are needed to account for explicit solvation of redox species in RTIL media.

Table 5: Calculated ($E_{1, Calc}$ and $E_{2, Calc}$, V) and experimental ($E_{1, Exp}$ and $E_{2, Exp}$, V) vs Fc^+/Fc and potentials differences ($\Delta E_{1\text{-}2, Exp}$ and $\Delta E_{1\text{-}2, Calc}$, V) in several solvents[65]

Reactant	**Solvent**	**$E_{1, Calc}$**	**$E_{1, Exp}$**	**$E_{2, Calc}$**	**$E_{2,Exp}$**	**$\Delta E_{1\text{-}2, Exp}$**	**$\Delta E_{1\text{-}2, Calc}$**
Chloranile	$BMImBF_4$	-0.39	-0.28	-1.22	-0.78	0.5	0.83
	Acetonitrile	-0.23	-0.16	-0.91	-0.95	0.79	0.68
	Propylene Carbonate	-0.33	-0.17	-0.92	-0.88	0.71	0.59
	Dimethylformamide	-0.26	-0.13	-0.99	-1.04	0.91	0.73
	Dimethyl Sulfoxide	-0.25	-0.12	-0.79	-0.95	0.82	0.54
	Benzonitrile	-0.36	-0.17	-1.06	-0.93	0.77	0.7
	Dimethylacetamide	-0.26	-0.12	-0.98	-1.05	0.94	0.73

1.3 Redox systems

1.3.1 Dinitrobenzene (DNB)

Ion pairing effects on the reductions of dinitrobenzene in molecular solvent have been investigated by Evans et al.[67] Based on their results, it was shown that structural effects due to solvation are by far the most important factors in reducing the difference in potentials on going from gas phase to solution. Using DFT calculations, the gas-phase free energies of the neutral, anion radical and dianion were calculated, where the difference in potentials $(\Delta E_{12})_{vac}$ was +4.496 V. Upon solvation in acetonitrile solution, the value $(\Delta E_{12})_{CH3CN}$ is +0.254, while presence of an electrolyte in experimental analysis decreased the $\Delta E_{12,CH3CN,TBAP}$ to +0.221 V (*Figure 8*). The inclusion of four methyl groups onto the aromatic ring, forming 3,6-dinitrodurene, led to contraction of the reduction waves with a potential difference ΔE_{12}= -0.170V (*Figure 9*).[68] This negative difference was described as potential inversion, where the second reduction occurs more easily than the first reduction. Theoretical calculations showed that such inversion was mostly due to structural change of the dianion to a folded form, compared to twisted forms of the neutral and radical anion. In general, these structural changes are associated with the relief of steric stress when the electron transfer affects the bond strength. The extent of the stabilization of the frontier orbitals LUMO and SOMO, respectively for the neutral and radical anion, upon electron transfers would determine the magnitude of the potential inversion. Ion pairing interactions have been also reported as a factor that may lead to potential inversion.[69] The effects of hydrogen bonding interactions, solvent and electrolytes nature on potential inversion have been also reported in literature.[70,71]

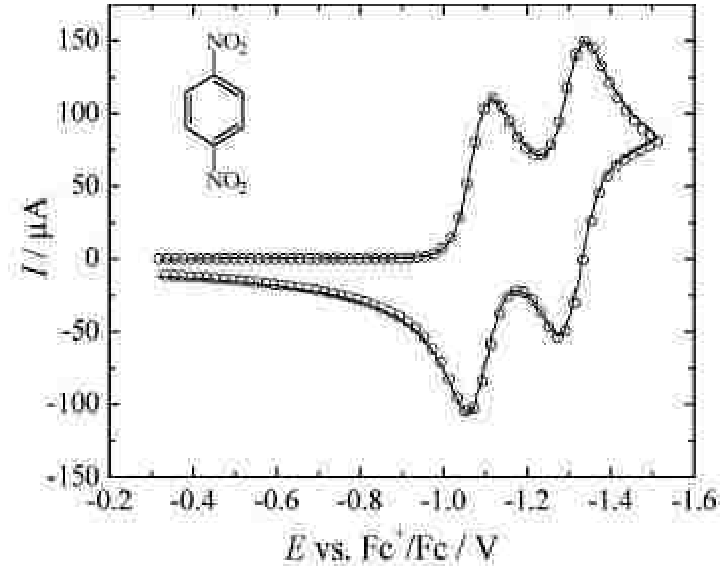

Figure 8: Cyclic Voltammogram of DNB in acetonitrile. Simulation potentials: $E_{1/2,1}$ *= - 1.084 V,* $E_{1/2.2}$*=-1.305 V.*[67]

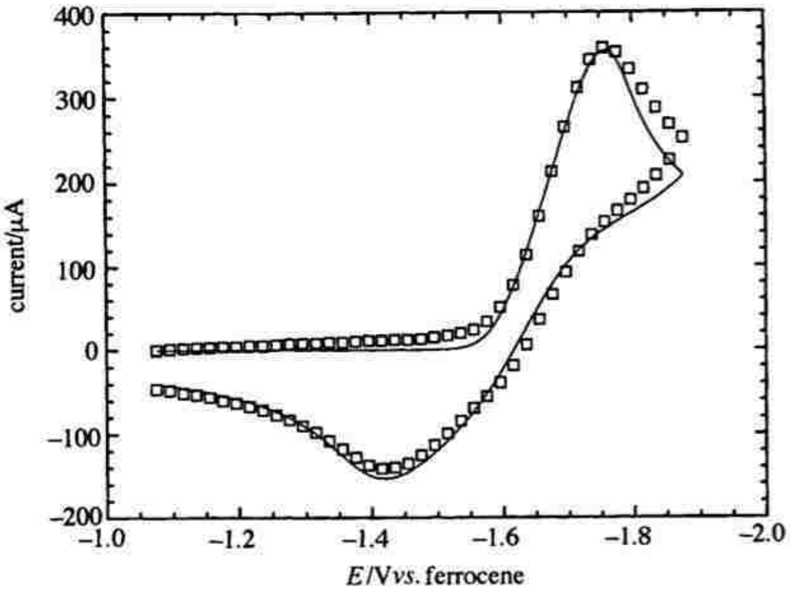

Figure 9: Cyclic voltammogram of 2.00 mM 3,6-dinitrodurene in acetonitrile containing 0.10 M $TBAPF_6$*, at 2V/s. Simulation potentials:* $E_{1/2,1}$ *= - 1.61 V,* $E_{1/2.2}$*=-1.44 V.*[68]

The UV-Visible spectrum of DNB anion radical was reported in the work of Sauer et al, with spectral features at 400 nm and a broad band at 800nm. The spectrum of the dianion has not been reported.[72] Delocalization of the spin of the radical anion, on both nitro groups through the aromatic ring, has been observed by spectroelectrochemistry and ESR. While the second electron transfer leads to dianion formation, with no unpaired electrons, the ESR signal of the first reduction was not consumed even at the second wave potential. This was indicative of comproportionation of the dianion with neutral species to form the radical anion.[73] Their DFT calculations also showed that spin densities were equivalently located on the nitro groups of the radical species. Tian and Jin used FTIR spectroelectrochemistry to track the change of intermediates and products during electrochemical reduction of DNB in protic and aprotic media. In their experimental conditions, both radical anion and dianion were stable, where the dianion was shown to be a better hydrogen-bonding acceptor than the radical anion.[74] Although the electrolysis experiments revealed significant changes in the IR spectrum, the basis for the assignment of the relevant bands and their shifts was not well characterized. For instance, the shifts of the N=O vibration from 1549cm^{-1} to 1210 cm^{-1} upon first reduction and to 1356 cm^{-1} upon second reduction were not discussed. In general, the bands assignment, specifically, in the finger print region is not straightforward and requires additional analysis like isotopic analysis or computational calculations.

Fry has reported a single two-electrons reduction wave in BMImBF$_4$, with a ΔE_{12} value around 0 mV based on the ΔE_p value of the cyclic voltammogram, suggesting a “potential inversion” in the RTIL (*Figure 10*).[75] The shift from two one-electron waves to one two-electron wave was ascribed to strong ion pairing in the ionic liquid.

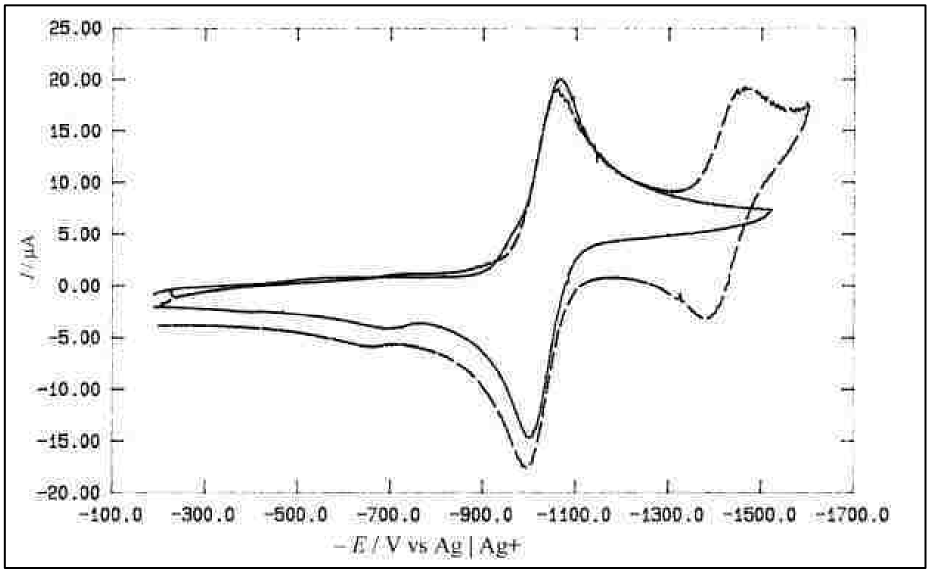

Figure 10: (a) Solid line: cyclic voltammogram of 1,4-dinitrobenzene in $BMImBF_4$ *at a glassy carbon electrode and a scan rate of 100* $mV\ s^{-1}$*. (b) Dashed line: nitrobenzene (3 mM) added to the solution of (a).*[75]

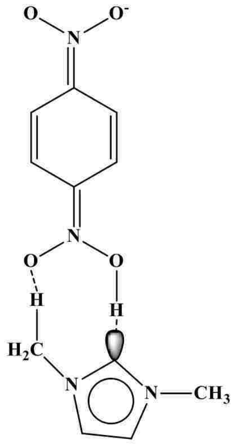

Figure 11: ion paring of imidazolium cation with DNB dianion.[76]

Later on, Minami and Fry have examined the interactions between solvent, electroactive species and electrolyte ions.[76] DFT calculations predicted that the dianion of DNB interacts with imidazolium cation in a very specific manner. Rather than a stacking arrangement, the imidazolium ion forms an adduct where the hydrogen of the central ring carbon (C-2) can be transferred to the oxygen of the DNB^{2-} ion (*Figure 11*). Ion pairing effects of imidazolium cations, as RTILs, on DNB reductions in molecular solvent, have been reported by Syroeshkin et al.[77] Addition of about 0.5mM of the RTIL in DNB solution in DMF reduced the reduction potential difference (ΔE_{12}) by about 0.16V (*Figure 12*). We note that even at these high concentrations of $BMIm^+$, two separate waves were observed in DMF. Evaluation of association constants revealed that up to four BMIm cations were coordinated to the DNB dianion, through hydrogen bonding interactions. In regard to our investigation, such observation is consistent with the formation of RTIL nanostructures in mixture solvents.

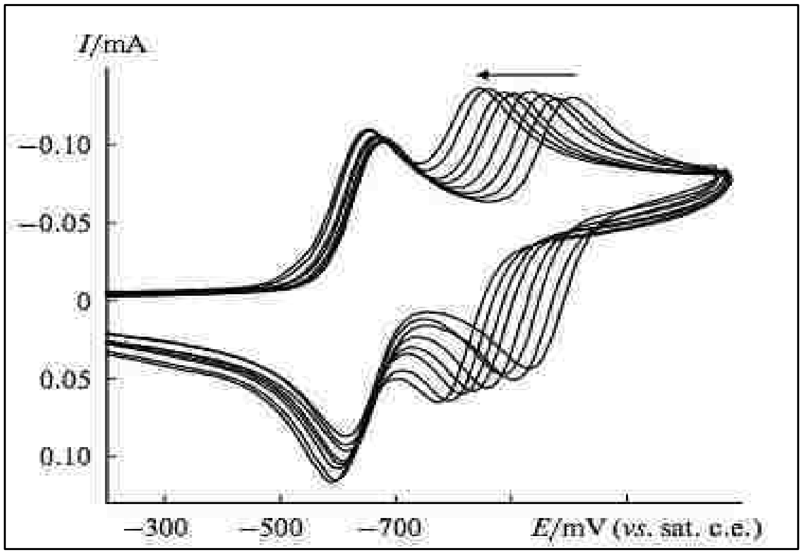

Figure 12: Cyclic voltammograms of 5 mM solution of DNB in 0.1 M Bu_4NClO_4/DMF in the presence of 0, 0.025, 0.050, 0.100, 0.175, 0.250, 0.350 and 0.475 M $BMImBF_4$. 0.1 V/s.[77]

1.3.2 Tetracyanoquinodimethane (TCNQ)

7,7,8,8-Tetracyanoquinodimethane (TCNQ) forms organic conductors including radical and charge-transfer salts. TCNQ has been the subject of many electrochemical and spectroscopic studies on account of its high potential use in electrochemical applications.[78,79] TCNQ can be reduced in two sequential one-electron transfers to form the radical anion and dianio.[80,81] The two reduction waves are separated by about 0.5V in molecular solvents. UV-Visible spectroelectrochemistry for the first reduction of TCNQ in acetonitrile has been done and the absorbance spectrum of the radical anion has been reported.[81]

The infrared spectroelectrochemistry of TCNQ reduction has been reported in molecular solvents.[82,83] The characteristic cyanide vibrations of the redox products were observed between 2000-2300 cm^{-1}. TCNQ had one band at 2224 cm^{-1} for two degenerate states (ν_{19} and ν_{33}). Upon reduction the two levels split, and gave separate bands. For TCNQ^{-}, the bands were observed at 2156 and 2182 cm^{-1} in acetonitrile/TBAP. Further reduction to TCNQ^{2-} caused an additional downshift to 2106 and 2153 cm^{-1}. The LUMO for TCNQ is anti-bonding with respect to the CN triple bond, which led to the downshift of the ν_{CN} stretching bands.[82] Addition of Na^{+} and Li^{+} ions caused no significant changes in the TCNQ^{-} spectrum. For the dianion, though, the bands were upshifted due to ion pairing. The larger shift was for the lithium salt with the 2153 cm^{-1} band upshifting to 2166 cm^{-1}, and the 2106 cm^{-1} band upshifting to 2118 cm^{-1}. A larger upshift of 2130cm^{-1} was reported by Lipping and Xiangqin.[84]

The current of the two-electron reduction was evaluated in respect to differences in measured diffusion coefficients of TCNQ redox products in molecular solvent.[85] It was shown that comproportionation of dianion with neutral species would have more impact on the observed current, when diffusions are significantly unequal. Hence, the current ratio of the two waves (n_{app}) was predicted to increase when the diffusion coefficient of radical anion is significantly greater than the neutral (*Figure 13*).

Outside the work of Zhao et al., little work has been done on the voltammetry of TCNQ in RTILs.[40] In that work, effects of purging the $BMImBF_4$ ionic liquid with nitrogen on the voltammetry of TCNQ have been studied. Mainly, the drop in oxygen concentration in the ionic liquid, upon nitrogen purging, was accompanied by removal of water. In $BMImBF_4$, the potential difference between the waves was about 0.4V.

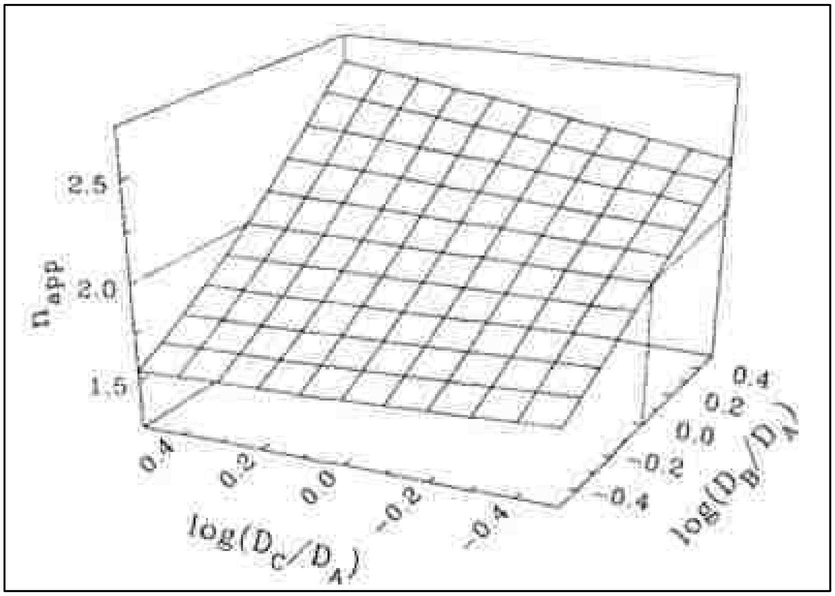

Figure 13: Apparent n value for chronoamperometry for a potential where the two-electron reaction of A (neutral) occurs as a function of the diffusion coefficients of species B (anion) and C (dianion) relative to the diffusion coefficient of A.[85]

1.3.3 Fullerene (C_{60})

Buckminsterfullerene, C_{60}, can be reduced in aprotic solvents in six one-electron waves.[86–89] Five reversible waves were observed by Dubois et al. using cyclic voltammetry.[90] A reversible sixth wave was observed at low temperatures by Xie et al.[91] and by Ohsawa and Saji (*Figure 14*).[92] The effect of supporting electrolyte and solvent properties on the redox potentials was studied by Dubois et al.[93] For the first reduction (C_{60} to C_{60}^-), a plot of the first $E_{1/2}$ values ($E_{1/2,1}$) correlated well with the Gutmann donor number (DN), with the reduction shifting to more positive values with higher DN (*Figure 15*). The results indicated that solvents of higher donor abilities stabilized C_{60}^- better than C_{60}. These shifts in the $E_{1/2,1}$ values were interpreted in terms of the solvophobic effect. The solvophobic effect caused a relative stabilization of C_{60}^- over C_{60} due to donor solvents and/or the presence of large cations. The $E_{1/2,2}$ values continued to exhibit solvophobic effects, but electrostatic ion pairing was more significant for the higher charged anion. The $E_{1/2,3}$ values were essentially independent of the Gutmann DN, but the $E_{1/2,3}$ was linearly correlated with the Gutmann AN. This result was somewhat discounted because of the significant effect that THF (which had the lowest AN) had on the overall slope.

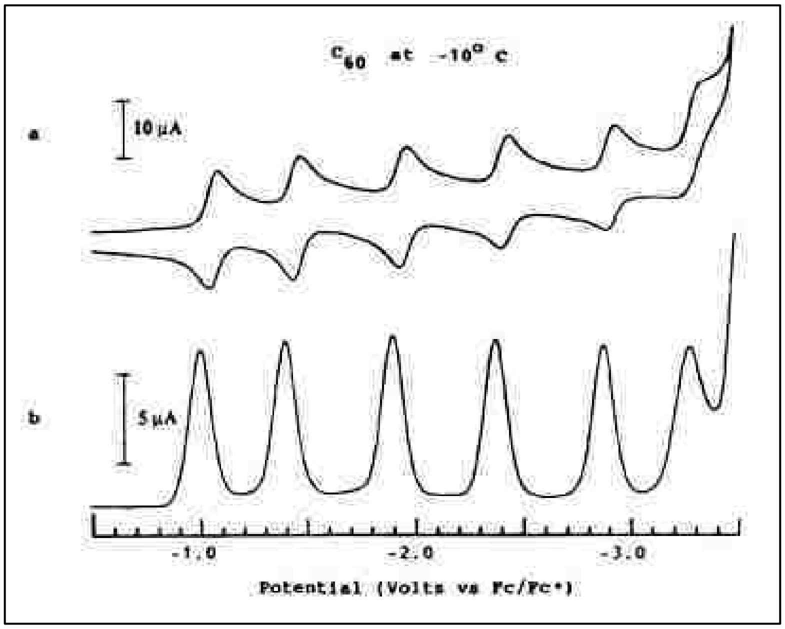

Figure 14: Reduction of C_{60} in acetonitrile-toluene with $TBAPF_6$ as supporting electrolyte at -10 °C. Cyclic voltammetry (a). Differential pulse voltammetry (b). 50 mV pulse, 50 ms pulse width, 30 ms period, 25 mV/s scan rate.[91]

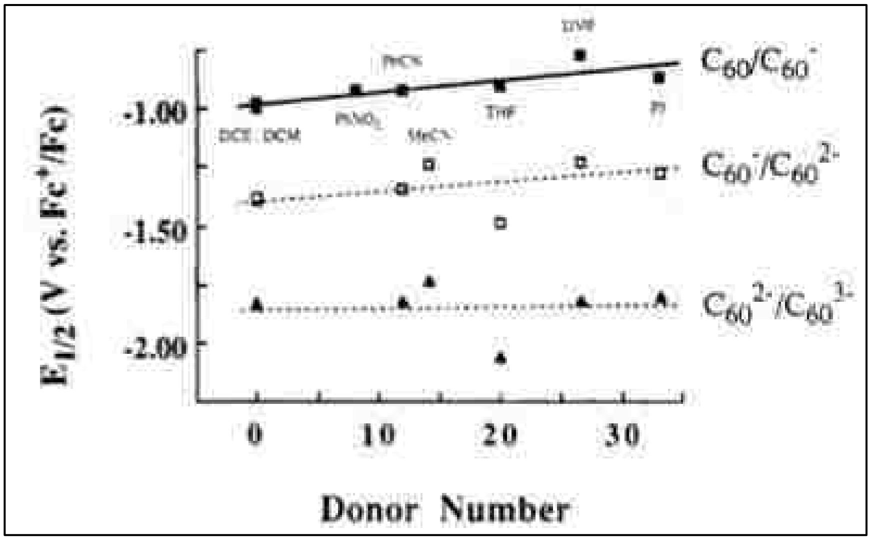

Figure 15: Correlation of half-wave potentials for the first three electron transfers of C_{60} and the Gutmann DN of the solvent in solutions containing 0.1 M TBAP.[93]

In later studies, Noviandri et al. reexamined the potential shifts using a different reference system.[94] They emphasized the importance of using decamethyl ferrocenium (DmFc) as the reference potentials in order to minimize the effect of solvent on the reference potential.[95] Using the DmFc reference system, the formal redox potentials of the C_{60} couples exhibited substantial dependences on the solvent and become more solvent-dependent as the charge increases. Variation of the half-potential of the third reduction wave (versus $DmFc^{+/0}$) as a function of Gutmann AN of molecular solvents is shown in *Figure 16*. A positive slope of $E_{1/2}$ as a function of the Gutmann acceptor number (AN) was observed for all studied waves, as expected for the stabilization of the anionic species by the Lewis acidity of the solvent.[94]

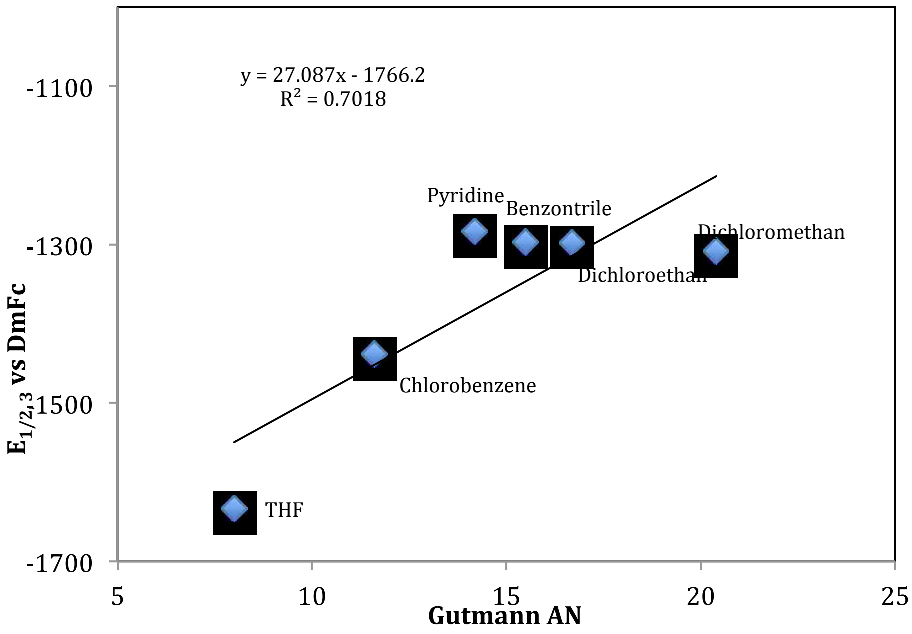

Figure 16: Correlation of $E_{1/2,3}$ of C_{60} reduction and the Gutmann AN of molecular solvent.[94]

The products of the first three waves, which can be generated by coulometry or spectroelectrochemistry[86,88,93] or isolated as salts by chemical reduction[96–98] were reported in literature. The spectroelectrochemical reduction of C_{60} caused the bands at 257 and 330 nm to shift to 262 and 339 nm, respectively, with a decrease in absorbance. Further reduction to C_{60}^{2-} led also to small red shifts in the λ_{max} values (263, 340 nm). Changes in the near infrared spectrum though were much more informative of the oxidation state of the fullerides. The near infrared spectrum of C_{60}^{-} had a strong band at 1073 nm, with weaker bands at shorter wavelengths (995, 917 nm).[99–102] The major band has been assigned to the allowed $t_{1u} \rightarrow t_{1g}$ transition, and the weaker bands to vibrational fine structure.[89] The C_{60} dianion has bands at 952 and 830 nm and the trianion at 1367, 956, 878 and 788 nm (*Figure 17*).[99,101,103–105]

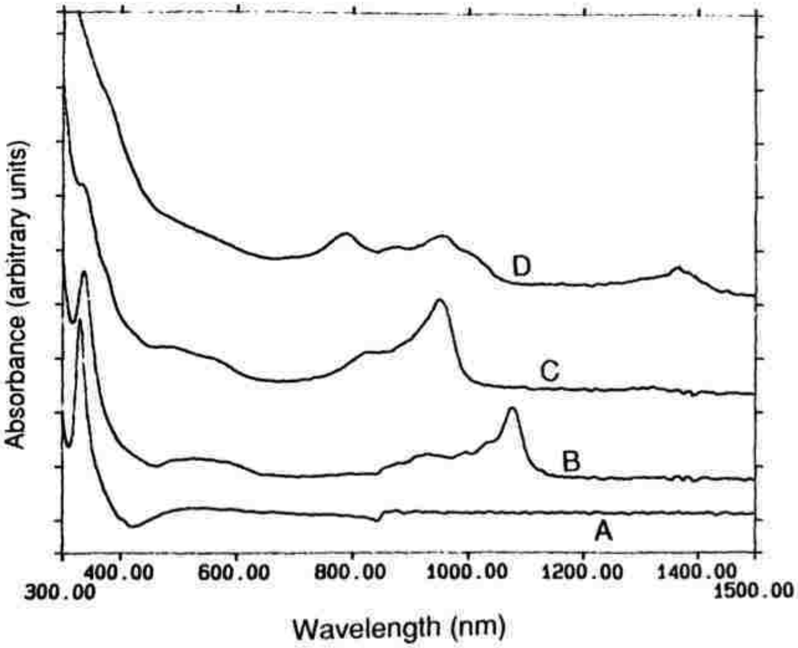

Figure 17: UV-visible-Near IR absorption spectra for (A) C_{60}, (B) C_{60}^{1-}, (C) C_{60}^{2-}, and (D) C_{60}^{3-}. The feature at -840 nm corresponds to an instrument grating change.[103]

Limited studies have been carried out in RTILs because of the insolubility of C_{60} in those solvents. Duffy and Bond have studied the voltammetry of C_{60} in toluene using a phosphonium-phosphate ionic liquid as an electrolyte.[106] Addition of the ionic liquid enabled sufficient conductivity for voltammetric analysis of C_{60} in toluene, a very low dielectric solvent, while potentially retaining its solvation beneficial properties. The electrochemistry of C_{60} films in contact with N-butyl-N-methylpyrrolidium-based ionic liquids was studied by Ueda et al.[107] In this case, six waves were observed using cyclic voltammetry (*Figure 18*). A decrease in the currents upon additional scanning indicated significant solvation of the highly charged C_{60} anions in the RTIL. Damlin et al. used ATR-FTIR to study cast C_{60} films in contact with three different imidazolium RTILs.[108] Under the conditions used, the film was stable over the first three reductions when RTILs were the solvents. These results indicated that the four redox species (C_{60}, C_{60}^{-}, C_{60}^{2-} and C_{60}^{3-}) had limited solubility under these conditions, though some dissolution was observed. On the other hand, the slow diffusion of redox species in RTILs may have masked the amount of dissolution.

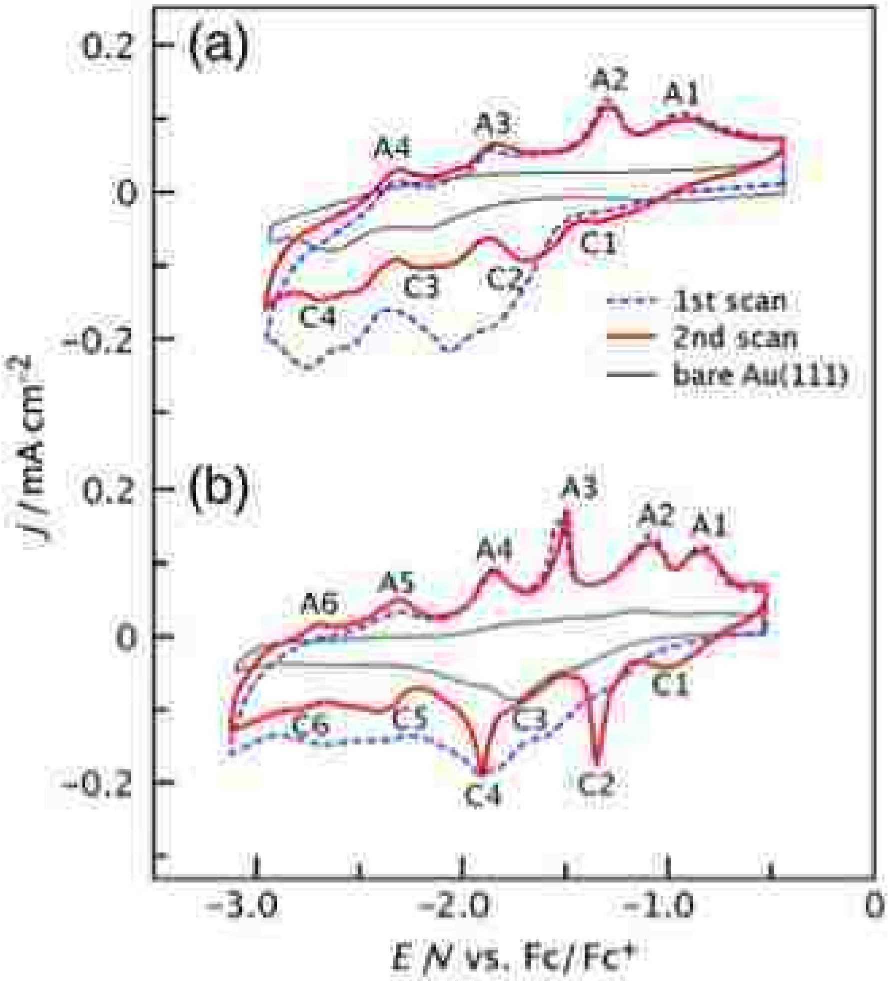

Figure 18: Cyclic voltammograms of a clean Au(111) electrode (gray line) and a C60-modified Au(111) electrode obtained in NTF-based ILs with (a) $N_{1,4,4,4}{}^{+}$, (b) C_4MPyrr^{+}, respectively, at 25 °C. The scan rate was 0.5 Vs^{-1}.[107]

1.3.4 Metalloporphyrins

Porphyrins and related tetrapyrrole macrocyclic ligands are one of the most prominent ligand types studied in electrochemistry. Metalloporphyrins have several accessible oxidation states, which is crucial in multi-electron transfer reactions. In most cases, a large number of these oxidation states are stable on the timescale of voltammetric experiments. This feature renders them suitable model compounds to evaluate the effect of RTILs on electrochemical processes. In our investigation, two types of metalloporphyrins were selected, which contain two different metals and ligands: iron and nickel metal centers, with tetraphenylporphyrin (TPP) and octaethylporphyrin (OEP) as ligands.

1.3.4.1 Nickel octaethylporphyrin (NiOEP)

The voltammetry of nickel porphyrin complexes exhibits at least one reversible reduction wave and two one-electron oxidation waves.[109–113] In their work on voltammetry of nickel porphyrins in DMF, Kadish et al. reported formation of π-radicals anion and cation formation upon first reduction and oxidation, respectively. At room and higher temperatures, the first oxidation may lead to dimerization of the cation, forming a film on the electrode surface. At lower temperature, the electrogenerated cation could be stabilized, resulting in one-electron reversible oxidation waves.[114] Three waves have been observed for the oxidation of NiOEP. The first two were reversible, while the third wave's reversibility depended upon the porphyrin ligand. The product of the first wave led to a π-cation radical, ($Ni^{II}(OEP^{+\cdot})$), as shown by UV-visible, EPR and resonance Raman spectroscopy.[110,115–121] Scheidt and co-workers have shown that mixed valence dimers, $[(Ni(OEP)_2]^+$, can also be formed. The mixed dimer can be reduced/oxidized at about the same potential as the Ni(OEP) oxidation wave.[118,119] The second wave led to further oxidation of the porphyrin to the dication. A weak broad visible spectrum with a Soret band at 330 nm was observed (*Figure 19*).[117] This spectrum was similar to the zinc and magnesium dications.[120] A third oxidation wave was observed by Kadish et al. which was deduced to be a Ni(III) porphyrin species.[110] The wave was irreversible for Ni(OEP) due to an EC mechanism, but reversible waves were observed for other porphyrin structures.

While an early report by Kadish and co-workers reported ligand centered reduction, Lexa et al. formulated the first reduction product to be $Ni^I(OEP)^-$ using UV/visible and EPR spectroscopies.[122] Comparison of the absorption spectrum of the reduced $[NiOEP]^-$ to M(I) spectra compared to M(II) radical anion, indicated that the first reduction product is Ni(I) species (*Table 6*). This result was confirmed by Nahor et al., though they did observe that some nickel porphyrins could form π-anion radicals.[121] Further studies about the parameters determining the site of the electron transfer were reported by Kadish et al.[110,123] The temperature, type of porphyrin macrocycle, solvent and axial ligand coordination were the main factors that influence the electroreduction site in (P)Ni. These factors can lead to the formation of Ni(I) porphyrins, Ni(II) porphyrin π-anion radicals, or Ni(II) porphyrin π-anion radicals with some Ni(I) character. The product of the second wave has not been studied in detail. The redox processes of NiOEP can be formulated as follow:

$$Ni^{II}(OEP) \rightarrow Ni^{II}(OEP^{\cdot})^{+} + e^{-}$$

$$Ni(OEP) + Ni^{II}(OEP^{\cdot})^{+} \rightarrow [Ni(OEP)]_2^{+}$$

$$Ni^{II}(OEP^{\cdot})^{+} \rightarrow Ni^{II}(OEP)^{2+} + e^{-}$$

$$Ni^{II}(OEP) + e^{-} \rightarrow Ni^{I}(OEP)^{-}$$

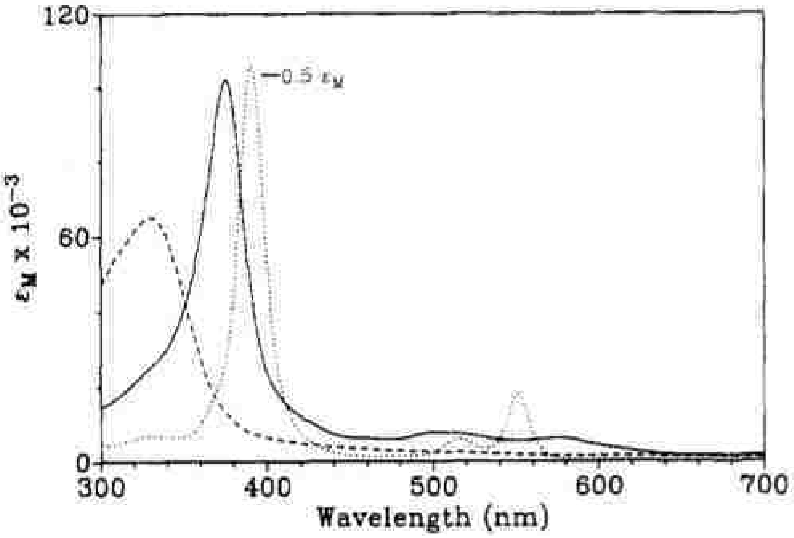

Figure 19: UV-vis spectroelectrochemical oxidation of Ni(OEP) (pointed line) to Ni(OEP)$^{\cdot+}$*(solid line) and Ni(OEP)*$^{2+}$*(dashed line) in* CH_2Cl_2*, 0.1 M TBAP.*[117]

Table 6: Comparison of the spectral characteristics of (OEP)Ni^{I} *with those of (OEP)Co*^{I}*, (OEP)Fe*^{I} *and the anion radical of (OEP)Zn*^{II}*.*[111]

Complexes	**Bands**
Ni(I)OEP^{-}	346, 407, 506, 545, 617
Co(I)OEP^{-}	352, 413, 510, 546
Fe(I)OEP^{-}	374, 400, 493, 524, 565, 684
Zn(II)OEP$^{\cdot-}$	410, 421, 624, 750

1.3.4.2 Iron tetrakis-pentafluorophenyl porphyrin (FeF$_{20}$TPP)

Halogenated metalloporphyrins complexes are very efficient catalysts for the direct reaction of alkanes with molecular oxygen. The iron tetrakis pentafluorophenyl porphyrins, in particular FeF$_{20}$TPPCl, show very high catalytic activity. This iron porphyrin has unique properties in that the electron-deficient porphyrin induces a high affinity of iron for axial ligands, efficiently stabilizes high-valent iron porphyrin complexes and therefore serves as an efficient catalyst for oxidation of hydrocarbons.[124] Ligand exchange of this complex has been reported when methanol was added to solution of acetonitrile. In acetonitrile, a Soret peak was observed at 407 nm, which was assigned to FeF$_{20}$TPPCl. When acetonitrile was progressively replaced by methanol, the Soret peak shifted to 390 nm (*Figure **20***). This shift was attributed to an exchange of the chloride ligand for a methanol solvent molecule.[125,126] It has been shown recently that FeF$_{20}$TPPCl is catalytically inactive for cyclooctene epoxidation by hydrogen peroxide or hydrogen peroxide decomposition, when dissolved in acetonitrile, but it is active if the solvent contains methanol. This solvation effect on the FeF$_{20}$TPPCl dissociation in protic solvents was attributed to their ability to solvate the Cl^- anion and to coordinate to the FeF$_{20}$TPP$^+$ cation.[127] Absorption spectra of low valent iron pentafluorophenyl porphyrin in molecular solvents have been reported by Lexa et al.[128] Based on UV-visible and resonance Raman spectroelectrochemistry, the two electron reduction of Fe(II)F$_{20}$TPP led to a metal centered reduction Fe('0') rather than Fe(I) radical porphyrin anion (*Table 7*).

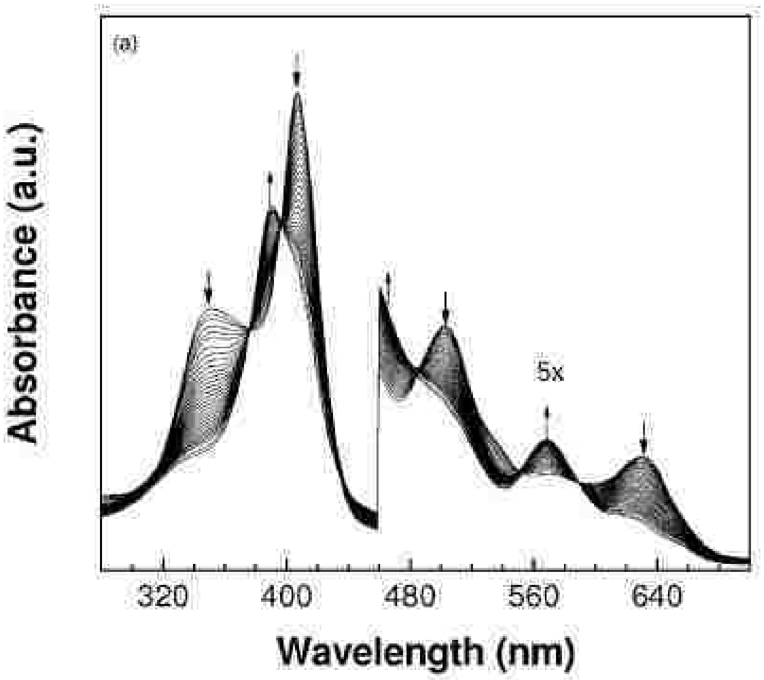

Figure 20: UV-visible spectra obtained by methanol addition to FeF$_{20}$TPPCl dissolved in acetonitrile. Arrows indicate the direction of the absorbance change with an increase in the methanol concentration.[129]

Table 7: UV-visible spectra of low valent iron fluorinated porphyrins obtained by spectroelectrochemistry in molecular solvents.[128]

Redox State	**Solvent**	**Spectral features (nm)**
Fe(I)F$_{20}$TPP^{-}	Butyronitrile	380, 410, 506, 578, 665, 702
	Dimethylsulfoxide	384, 418, 514, 578, 672
Fe('0')F$_{20}$TPP^{2-}	Butyronitrile	352, 450, 520, 760, 834
	Dimethylsulfoxide	354, 456, 524, 770, 865

Fluorine-19 NMR chemical shifts enable the extraction of the information on ligand exchange, structural solvation and the electronic structure of fluorinated iron porphyrin complexes (*Figure 21*).[130] Fluorine signal splitting is due to inequivalence of phenyl fluorine groups with respect to axial ligation at the iron center. While this splitting would provide useful information with regard to the symmetry of axial ligation, its absence should not be taken as indicative of symmetric axial ligation, as the splitting may not be resolved due to large linewidths.

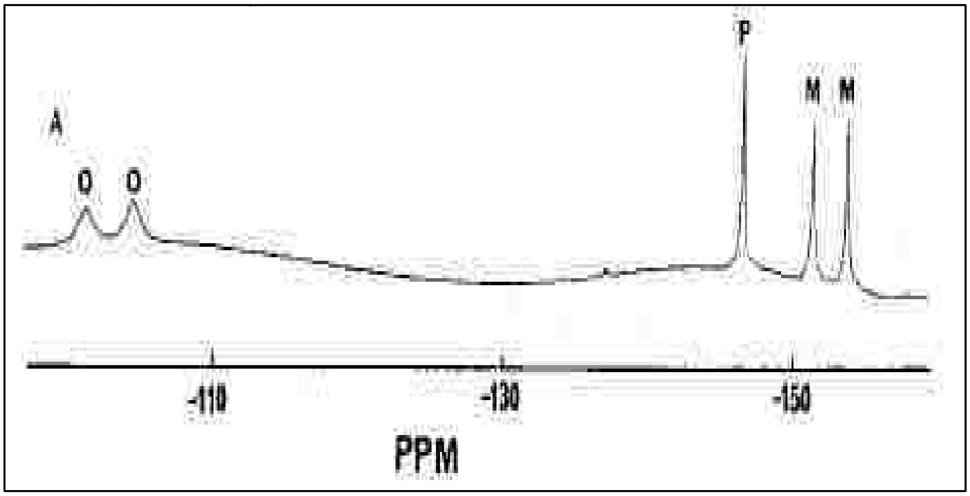

Figure 21: Fluorine-19 NMR of TPPF$_{20}$FeCl in CD$_2$Cl$_2$.[130]

1.3.4.3 Metalloporphyrins in RTILs

There have been few electrochemical studies of porphyrins and metalloporphyrins in RTILs. It has been demonstrated that solvation of porphyrins in RTILs can cause protonation reactions. Spectroscopic studies on the solvation of sulfonated tetraphenylporphyrin (TPPS) in protonic 1-butylimidazolium p-toluenesulfonate (HBImTS) showed the protonation of H_2TPPS^{4-} to H_4TPPS^{2-}, whereas in 1-butylimidazolium tetrafluoroborate ($HBImBF_4$), the appearance of a new band at 483 nm was indicative of TPPS aggregation in the RTIL. Large shifts of the Soret and Q bands were observed in RTIL solutions.[131] The aggregation of TPPS was reported to occur in neat $BMImBF_4$ (*Figure 22*). This was illustrated by looking at the concentration-dependent absorption behavior of TPPS in neat $BMImBF_4$. A plot of absorbance of TPPS at 418 nm as a function of TPPS shows a clear deviation from the Beer–Lambert law at about 15 mM TPPS, indicating the formation of aggregates of TPPS in neat $BMImBF_4$. The characteristic band, around 490nm, for porphyrin aggregation was also observed in the RTIL solution.[132]

Reactivity of iron(III) porphyrin in RTILs was studied by investigating the effects of imidazolium-based RTIL on the reversible binding of NO to Fe^{III}(meso-[tetra-(3-sulfonatomesityl)porphin]). UV-visible spectroscopy showed the presence of a six-coordinate iron porphyrin $(TMPS)Fe^{III}(OH)(MeIm)$ (S 418, Q 550nm) in $EMImNTF_2$. While in aqueous solution $(TMPS)Fe^{III}(OH)(MeIm)$ was only generated by the addition of a larger excess of MeIm, the presence of trace amount of MeIm in the RTIL led to $(TMPS)Fe^{III}(OH)(MeIm)$.[133]

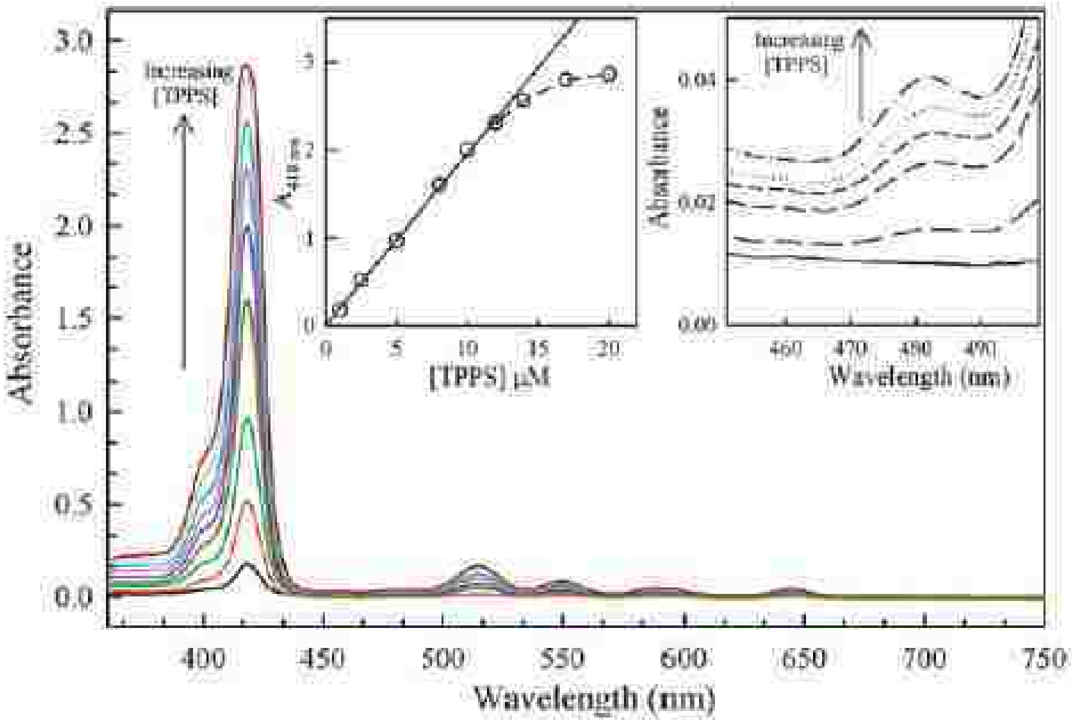

Figure 22: Concentration-dependent absorption behavior of TPPS in neat $BMImBF_4$.[132]

Compton and Laszo studied the voltammetry of hemin in mixed molecular/RTIL solutions (pyridine/N-methyl imidazole (NMI) and $BMImPF_6$/$OMImPF_6$; BMIm: 1-butyl-3-methyl imidazolium, OMIm: 1-octyl-3-methyl imidazolium). Hemin had little solubility in the ionic liquids, and was studied as an adsorbed layer on a gold electrode in contact with $BMImPF_6$ or $OMImPF_6$. Reversible waves for hemin were observed in both solvents. The results suggested that hemin and hemin-modified electrodes could be used in IL without electrolyte, as biomimetic equivalents of heme-containing proteins for a variety of bioelectrosyntheses. The reduction potential of the hemin could be adjusted by varying the polarity of the IL or the basicity of the coordinating ligand.[134]

1.4 Objectives

Although RTILs exhibit unique features as attractive solvents, the above review on electrochemical studies in these media revealed important limitations for their use in electrochemical applications. One major limitation is their high viscosity, which consequently reduces their intrinsic conductivity. Repercussions of the high viscosity on redox processes could be also seen through the difficulties in evaluating diffusion coefficients and electron transfer kinetics. Interpretations of reported values of electron transfer kinetics and thermodynamics obtained in RTILs were often subject to controversies. The choice of the electrochemical method has been shown to be crucial for a precise determination of these parameters. An accurate evaluation of potentials shifts in RTILs depended, in the first place, upon the choice of reference systems. The high polarity of RTILs resulted in limited solubility of non-polar substrates. Ironically, the non-volatility of RTILs, a one great feature for their use as “greener” solvents, makes their purification a challenging task for electrochemical experiments. Impurities like water and halides were reported to shrink the electrochemical windows of these media. In addition to water, residual imidazole derivatives have been shown to affect the chemical stability of solutes in theses media.

While extensive work has been carried out on reduction processes in RTILs, not much effort was done on oxidation processes. Investigations on the reactivity and solvation of multi-charged electrogenerated species in RTILs are still lacking. Due to the complexity of RTILs structures, little computational work has been done to investigate redox processes in these media. At their best, theoretical investigations could only approach the qualitative aspect of redox potentials.

One way to circumvent the above mentioned challenges for the electrochemical use of RTILs would be their introduction as mixtures with molecular solvents (MS). Along with lowering the cost for their application, RTIL-MS mixtures will lower the viscosity, increase the conductivity and reduce the impacts of impurities. In addition, the electrochemical properties and the solvation abilities of the mixture system can be tuned by introducing specific co-solvents.

One of the most attractive features that have appealed our attention to RTILs is their physical structure. As reviewed above, these salts have been shown to maintain an internal ordering that results in formation of nano-structures in the liquid phase. Preliminary indications of the presence of nano-structures in mixtures with molecular solvents have been reported, both computationally and experimentally. We believe that these RTIL nano-heterogeneities would play a major role in altering the electrochemical processes. Presence of RTIL nano-clusters in mixed solution will have a significant impact on the solvation and reactivity of the redox products. One major impact would be the preferential solvation of solutes into molecular and ionic nano-domains. On this basis, one would probably be able to resolve controversies that have been reported in RTIL media.

To the best of our knowledge, no work has been carried out on the effect of RTIL nano-structures on electrochemical processes in RTIL-molecular solvent mixtures. Proper knowledge and understanding of these effects are critical to their development and applications. In this regard, the present work is devoted to investigate the impact of RTIL nano-domains on redox systems in mixture solutions.

Through this work, we aim to establish analytical approaches that will allow a systematic interpretation of the electrochemical data obtained in RTILs. The combination of voltammetric, spectroscopic and computational methods would be a powerful approach to investigate the effect of RTIL structures on the redox chemistry. In this work, the focus will be on substrates that undergo multi-electron reductions and/or oxidations. Examples of these substrates are: dinitrobenzene, tetracyanoquinodimethane, fullerene and metalloporphyrins

The two electron reduction of DNB in RTILs exhibited one of the most spectacular effects of RTIL on the voltammetry of organic compounds. The cyclic voltammetric analysis showed coalescence of the two waves into one wave in RTILs, suggesting a "potential inversion" in these media. Potential shifts in RTIL-molecular solvent mixtures indicated clustering of ionic liquids cations around DNB dianion. In fact, a more detailed investigation is needed to evaluate the "potential inversion" in mixtures and the ability of RTIL nano-structures to interact with reduced species, where solutes are planar shaped and the charge is localized on nitro groups.

In contrast to DNB, where the two waves coalesce into one wave in RTIL, two well-separated reduction waves of TCNQ were still observed in the ionic liquid. This would allow further investigation on the impact of RTIL on redox potentials and electronic structures of organic radicals. The characteristic cyanide vibrations can be used to study the interactions of RTIL components with electrogenerated species by FTIR spectroelectrochemistry. The voltammetric analysis in ionic liquids would enable the evaluation of change in diffusion coefficients in comparison with obtained values in molecular solvents.

Electrochemical reductions of fullerene C_{60} exhibit successive multi-electron transfers in molecular solvents. Extensive work has been done on the correlation between potential shifts and molecular solvents properties (Gutmann AN/DN). Although C_{60} is insoluble in RTILs, significant solubility of the charged fullerides could be observed. Hence, electrochemical reduction in RTIL-molecular solvent mixtures would enable the evaluation of RTIL solvation of spherical shape species.

While the redox chemistry of metalloporphyrins (M-Porph) in molecular solvents has been extensively reported, very little work has been carried out in RTILs. We believe that is mainly due to the poor solubility and complexity that occurs when combining two complicated systems: solute (M-Porph) and solvent (RTIL). In addition to multi-electron transfers, investigations on the electron transfers sites for these complexes are well documented in literature. The NiOEP redox processes exhibits two main features that make it suitable model M-Porph to investigate in RTILs. First, the voltammetry in molecular solvents shows two reductions and two oxidation waves in a fairly small electrochemical window that can fit within RTILs windows. This will allow evaluating the RTIL interactions with positively and negatively electrogenerated species for the same system. Second, no coordination to the nickel metal center by anions has been reported in molecular solvents.

In contrast to NiOEP, changes in axial ligation to the metal center are well reported for iron porphyrins redox complexes in molecular solvents. Such systems are suitable model compounds to evaluate the effect of RTIL solvation on coordination to the metal center. In addition to enhancing the solubility in RTILs, fluorinated iron porphyrin would enable to probe changes in electronic structures of redox species using ^{19}F-NMR.

Chapter 2 Methods and Materials

2.1 Chemicals

High purity RTILs 1-butyl-3-methylimidazolium hexafluorophosphate ($BMImPF_6$), 1-butyl-3-methylimidazolium tetrafluoroborate ($BMImBF_4$) and 1-butyl-3-methylimidazolium bis(trifluoromethylsulfonyl)-amide ($BMImNTF_2$) were purchased from Merck and TCI and employed without further purification, except as noted in the text. Ethyldimethylpropylammonium bis(trifluoromethylsulfonyl)imide ($AmNTF_2$), 1-butyl-3-methylimidazolium chloride (BMImCl), tetrabutylammonium perchlorate (TBAP), tetra-n-hexylammonium perchlorate (THAP), tetrabutylammonium borohydride ($TBABH_4$, 98%), silver perchlorate ($AgClO_4$), nickel(II) acetate tetrahydrate ($Ni(OCOCH_3)_2 \cdot 4H_2O$, 98%), 1,4-dinitrobenzene (DNB), 7,7,8,8-tetracyanoquinodimethane (TCNQ), fullerene (C_{60}, sublimed, 99.9%), nickel(II) octaethylporphyrin (NiOEP), iron pentafluoro-tetraphenyl-porphyrin chloride ($FeF_{20}TPPCl$, 98%), anhydrous benzonitrile (BzCN), anhydrous acetonitrile (ACN, 99.8%), acetonitrile-d_3 (ACN-d_3, 99.8 atom % D), anhydrous tetrahydrofuran (THF, 98.9%), triethylphosphine oxide ($POEt_3$) and diphenylphosphorus oxychloride (Ph_2POCl) were purchased from Sigma-Aldrich Chemical Co.

2.2 Instruments

Cyclic voltammetry was carried out at a platinum electrode (1.6 mm or 10μ), a platinum wire was used as auxiliary electrode. Potentials were measured relative to the Ag/$AgNO_3$ (in CH_3CN) reference electrode. For controlled potential electrolysis, a homemade small volume cell was used. A gold mesh was used as a working electrode, silver wire as pseudo-reference and platinum wire as auxiliary electrode. The two compartments were separated by glass frit. While stirring the solution during the electrolysis, electrogeneration of reduced species was obtained by setting the potential at the corresponding wave. The measurements were carried out using a Model 600D Series Electrochemical Analyzer/Workstation (CHI Version 12.06).

A low-volume thin layer quartz cell, which was purchased from BAS Instruments, was used for UV-visible spectroelectrochemical experiments. A platinum mesh was used as working electrode, a platinum wire was used as an auxiliary electrode, and the reference electrode was an Ag/$AgNO_3$ (in CH_3CN) electrode. UV/visible spectra were recorded on a HP8452A diode array spectrophotometer. All solutions were prepared and filled into the voltammetric or spectroelectrochemical cells in the glovebox under an argon environment.

Near infrared (NIR) spectroelectrochemistry experiments were carried out using the same cell. NIR spectra were recorded using Cary Series UV-Vis-NIR spectrophotometer (Agilent Technologies)

A homemade infrared spectroelectrochemical cell was made by modifying a Wilmad semi-permanent cell. The Teflon spacer between two CaF_2 windows was replaced by a polyethylene spacer in which the working, reference and auxiliary electrodes were melt-sealed. The working and auxiliary electrodes were fabricated from 100-mesh platinum gauze (Sigma Aldrich Chemical Co.), and a silver wire (0.05 mm diameter, Johnson Matthey) was used as a pseudo reference electrode. Alternatively, a *Specac* spectroelectrochemical transmission cell (Specac Ltd., Kent, UK) was also used. The cell was comprised of two CaF_2 windows separated by a 100 micron sample layer, where gold grid working electrode and counter electrodes, and a silver reference electrode, were photolithographically imprinted on surface of the front window in contact with the sample. The infrared spectra were obtained using 64 scans and 2 cm^{-1} resolution, recorded with a Thermo Nicolet-FTIR spectrophotometer (Model 670 Nexus) with a MCT detector. Resonance Raman (rR) experiments were carried out using excitation lines at 406 and 442 nm for DNB^{1-} and DNB^{2-}, respectively. Measurements were carried out with 1 mW laser power, using cylindrical lens. The slit was 150 μm and the total collection time of each spectrum was 10 min. Proton, ^{31}P and ^{19}F NMR measurements were performed using a Varian 400 MHz FT spectrometer. EPR measurements were performed liquid nitrogen temperature, using a Bruker ELEXSYS E600 equipped with an ER4415DM cavity resonating at 9.63 GHz, an Oxford Instruments ITC503 temperature controller and ESR-900 He flow cryostat. Viscosities of the solutions were measured using a Brookfield DV2T viscometer, and the temperature was controlled at 25°C using a water bath.

2.3 Procedures

2.3.1 Experimental

For electrochemical experiments, all solutions were prepared and filled into cells in the glovebox under an argon environment. Tetrabutylammonium perchlorate was used as electrolyte in molecular solvent experiments. UV-visible and FTIR spectroelectrochemical experiments were carried out by either scanning or stepping the potentials at the corresponding waves. For UV-visible experiments, the entrance window of the cell was masked so that the spectral beam passed only through the working electrode.

For mixtures of molecular/RTIL solvents, a total volume of 0.3-0.5mL was used for voltammetry, 0.5mL for viscosity, 0.2-0.5mL NMR and 0.1-0.2mL for spectroelectrochemistry. The solutions were prepared using a micropipette. Due to the high viscosity of RTILs solvents and volume contractions in mixtures, a careful practice had to be taken during measurements.

Anhydrous tetrahydrofuran (THF) was refluxed in the presence of sodium and benzophenone under nitrogen until the solution was blue. Other molecular solvents were used as received. Water was removed from the RTIL by passing N_2 over the solvent, which was heated at 70 to 90°C. The amount of water in the RTIL was measured by monitoring the stripping peak on a gold electrode due to water (*Figure 23*). Substantial reduction in the water concentration was obtained as shown by the complete disappearance of the water stripping peak.[37]

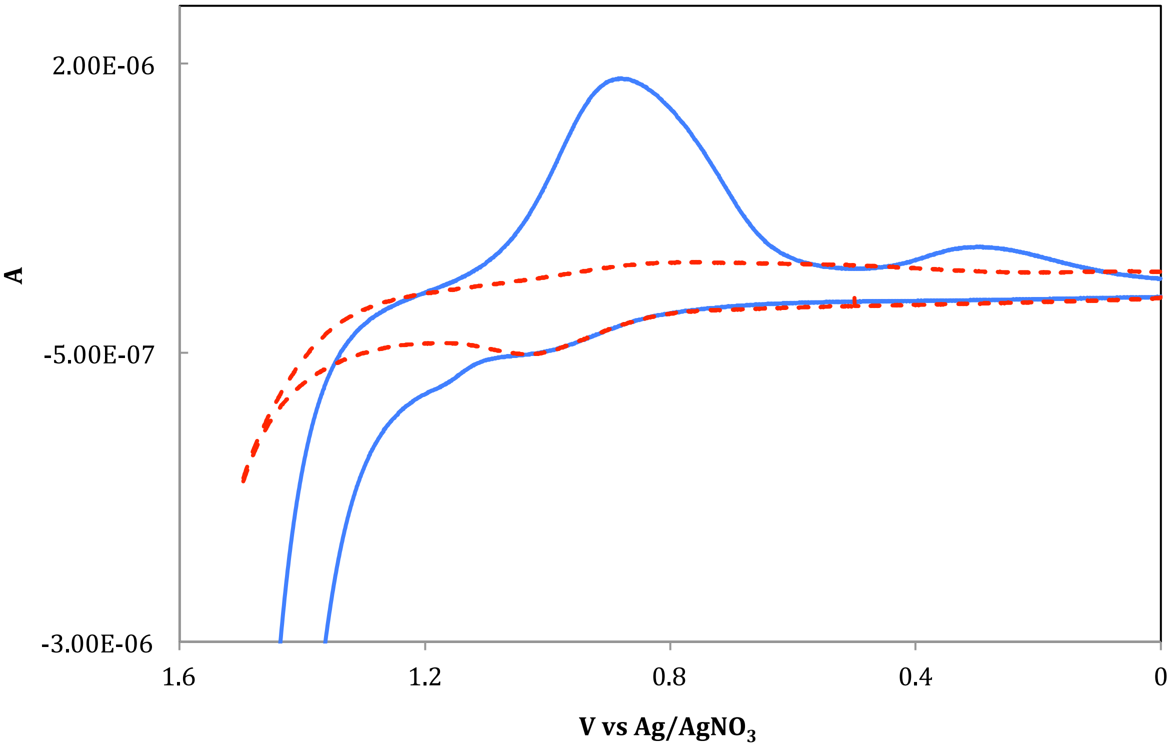

Figure 23: Voltammograms of AmNTF$_2$ before (solid line) and after (dashed line) water removal obtained at gold electrode.

A small volume (0.5mL) homemade electrolysis cell was used to prepare high concentrations of electrogenerated (DNB radicals and fullerides) for in-situ voltammetric and ex-situ spectroelectrochemical analysis. The samples were prepared inside the glovebox, sealed and used for the spectroscopic measurements.

The octaethylporphinone (H_2OEPone) ligand was synthesized by literature procedure.[135] To form Ni(OEPone), nickel(II) acetate tetrahydrate was refluxed with H_2OEPone in $CHCl_3$/MeOH (20/10 mL) for one hour. The resulting solution was cooled at room temperature and washed 3 times with 300mL of water. After removing the solvent, the crude product was purified using an alumina column and elution was initiated with chloroform. The product was characterized by UV-visible (*Figure 24*) and IR spectroscopy (the carbonyl band).

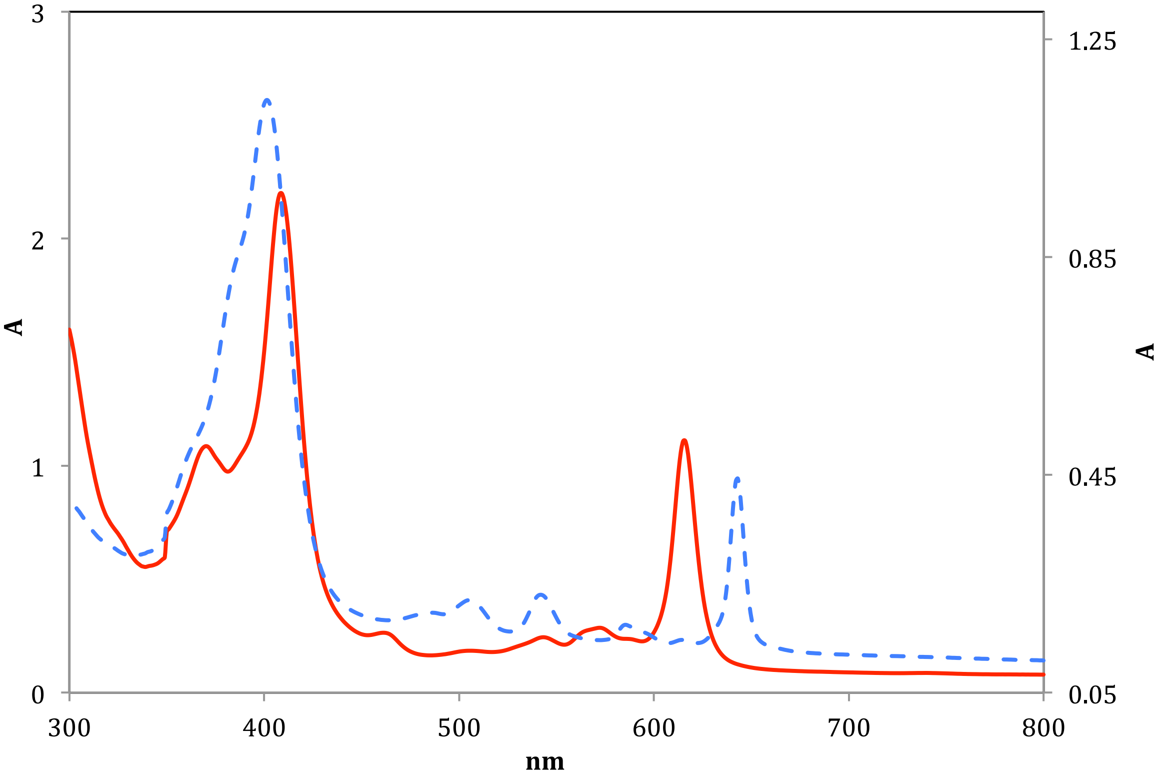

Figure 24: UV-visible spectra of prepared H_2OEPone (dashed line) and NiOEPone (solid line)

$FeF_{20}TPPClO_4$ was prepared by exchanging the chloride ligand in $FeF_{20}TPPCl$ using equimolar solution of silver perchlorate in THF. After heating the solution at 90°C for 10min, the solution was cooled to room temperature and filtered. The product was precipitated by addition of heptane. The redox potentials of the first two waves lay within the redox potential of $TBABH_4$. Hence, the two electron chemical reduction of $FeF_{20}TPPClO_4$ was straightforward using $TBABH_4$. The ferrous product was obtained by an equimolar reaction of $FeF_{20}TPPClO_4$ with $TBABH_4$ in THF. Precipitation was done by addition of heptane. Addition of 1.5 molar equivalent of $TBABH_4$ to the ferrous solution led to the low valent $Fe(I)F_{20}TPP^-$ (*Figure 25*).

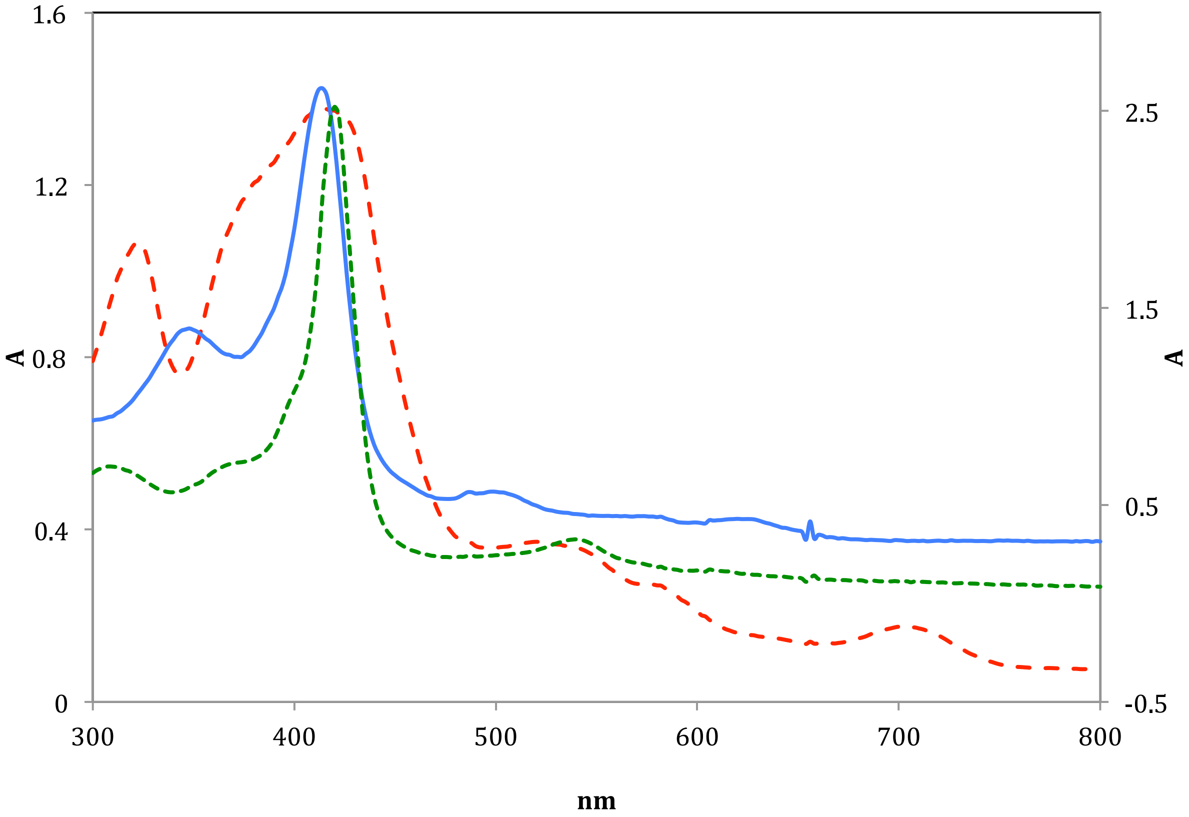

Figure 25: UV-visible spectra of the ferric $Fe(III)F_{20}TPPCl$ (solid line), the chemically reduced ferrous $Fe(II)F_{20}TPP$ (pointed line) and low valent $Fe(I)F_{20}TPP^-$ (dashed line).

For the ^{31}P-NMR measurements, appropriate amounts of the probe $POEt_3$ were dissolved in the solvent system to prepare solutions of four different concentrations (0.025, 0.035, 0.05 and 0.1 M). These solutions were then the transferred into co-axial NMR tubes, where the inner capillaries contained reference solution of 0.2M Ph_2POCl in the same studied solvent system. All preparations were carried out in the glovebox. The Gutmann acceptor numbers (AN) were obtained using the method of Schmeisser et al.[136] The ^{31}P NMR chemical shift of Et_3PO relative to Ph_2POCl, was measured at a series of concentrations and extrapolated to infinite dilution. From the chemical shift, the acceptor number was calculated using an empirical equation: AN = 3.76112-(2.34326 x *Shift* (ppm)). Example of variation AN in mixture RTIL-MS is shown in *Figure 26*.

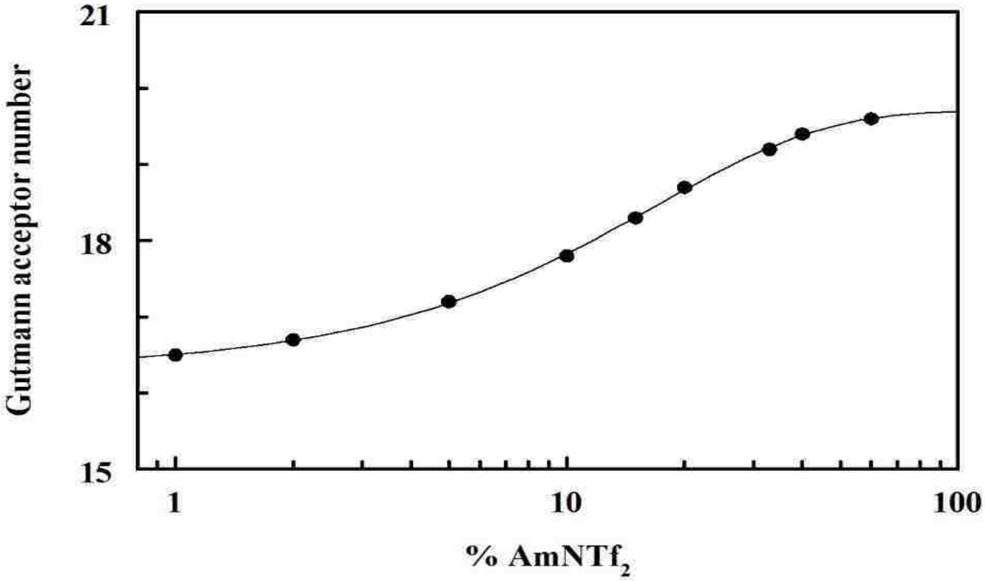

Figure 26: The relationship between the Gutmann acceptor number and the %$AmNTf_2$ in benzonitrile. The line is the best fit line for the following equation: AN = 19.70 – 3.387 exp(-%$AmNTF_2$/16.85)

2.3.2 Computational

2.3.2.1 Factor analysis

For some redox systems, it was not possible to obtain the pure spectra of each redox species. In order to extract the spectrum, factor analysis was used to obtain the individual spectra. The spectroelectrochemical data was set up in a bilinear data matrix D (m × n) where the m rows correspond to absorbance readings at each wavelength and n columns represent spectra of the solution at each potential (or time). A bilinear data matrix can be decomposed into the product of two matrices, one containing the concentration profiles, C ($m \times n_c$), and the second the individual spectra, E ($n \times n_c$), where n_c is the number of principal factors (species):

$$\mathbf{D} = \mathbf{C} \,.\, \mathbf{E}^{\mathrm{T}}$$

In order to obtain these two matrices (C and E), the first step is the singular value decomposition (SVD) of the D matrix as follow:

$$\boldsymbol{D} = \boldsymbol{U} \,.\, \boldsymbol{S} \,.\, \boldsymbol{V}^{\boldsymbol{T}} + \boldsymbol{E}$$

Where the matrix U ($m \times n_c$) contains the abstract concentrations, V ($n \times n_c$) consists of the abstract spectra, S ($n_c \times n_c$) is a diagonal matrix, where the square of the diagonal elements is the eigenvalue. E corresponds to the error. Changes in the eigenvalues during in the forward direction (starting from the first spectrum until the last one) and backward direction (starting from the last spectrum and going back to the first one) give information about the appearance and the disappearance of the principal factors. It is assumed that the first component appearing will be the first to disappear and the ith component will be the ith to disappear. The concentration window (the region of existence) for each compound is defined by performing that process in the forward and backward directions. This procedure is called evolving factor analysis (EFA). Knowledge of these concentration windows is sufficient to determine the real concentration profiles and thereby the individual compounds spectra. The true concentration profiles (C) are linear combinations of the abstract matrix U. The problem is then reduced to finding a transformation matrix T (n_c x n_c) that relates the true and abstract matrices:

$$\mathbf{C = U.\,T}$$

For: $\mathbf{i = 1 ..... n_c}$ $$\mathbf{C_i = U \times t_i}$$

Each column of T, t_i, transforms U into the true concentration profile for the i_{th} compound, c_i. The transformation vector t_i can be determined using the zero-concentration window for the i_{th} compound, $c_{0,i}$, where the concentration of that compound is known to be equal to zero:

For: $\mathbf{i = 1 ..... n_c}$ $$\mathbf{c_{0,i} = U_{0,i} \times t_i}$$

The subscript 0,i indicates that only the rows of U with no contribution from the i_{th} compound are used (i.e., the zero-concentration window). Matrix $U_{0,i}$ is rank deficient due to the elimination of the concentration window for the i_{th} compound. This leads to an underdetermined set of linear equations, making it necessary to give an arbitrary value for one of the elements of the transformation vector t_i. This approach is similar to Windows Factor analysis (WFA).[137]

2.3.2.2 Derivative Cyclic Voltabsorptometry (DCVA)

For an electrode process:

$$i = dq/dt \qquad ; \qquad q = nF \,\#\mathrm{mol}_A = nF\, V\, dC_A/dt$$

The concentration of A can be found form Beer's law:

$$A = E\, l\, C_A \ ,$$

Therefore: $$i = nFV/El \ \ \mathrm{x} \ \ dA/dt$$

The derivation of the absorbance with respect to time is proportional to current. Therfore, the voltammetric wave is morphologically identical to the derivative of absorbance. If the potential waveform is cyclic voltammetry, the derivative of absorbance is called derivative cyclic voltabsorptometry. For multi-electron transfers, spectral overlap will make the analysis more complex. To simplify the process, it is simpler to calculate the concentration of each redox species and take the appropriate derivative to generate the DCVA curve.

2.3.2.3 Bulter-Volmer fitting

Electron transfers kinetics can be evaluated by Bulter-Volmer simulations, using calculated concentrations. The concentrations as a function of time (potential) are given by the differential equations for the three concentrations species:

$$\frac{dC_1}{dt} = -\frac{k_1^0}{\delta}\{C_1 \exp[-\alpha_1 f(E - E_1^0)] - C_2 \exp[-(1-\alpha_1) f(E - E_1^0)]\}$$

$$\frac{dC_2}{dt} = \frac{k_1^0}{\delta}\{C_1 \exp[-\alpha_1 f(E - E_1^0)] - C_2 \exp[-(1-\alpha_1) f(E - E_1^0)]\} - \frac{k_2^0}{\delta}\{C_2 \exp[-\alpha_2 f(E - E_2^0)] - C_3 \exp[-(1-\alpha_2) f(E - E_2^0)]\}$$

$$\frac{dC_3}{dt} = \frac{k_2^0}{\delta}\{C_2 \exp[-\alpha_2 f(E - E_2^0)] - C_3 \exp[-(1-\alpha_2) f(E - E_2^0)]\}$$

Where, $f = F/RT$. k_1 and k_2 and α are the electron transfer rates and coefficient, respectively.

2.3.2.4 DFT calculations

Quantum chemical calculations were performed using density functional theory (DFT) as implemented in the Gaussian 09 program. Optimized geometries of ion pairs of redox products and RTIL cations were computed using several DFT methods and basis sets. Selection of DFT methods was based on similar calculations for the redox properties of organic radicals.[65,138–143] The impact of the method on the calculated redox potentials was illustrated for B3LYP, M06, PBE and B1LYP40 methods, along with three basis sets: 6-31G(d), 6-31++G(2d,p) and aug-cc-pvdz. Implicit solvation in molecular solvent was included by polarizable continuum model (PCM). When using PCM/SMD models for RTILs, solvent parameters obtained from literature were introduced in the calculations.[144] All calculations converged to minima and all frequencies were positive numbers. The redox potential difference ΔE were calculated from the disproportionation energies: $\Delta E = \Delta G_{disp}/F$, using 1H = 2626.7 kJ/mol and 1V= 96.529 kJ/mol.[143]

2.3.2.5 Software

Factor analysis, DCVA and Bulter-Volmer calculations were carried out using MATLAB-R2011b (Mathworks). Digital simulations of voltammetric data were done using Digisim 3.01 (BAS Instruments) software. Deconvolution of FTIR spectra was carried out using Grams/32 AI software (Galactic Industries, Salem, NH). DFT calculations were carried out using Gaussian 09, available on Marquette Pere cluster.

Chapter 3 Electrochemistry and Spectroelectrochemistry of 1,4-Dinitrobenzene in Acetonitrile-RTIL mixtures

As introduced earlier, Fry reported an inverted potential for 1,4-dinitrobenzene (DNB, *Figure 27*) reductions in $BMImBF_4$ ionic liquid.[75] Two one-electron waves were observed for DNB in molecular solvent with a ΔE_{12} (E_1- E_2) of about 200 mV. In $BMImBF_4$, a single wave was observed, where ΔE_{12} was estimated to be about 0 mV, based on peak potentials (E_p) values of the cyclic voltammogram. The shift from two-one electron waves to one two-electron wave was ascribed to strong ion-pairing interactions in the ionic liquid. It is evident that determination of ΔE_{12} values by cyclic voltammetry, becomes more problematic when the two waves merge into one. Alternatively, a more accurate determination can be made from the concentrations of the redox species as a function of potential. This approach will be used in the first part of this investigation, in order to evaluate change of ΔE_{12} value for 1,4-dinitrobenzene in ACN-RTIL mixtures.

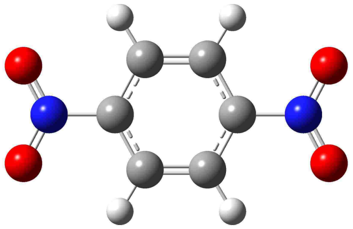

Figure 27: 1,4-dinitrobenzene structure

3.1 Voltammetry in Acetonitrile

3.1.1 Cyclic voltammetry

Voltammetry of DNB was carried out in acetonitrile, where two one-electron waves were observed (*Figure 28*). The half potentials of the first and second wave were evaluated at -1.007 and -1.230 V, resulting in a potential difference of 223 mV. This potential difference was consistent with the reported values in molecular solvents.[75] The peak current was proportional to the square root of the scan rate, which indicated that the reduction was diffusion controlled.

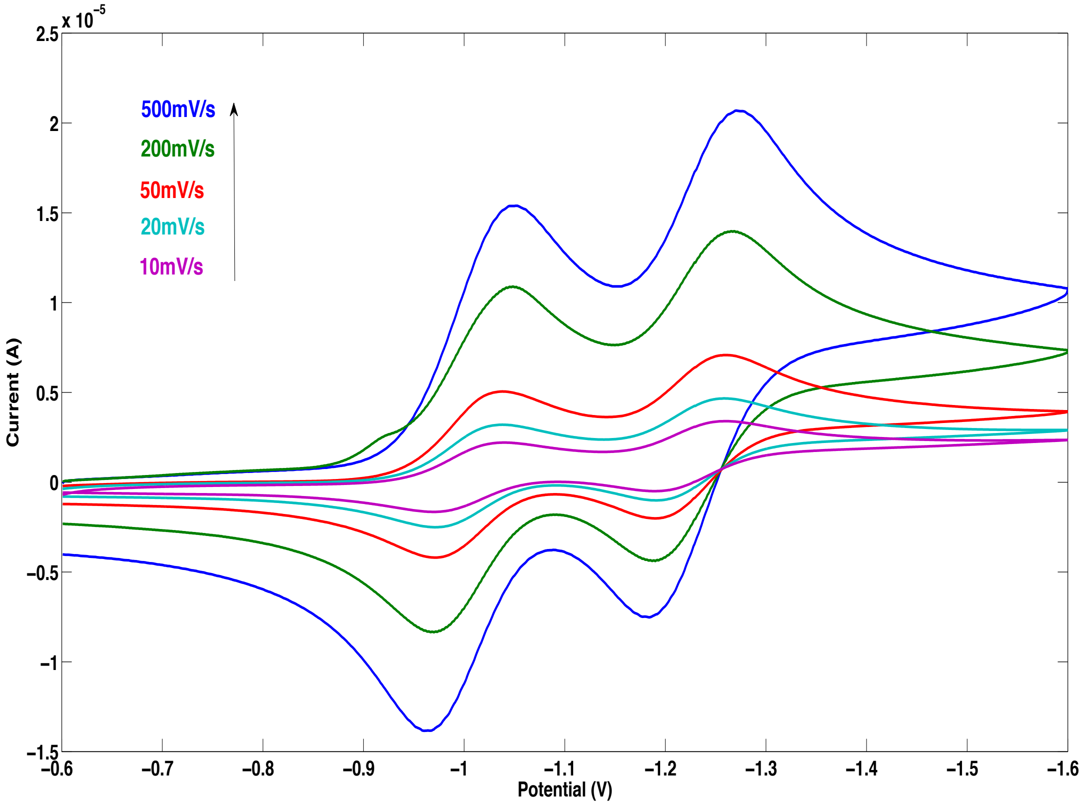

Figure 28: Voltammograms of 1mM DNB in ACN, at different scan rates

3.1.2 UV-visible Spectroelectrochemistry

In order to evaluate the spectral changes of the dinitrobenzene radical anion ($DNB^{-\cdot}$) and the dianion (DNB^{2-}) in going from organic solvents to ionic liquids, the spectroelectrochemistry (SEC) of DNB reductions was first carried out in acetonitrile. *Figure 29* shows the UV-visible SEC of DNB in acetonitrile, at the potential range of the two reductions waves. The first reduction gave rise to the $DNB^{-\cdot}$ (radical anion) spectrum, with a band at 398 nm and broad feature starting above 600 nm. Further reduction produced the DNB^{2-} spectrum with a band at 454 nm. Because the waves were well separated, there were potential regions where only the radical anion and the dianion species were present.

The spectra of the radical anion and the dianion were obtained at -1.196 V (forward scan) and -1.324 V (reverse scan), respectively. The spectra of the two species are shown in *Figure 30*. The spectrum for DNB^{-} compared well with the previously reported spectrum in DMF.[72] No spectrum has been reported for DNB dianion. From these spectra, the concentrations of the radical anion and dianion at each potential could be determined, using Beer's law. Because DNB was colorless, its concentration was determined from the difference between the starting concentration and the sum of the radical anion and dianion concentrations.

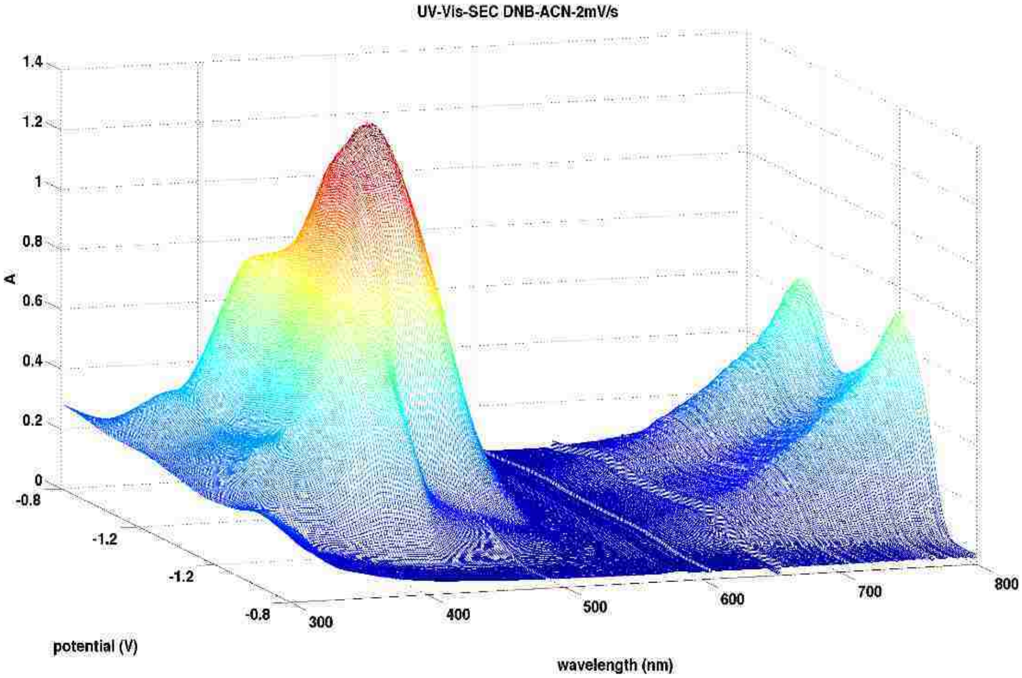

Figure 29: UV-Visible SEC of 0.1mM DNB reduction in ACN at scan rate 2mV/s. Potentials are versus Ag/AgNO$_3$

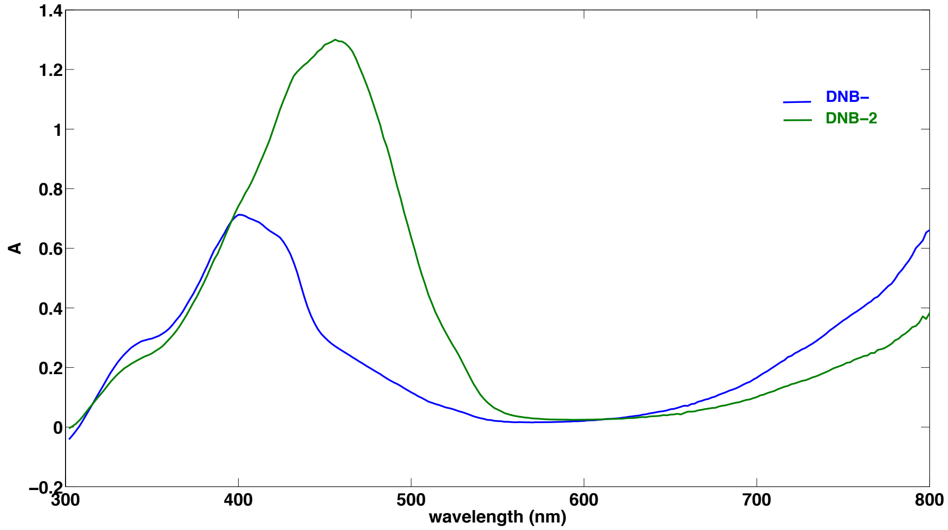

Figure 30: Spectral profiles of the DNB radical anion (blue) and dianion (green) in ACN

We noted that at lower scan rate, some diffusion of products from the auxiliary electrode could be observed at the end of the scan. The spectra obtained at these rates could be used to calculate the concentrations of the radical anion and dianion at higher scan rates. The spectrum of the interference was obtained from the final scan when the radical anion and the dianion were completely re-oxidized. Because of the sloping background at short wavelengths, probably due to the cell, this background was subtracted from all spectra. The calculated concentrations of radical anion and dianion in acetonitrile are shown in the *Figure 31*.

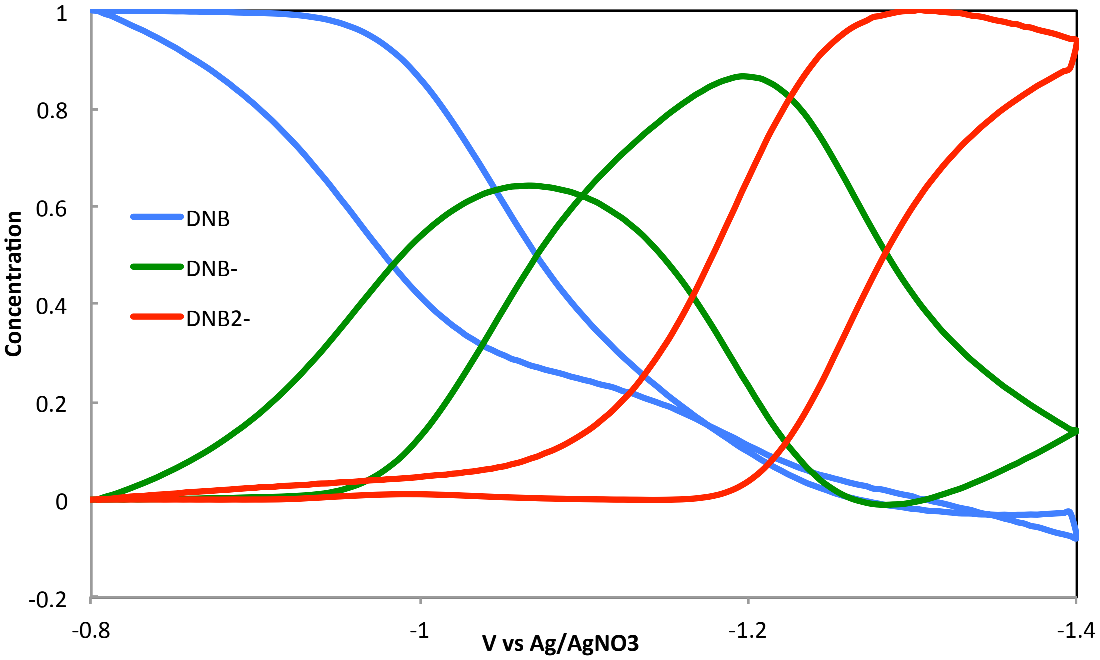

Figure 31: Concentrations of neutral, radical and dianion DNB during electrolysis in ACN at 2mV/s.

Using these concentrations, the DCVA (derivative cyclic voltabsorptometry) for the first and second electron transfer was calculated using the procedure described in Chapter 2 (*Figure 32*). The DCVA is morphologically equivalent to the cyclic voltammogram. From these results, the E_1 value was found to be -1.002 V and the E_2 value was -1.222 V, giving a ΔE_{12} of 220 mV. The potentials compare quite favorably with the voltammetrically obtained.

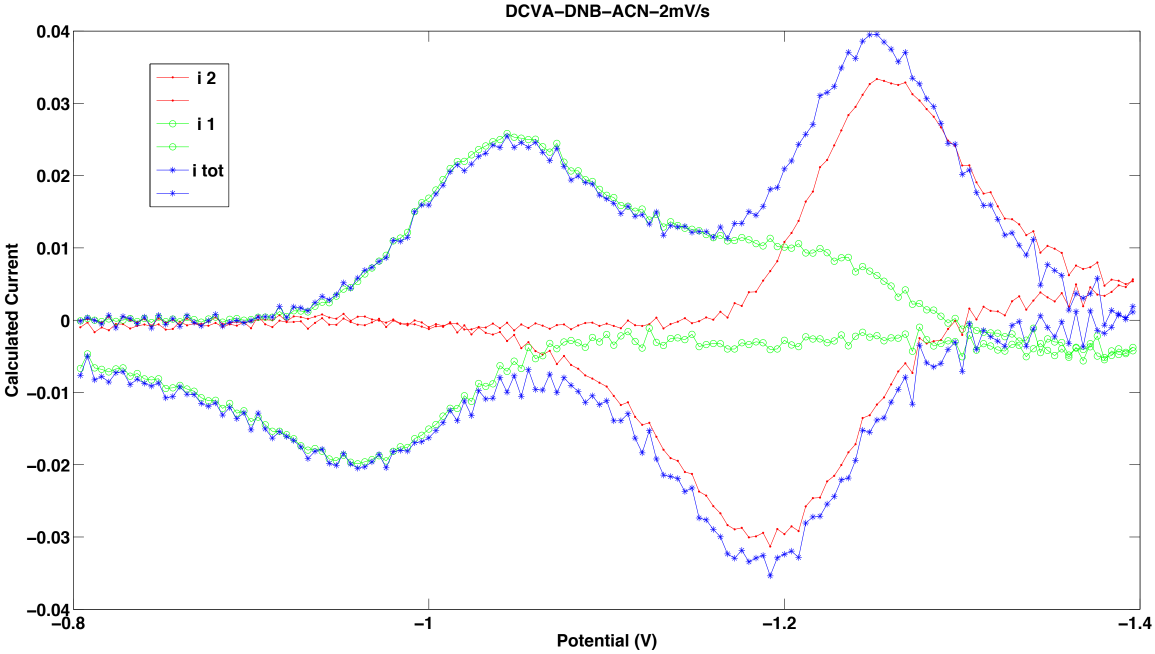

Figure 32: DCVA current during 0.1mM DNB electrolysis in ACN. Potentials are versus Ag/AgNO$_3$

Bulter-Volmer Simulation:

In an attempt to evaluate the electron transfers kinetics (k_1 an k_2), Butler-Volmer simulations were carried out, based on calculated concentrations (see Chapter 2). Excellent agreement between the calculated and experimental concentrations was achieved (*Figure 33*). The rates values k^0_1 and k^0_2 were, respectively, 0.1 and 0.08 cm s^{-1}, consistent with fast electron transfers in ACN (see Chapter 1).

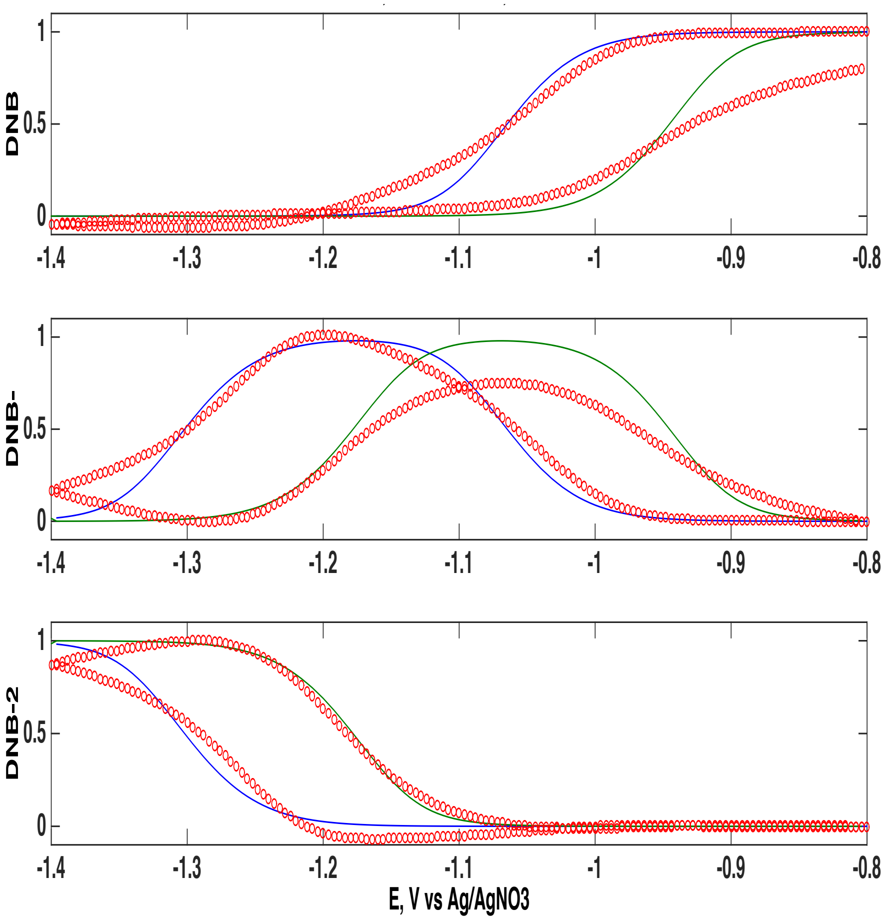

Figure 33: Variation of calculated (open circles) and experimental (lines) concentrations in ACN. Scan rate: 2mV/s.

3.2 Voltammetry in BMImPF$_6$

3.2.1 Cyclic voltammetry

The cyclic voltammetry of DNB in pure BMImPF$_6$ showed only one wave, which was consistent with the literature (*Figure 34*). The variation in the current with square root of the scan rate, which indicated that the reduction was diffusion controlled. Smaller currents were observed though in the ionic liquid, due to slower diffusion in highly viscous media.

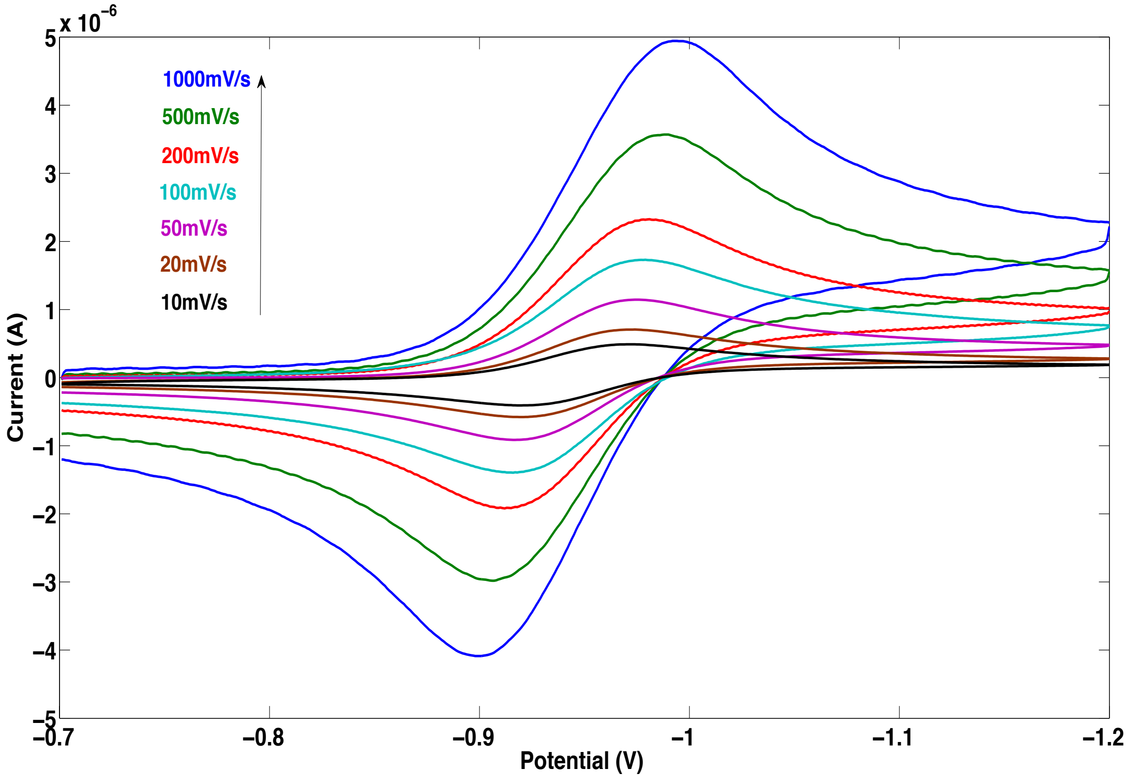

Figure 34: Voltammograms of 1mM DNB in BMImPF$_6$, at different scan rates. Potentials are versus Ag/AgNO$_3$

3.2.2 UV-visible Spectroelectrochemistry

In order to determine the difference between the ΔE_{12} in ionic liquid media, the spectroelectrochemical analysis was carried in $BMImPF_6$. Due to the higher viscosity of the ionic liquid as compared to acetonitrile, lower scan rates were used. The spectroelectrochemical data for the forward scan is shown in the *Figure 35*. As the initial reduction occurs the spectra showed features of the radical anion around 400 nm. As the scan potential became more negative, the spectrum of the dianion dominated.

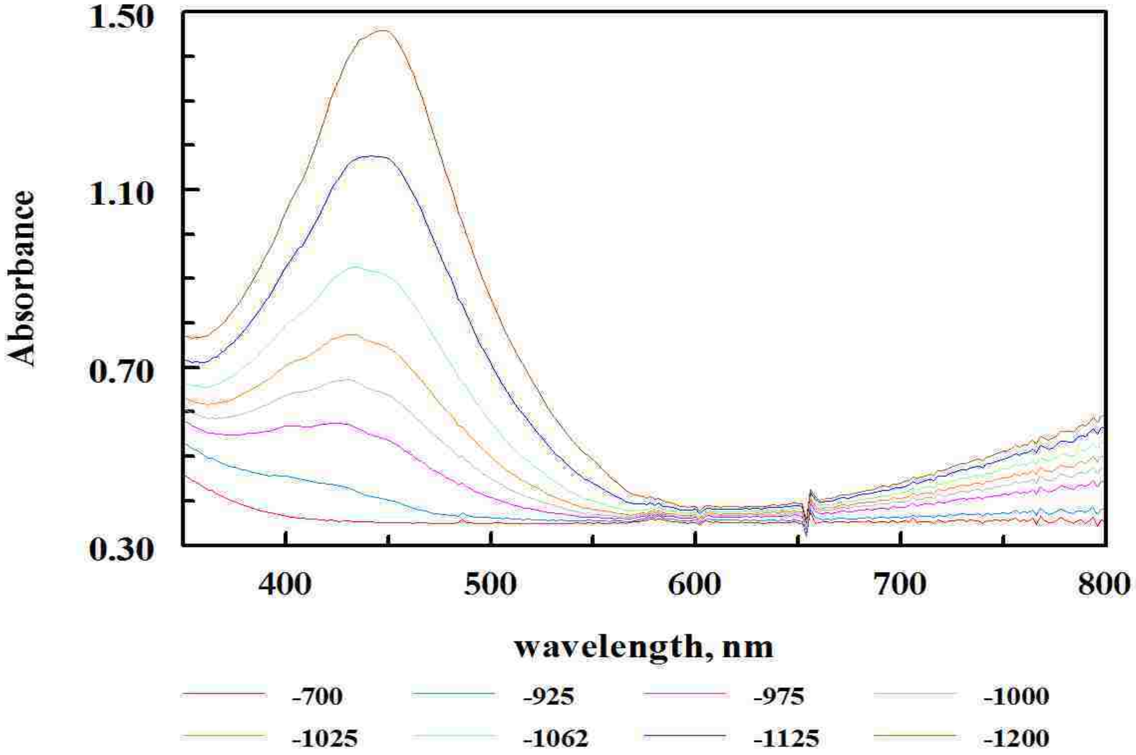

Figure 35: UV-Visible SEC of 0.1mM DNB upon two electron reduction in $BMImPF_6$*. Spectra obtained upon the forward scan. Potentials are given in mV and versus* $Ag/AgNO_3$

Because of the significant overlap between the spectra for the radical anion and the dianion, windows factor analysis (WFA) was used to solve this problem (see Chapter 2). The advantage of WFA is that the concentration of one of the species can be calculated without knowledge of the concentration of the other species. As a result, it was not necessary to calculate all the concentrations in order to solve the problem.

As was done for acetonitrile, the background was subtracted from all spectra. Using WFA, the concentration of the dianion was calculated as a function of potential in the forward reaction (see Appendix). Using the spectrum where the absorbance due to the dianion was the largest as the spectrum for the dianion and the WFA calculated concentration, the dianion spectrum was subtracted from all the spectra in the forward scan. The residual spectra around -0.9 to -1.0 V look very much like the spectrum for the radical anion in acetonitrile. These spectra are shown in *Figure 36*.

Using the radical ion spectra obtained from this subtraction, the unnormalized concentrations of the radical anion and the dianion were calculated using Beer's Law. While the shape of the concentration changes as a function of potential were morphologically correct, their actual concentrations were not. As a result, it was not possible at this point to calculate the concentration of the starting material by difference as was done in acetonitrile.

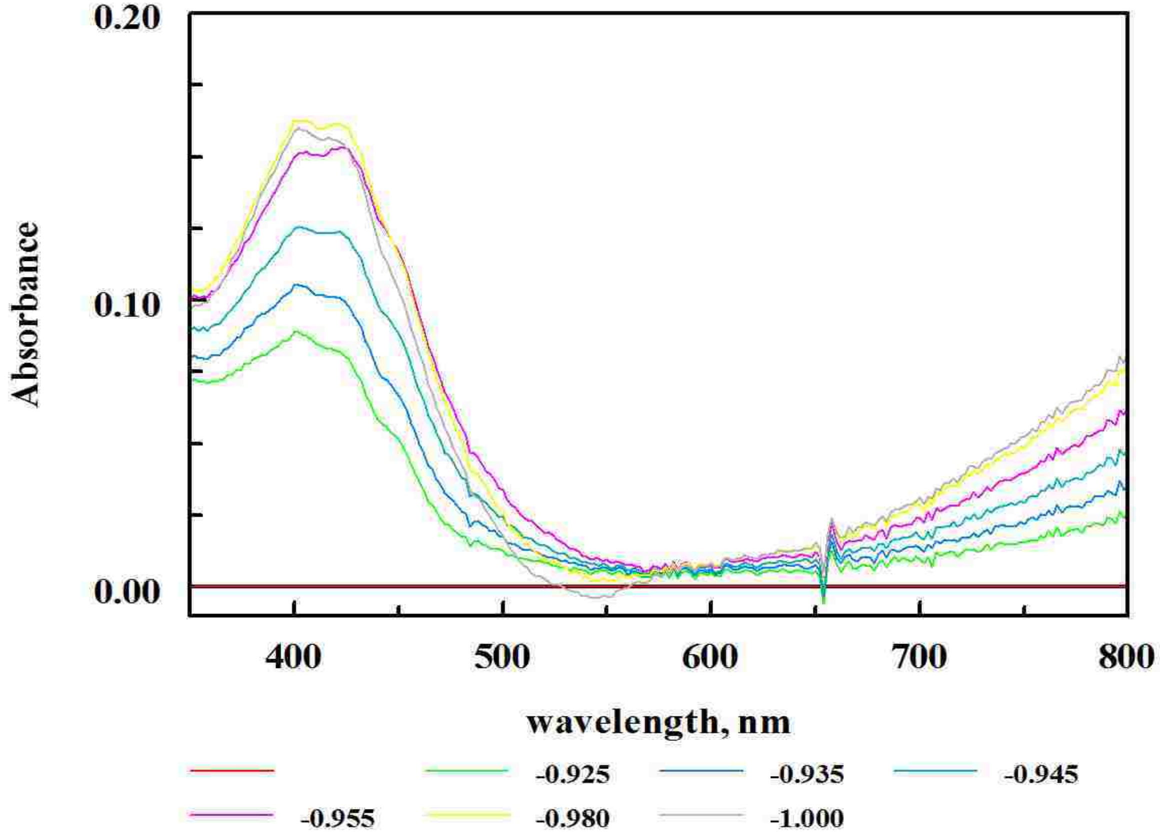

Figure 36: DNB radical anion absorbance in the forward scan in BMImPF$_6$. Potentials are given in V and versus Ag/AgNO$_3$

The examination of the two spectra of the radical anion and dianion shows that their shapes and their λ_{max} are quite similar to the spectra in the acetonitrile (*Figure 37*). It is reasonable to expect that the ratio of ε's at their respective λ_{max} values to be similar. Using this assumption, the spectra for the dianion and the radical anion were normalized and the concentrations recalculated. As was done for the concentrations in acetonitrile, the concentration of the starting material could now be calculated by difference (*Figure 38*).

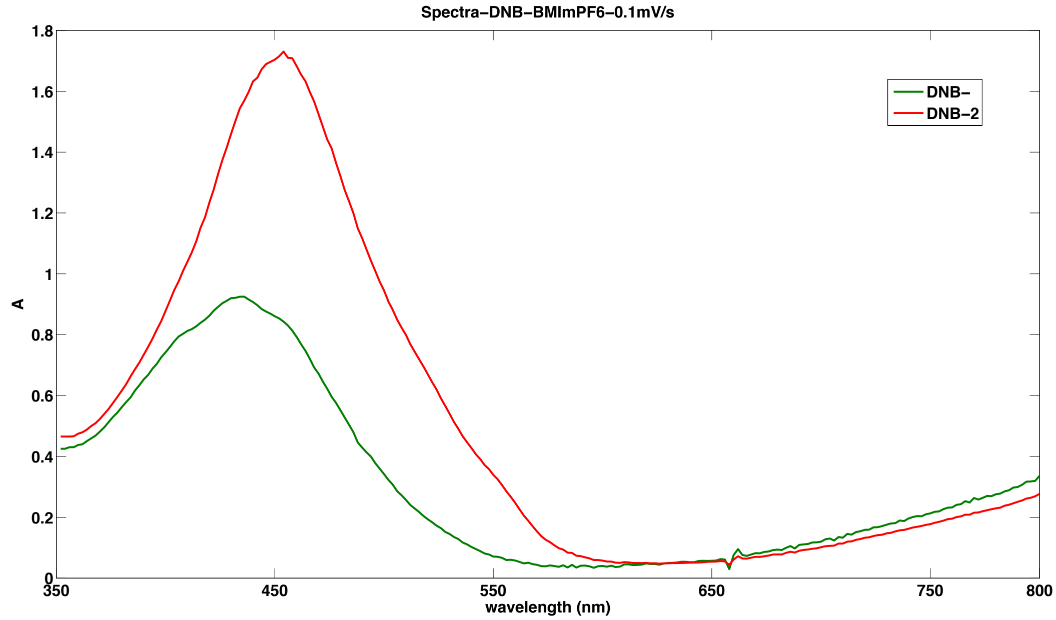

Figure 37: Spectral profiles of the DNB radical anion and dianion in $BMImPF_6$

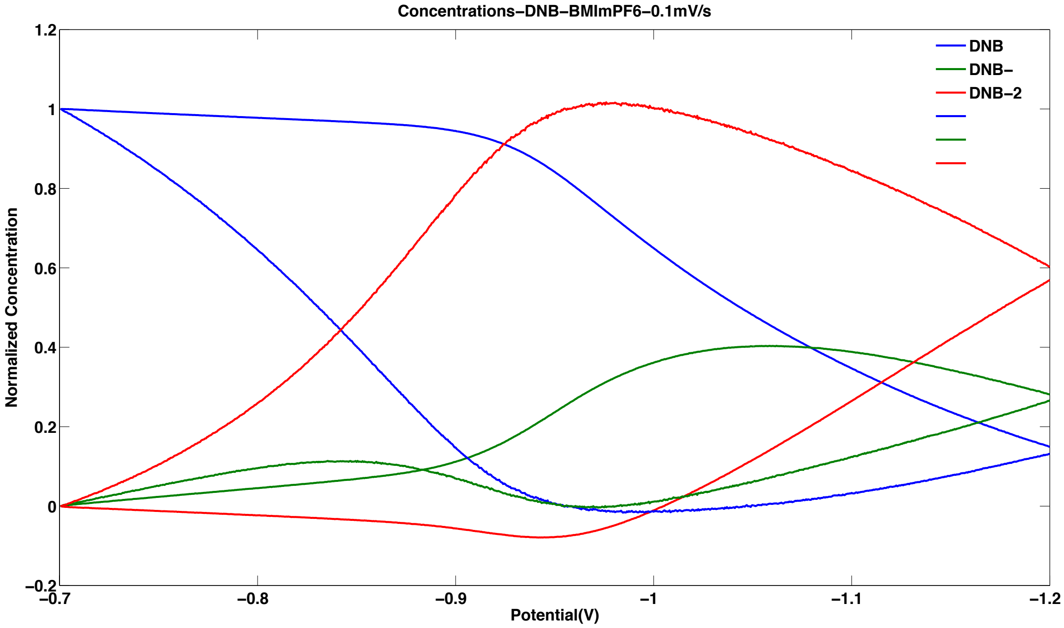

Figure 38: Concentrations of the neutral, radical anion and dianion DNB in $BMImPF_6$. Scan rate: 0.1mV/s. Potentials are versus $Ag/AgNO_3$

Using these concentrations, the currents due to the first and the second electron transfer (DCVA) were calculated. The potential of the first and second waves were found to be -0.920 and -0.944V, resulting in ΔE_{12} of 24mV. The shape of the DCVA compares well with the measured cyclic voltammogram (*Figure 39*). While the cyclic voltammetric data are similar to the DCVA trace, the DCVA curve was somewhat broader than the cyclic voltammograms. Both sets of data were obtained at the same time but the spectral data were obtained in the center of the electrode where Ohmic resistance was higher. As this affects both the forward and reverse scan, the calculated potentials will be minimally affected by this.

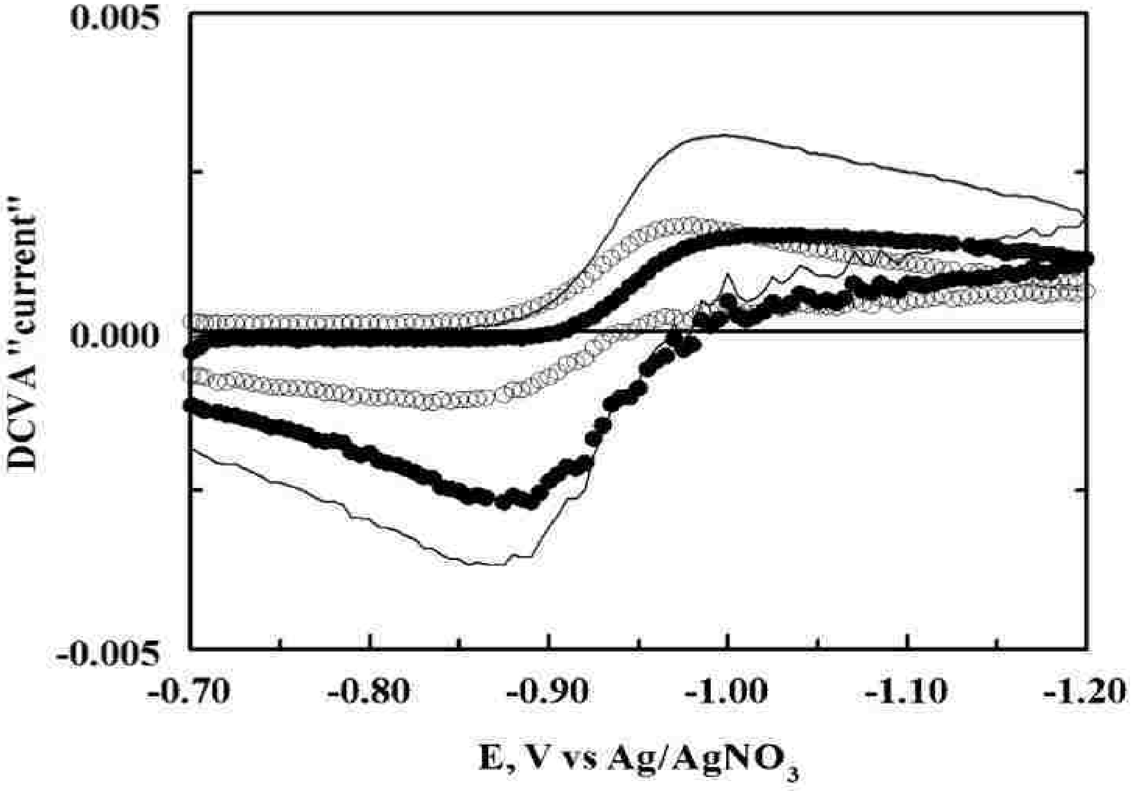

Figure 39: DCVA current during 0.1mM DNB electrolysis in BMImPF$_6$ at 0.1mV/s

Butler-Volmer Simulation

Using the Bulter-Volmer simulations, the electron transfer rates were fitted with experimental concentrations at a good correlation level (*Figure 40*). The rates values k^0_1 and k^0_2 were, respectively, 0.8 10^{-4} and 0.05 10^{-4} cm s^{-1}.

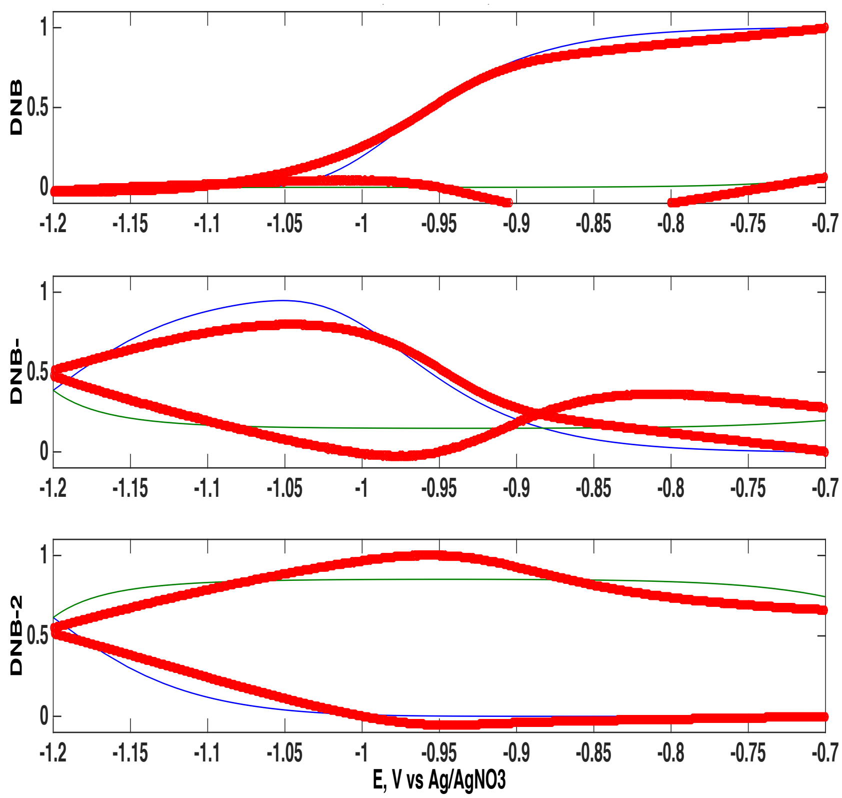

Figure 40: Variation of calculated (open circles) and experimental (lines) concentrations in $BMImPF_6$. Scan rate: 0.1mV/s

The results showed that in pure RTIL, the electron transfer kinetics were one order of magnitude slower than in acetonitrile, in agreement with literature (Chapter 1). The main factors can be attributed to significant inner and outer reorganization energies contributions in the RTIL solution.[52]

3.3 Voltammetry in ACN-BMImPF$_6$

The effect of ionic liquid fraction on the potential differences in ACN-BMImPF$_6$ mixtures was investigated. As was expected, voltammograms obtained in mixtures showed a decrease of ΔE_{12} as the RTIL concentration increased (*Figure 41*).

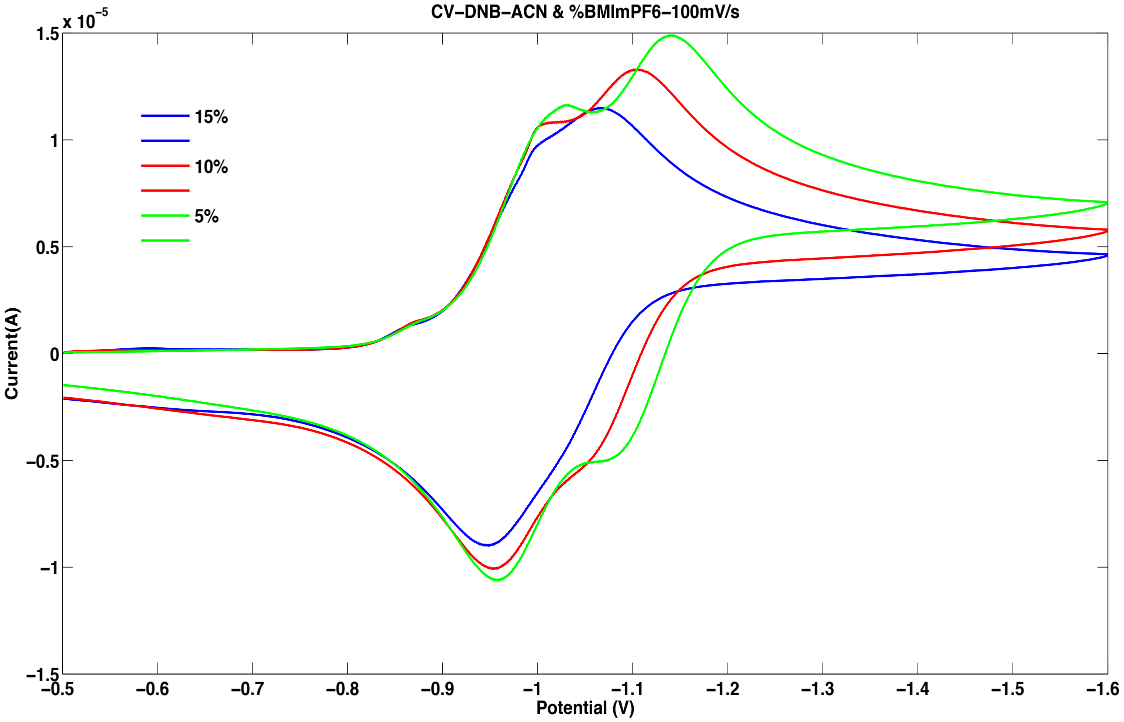

Figure 41: Voltammograms of 1mM DNB in mixtures ACN with 5, 10 and 15%BMImPF$_6$, at scan rate 100mV/s. Potentials are versus Ag/AgNO$_3$

Similar to previous analysis, UV-Visible SEC was carried out in mixtures of ACN-BMImPF$_6$, the concentrations and DCVA currents were calculated.

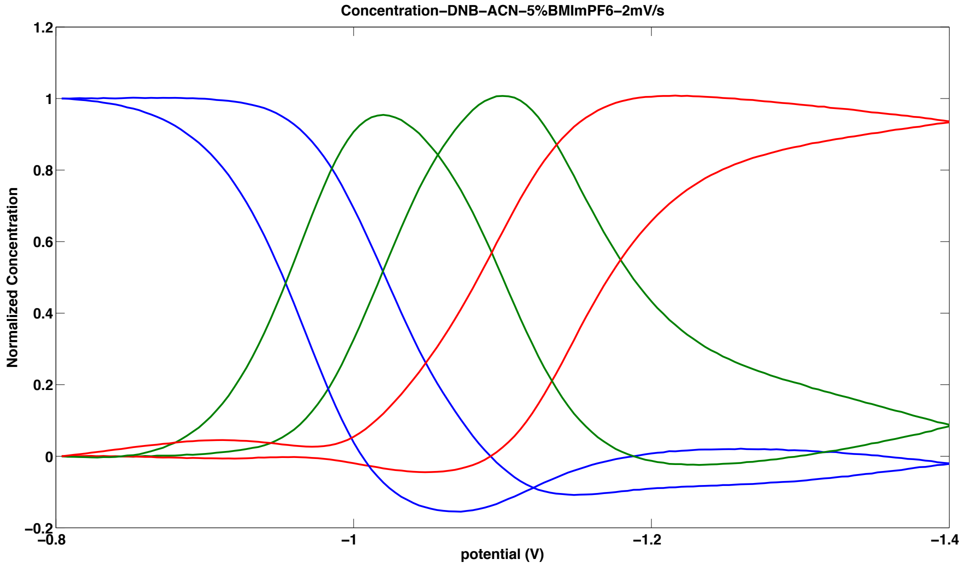

Figure 42: Concentrations of neutral, radical and dianion DNB during electrolysis in 5% BMImPF$_6$ mixture at 2mV/s. Potentials are versus Ag/AgNO$_3$

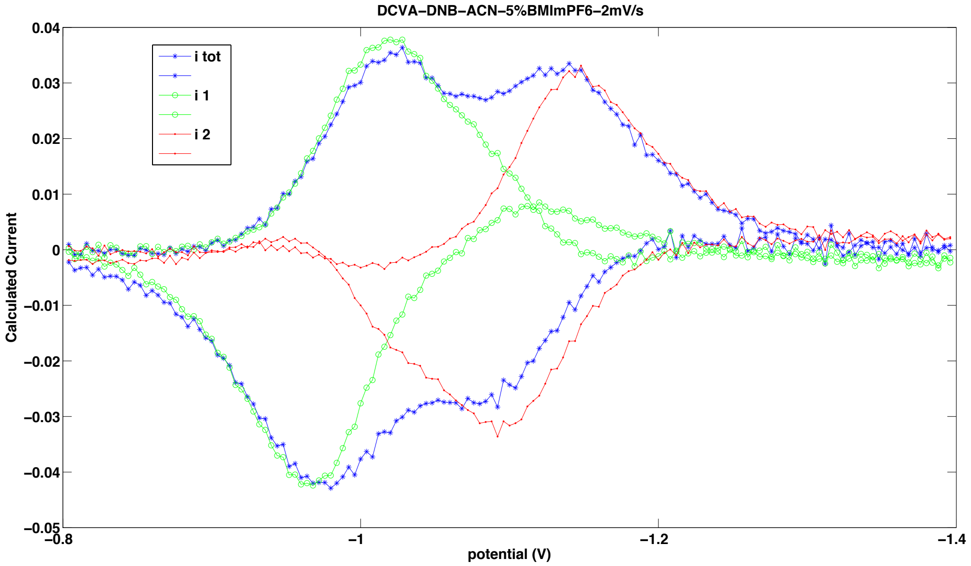

Figure 43: DCVA current during 0.1mM DNB electrolysis in 5% BMImPF$_6$ mixture at 2mV/s. Potentials are versus Ag/AgNO$_3$

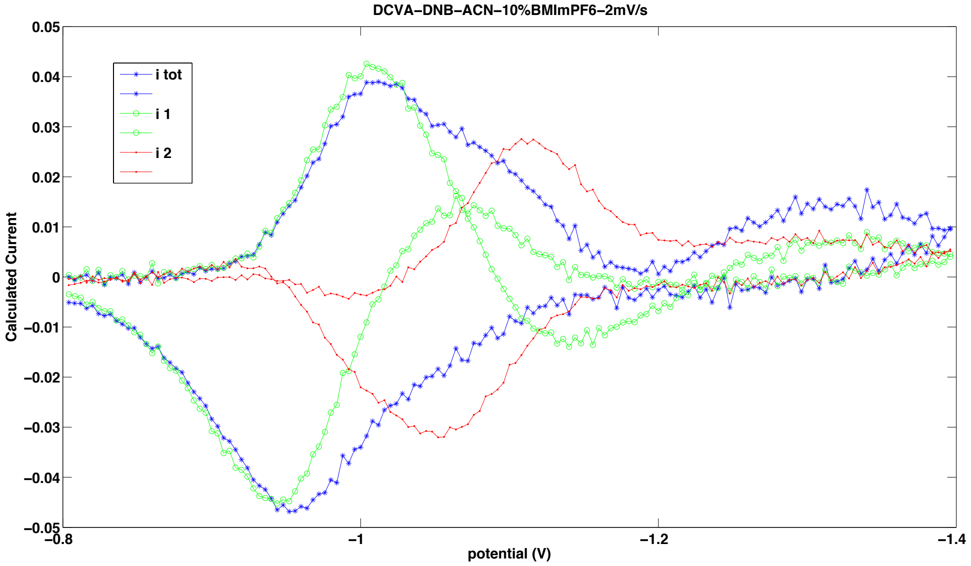

Figure 44: DCVA current during 0.1mM DNB electrolysis in 10% BMImPF$_6$ mixture at 2mV/s. Potentials are versus Ag/AgNO$_3$

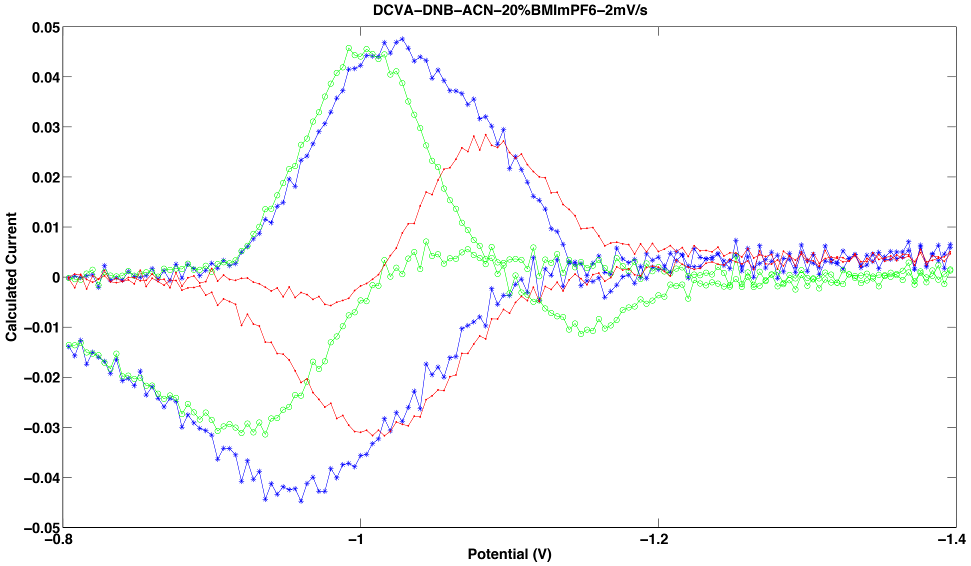

Figure 45: DCVA current during 0.1mM DNB electrolysis in 20% BMImPF$_6$ mixture at 2mV/s. Potentials are versus Ag/AgNO$_3$

In *Figure 42* (5%BMImPF$_6$), the concentrations of the three species (DNB, DNB$^-$ and DNB^{2-}) were calculated. By taking the derivative of the concentrations with respect to time, the DCVA was obtained (*Figure 43*). From the DCVA, the calculated potential of the first and second reduction were -1.004 and -1.118V, respectively. The ΔE_{12} values dropped from 220mV (0%) to 116mV (5%). Using similar analysis at 10%RTIL, the potentials of the first and the second were calculated as -0.982 and -1.082 V, respectively, with ΔE_{12} = 100mV (*Figure 44*). At 20% RTIL (*Figure 45*), the potential of the first and second reduction were found to be, -0.966 and -1.048, respectively (ΔE_{12} = 82mV).

The *Figure 46* shows the shift in ΔE_{12} upon introduction of the RTIL to the solution for a wide range of ACN-BMImPF$_6$ mixture. Of note, the decrease in the ΔE_{12} values with an increase of ionic liquid fraction was mostly due to stabilization of the second reduction wave.

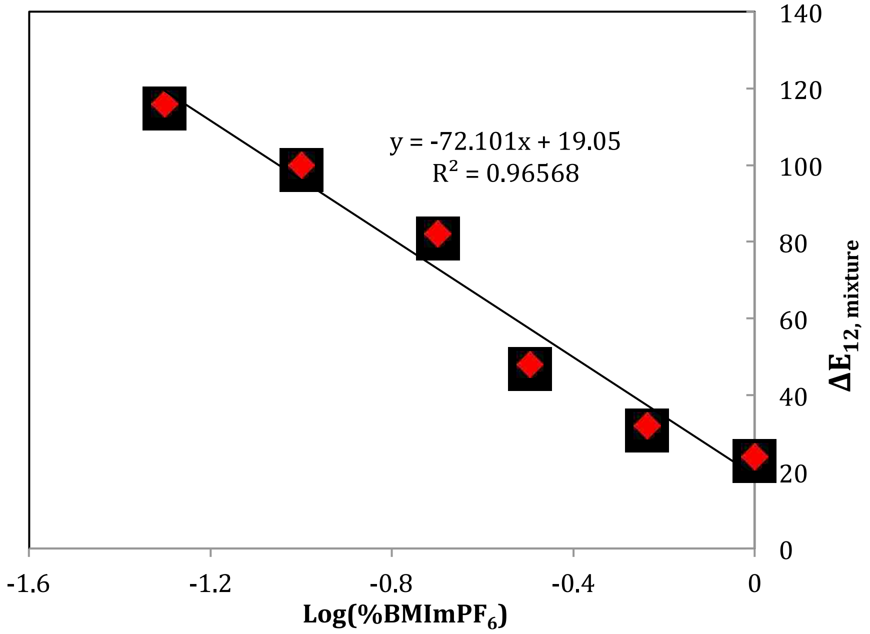

Figure 46: Variation of ΔE_{12} versus Log(%BMImPF$_6$) in ACN

Interestingly, a linear relationship was observed with the log %BMImPF$_6$. Such relationship could be rationalized if a mixture between RTIL and an organic solvent is not homogeneous. In an heterogeneous solution, solutes may partition between the organic solvent domains and the RTIL domain. This can be expressed with a partition coefficient, K:

$$K_{\mathrm{DNB}} = \frac{[\mathrm{DNB}]_{\mathrm{AN}}}{[\mathrm{DNB}]_{\mathrm{RTIL}}} = \frac{\mathrm{no.\,mol}_{\mathrm{DNB,AN}}/V_{\mathrm{AN}}}{\mathrm{no.\,mol}_{\mathrm{DNB,RTIL}}/V_{\mathrm{RTIL}}}$$

The total moles of DNB is equal to:

$$\#_{\text{mol tot,DNB}} = \#_{\text{mol DNB,AN}} + \#_{\text{mol DNB,RTIL}}$$

Substituting in the K expression, the #mol DNB is equal to:

$$\#mol\ DNB, RTIL = \#mol\,tot\left(\frac{V_{RTIL}}{K_{DNB}V_{AN} + V_{RTIL}}\right)$$

This same equation can be written for DNB$^-$ and DNB^{2-}. The value of K for DNB and DNB$^-$ is probably near unity as the potential for the first reduction is not significantly affected by the presence of the RTIL. The final product, DNB^{2-}, would be strongly attracted to RTIL domain, causing the $K_{\mathrm{DNB2-}}$ to be much less than 1.

$$\boldsymbol{K_{DNB} = K_{DNB-} = 1 \quad ; \quad K_{DNB2-} << 1}$$

Under these conditions:

$$\#\,mol_{DNB2-,RTIL} = \#\,mol\,tot_{DNB-2}\left(\frac{V_{RTIL}}{K_{DNB2-}V_{AN} + V_{RTIL}}\right) \approx \#\,mol\,tot_{DNB2-}$$

The Nernst equation for the DNB^{-}/DNB^{2-} electron transfer is given by:

$$E^{2}_{1/2,mixed} = E^{2}_{1/2,RTIL} - 0.059\log\frac{\left[DNB^{-}\right]}{\left[DNB^{2-}\right]} = E^{2}_{1/2,RTIL} - 0.059\log\frac{\#mol\ DNB^{-}}{\#mol\ DNB^{2-}}$$

$$= E^{2}_{1/2,RTIL} - 0.059\log\frac{\#mol\ tot_{DNB^{-}}\left[V_{RTIL}/\left(K_{DNB-}V_{AN}+V_{RTIL}\right)\right]}{\#mol\ tot_{DNB2-}}$$

$$E^{2}_{1/2,mixed} = E^{2}_{1/2,RTIL} - 0.059\log\frac{\#\ mol\ tot_{DNB-}}{\#\ mol\ tot_{DNB2-}} - 0.059\log\frac{V_{RTIL}}{K_{DNB-}\ V_{AN}+V_{RTIL}}$$

At $E_{1/2,mix}$, $\#_{mol\ totDNB-} = \#_{mol\ totDNB2-}$, and assuming $K_{DNB-} \approx 1$,

$$E_{1/2,\mathrm{mixed}} = E_{1/2,\mathrm{RTIL}} - 0.059\log\frac{V_{\mathrm{RTIL}}}{V_{\mathrm{AN}} + V_{\mathrm{RTIL}}}$$

$$\Delta E^{12}_{1/2,mixed} = \Delta E^{12}_{1/2,RTIL} - 0.059\log\frac{V_{RTIL}}{V_{AN}+V_{RTIL}}$$

The slope of *Figure 46* was 72 mV, reasonably close to the predicted 59 mV, given the solution resistance and the assumptions of the derivation.

The above rational indicated that RTIL/organic solvent mixtures can be better envisioned as RTIL domains and organic solvent domains, much like micellar behavior in aqueous solutions. Similar observations were reported by Syroeshkin et al. in $BMImBF_4$/DMF, where association of DNB^{2-} with four cations was predicted.[77] That is consistent with small domains of RTIL being formed within the molecular solvent, which can readily solvate DNB dianion.

3.4 Voltammetry in ACN-BMImNTF$_2$

Cyclic voltammetry was carried out in an imidazolium ionic liquid containing different anion, NTF$_2^-$. The voltammograms in mixtures with ACN are shown in *Figure 47*. In contrast to BMImPF$_6$ experiments, the acetonitrile was added to a starting solution of BMImNTF$_2$. As expected, the voltammograms showed separation of the coalesced wave into two single waves upon increasing the ACN fractions.

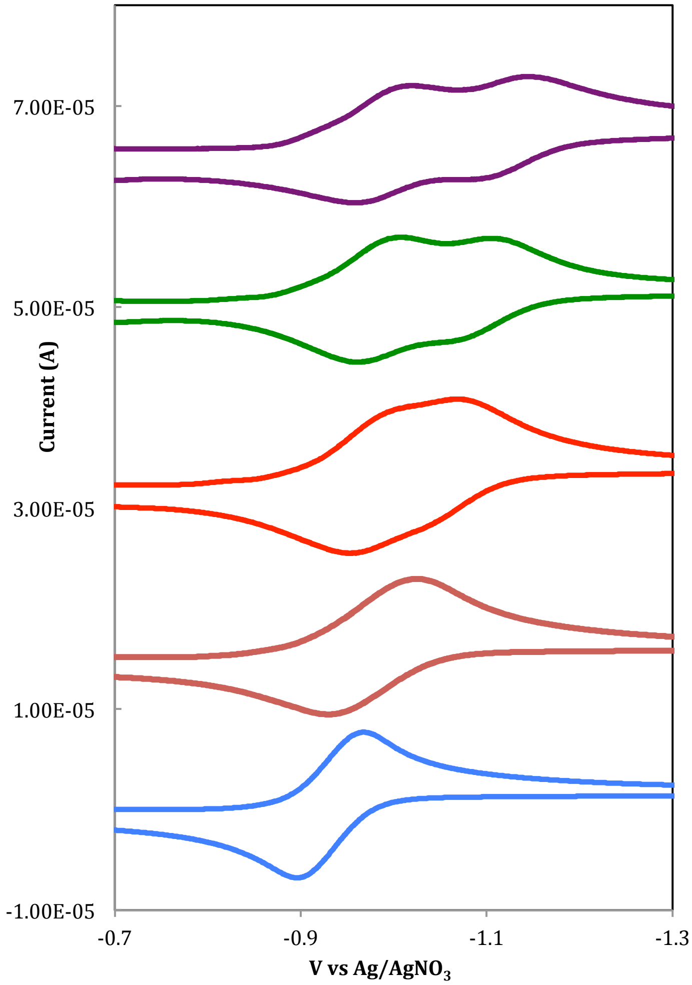

Figure 47: Cyclic voltammetry of 2.0 mM DNB in BMImNTF$_2$, 50, 80, 90 and 95% ACN, respectively from bottom to top.

It is worth noting that in many cases, the cyclic voltammetry in $BMImNTF_2$ was quite distorted, as shown in *Figure 48*. Two irreversible waves were observed at low concentrations of DNB. The first wave was at −0.85 V and the second at −1.2 V. At higher concentration of DNB, a reversible wave appeared with an $E_{1/2}$ of −0.954 V. This was consistent with the observed $E_{1/2}$ of DNB in $BMImPF_6$ of −0.93 V.

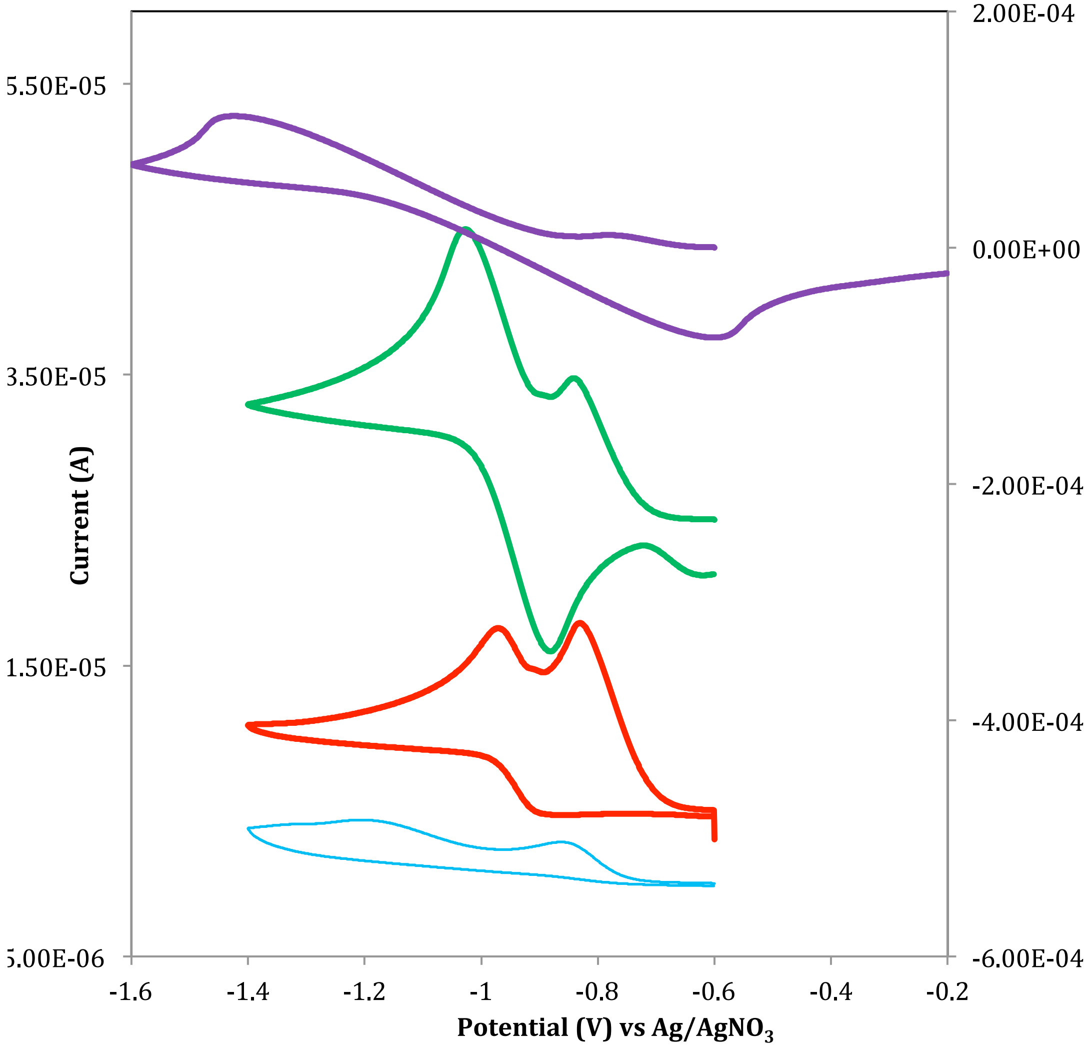

Figure 48: Cyclic voltammetry of DNB in $BMImNTF_2$ before water removal. 1, 5, 10, 100 mM DNB, respectively from bottom. Scan rate = 100 mV/s.

Such increase in stability of very basic dianions in RTIL at higher substrate concentrations was also reported by Abdul-Rahim et al. for the voltammetry of trans-stilbene in another NTF_2-based RTIL.[63] In their work, the chemical irreversibility of the wave was attributed to the reaction of the stilbene dianion with trace water. Although trace of water was a reasonable source of protonation, the theoretical work of Minami and Fry showed that protonation by the hydrogen attached to the C-2 carbon is also possible.[76]

In *Figure 49*, the cyclic voltammogram of DNB in the dried solvent is shown. While a decrease in the water content eliminated the second wave, little change was observed in the first wave. The concentration of DNB was then increased in the dried $BMImNTF_2$. The voltammetric results were similar to the untreated $BMImNTF_2$ solution, except for the disappearance of the second (water related) wave in the dried solvent. At this stage, the results suggest that either the dianion is protonated by the RTIL cation or there are other sources contributing to this subsequent chemical reaction with DNB^{2-}. A more detailed discussion of possible sources of such chemical reaction in RTIL solutions will be presented in Chapter 4.

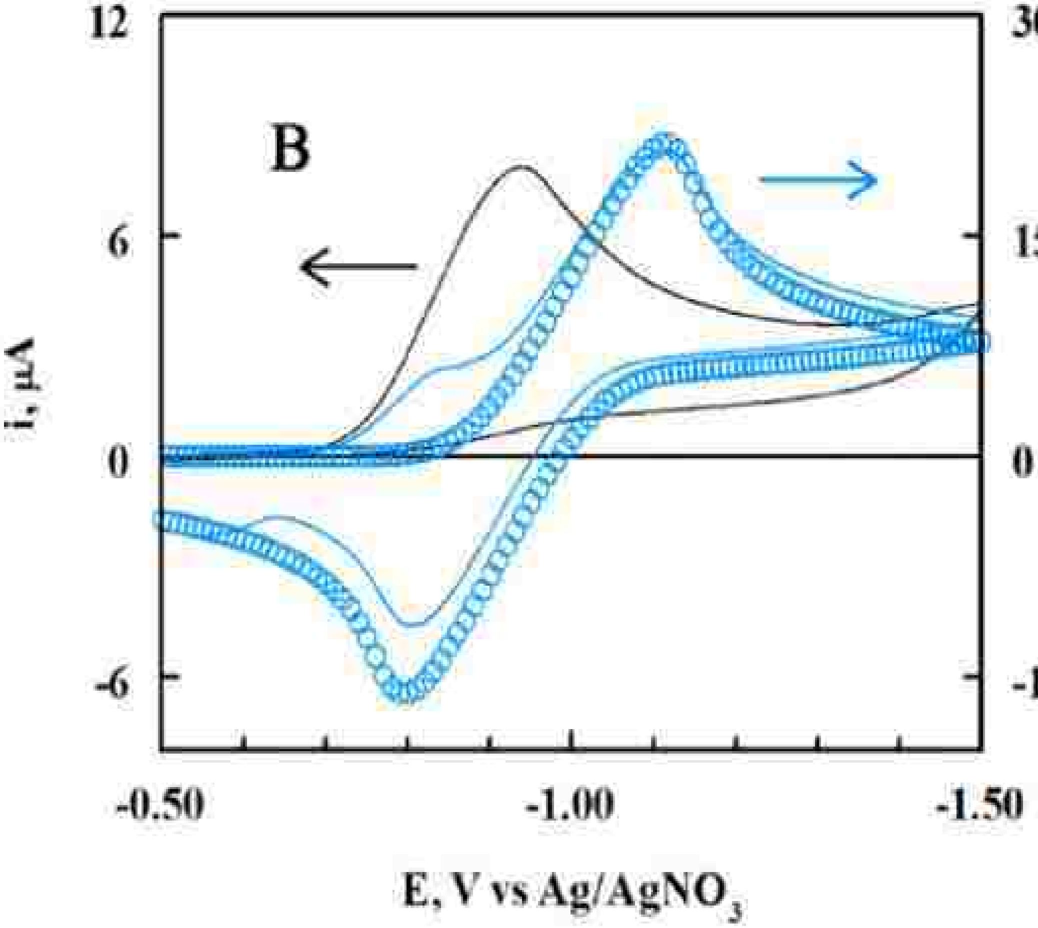

Figure 49: Cyclic voltammetry of DNB in BMImNTF$_2$ after water removal. Black lines: 1.0 mM DNB. Blue lines: 10 mM DNB. Scan rate = 100 mV/s. Simulated data: blue circles. For 10 mM DNB: $E_1 = -0.93$ V, $E_2 = -0.95$ V. Uncompensated resistance = 6000 Ω, ΔE_{12} value of 20mV.

3.5 Voltammetry in ACN-AmNTF$_2$

An ammonium-based RTIL was also used to evaluate the drop in the ΔE$_{12}$ values in mixtures. Similar to previous RTILs, the waves coalesced into one wave at a low volume fraction of RTIL (*Figure 50*). Voltammograms in 10% and pure AmNTF$_2$ solutions are shown in the figure below. The stability of the dianion in this ionic liquid ruled out NTF$_2^-$ as the source of the chemical reaction seen in BMImNTF$_2$.

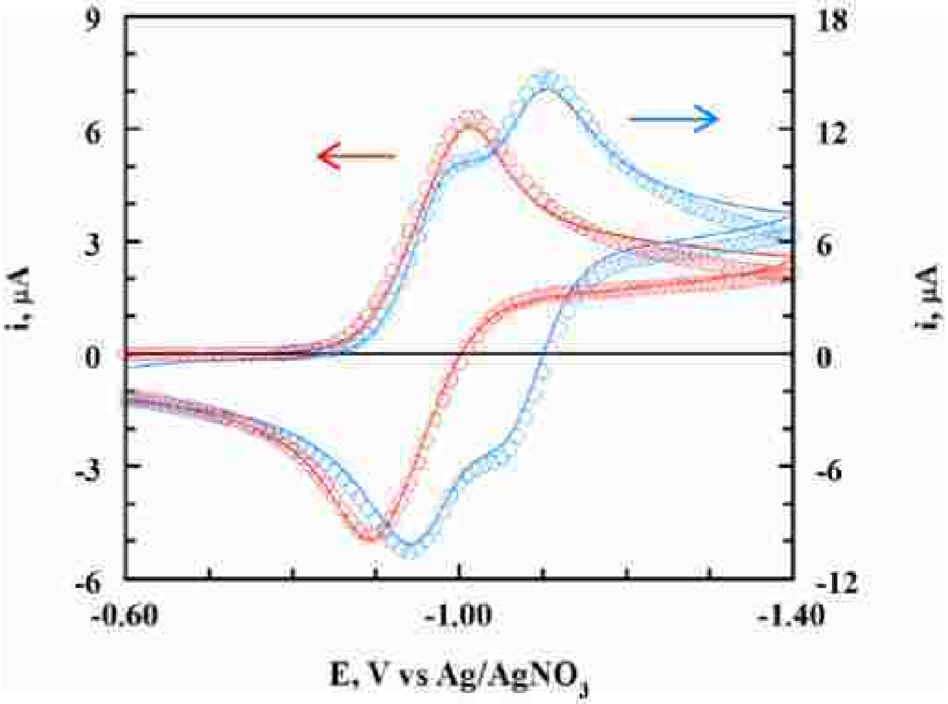

Figure 50: Cyclic voltammetry of 1.0 mM DNB in AmNTF$_2$ (red line) and 10% AmNTF$_2$/acetonitrile (blue line). Scan rate = 100 mV/s. Simulated data: red circles, $E_1 = -0.933$ V, $E_2 = -0.972$ V. Uncompensated resistance: 4000 Ω. Blue circles: $E_1 = -0.964$ V, $E_2 = -1.079$ V.

3.6 Voltammetry in ACN-BMImCl

The effect of ion pairing by a salt that does not form an ionic liquid (BMImCl) is shown in *Figure 51* (in this case, concentration is given in % mol/volume). The effect of ion pairing levels off at higher concentrations of the salt. In fact, ion pairing between the cation and anion of the salt becomes significant at higher concentrations. As result, the concentration of “free” cation (not ion paired) increases slower than the molar concentration of the salt. Higher currents were observed with the increase of the salt, due to increase of the ionic strength of the solution.

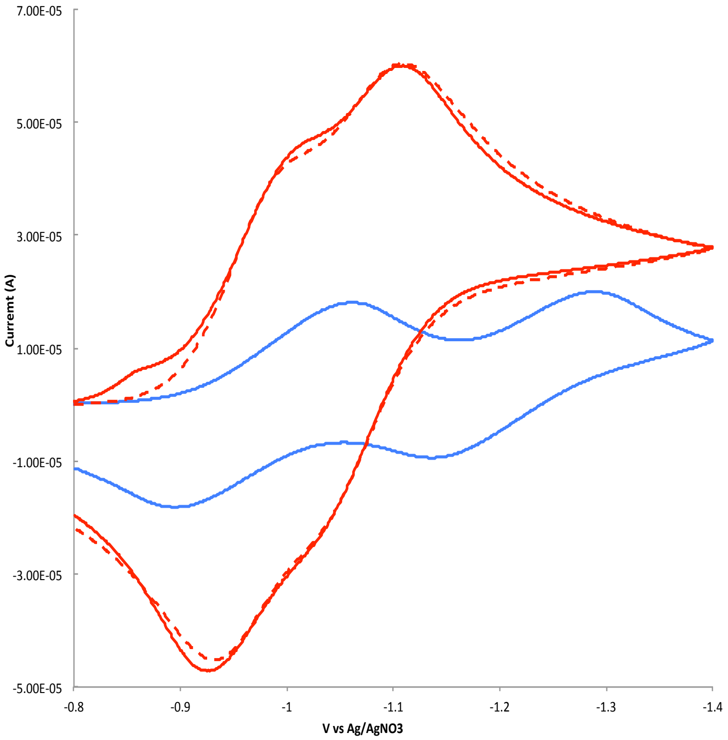

Figure 51: Cyclic voltammetry in ACN (blue line) and in 23% BMImCl (mol/mol): red line is the experimental data, dashed line is the simulated data, EE mechanism. $E_1 = -0.995$ *V,* $E_2 = -1.188$ *V. 100 mV/s.*

3.7 Potential shifts vs %RTIL

Variation of ΔE_{12} values in mixture systems for the three RTILs and one solid salt investigated in this work are shown in *Figure 52*. The three RTILs yielded quite similar ΔE_{12} values over a wide range of mixtures concentrations. Although Am^+ is somewhat smaller than TBA^+ (tetrabutylammonium) ion, the difference in ion pairing between these two ions should not be great. Considering that 0.10 M TBAP has a mole fraction of about 0.005 in acetonitrile, the presence of a smaller amount of $AmNTF_2$ (0.0037) decreases the ΔE_{12} value by an additional 60−65 mV, more than can be explained simply by invoking ion pair formation alone.

Similar studies were also carried out by Evans for tetraalkylammoium salts.[67] As was observed for BMImCl, the ΔE_{12} values leveled off at higher ionic strengths, and two waves for DNB were always observed. Stronger ion pairing was observed for $BMIm^+$ in solid salt, by the ΔE_{12} value leveling off at about 100 mV versus 160 mV for tetramethylammonium or 220 mV for tetrabutylammonium.

These results were consistent with partitioning of electrogenerated species into RTIL nano-domains in the mixture. The higher partition of the dianion into ionic liquid domain is mostly the driving force for the merging of the two reduction waves. Observation of this coalescence in low fraction mixtures indicated formation of RTIL nano-domains in these media, mimicking the voltammetry in pure RTIL.

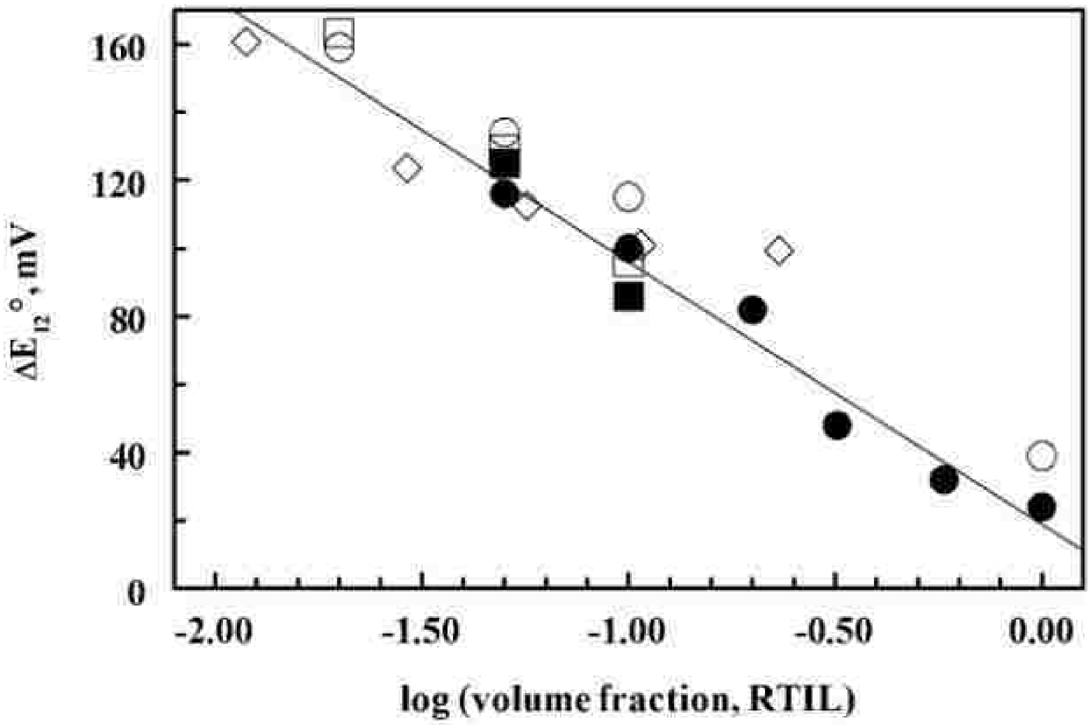

Figure 52: Variation in the ΔE_{12}° for DNB as a function of % BMImPF$_6$ (filled circles), % AmNTF$_2$ (open circles), %BMImNTF$_2$ (filled squares), dried % BMImNTF$_2$ (open squares), and % (mol/volume) BMImCl (diamonds) in acetonitrile.

3.8 FTIR Spectroelectrochemistry in ACN-RTILs

As previously discussed, the FTIR SEC of DNB was carried out in acetonitrile, where most changes upon reductions were unambiguously investigated in the fingerprint region.[74] In our case, addition of the RTIL to acetonitrile solutions increases the background absorption of this region by the solvent system, making the study of the electro-reductions more difficult.

Interestingly, our electrolysis experiment in acetonitrile revealed changes in the IR spectrum, in the region 1800 – 2800 cm^{-1}, where the solution itself was relatively transparent. *Figure 53* shows these changes in the reduction and re-oxidation of DNB solution in acetonitrile, after subtraction of the starting spectrum. The reduction showed clearly the emergence of a set of bands at 1934, 2131, 2353 and 2673 cm^{-1}. Electrolysis at more negative potentials led to disappearance of these bands and appearance of new bands at 1855, 1880, 1952, 2002, 2096, 2150, 2389, 2480, 2498 and 2736 cm^{-1}. The re-oxidation showed a reversible behavior of these changes, with isosbestic points at 1940, 2010 and 2140 cm^{-1}. Bands due to the background and/or subsequent chemical reactions were also observed at the end of the electrolysis. These variations were indeed correlated with electron transfer, where the first and second sets of bands corresponded to the first and second reductions, respectively. To the best of our knowledge, these bands have not been reported for DNB radicals. Whereas assignments of their nature would require further investigation, we believe that these bands are very likely due to overtones and/or combination bands.

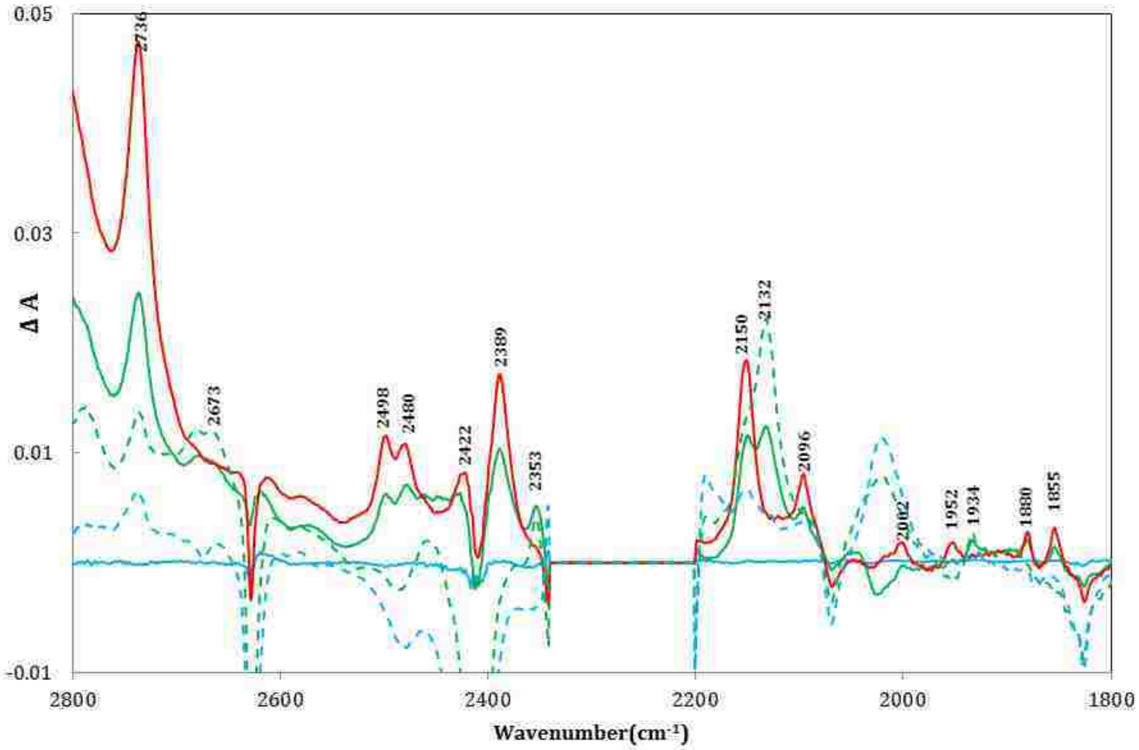

Figure 53: FTIR SEC of DNB in ACN. Solid lines correspond to the forward electrolysis: DNB^{1-} (green line) and DNB^{2-} (red line). Dashed lines correspond to backward electrolysis: DNB^{1-} (green line) and DNB (blue line).

FTIR SEC of DNB in ACN-RTIL mixtures were also carried out, and the results are shown in Figures 54-56. In general, addition of RTIL didn't screen the characteristic bands of DNB radicals in the selected region. Electrolysis experiments in mixtures gave similar variations as seen in acetonitrile, where radical anion features could be observed even at higher RTIL fractions. In the pure RTIL, these features were observed more clearly in the re-oxidation scan. The evolution of the IR spectrum was reversible in the electrolysis timescale.

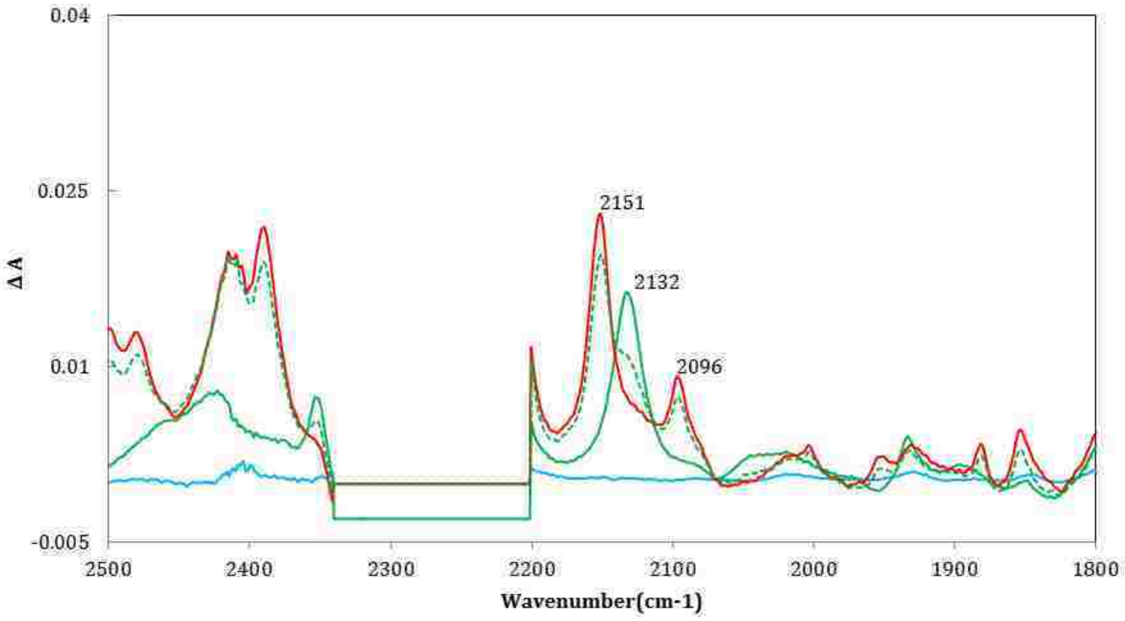

Figure 54: FTIR SEC of DNB in ACN-20%AmNTF$_2$. Solid lines correspond to the forward electrolysis: DNB^{1-} (green line) and DNB^{2-} (red line). Dashed lines correspond to reverse scan

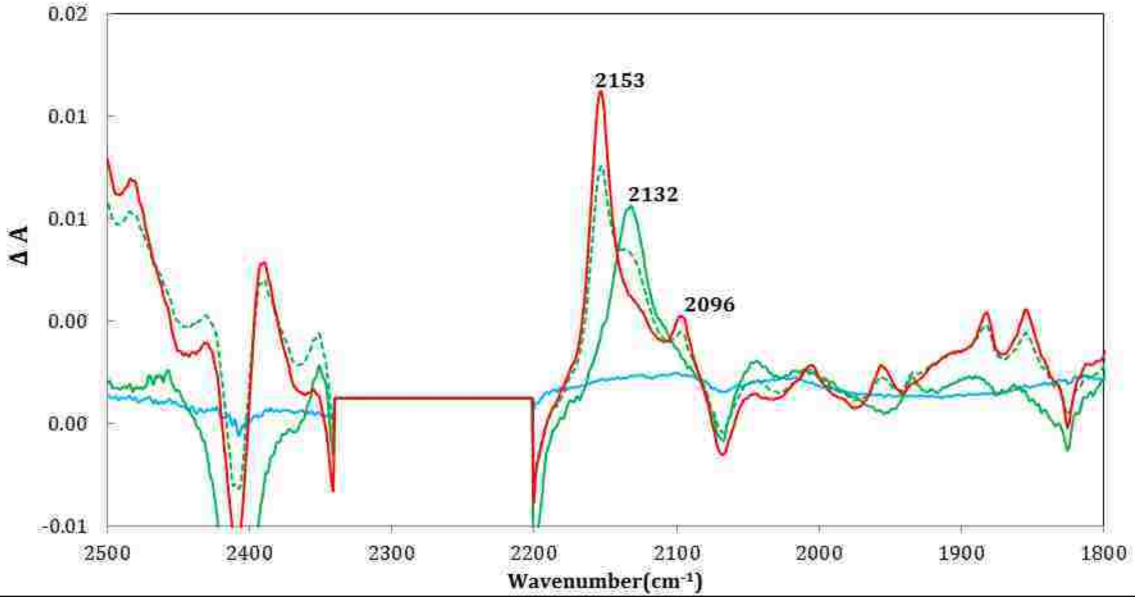

Figure 55: FTIR SEC of DNB in ACN-20%BMImBF$_4$. Solid lines correspond to the forward electrolysis: DNB^{1-} (green line) and DNB^{2-} (red line). Dashed lines correspond to reverse scan

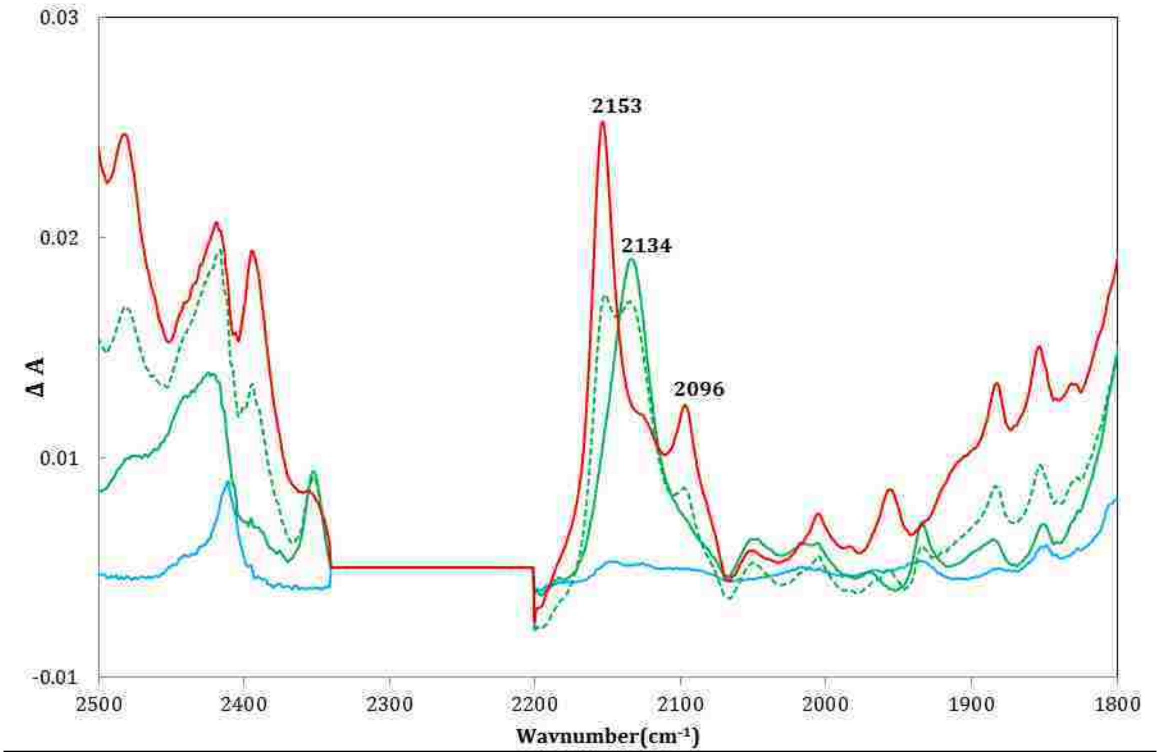

Figure 56: FTIR SEC of DNB in ACN-20%BMImNTF$_2$. Solid lines correspond to the forward electrolysis: DNB^{1-} (green line) and DNB^{2-} (red line). Dashed lines correspond to reverse scan

For an easier evaluation of the RTIL effects, we limited our analysis to the most intense bands, with clear isobestic changes. These bands are summarized in *Table 8*. From the results, the nature of the cation had a measurable effect on the shift in these vibrations. While the ammonium cation had a small effect on the anion and dianion features, the imidazolium showed stronger interactions with the radicals. This strong interaction shifted the radical and dianion features from 2132 to 2141 cm^{-1} and from 2151 to 2154 cm^{-1}, respectively, when going from ACN to BMImNTF$_2$.

Table 8: IR frequencies for DNB^{-1} and DNB^{2-} in ACN and %RTIL mixtures

Solvent system	DNB^{-}	DNB^{2-}
ACN	2131	2096, 2151
20%$AmNTF_2$	2132	2096, 2152
$AmNTF_2$	2132	2096, 2152
20%$BMImBF_4$	2132	2096, 2153
50%$BMImBF_4$	2133	2097, 2153
20%$BMImNTF_2$	2134	2096, 2153
50%$BMImNTF_2$	2136	2097, 2154
$BMImNTF_2$	2141	2097, 2154

The FTIR electrolysis results in mixtures revealed two main outcomes. First, the observation of the radical anion features at very high concentrations of the RTIL is a further indication that no potential inversion occurs in these media. This observation consolidates our results based on calculated ΔE_{12} in mixtures, using UV-visible SEC method. Second, compared to the electronic spectra, the vibrational spectra of DNB radicals seem to be more sensitive to RTIL introduction. The shift of the characteristic bands of DNB radicals appeared to be dependent on the nature of the RTIL cation (Figures 57-58). In fact, partitioning of the radicals into ammonium RTIL domain results in no significant shift of the radicals vibrations. In contrast, solvation by imidazolium RTIL led to significant shift of about 10 cm^{-1}. This shift was more pronounced in the NTF_2 compared to BF_4^- based RTIL.

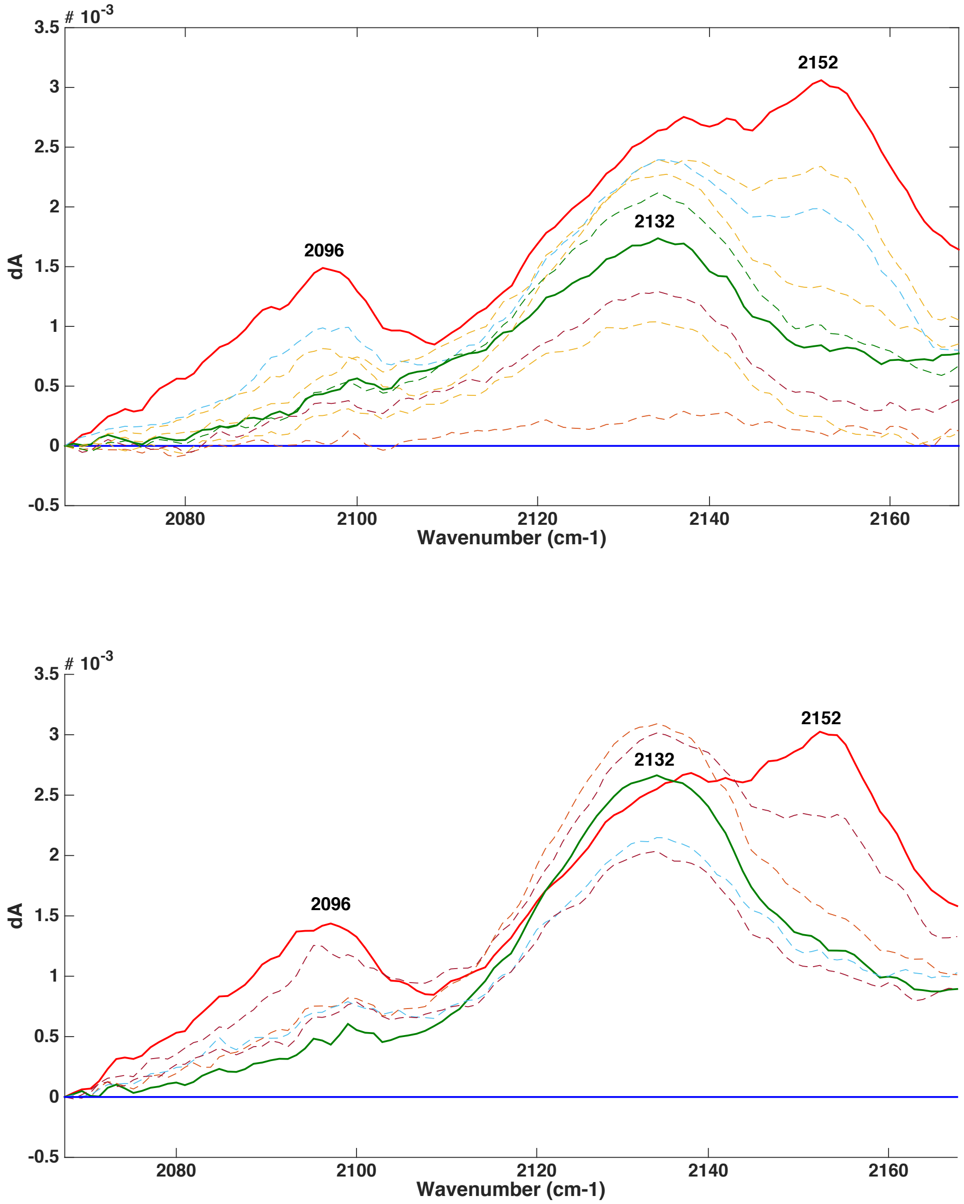

Figure 57: FTIR-SEC of DNB in AmNTF$_2$ during forward and reverse scan. Solid lines: DNB$^-$ (Green line) and DNB^{2-} (red line). Dashed lines are intermediate spectra.

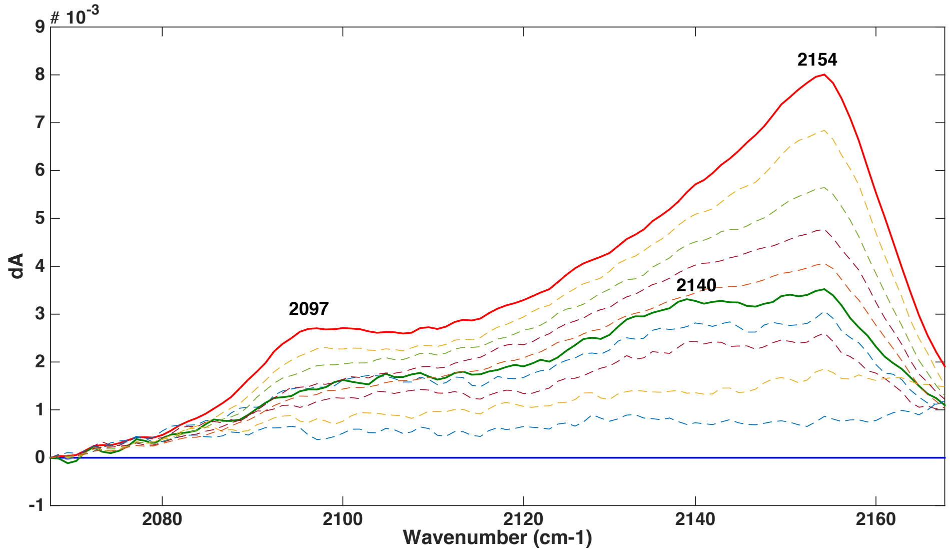

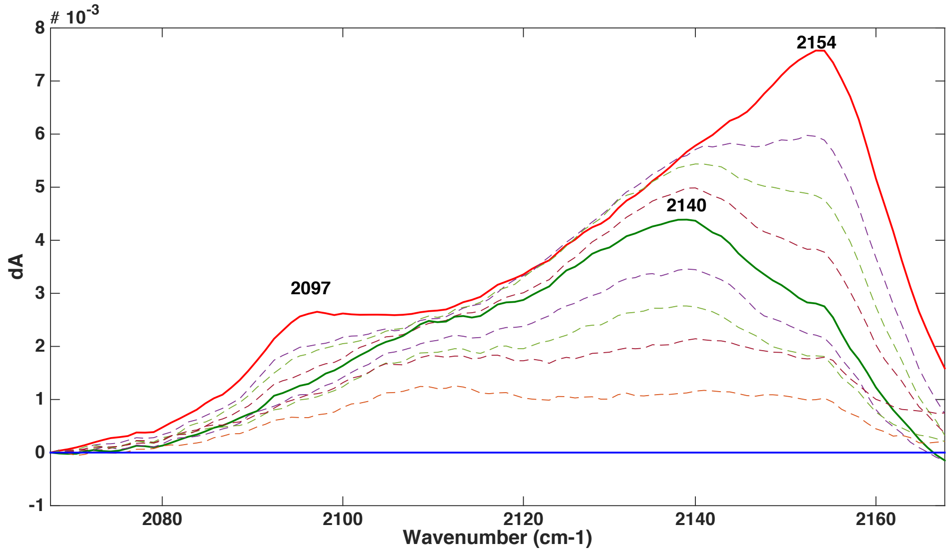

Figure 58: FTIR-SEC of DNB in BMImNTF$_2$ during forward and reverse scan. Solid lines: DNB$^-$ (Green line) and DNB^{2-} (red line). Dashed lines are intermediate spectra.

These results are consistent with electrostatic interactions that are dependent on the charge localization and the structure of the RTIL cation. The flexibility of the ammonium cation to arrange itself around charged radicals led to less electrostatic interactions within the RTIL domain. This resulted in minimal changes in the IR spectrum. The planarity and the localized charge in the imidazolium ring make this cation less flexible to adopt several arrangements, when interacting with negatively charged DNB radicals. Such cation rigidity would favor a unique ion paring through the polar groups, imidazolium ring with the charged nitro-groups. Such interactions would be the origin of the shifts seen in $BMIm^+$ ionic liquids. The larger shifts with imidazolium RTILs were consistent with stronger stabilization of ΔE_{12} by imidazolium compared to ammonium solid salts. The basicity of the RTIL anion may also enhance this effect. For NTF_2^-, a less basic anion than BF_4^-, the $BMIm^+$ cation is relatively free to interact strongly with DNB radicals, leading to larger shifts.

Interestingly, the highest shift was observed for the radical anion, implying that electrostatic interactions with the imidazolium cation are stronger for this species compared to the dianion. This may be interpreted in terms of the symmetry of the charge distribution over the radical backbone. Ion paring interactions would tend to localize the charge onto one nitro group over the other, leading to inequivalent charge distribution for the radical anion. RTIL introduction increases ion paring with the anion radical, resulting in higher shift of the overtone/combination bands. The balanced interactions with two cations in each side would make the dianion vibrations less sensitive to ion paring effects.

3.9 rRaman Spectroelectrochemistry in ACN-RTILs

In an attempt to further understand the RTIL effects on the vibrational structure of DNB radicals, rRaman spectroelectrochemistry was carried out in mixtures ACN-%RTILs. In contrast to UV-visible and FTIR SEC, the electrogeneration of radicals and the acquisition of spectra were separately carried out (ex-situ SEC). The power of rRaman over other spectroscopic methods enabled the acquisition of the spectrum for the radical anion even at higher RTIL concentrations in the mixture, where it would be significant disproportionation to the neutral and dianion species. At 50% of RTIL mixture, the ΔE_{12} is about 32mV, corresponding to a disproportionation constant K of 0.29 versus 1.6 10^{-4} for ΔE_{12}= 224mV in acetonitrile. In this mixture, more than half (52%) of the anion molecules disproportionate into neutral and dianion.

Figure 59 shows the rRaman SEC of the radical anion in the mixtures. In addition to small shifts to higher energies, increasing the RTIL fraction in mixture led to significant changes in intensities of Raman vibrations of the mono-anion. Introduction of $BMImBF_4$ or $AmNTF_2$ shifted the vibrations 1264, 1430, 1606 and 1896 respectively to 1268, 1432, 1609, 1901, increased the intensities of 1264, 1292, 1552, 1623, 1638, 2115 and decreased the intensities of 1606, 2327 and 2382 cm^{-1}. In comparison with the imidazolium RTIL, the strong band at 1430 cm^{-1} almost disappeared at 50% fraction of the ammonium salt. Similarly to radical anion, rRaman spectra were collected for DNB dianion in mixtures ACN-RTILs (*Figure 60*). While there was no significant shifts, important changes of the intensities of the dianion were overserved upon increasing the RTIL fraction in the mixture.

Addition of RTILs increased the intensities of 1037, 1101, 1155, 1279, 1370, 1469, 1520, 1589, 1650, 1936 and 2215 cm^{-1}. It is worth noting that both radicals exhibit strong Raman bands in the range of 2000 to 2300 cm^{-1}, with shapes similar to the IR features. Hence, these features would be very likely overtones/combination bands.

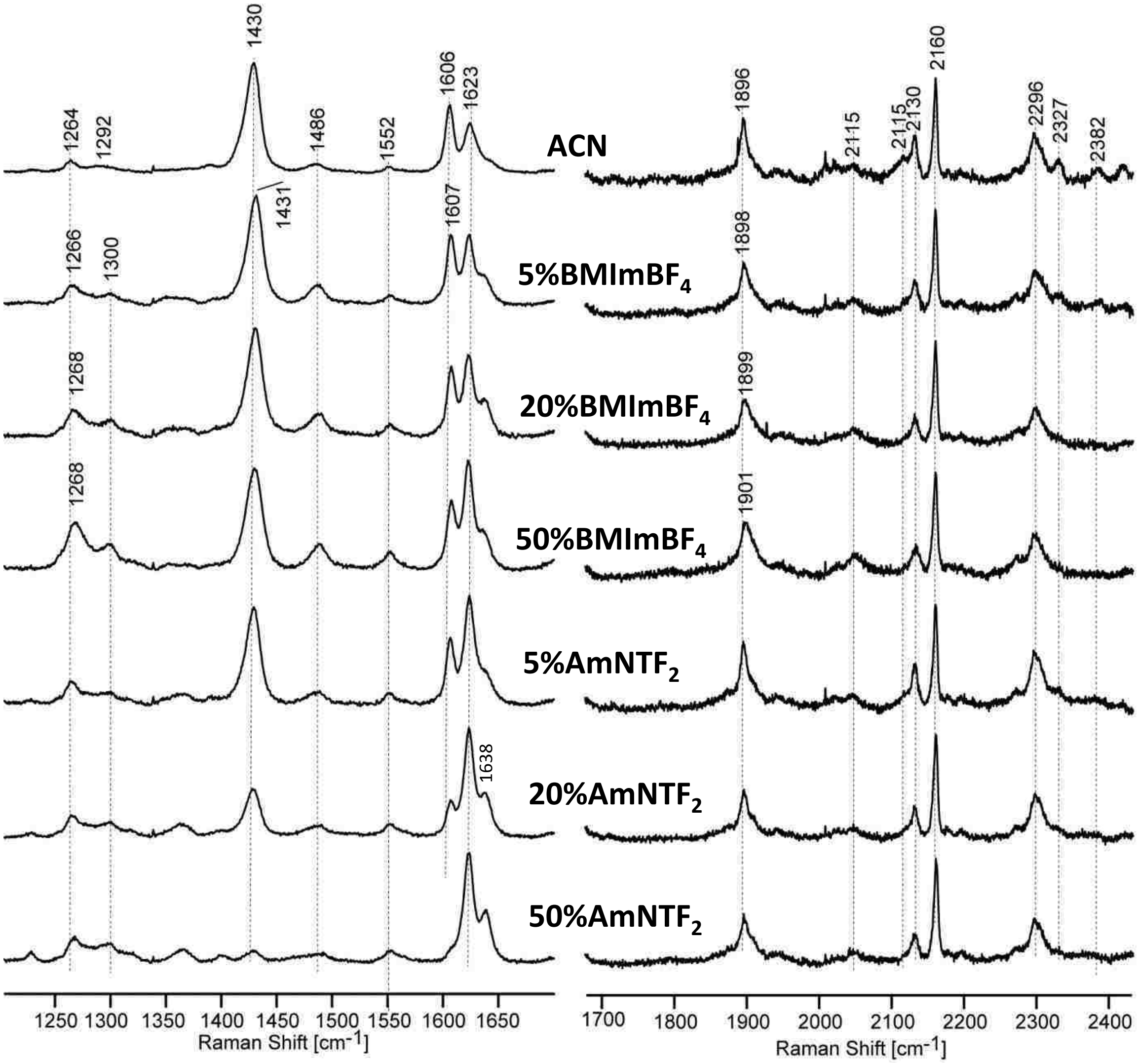

Figure 59: rRaman of DNB^{1-} in ACN in mixture with BMImBF$_4$ and AmNTF$_2$. Excitation at 406nm

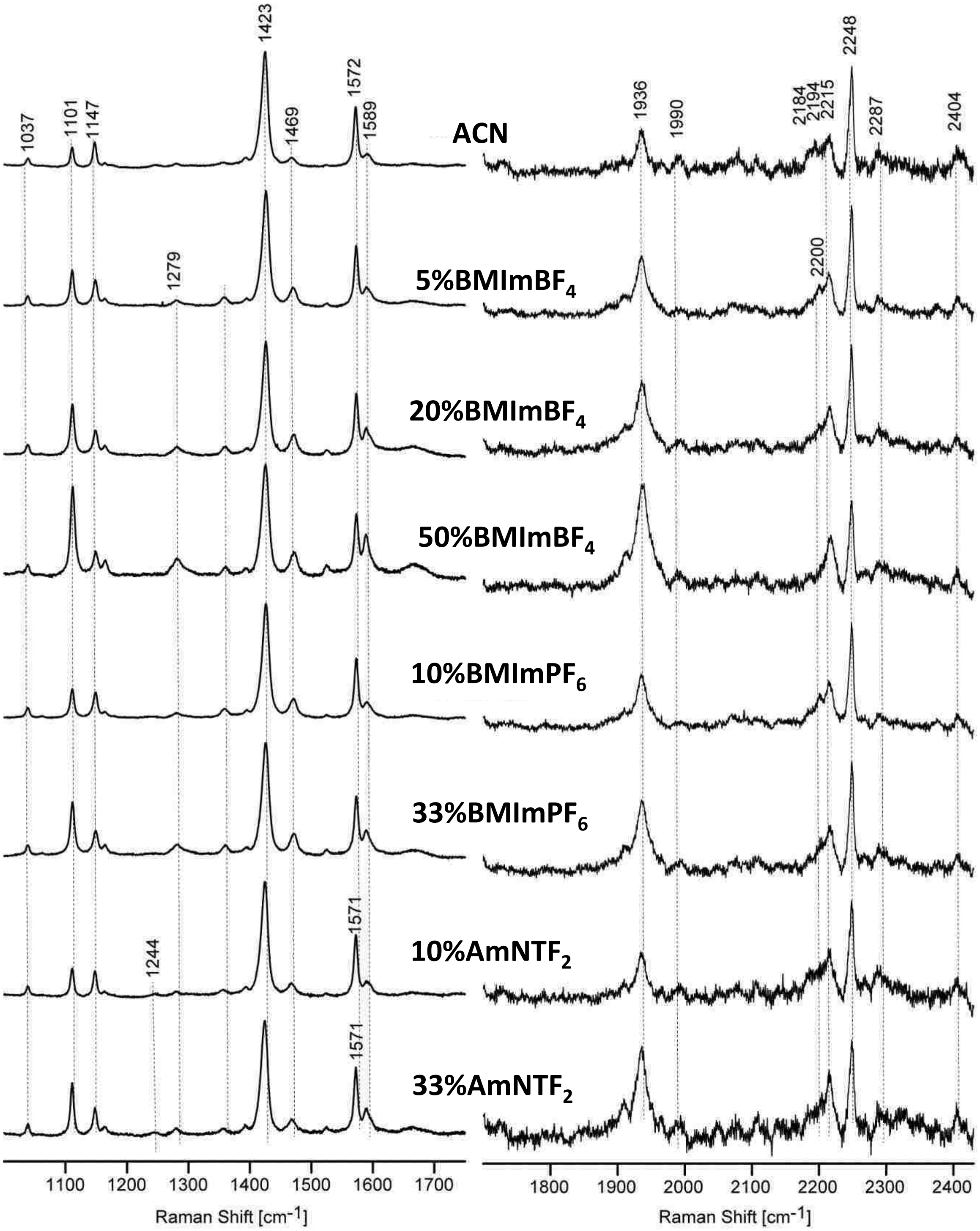

Figure 60: rRaman of DNB^{2-} in ACN in mixture with BMImBF$_4$, BMImPF$_6$ and AmNTF$_2$. Excitation at 442 nm.

3.10 DFT calculations

As introduced earlier, there has been significant computational work in the literature about ion pairing effects between RTIL cations and organic radicals.[65,76,141–143] In order to obtain more insight on solvation and ion paring effects on the electronic structure of DNB radicals, DFT calculations were carried out to in gas and solution phases. *Table 9* summarized the calculated ΔE_{12} based on free energies of the disproportionation reaction, at the level of DFT methods. All calculations converged to minima, based on the absence of imaginary frequencies.

Table 9: DFT calculations of ΔE_{12} (V)

Method			**Gas**	**ACN**	**$BMImPF_6$**
Model	**Basis set**	**DFT**			
SMD	**Aug-cc-pvdz**	***PBE1***	**4.48**	**0.91**	**1.02**
		M06-2X	**4.29**	**0.75**	**0.83**
		B3LYP	**4.26**	**0.88**	**0.84**
PCM	**6-31++G(2d,p)**		**4.45**	**0.90**	**-**
				0.54*	**-**
	6-31G(d)	**B1LYP40**	**4.51**	**1.17**	**1.38**
				0.84*	**0.85***

***Ion paired radicals with $BMIm^+$ cations.**

As expected, the ΔE_{12} values were significantly reduced by solvation effect, using either SMD or PCM models. Inclusion of the ion paring effects in the calculations, through interactions with $BMIm^+$ cations led to further decrease of ΔE_{12} values. The smaller values obtained when using M06-2X might be due to higher contribution of Hartree Fock (HF) exchange (54%), which tends to localize the charge on the radicals, compared to PBE1 and B3LYP methods (about 25% HF). Using larger basis sets with more diffuse orbitales did not improve the results. For our systems, the use of B1LYP40 (40% HF) with small basis set gave comparable ΔE_{12} values obtained by other methods, but calculations converged in shorter times. In fact, none of the calculated values approached the experimental values obtained in either the molecular or ionic liquid solvent. This difference is very likely due to difficulty to account for specific interactions of the radicals (here mostly for dianion) with electrolyte species. This limitation becomes more important for describing the solvation of charged species by RTIL solutions, based only on standard approaches like PCM or SMD models.

Attempting to get around this limitation, efforts have been dedicated to calculate the ΔE_{12} for tetramethyldinitrobenezene (*TmDNB*) using DFT methods. The two electrons reduction of this compound shows one wave in molecular solvents.[68] In our calculations, the neutral and radical anion exhibited twisted nitro groups, due to steric effects of methyl groups. The dianion geometry had a boat-like structure, consistent with the predicted structure reported by Evans[68] (*Figure 61*). This structural change reduced the calculated ΔE_{12} to 0.32V. Hence, the driving force for the coalescence of the voltammetric waves of TmDNB is very likely due to structural changes of the dianion. By analogy to the voltammetry of DNB, similar changes would be expected for the dianion in ionic liquid solutions. The geometry of DNB dianion was then constrained to twisted and boat-like structures and ΔE_{12} were calculated for ion paired species. *Table 10* summarizes obtained ΔE_{12} from these calculations. For TmDNB, inclusion of ion pairing narrowed the ΔE_{12} value. Restriction of the nitro groups to a twisted geometry also reduced the $\Delta E_{12,}$ while the boat shape led to potential inversion.

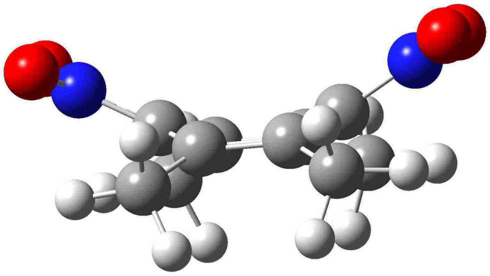

Figure 61: TmDNB^{2-} geometry in ACN

Table 10: DFT calculations of ΔE_{12} (V) TmDNB and constrained DNB

Method		**B1LYP40/PCM** **6-31G(d)**	**M06/PCM** **6-31++G(2d,p)**
TmDNB	**NP**	**0.47**	**0.29**
	IP	**0.32**	**-**
DNB (IP)	**Twisted**	**0.60**	**-**
	Boat-like	**-0.44**	**-**

NP: Non-paired. IP: Ion paired with BMIm^{+} cation.

Although the thermodynamic aspect of our calculations for DNB radicals were not satisfactory, the calculated charge densities and frequencies could be used to get some insight on ion paring effects. *Figure 62* showed significant localization of the charge onto the nitro groups near the acidic proton of the BMIm$^+$ cation for the radical anion, while the charge was equivalently distributed for the paired dianion. In addition, calculations that started with stacking geometries of the paired radicals with imidazolium cations always converged to side-by-side arrangements. Hence, these results predicted that most of the ion pairing interactions would be between the nitro groups and the acidic proton of the imidazolium cation.

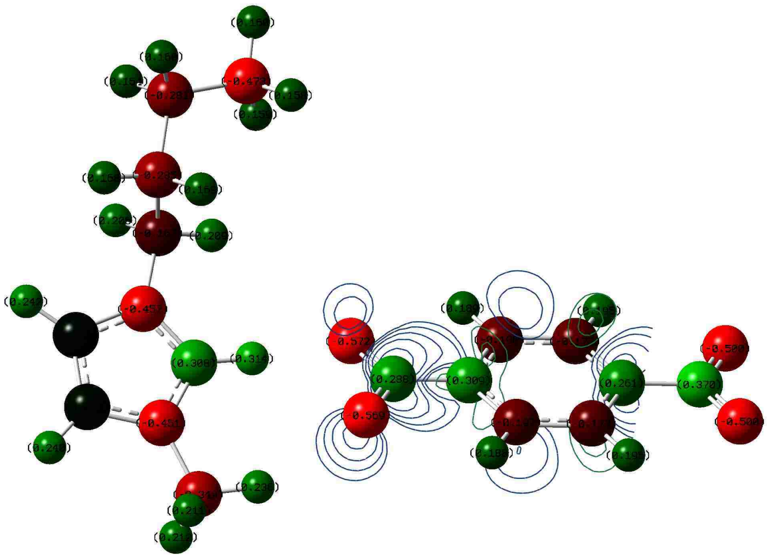

Figure 62: Charge distribution and spin density of DNB^{1-} paired with BMIm$^+$ cation in ACN

It is interesting to note that none of calculated spectra of all the considered species, including TmDNB, have showed vibrations in the range of 2000-2500 cm^{-1}. This further confirmed that the observed vibrations (in the range 2000-2500 cm^{-1}) in FTIR spectroelectrochemical experiments were indeed overtones/combinations bands. In the following, the calculated frequencies will be initially used to assign the Raman bands in the finger print region and may be ultimately employed to ascribe the overtones/combination bands.

By comparing trends of predicted shifts with changes observed in rRaman spectra in the mixture solutions, vibrations that are more sensitive to ion pairing might be identified. However, it is important to keep in mind that variations in calculated spectra are mainly due to presence or absence of electrolyte species, whereas changes in experimental spectra are more likely due to increase of electrolyte concentration. Hence, changes in frequencies and intensities are not expected to be perfectly the same, whereas the trends might be.

Inclusion of ion paring interactions in the calculations shifted the IR spectrum of DNB radicals. The most remarkable change was the appearance of a strong band at 1300cm^{-1} for the paired radical anion (*Figure 65*). Interestingly, this vibration was also Raman active with a high intensity (*Figure 64*). Normal mode analysis of this band showed high contribution of nitro groups stretching, in association with the aromatic group vibration (*Figure 63*). The stretching was stronger for the nitro group at the opposite side of the BMIm$^+$ cation. This illustrated very well the ion pairing effect of the cation, which constrained the stretching of the neighboring nitro group. Hence, this vibration should be envisioned as characteristic for ion paring interactions and expected to be very sensitive to RTIL introduction. Indeed, rRaman spectra have remarkably showed a growing intensity of the 1264cm^{-1} band upon increasing the RTIL concentration. As result, this vibration can be reasonably assigned to the normal mode of the predicted 1300cm^{-1} by DFT. The other bands at 1486, 1552 and 1623 cm^{-1} which increased in intensity, were then assigned to the predicted 1485, 1554 and 1694 cm^{-1} frequencies, respectively.

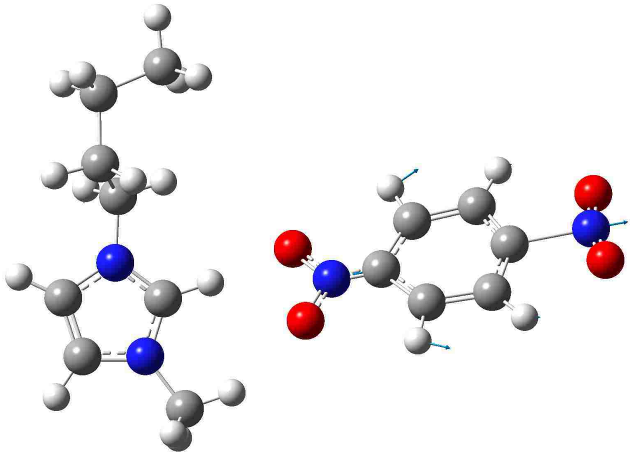

Figure 63: Normal mode of the 1300cm^{-1} Raman vibration for paired DNB^{1-} with BMIm^{+} cation in ACN

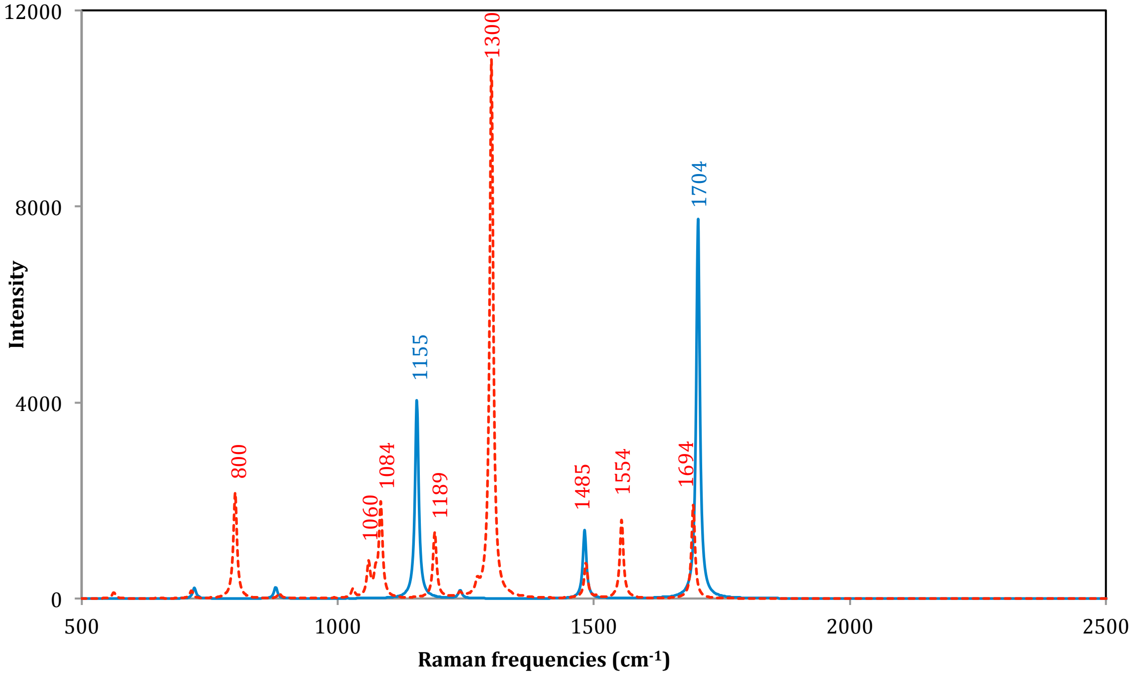

Figure 64: Calculated Raman spectra of paired (dashed) and unpaired (solid line) DNB^{1-} radical anion (non-scaled frequencies)

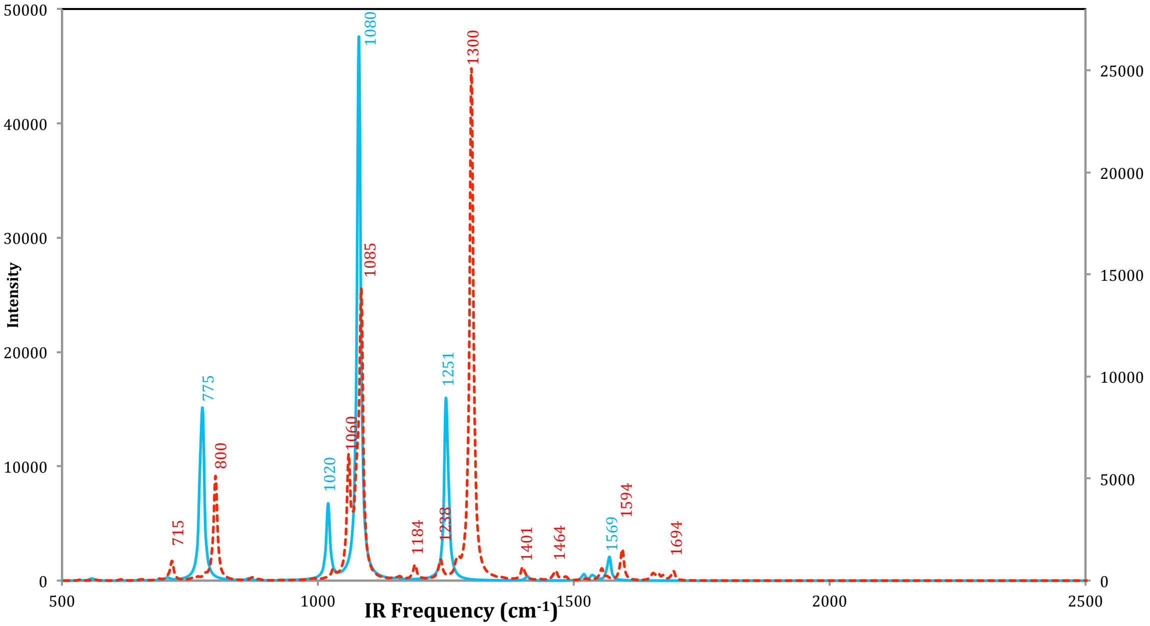

Figure 65: Calculated IR spectra of paired (dashed) and unpaired (solid line) DNB^{1-} radical anion (non-scaled frequencies)

Compared to radical anion, a smaller shift of 12 cm^{-1} (from 1569 to 1581 cm^{-1}) was seen for dianion spectrum upon ion pairing with the imidazolium cation (*Figure 66*). This shift was consistent with the increased band in rRaman spectra at 1589cm^{-1} which increased in intensity as the RTIL concentration increased. The normal mode analysis of this vibration indicated that it was a stretching of the C-N bonds of the dianion. Similarly, the growing bands at 1101, 1279 and 1469 cm^{-1} in rRaman spectra were assigned to the predicted vibrations at 1121, 1227 and 1504, respectively. The *Table 11* shows the assignment of the observed bands in rRaman for DNB radicals.

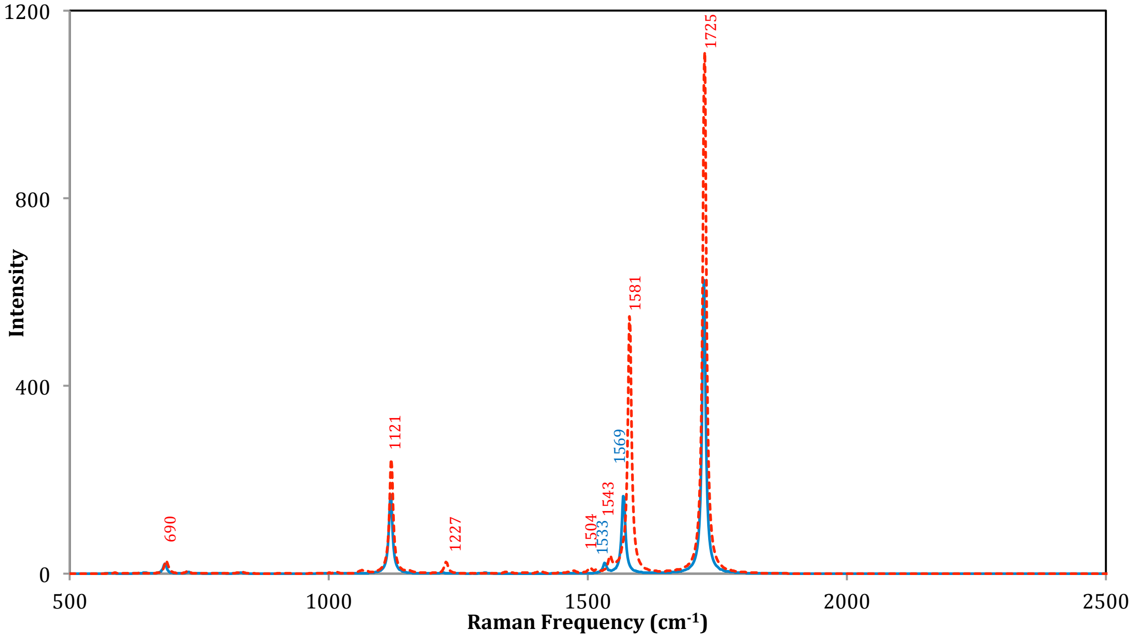

Figure 66: Calculated Raman spectra of paired (dashed) and unpaired (solid line) DNB^{2-} radical anion (non-scaled frequencies)

Table 11: Assignment of rRaman bands for paired DNB radicals

Calculated Species	**Experimental**	**Predicted**	**Mode**
DNB^{1-} $BMIm^{+}$	**1264**	**1300**	**NO_2 Str**
	1486	**1485**	**NO_2 Str**
	1552	**1554**	**Ar Str**
	1623	**1694**	**Ar Str**
DNB^{2-} $2BMIm^{+}$	**1101**	**1121**	**NO_2 + Ar Str**
	1279	**1227**	**Ar Str**
	1469	**1504**	**Imidazole ring Str**
	1589	**1581**	**C-N Str**

3.11 Recapitulation

The use of spectroelectrochemistry to determine the ΔE_{12} values, when they are close to zero, was exemplified in this investigation. The merging of the first and second waves into a single wave could be followed over a range of organic solvent/RTIL mixtures. Coalescence of the waves resulted in significant overlap between the radical and the dianion spectra during the electrolysis time scale. The use of the WFA combined with the hard modeling approach enabled us to extract the UV-visible spectra of the electrogenerated species in the RTIL. The spectral profiles were quite similar, but not identical, to the ones observed in the molecular solvent (*Figure 67*). Small shifts of 4nm, to lower energies for the radical anion and to higher energies for dianion, were observed in RTIL. In pure RTIL, the DCVA results showed that the second electronic transfer was still negative of the first electron transfer by about 20mV, ruling out the possibility of potential inversion.

The electrolysis in mixtures ACN-RTIL showed that only 20%RTIL would be enough to mimic the environment in pure ionic liquid, resulting in coalescence of the two waves and dropping the potential difference by over 140mV. More interestingly, this drop in mixtures indicated partition of the electrogenerated species into RTIL nano-domains. The partitioning into ionic liquid domains was more pronounced for the dianion compared to the radical anion, leading to higher stabilization of the second wave. Formation of these nano-domains in the mixture might be due to either a self-organization (aggregation) of the RTIL in the mixture and/or the presence of electrogenerated species that template these structural features. Using a neutral probe, Li et al. have reported no aggregation of

$BMImPF_6/BMImBF_4$ RTIL in acetonitrile solutions.[35] Considering this report, it is reasonable to believe that presence of DNB^{2-} dianion could be a driving force for RTIL clustering in acetonitrile. The separation of the single wave into two waves could be achieved, when adding acetonitrile to RTIL solution, at almost same fraction in the opposite direction of the binary. This showed that RTIL clustering is a reversible process.

The voltammetry using solid salt solutions enabled quantifying the ion paring interactions separately from the solvation effect in the RTIL. For DNB reductions in imidazolium salts, these two factors had comparable stabilization effects. The former led to 100mV potentials drop, while the second leads to additional 100mV stabilization.

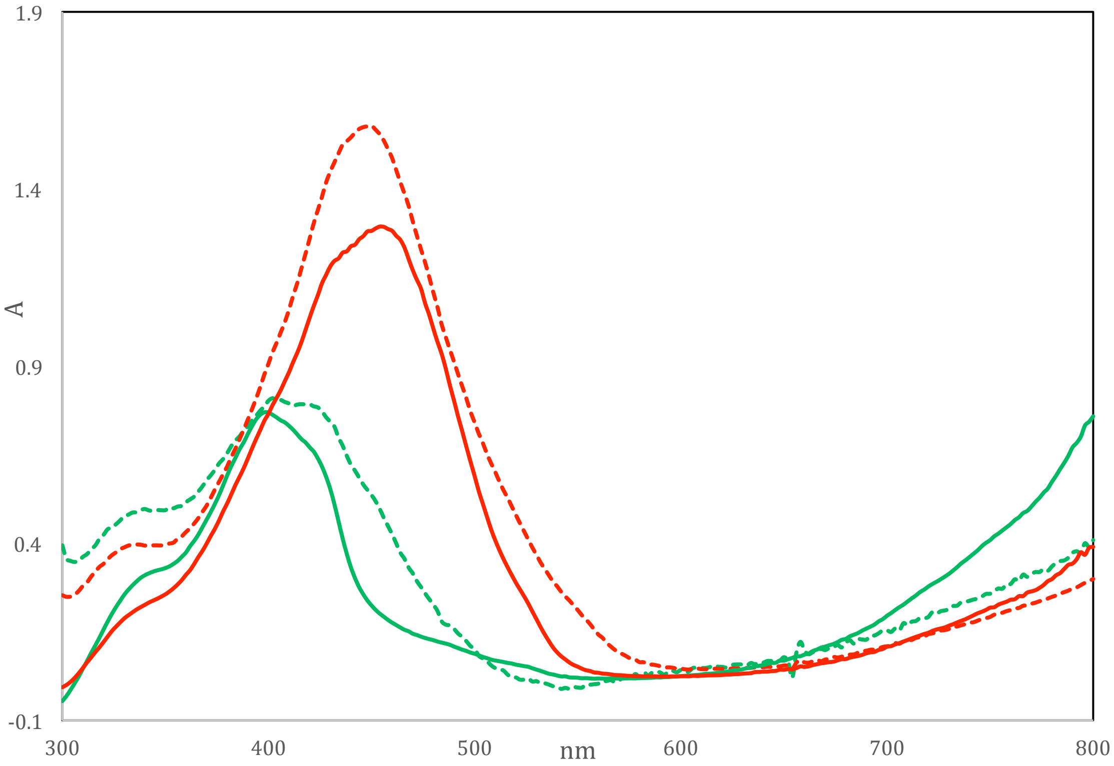

Figure 67: UV-visible spectra of DNB radical anion (green) and dianion (red) in ACN (solid) and RTIL (dashed).

The FTIR SEC could be successfully used to study the impact of RTIL on the vibrational spectra of DNB radicals. Presence of characteristic bands of DNB radicals above 2000cm^{-1} avoided the difficulty of carrying out the analysis in the finger print region (*Figure **68***). As the neutral species doesn't show features in this region, these bands have been primary assigned to overtones/combination bands. Their magnitude is very likely related to change of charge distribution upon ion paring interactions. Alternatively, ex-situ rRaman spectroelectrochemistry has been carried out for DNB radicals in mixture solutions. The results showed significant changes upon increasing RTIL concentration, with bands in the range 2000-2500cm^{-1}. These bands were consistent with the observed features in the IR spectra. Because the nature of these vibrations has not been reported in literature, some efforts were directed toward using DFT calculations in this regard.

While calculated ΔE_{12} values were not quite close to the experimental values, variations due to ion parings and structural changes of the dianion were consistent with coalescence of the voltammetric waves. Our calculations showed that standard models like PCM or SMD are not enough to describe for the solvation of highly charged species. Explicit solvation models are needed to account for specific interactions between the redox products and the electrolytes systems. Similar conclusions have been addressed recently by Neese et al.[145] on the use of DFT methods in calculating the redox potentials. In their calculations for one electron oxidation potentials, the explicit inclusion of small number of the solvent molecules improved the accuracy of their predictions. On the other hand, addition of larger number of solvent molecules increased the error of the predictions.

Analysis of charge distribution and calculated frequencies enabled to predict the sites of ion parings interactions. Based on rRaman spectroscopy, modes of the finger print vibrations have been successfully identified for both radicals. The results showed that ion pairing was mostly through interactions between the polar group of the imidazolium cation and nitro groups of the radicals. These interactions resulted in a larger shift of radical anion features compared to dianion, consistent with observed shifts in IR spectra. While ongoing efforts are still directed toward understanding the nature of observed overtones/combination bands, it is reasonable to relate their vibrations to the ion paring sensitive modes predicted at 1300 and 1581 cm^{-1}, respectively for the radical anion and dianion.

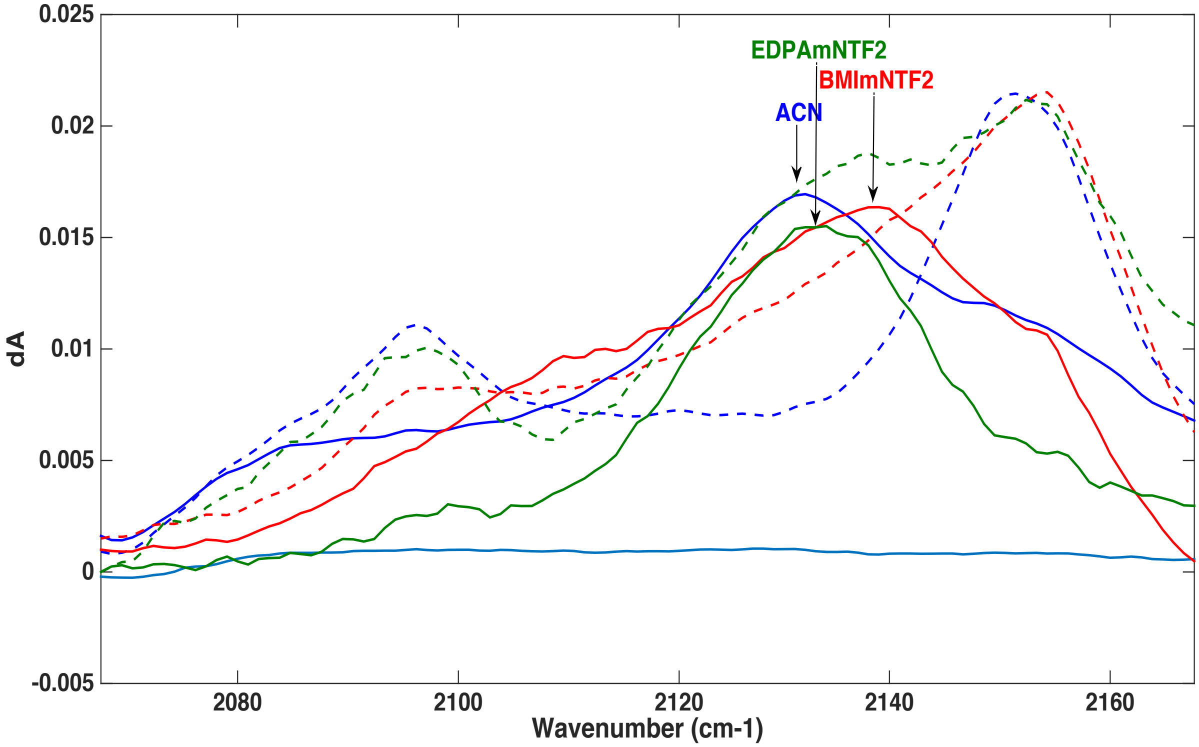

Figure 68: IR features of DNB radical (solid) and dianion (dashed) in ACN (blue line), BMImNTF$_2$ (red) and EDPAmNTF$_2$ (green).

Chapter 4 Electrochemistry and spectroelectrochemistry of TCNQ in mixed acetonitrile-RTIL solvents

In contrast to DNB, where a small ΔE_{12} of 0.2V in ACN led to coalescence of the two waves in RTIL, the two reductions of TCNQ (*Figure 69*) are separated by about 0.5V in the molecular solvent. Such a large ΔE_{12} would enable to investigate further impacts of RTILs on the reduction of organic compounds. In examining these impacts, the effect of RTIL impurities on the voltammetry of TCNQ in the mixture solutions was found to be significant.

In this chapter voltammetry and spectroelectrochemistry of TCNQ reductions were carried out in ACN-RTILs mixtures. The cyanide groups had strong characteristic bands in the infrared that could be used to investigate the effect of the RTIL on the vibrational configuration of TCNQ radicals.

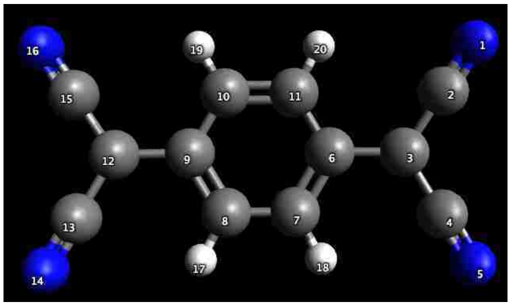

Figure 69: Structure of TCNQ

4.1 Voltammetry

4.1.1 Cyclic voltammetry in pure solvents

Figure 70 shows cyclic voltammograms of TCNQ obtained in ACN, $BMImPF_6$, $BMImBF_4$, $BMImNTF_2$ and $EDPAmNTF_2$. In all these solvents, the reductions waves were reversible. The peak currents increased with the square root of scan rate, indicating diffusion-controlled processes. While the first reduction was not significantly sensitive to nature of the solvent, the second wave was positively shifted by about 130mV in RTILs.

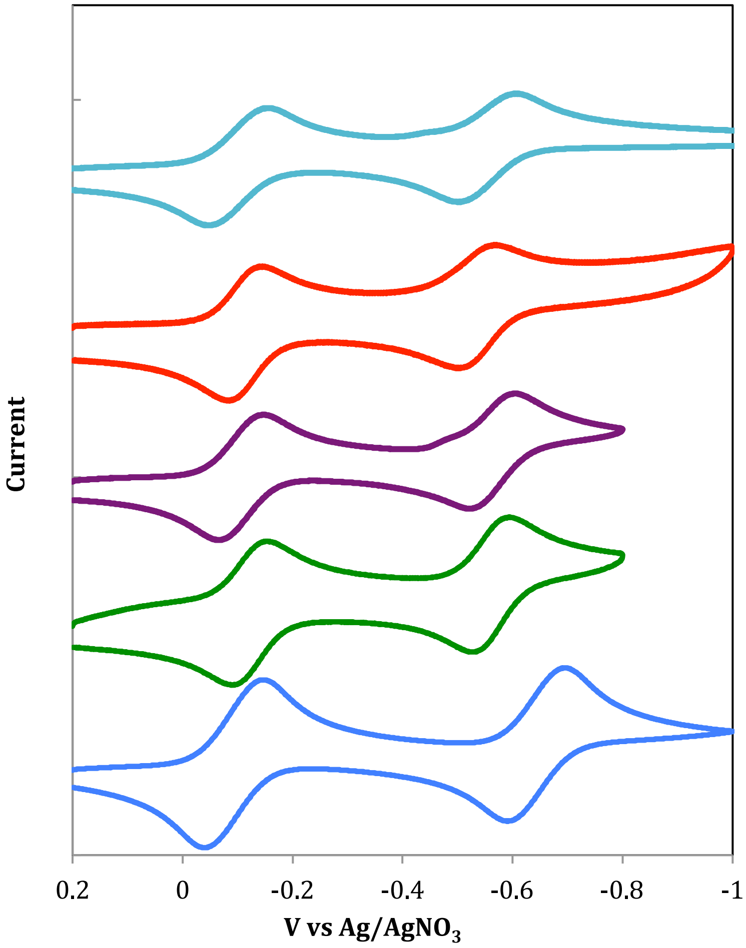

Figure 70: Voltammograms of TCNQ in ACN, $BMImPF_6$, $BMImBF_4$, $AmNTF_2$ and $BMImNTF_2$ at 100mV/s, respectively from bottom to top.

4.1.2 Cyclic voltammetry in *ACN-RTIL*

Cyclic voltammetry in ACN-RTILs mixtures enabled the evaluation of the shifts as a function of the RTIL fraction. *Figure 71* shows voltammograms obtained at 20%RTIL solutions. In contrast to dinitrobenzene where the shift was 140mV, the potential shift in 20%RTIL (a fairly high concentration) did not exceed 50mV.

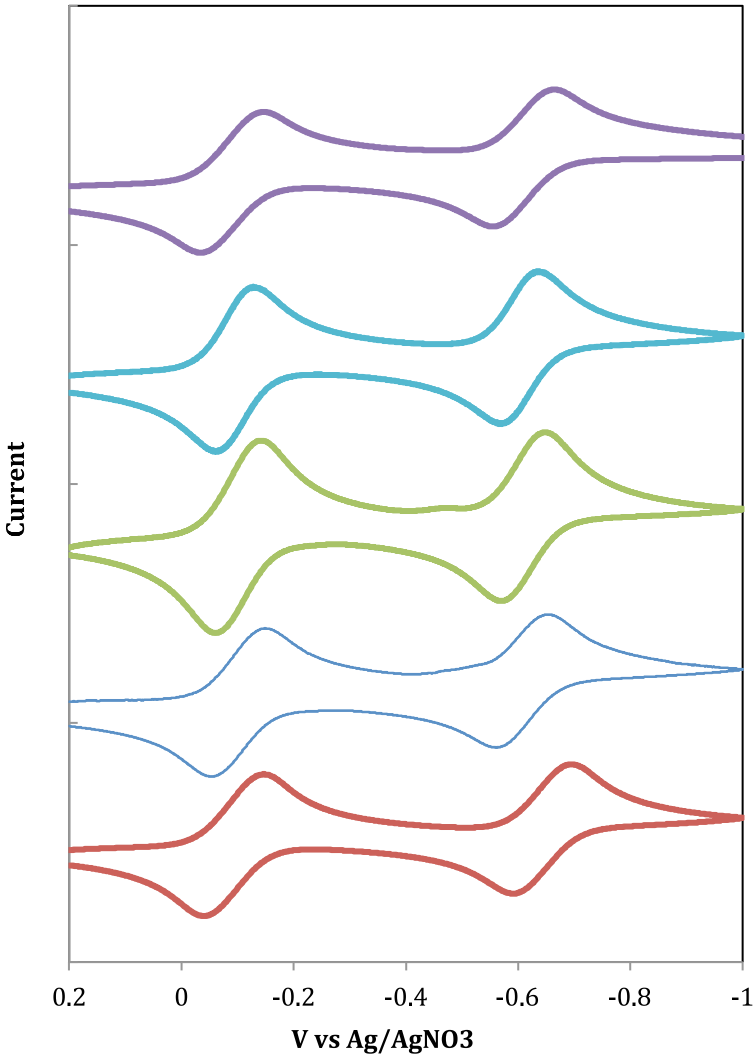

Figure 71: Voltammograms of TCNQ in ACN and 20%RTIL: BMImPF$_6$, BMImBF$_4$, EDPAmNTF$_2$ and BMImNTF$_2$ at 100mV/s, respectively from bottom to top.

The quantitative values of the observed shifts might be confounded with shifts in the reference system, due to change in electrode-liquid junction potential. In order to eliminate issues with the reference system, the difference between the first and second redox couples ($\Delta E_{12} = E_1 - E_2$) was evaluated as a function of %RTIL. The potential shifts in all RTILs showed quite linear relationship with RTIL fractions (*Figure 72*). The trend can't be explained only on the basis of ion-paring interactions, where the shifts would be expected to level off at higher concentration of RTILs. In fact, this stabilization was consistent with stronger interactions, upon partitioning of dianion within RTIL nano-domains.

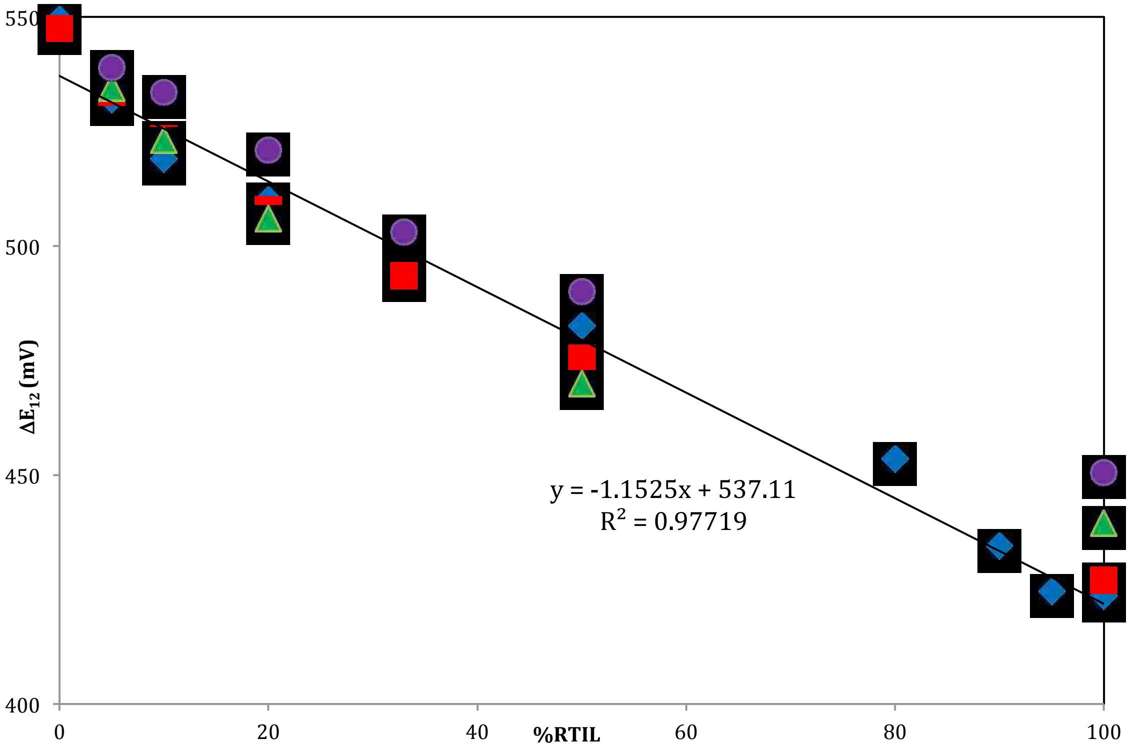

Figure 72: Variation of ΔE_{12} for TCNQ reduction in ACN %RTIL: $BMImPF_6$ (triangles), $BMImBF_4$, (squares), $AmNTF_2$ (diamonds) and $BMImNTF_2$ (circles)

4.1.3 Diffusion in ACN-RTIL

As introduced in first chapter, difference in diffusion coefficients of TCNQ radicals was shown to change the observed currents, when the comproportionation reaction is favored.[85] Switching the solvent from ACN to RTIL reduced the ΔE_{12} only by 130mV, indicating that comproportionation was still favored in the ionic liquid. The impact of the RTIL introduction on diffusion of TCNQ radicals was evaluated in the mixture system. In order to reduce the effect of the background, the peak currents were measured using the semi-derivative of cyclic voltammograms (*Figure 73*). The currents ratio, n_{app}, was calculated as $n_{app} = (e_1+e_2)/e_1$, where e_1 and e_2 were the semi-derivative of the currents (e) of first and second reduction waves, respectively. *Figure 74* shows the variation of n_{app} with RTIL fraction in the mixture. The results showed a plateau of the current ratio around 1.95 at lower RTIL fractions. At concentration above 50%RTIL, the n_{app} dropped to a minimum value 1.76 in pure ionic liquid. According to calculations done by Rongfeng and Evans, the drop of current ratio was an indication of significant decrease of radical anion diffusion coefficients compared to neutral.[85] The dianion diffusion coefficients had minimal effect on the current ratio. The dramatic change at higher RTIL fractions was consistent with a change in solvation environment of the radicals, through formation of nano-domains at these concentrations. The partitioning of radicals into viscous RTIL nano-domains is expected to slow down their diffusion in the mixture. Ongoing simulations are directed toward determination of absolute values of diffusion coefficient in the mixture.

It is important to mention that partioning of dianion into RTIL domain, while neutral into molecular solvent, might also affect the rate of the comproportionation reaction. This aspect needs to be taken into consideration in the simulation.

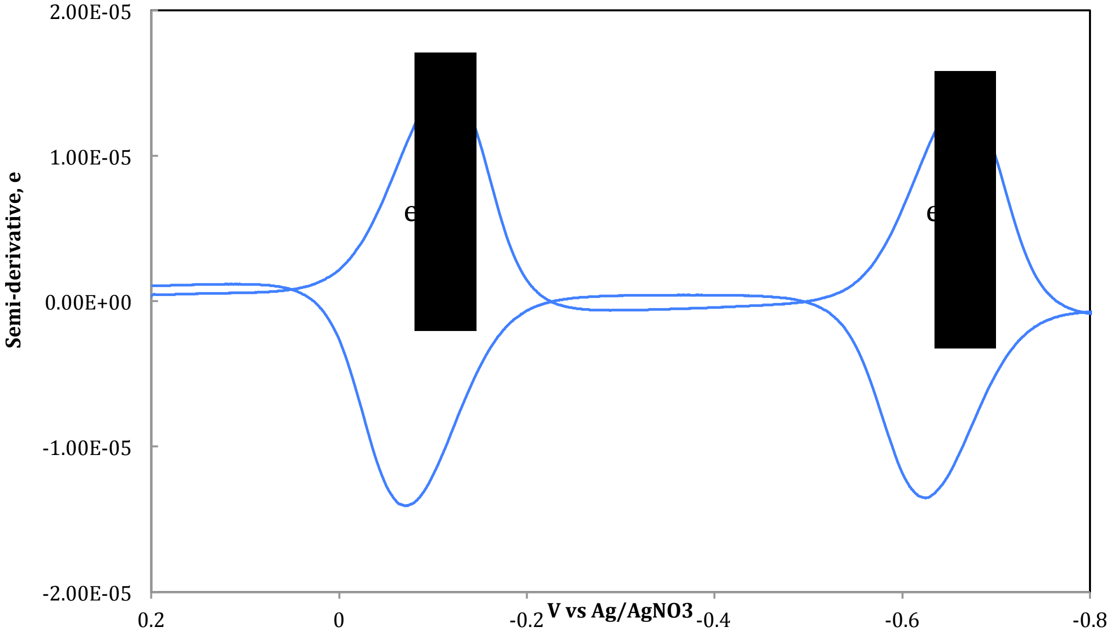

Figure 73: Semi-derivative cyclic voltammogram of 2mM TCNQ reduction in ACN. 100mV/s

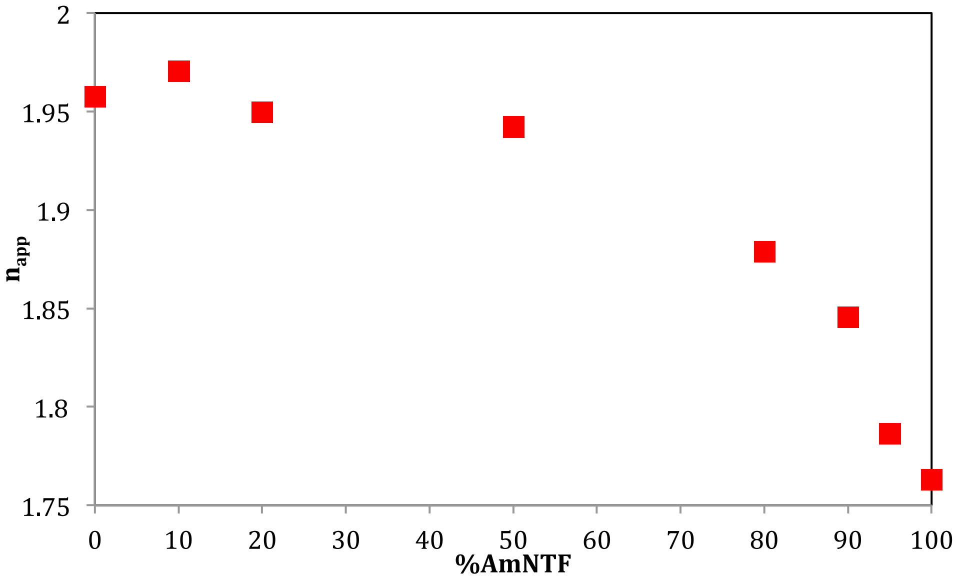

Figure 74: Variation of n_{app} of TCNQ reduction ACN-AmNTF$_2$ mixtures

4.2 Spectroelectrochemistry

4.2.1 UV-visible Spectroelectrochemistry

We noted that UV-visible spectrum of the radical anion in acetonitrile has been reported in literature, while the dianion spectrum has not.[81] The *Figure 75* shows the UV-visible SEC of TCNQ in acetonitrile, at the potential range of the two reductions waves.

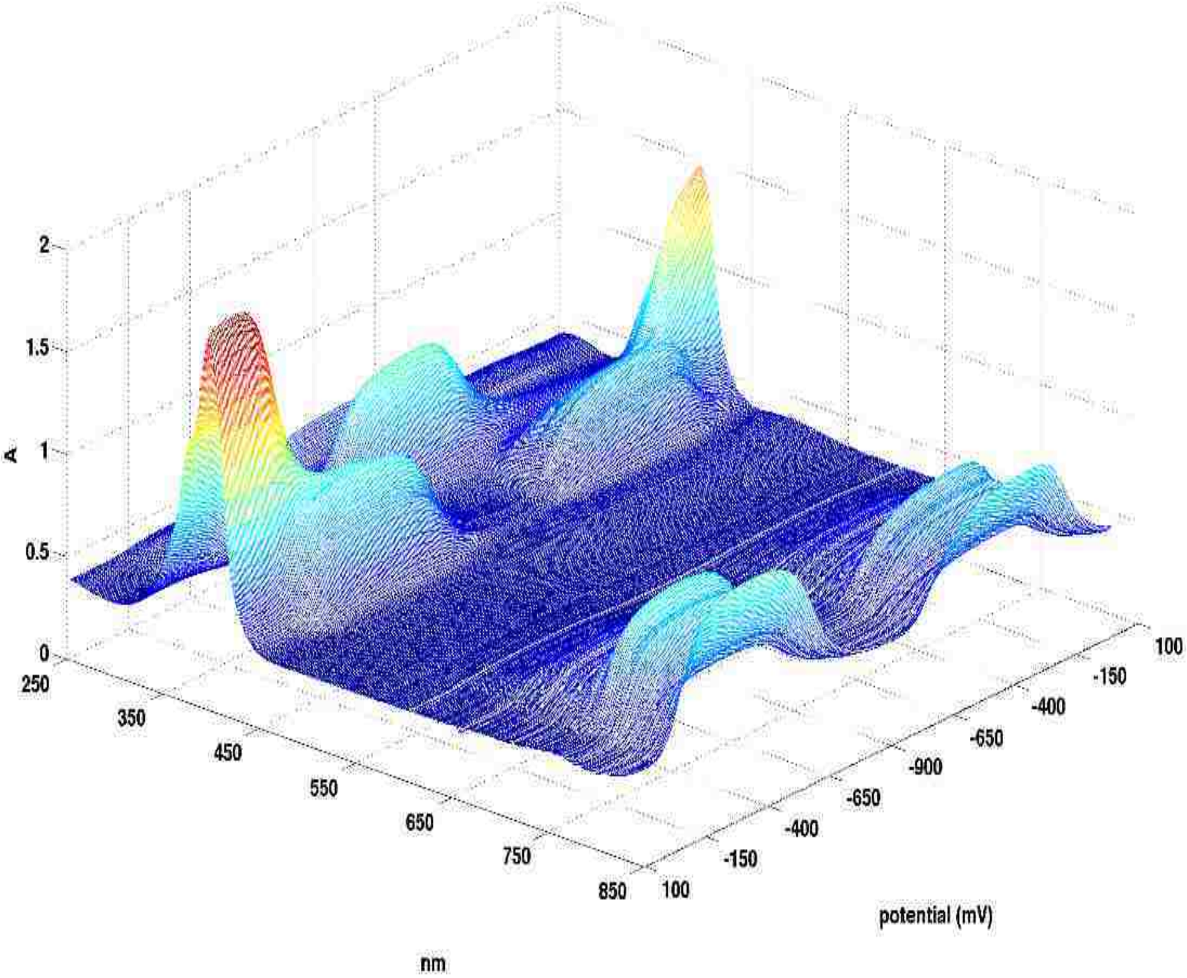

Figure 75: UV-Visible SEC of 0.1mM TCNQ upon two electrons reductions in ACN at 1mV/s

As was done for dinitrobenzene, the spectra of the three species present in the electrolysis solution are shown in *Figure 76*. The band at 418 nm and the feature around 700nm were characteristics for the radical anion, in agreement with the reported values. The band at 328nm was assigned to the dianion.

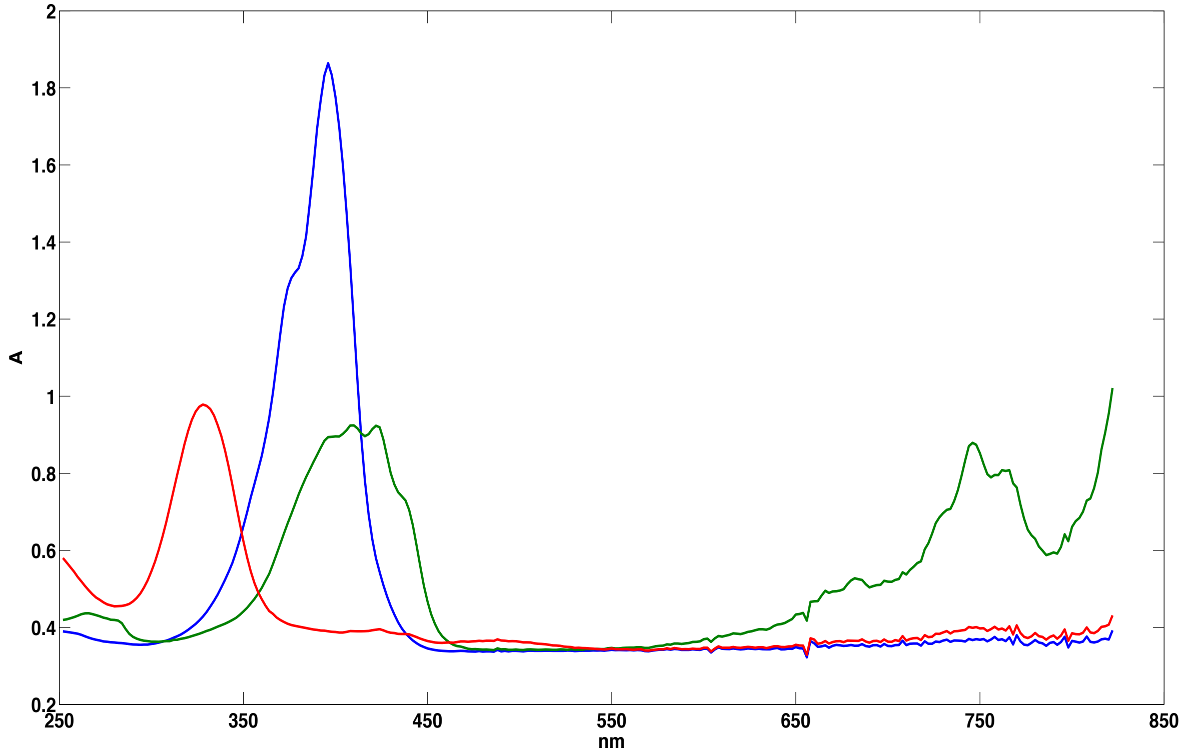

Figure 76: Spectral profiles of the neutral (blue), radical anion (green) and dianion (red) TCNQ in ACN.

Electrolysis experiments were also carried out in RTIL solutions and *Figure 77* shows the spectral features of the three species in the BMImNTF$_2$. In RTILs, the neutral and radical spectra looked similar to the ones observed in acetonitrile. However, the dianion spectrum in imidazolium ionic liquids was shifted to higher energies, from 328 to 318nm.

$AmNTF_2$ gave a similar spectrum for the dianion as was observed in ACN, with a small shift to 326nm (see Appendix). The shift seen in imidazolium ionic liquids indicated specific interactions of the dianion in these RTILs. This observation was examined in details in the following discussions. The reverse electrolysis showed almost complete reoxidation to the starting material. We noted that trace of chemical oxidation of the dianion could be seen in all solvents (including acetonitrile), resulting in a species with a feature around 490nm.

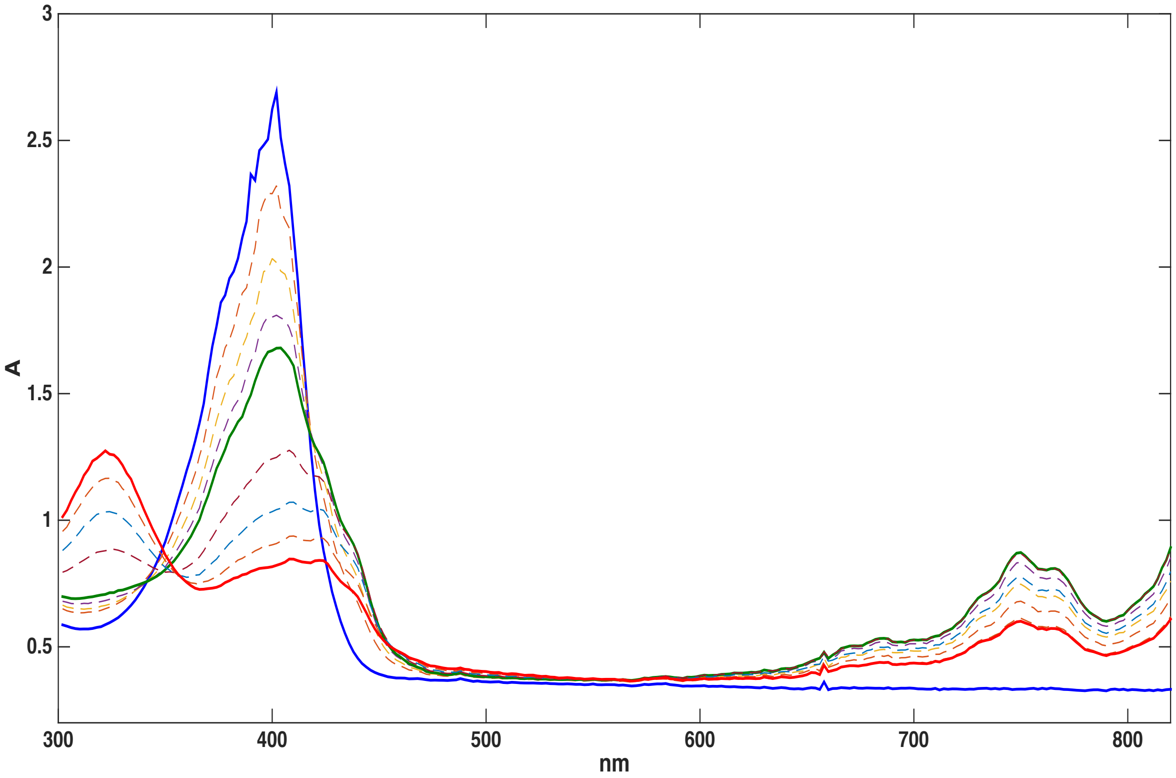

Figure 77: Spectral profiles of the neutral (blue), radical anion (green) and dianion (red) TCNQ in $BMImNTF_2$. Dashed are intermediate spectra

4.2.2 FTIR Spectroelectrochemistry

As introduced earlier, the FTIR SEC of the two reduction waves of TCNQ has already been reported in acetonitrile.[40] The vibrational spectrum of the radical was featured by 2186 and 2156 cm^{-1}, while 2153 and 2107 cm^{-1} were characteristics for the dianion in acetonitrile. In this work, FTIR SEC was carried out in RTILs for the two electron transfers, where we restricted our analysis to the range 2000-2300 cm^{-1}. *Figure 78* shows IR features of TCNQ radicals observed in $BMImNTF_2$ ionic liquid. The two bands at 2181 and 2155 cm^{-1} were characteristic of the radical anion. The dianion spectrum showed two features at 2155 and 2107 cm^{-1}. These frequencies were comparable to values observed in acetonitrile. Reverse electrolysis led to complete reoxidation of the radicals to the starting material. Similar features were observed in other RTILs.

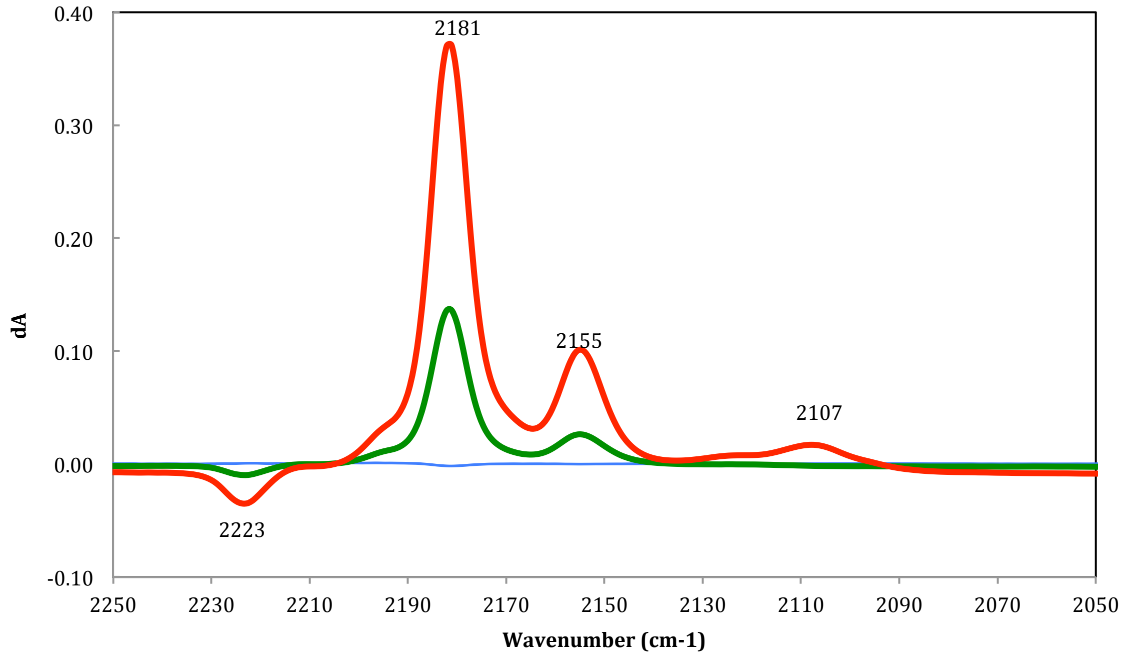

Figure 78: Difference spectra of FTIR SEC of 2 mM TCNQ in $BMImNTF_2$ at 0.2mV/s. Negative feature: TCNQ, positive features: $TCNQ^-$ (green) and $TCNQ^{2-}$ (red)

4.3 RTIL Impurities

4.3.1 Impact

Often enough, the cyclic voltammetry in pure RTILs and mixture solutions were quite different from acetonitrile. It is worth noting that this effect was limited to imidazolium RTILs and has not been detected in ammonium ionic liquid.

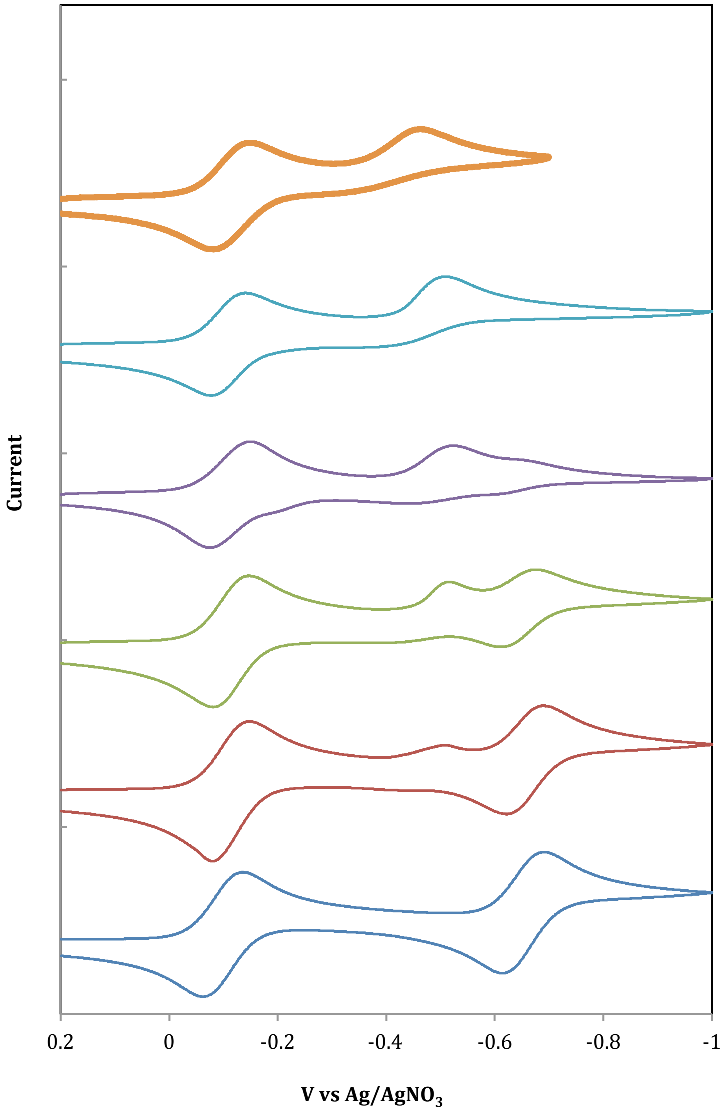

Figure 79: Voltammograms of 5mM TCNQ in ACN with 2, 5, 10, 20 and 100%BMImNTF$_2$, respectively, from bottom to top. 100mV/s

While the TCNQ dianion was quite stable in acetonitrile, its stability was strongly affected by the presence of trace of impurities in the RTIL. This effect was only observed for the imidazolium RTIL, but not for the ammonium ionic liquid. The *Figure 79* shows the evolution of the voltammogram as a function of %BMImNTF$_2$ fraction. Addition of the RTIL led to the appearance of a new wave at more positive potential, with as little as 2% of this ionic liquid. At 20% of BMImNTF$_2$, the voltammograms looked similar to that in pure ionic liquid. To study this in detail, imidazolium RTILs were purchased from two different companies (Merck and TCI). The voltammograms in 100% BMImNTF$_2$ showed are shown in *Figure 80*. The wave at about -1.3V (wave X) was higher in Merck solvent, and significantely attenuated in the TCI solvent. Wave X was greater in BMImNTF$_2$ than in BMImPF$_6$ and BMImBF$_4$. The presence of wave X was correlated to the shift and irreversibility in the wave C. Wave X was also present in the background voltammograms of contaminated RTIL solvents (*Figure 81*). Interestingly, repetitive cyclic voltammetry at very negative potentials eliminated the wave X, while switching the reductions to the ones seen in non-contaminated solvents (*Figure 82*). This switching could be also achieved by stepping the potential at the wave X before scanning through the first two reduction waves (*Figure 83*).

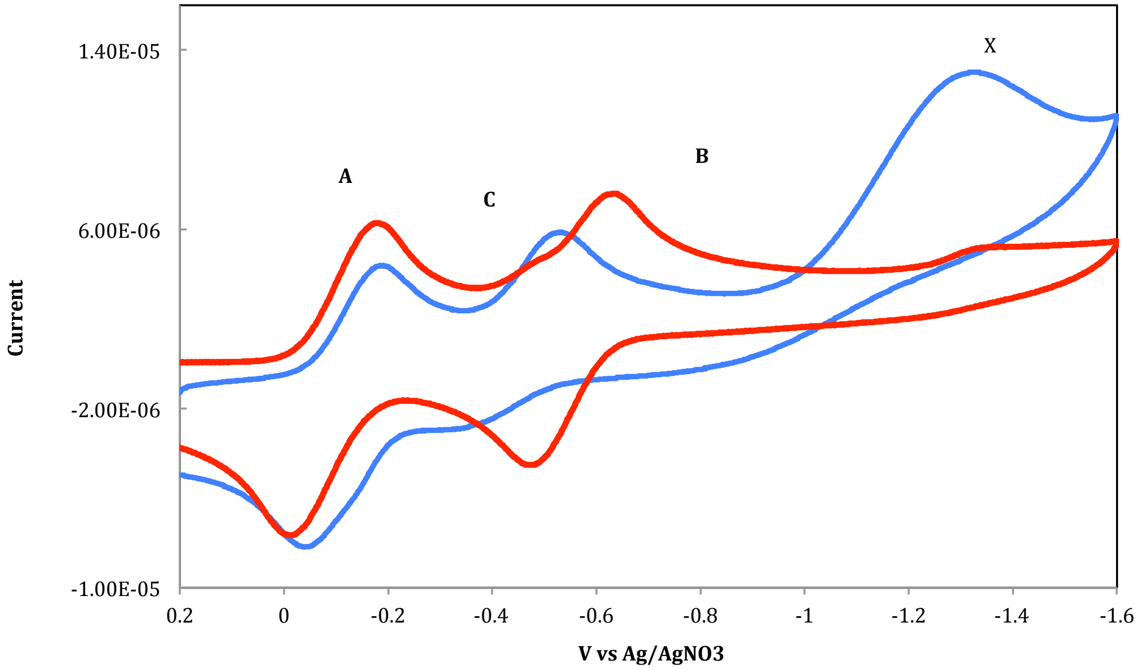

Figure 80: Voltammograms of 5mM TCNQ in BMImNTF$_2$, purchased from Merck (blue) and TCI (red). 100mV/s

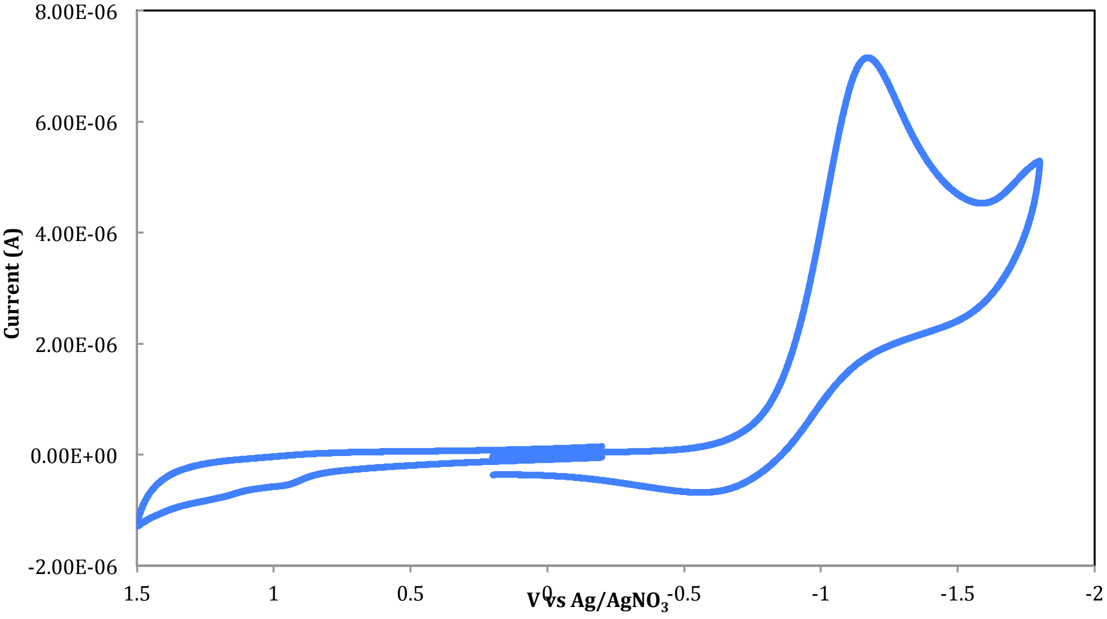

Figure 81: Background voltammograms of dried BMImNTF$_2$, purchased from Merck. 100mV/s

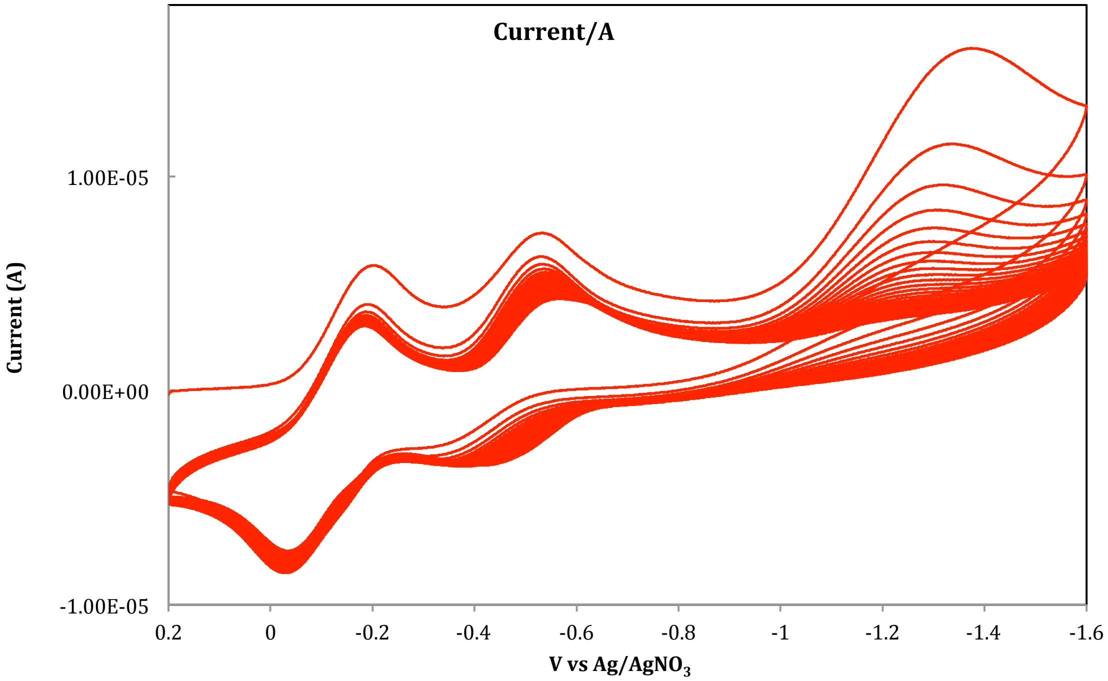

Figure 82: Repetitive cyclic voltammetry (25 cycles) of 5mM TCNQ in BMImNTF$_2$. 500mV/s

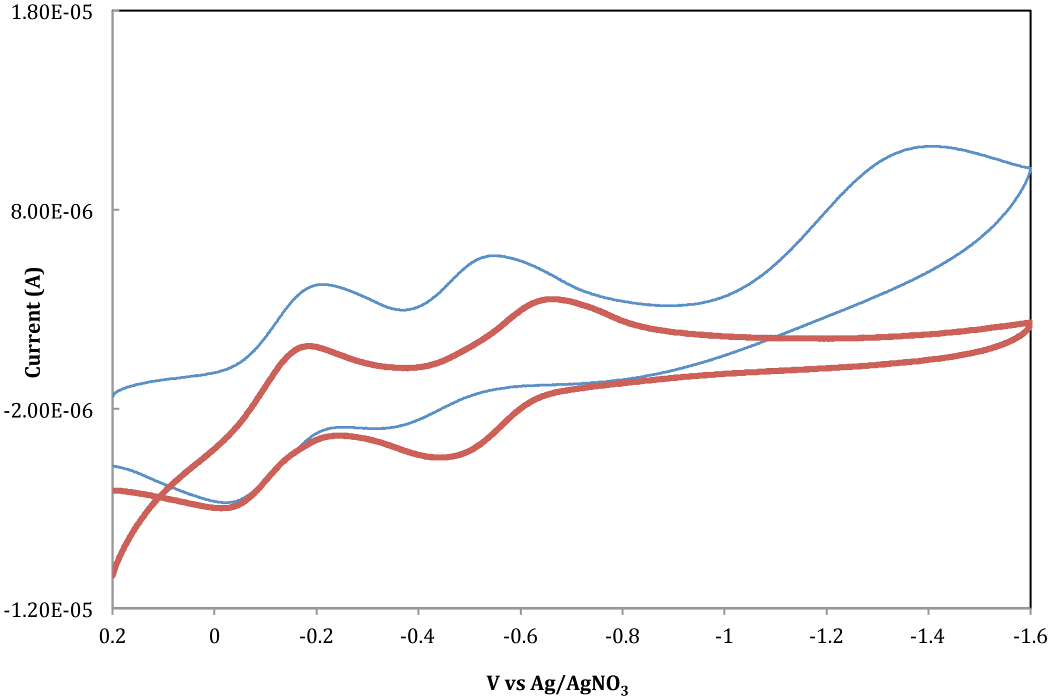

Figure 83: Cyclic voltammograms of 5mM TCNQ in BMImNTF$_2$, before (blue) and after (red) stepping at -1.6V for 50s. 500mV/s

From these results, the voltammetric mechanisms of the observed processes could be formulated as:

$\mathrm{TCNQ} + e^- \rightarrow \mathrm{TCNQ}^-$ (A)

$\mathrm{TCNQ}^- + e^- \rightarrow \mathrm{TCNQ}^{2-}$ (B)

$\mathrm{TCNQ}^{2-} + \mathrm{Ox} \rightarrow \mathrm{Product}$ (C)

$\mathrm{Ox} + e^- \rightarrow \mathrm{Red}$ (X)

Where Ox is an impurity present in RTIL solvents. When repeating the cycling at the reduction potential of the wave X, the diffusion layer is depleted from Ox upon its reduction to Red, which doesn't react with TCNQ^{2-}. Of note, the voltammetry of TCNQ in contaminated RTIL, using two different electrode areas, indicated a reversible wave at the microelectrode conditions (*Figure 84*).

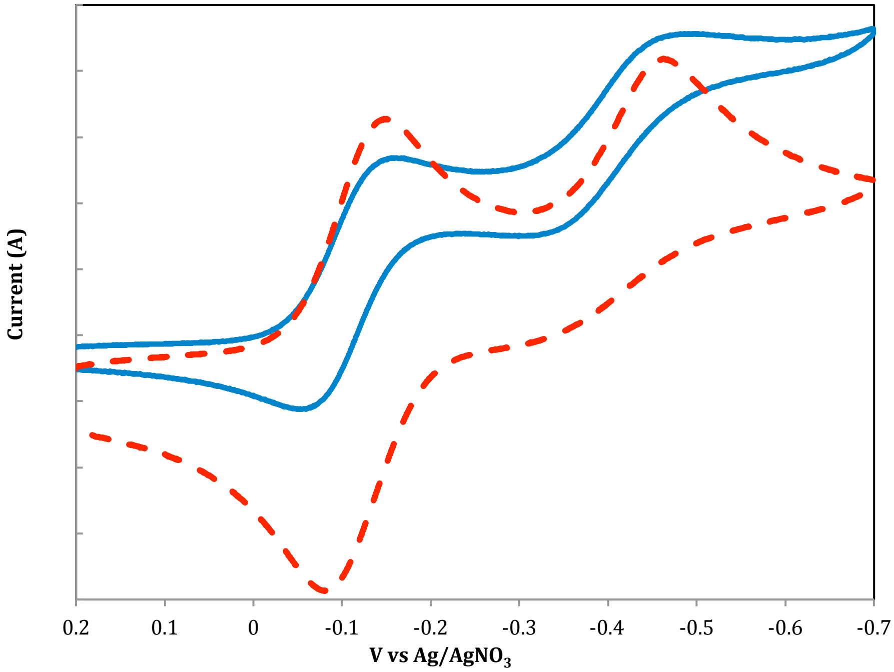

Figure 84: Voltammograms of 5mM TCNQ in BMImNTF$_2$, at 1.6mm (dashed) and 10um (solid) electrodes. 100mV/s

With the above results, we can now discuss some of the earlier results obtained by UV-visible SEC in pure RTILs. Electrolysis in mixtures ACN-%BMImPF$_6$ showed blue shifts of the dianion spectrum with as little as 5%RTIL, as shown in *Figure 85*. *Table 12* shows the spectral features of the redox species in these mixture solutions. In the case of BMImNTF$_2$, purchased from Merck, the electrolysis showed the presence of two species 318 with as little as 2% of RTIL (*Figure 86*). Even at this low fraction, the proportion of 318nm band over 326nm exceeded 50%. It is worth noting that reoxidation reaction to the starting material was completely reversible, indicating a high stability of all electrogenerated products in the electrolysis time scale.

Table 12: UV-visible spectral features of TCNQ redox products in ACN-%BMImPF$_6$

A$_{max}$ (nm)	**ACN-%BMImPF$_6$**						
	0	**5**	**10**	**20**	**50**	**75**	**100**
Neutral	**396**	**394**	**394**	**394**	**398**	**396**	**396**
Radial	**420, 742**	**420, 744**	**420, 744**	**420, 744**	**420, 746**	**420, 748**	**420, 748**
Dianion	**328**	**322**	**322**	**322**	**320**	**320**	**318**

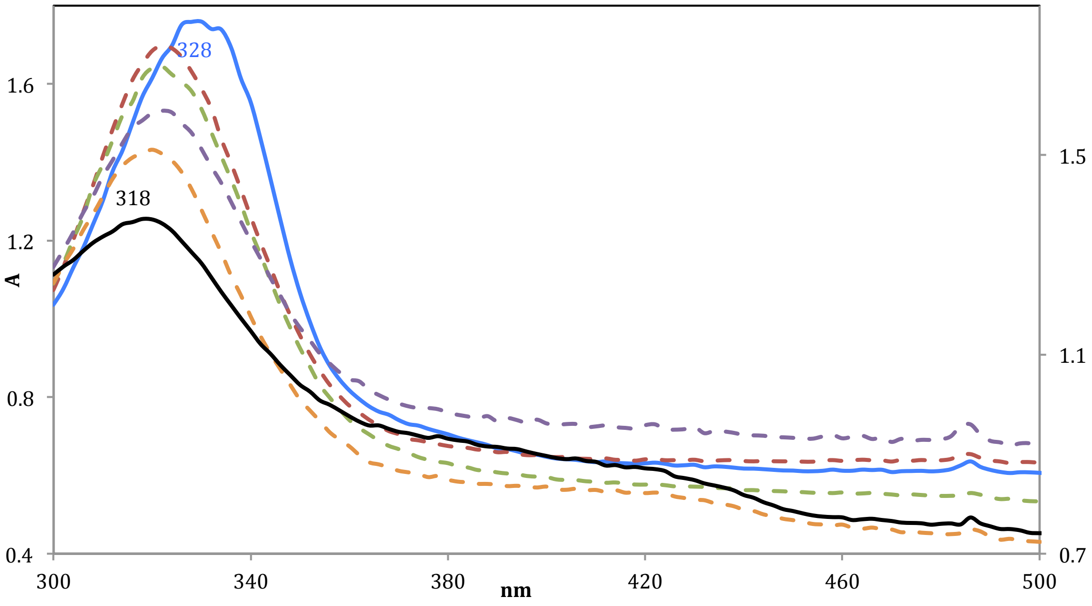

Figure 85: UV-visible spectral features of the TCNQ dianion in ACN (solid blue) and BMImPF$_6$ (solid black). Dashed: observed spectra in mixtures: 5, 10, 20 and 75%RTIL, respectively.

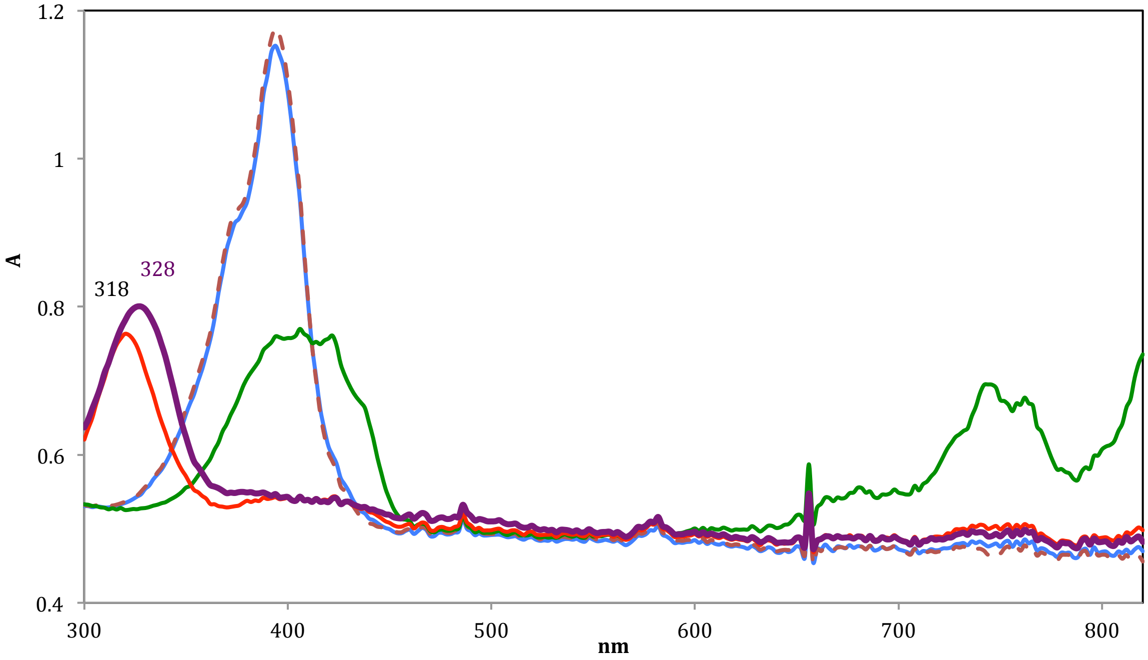

Figure 86: UV-visible SEC of TCNQ ACN-2%BMImNTF$_2$. Starting spectrum (blue), -0.35V (green), -0.7V (red), -0.9V in the backward (violet) and final spectrum (dashed. Potential scan from 0.2 to -1V at 2mV/s

The FTIR SEC in BMImNTF$_2$, purchased from Merck, showed significant shift of the dianion features to 2170 and 2125 cm^{-1} (*Figure 87*) compared to 2155 and 2105 cm^{-1} seen in the less contaminated solvent purchased from TCI (*Figure 78*). The reverse electrolysis was reversible in the electrolysis time scale and reoxidation regenerated the starting material.

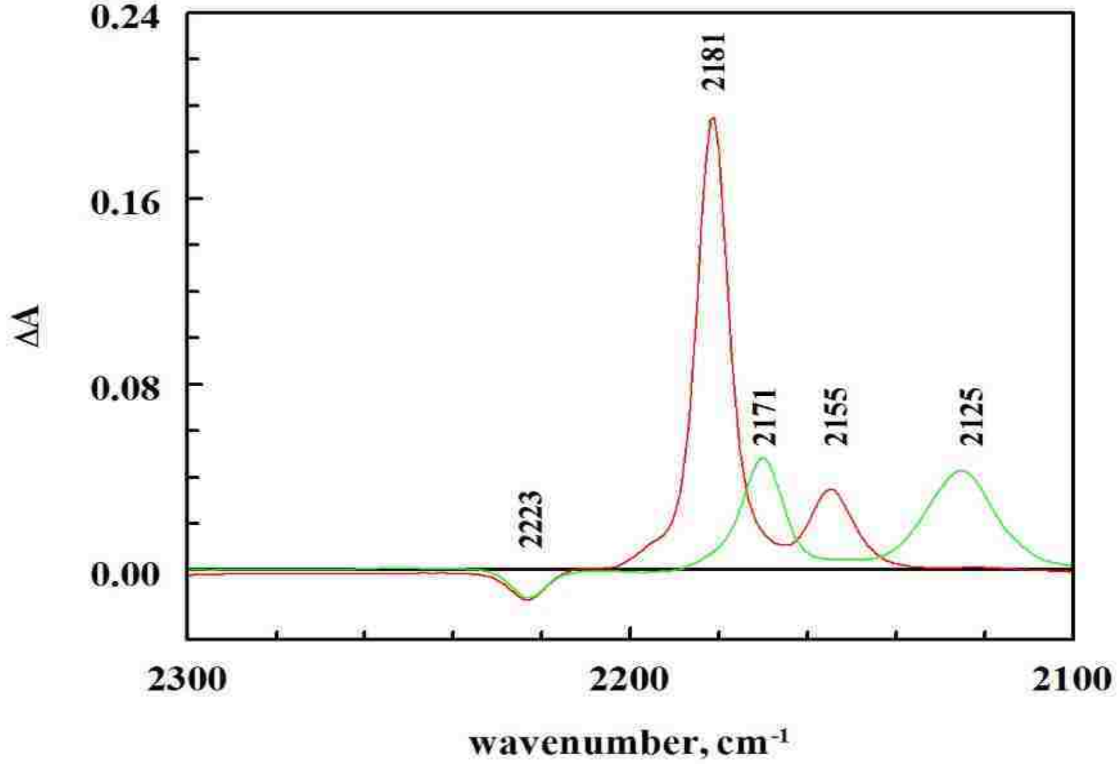

Figure 87: FTIR spectroelectrochemistry of TCNQ in BMImNTf$_2$. Negative feature: TCNQ, positive features: TCNQ$^-$ (red) and TCNQ^{2-} (green)

4.3.2 Identification

While different approaches can be adopted to identify the nature of these impurities in RTILs, we had to limit our investigation to electroanalytical methods. In fact, preliminary analyses have been directed toward using chromatographic and NMR methods in order to identify these contaminants. In addition to high cost of commercial columns, the chromatographic method appeared to require exhaustive efforts in methods development for achieving an accurate separation and detection of impurities in RTILs. The necessity of using highly pure co-solvents for impurities analysis with NMR restricted the detection limit of this approach. Preliminary experiments showed presence of several contaminants at the ppm level. As a result, all efforts were directed to adding different suspected contaminants, and by using voltammetric and UV-visible methods, to reproduce the changes seen in RTIL solutions.

First, the water content in all the RTILs was monitored, based on the characteristic peak of gold oxide around +0.7V vs Ag/AgNO$_3$. Water removal with heating under nitrogen didn't reduce the magnitude of the observed wave X in RTIL solvents (*Figure 81*). Beside water, 1-methylImidazole is a major impurities reported to be present in imidazolium RTILs. *Figure 88* shows voltammograms of TCNQ reduction in contaminated RTIL, before and after addition of MeIm. Addition of 1-MeIm later led to an intermediate wave at a potential similar the wave **C** and a new wave at more negative potentials comparable to the wave **X**. Addition of imidazole, a starting material in imidazolium RTIL synthesis, showed only the appearance of a new wave similar to the wave X, without intermediate wave (see Appendix).

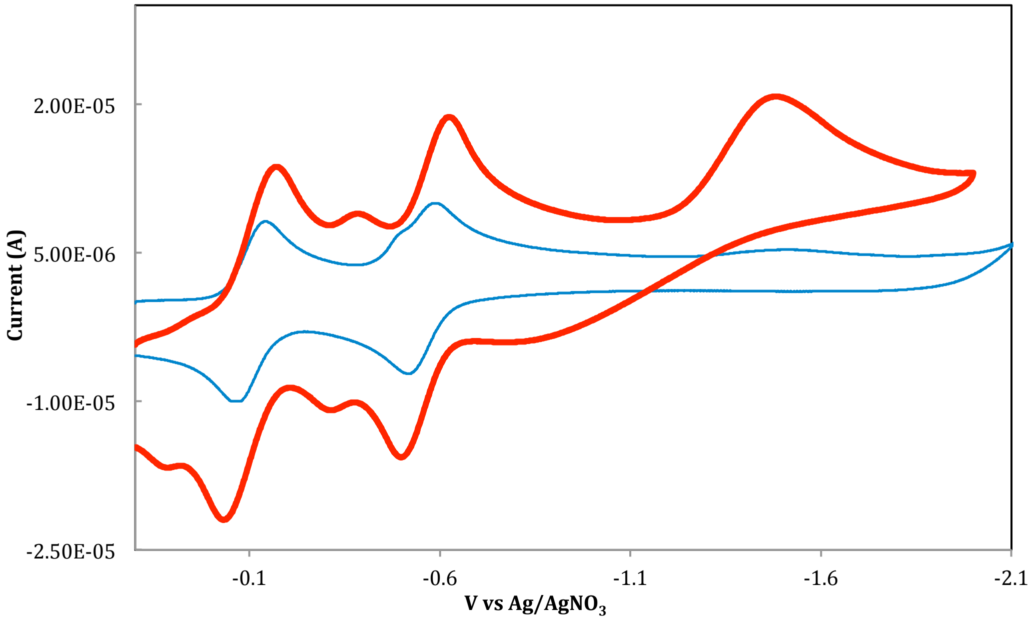

Figure 88: Voltammograms of TCNQ in BMImBF$_4$ before (blue) and after (red) addition of 1-MethylImidazole. 500mV/s

Specific effects of the impurities could be observed on the electronic structures of TCNQ redox species. Dissolution of TCNQ in contaminated solvents led to changes in the absorption spectrum, mostly the appearance of radical features at 420 and above 700nm (*Figure 89*). This was an indication of chemical reduction of neutral TCNQ by the impurities. Addition of 1-methylimidazole to TCNQ solution in ACN led to similar features seen in contaminated RTILs (*Figure 90*). Addition of imidazole to TCNQ solution led to different changes on the absorption spectrum than those seen in RTIL solutions (*Figure 91*).

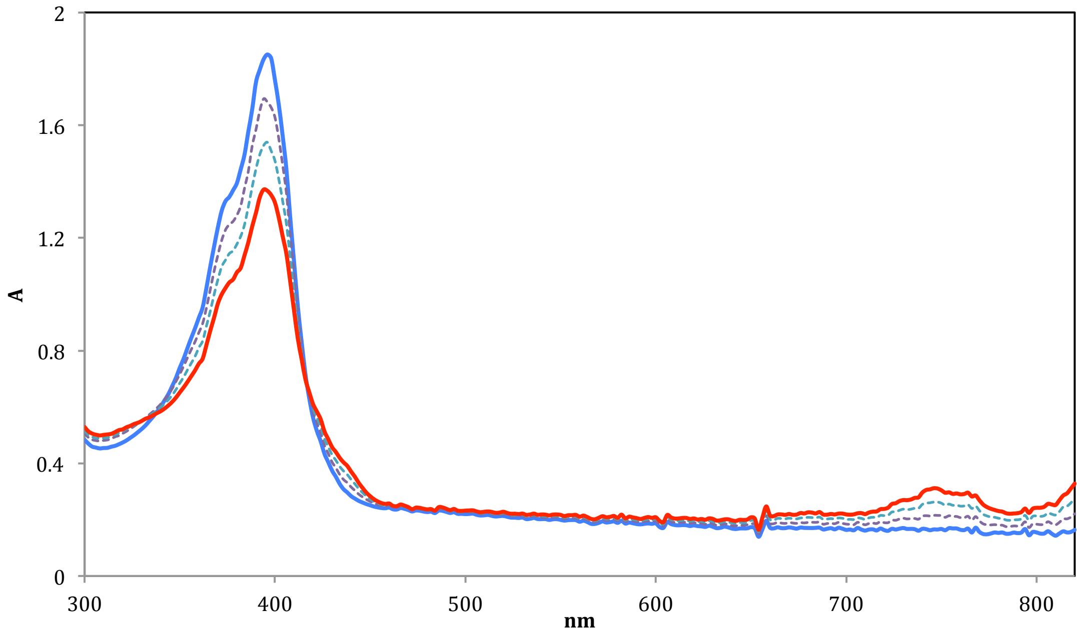

Figure 89: Spectral changes of dissolved TCNQ in contaminated BMImNTF$_2$. Starting spectrum (blue), after 10000s (red) and intermediate spectra (dashed).

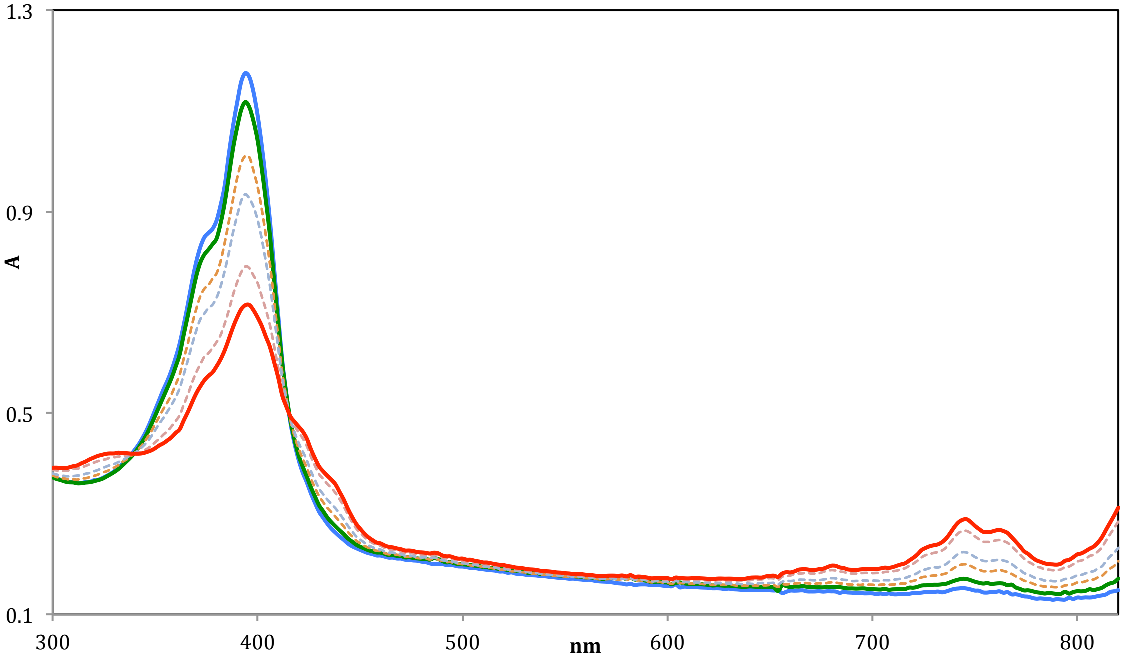

Figure 90: UV-visible changes of dissolved TCNQ in ACN. Starting spectrum (blue), 10s (green), 2500s (red) after addition of 1-MethylImidazole and intermediate spectra (dashed).

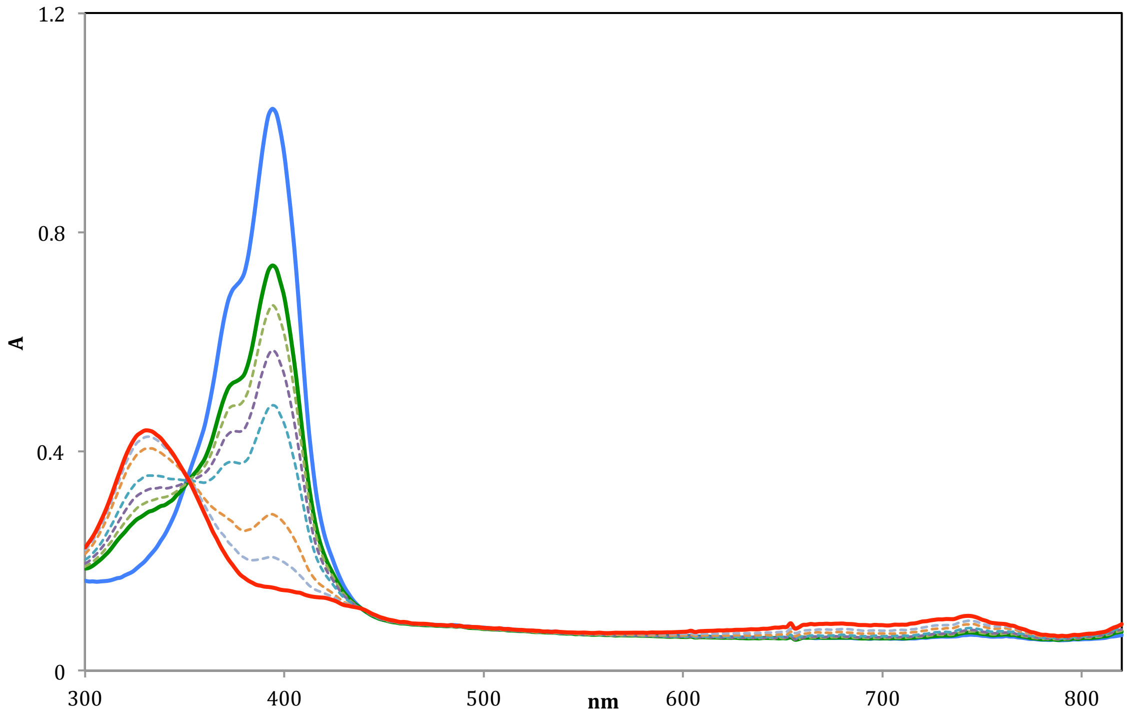

Figure 91: UV-visible changes of dissolved TCNQ in ACN. Starting spectrum (blue), 10s (green), 1000s (red) after addition of Imidazole and intermediate spectra (dashed).

At this stage, the results would infer that methylimidazole is a powerful candidate for RTIL contamination, leading to subtle changes seen in the electroreduction processes in these solvents. However, an important effect of the impurities was the blue shift of the dianion spectrum observed in pure RTILs and mixtures solutions. Hence, this feature was taken as a conclusive criterion to the contaminant nature. The electrolysis experiments revealed that addition of methylimidazole to TCNQ solution in ACN didn’t reproduce the blue shift of the dianion spectrum from 328 to 318nm (*Figure 92*). Thus, this latter wouldn’t be the major factor in explaining the changes observed in RTIL solutions.

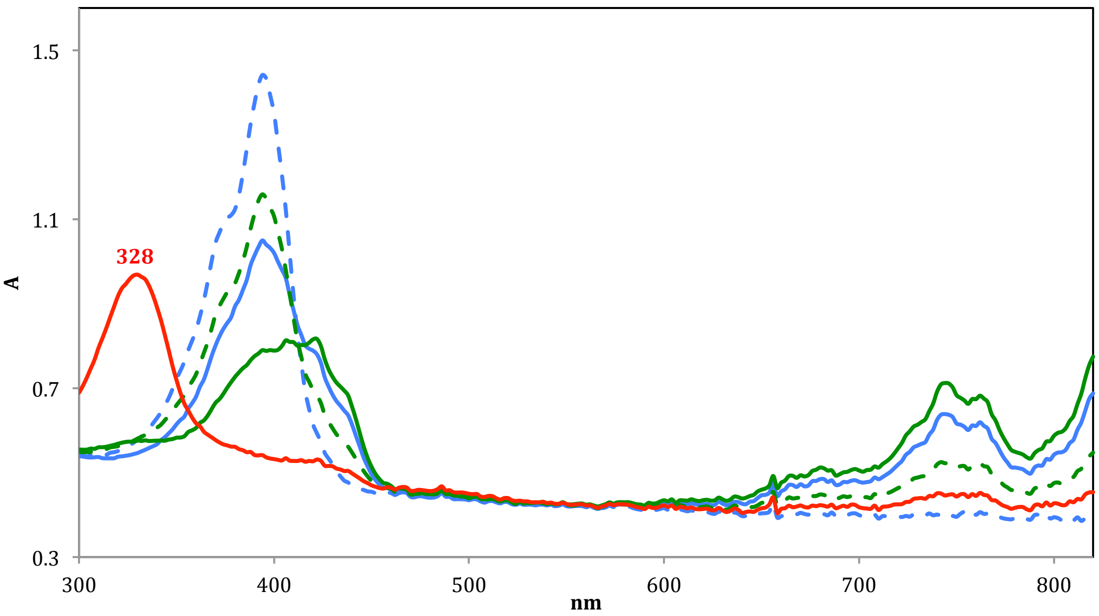

Figure 92: UV-visible SEC of TCNQ in ACN with added 0.5%MeIm. Starting spectrum (solid blue), -0.1V (dashed blue), -0.1V (dashed green), -0.2V (solid green) and -0.7V (solid red). Potential scan from 0.2 to -1V at 1mV/s

Finally, the cyclic voltammetry of TCNQ in ACN with added lithium salt, another plausible source of RTIL contamination, is shown in *Figure 93*. While there was no significant stabilization of the second wave, the reoxidation of the dianion showed a surface current at the reoxidation reaction. Then UV-vis SEC of TCNQ was carried out in contaminated ACN with lithium (*Figure 94*). In addition to partial reduction of the starting material, the electrolysis revealed a blue shift of the dianion spectrum from 328 to 318nm. These results indicated that residual alkali metals (Li^+, K^+ or Na^+) were very likely the major factor leading to changes seen in RTILs. High concentrations of up to 600ppm for lithium impurities have been reported in RTIL. These contaminants are usually introduced during the synthesis procedure of ionic liquids.[146]

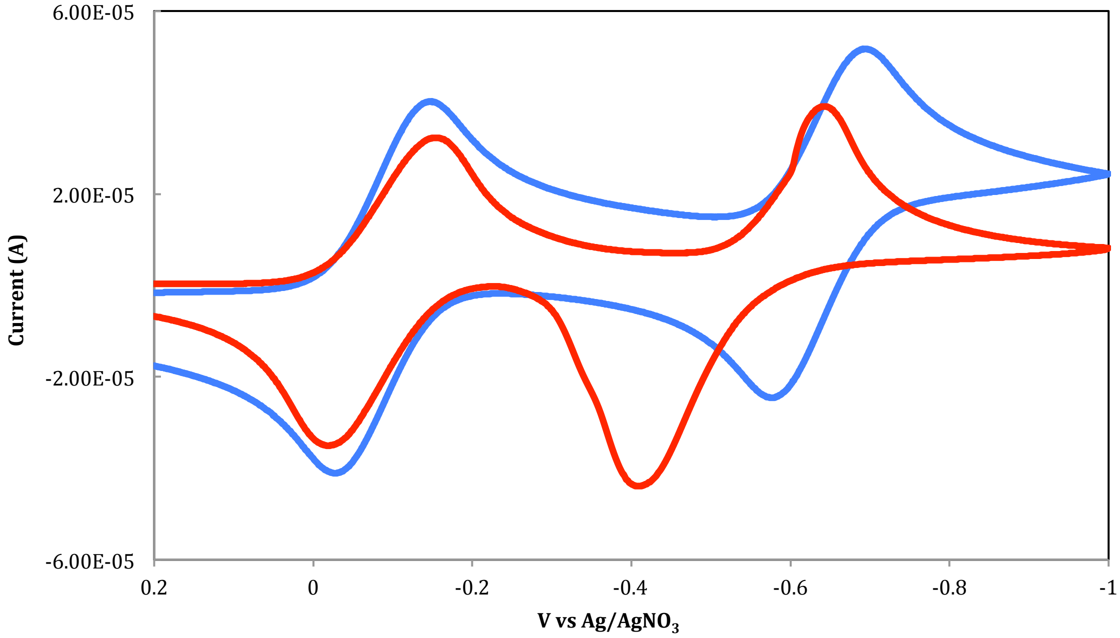

Figure 93: Voltammograms of TCNQ reduction in ACN, before (blue) and after (red) addition of LiClO$_4$. 100mV/s

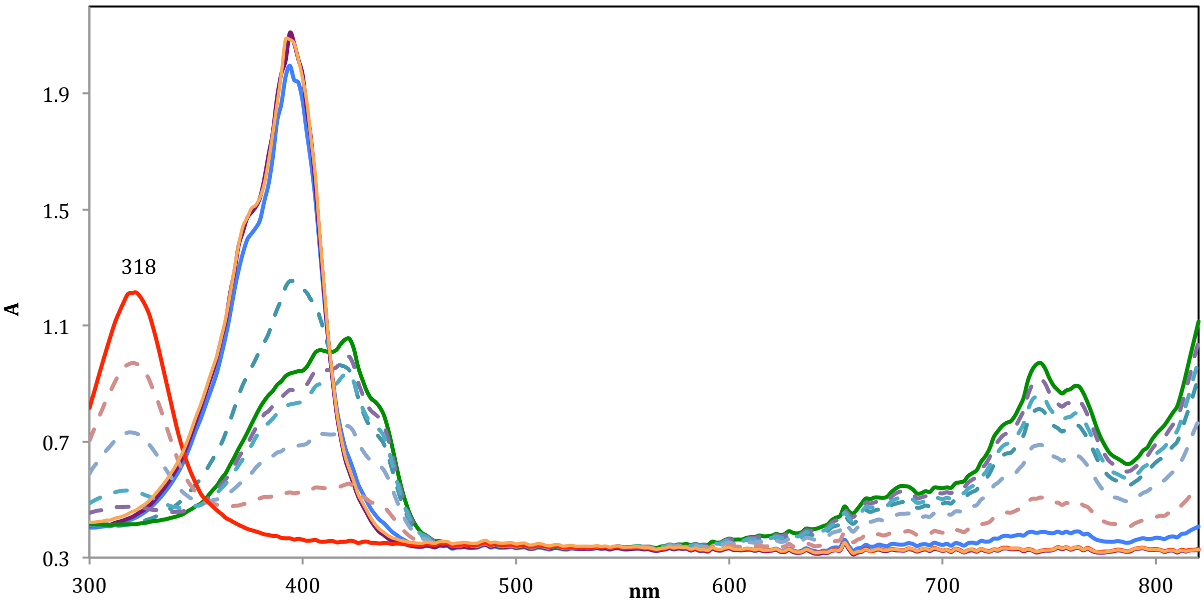

Figure 94: UV-visible SEC of TCNQ in ACN with added LiClO$_4$. Starting spectrum (blue), -0.05V (violet), -0.1V (green), -0.3V (green) and -0.8V (red), final spectrum at 0.2V (orange) and intermediate spectra (dashed). Potential scan from 0.2 to -0.8V at 2mV/s

4.4 Discussion

The two electron reduction of TCNQ in RTILs showed high stabilization of the reduction potential of the second wave. The potential difference between the two waves dropped by about 130mV, when going from ACN to RTILs. The voltammetry in ACN-RTILs mixtures showed a linear drop of ΔE_{12} as a function of RTIL fraction. This linearity is beyond simple ion-pairing interactions, which would level off at higher RTIL fractions. These results were consistent with additional solvation of the dianion by RTIL nano-domains. In contrast to dinitrobenzene, where 20%RTIL mixture led to drop of ΔE_{12} by about 140mV, for TCNQ the drop was only about 50mV. This observation implies that extensive interactions of RTIL components with the DNB dianion took place. More specifically the charged nitro groups were more sensitive to change in solvation environments than cyanide groups in RTIL solutions. As was seen for DNB, solvation by RTILs had no measurable effect on the absorption spectra of electrogenerated species. The spectroelectrochemistry of TCNQ in RTILs showed quite similar features to ACN for both electronic and vibrational transitions. The fact that no ion-pairing effects on cyanide vibrations of TCNQ radicals were observed, would infer that changes in solvation environment are the major driving force for potential stabilizations in RTILs. The partitioning of TCNQ radicals into the RTIL domains was shown to slow the transport in mixtures. The decrease in diffusion coefficient of the radicals in RTIL rich mixtures was in agreement with predicted drop in the current of the second reduction wave compared to the first reduction.

One of the most interesting outcomes of this investigation was the importance of the purity of RTIL solvents in electrochemical processes. The voltammetric analysis of TCNQ in some contaminated imidazolium ionic liquids revealed quite interesting features. In order to accurately interpret the observed changes, a careful examination of the impurities impacts had to be considered.

The presence of impurities in these solvents had a dramatic effect on the reduction potentials, mostly on the second electron transfer. Reaction of these contaminants with TCNQ dianion lowered the reduction potential by more than 200mV. The voltammetry in mixture solutions showed that this effect could take place with as little as 2% RTIL in mixture. In these media, the chemically coupled wave grew at the expense of the original wave with increasing RTIL concentrations. A first reading of these results would have been perfectly consistent with preferential solvation of dianion into two domains, leading to two different reduction processes. However, observation of similar behavior in less contaminated ionic liquids indicated that the chemical process was more related to impurities presence in these solvents. Cyclic voltammetry in microelectrode conditions showed that the chemically coupled reduction was fairly reversible.

Another major impact of these contaminants for redox processes was on the electronic structure of TCNQ dianion. A 10nm blue shift in dianion absorption spectrum has been observed when going from molecular solvent to imidazolium RTILs. UV-visible spectroelectrochemistry in mixtures showed a gradual shift of the spectrum as a function of %$BMImPF_6$. Interestingly, electrolysis experiment in as little as 2% $BMImNTF_2$ mixture, exhibited coexistence of two reduction products.

The nature of these impurities has been investigated using electroanalytical approaches, mainly through spiking with suspected contaminants. In addition to voltammetric changes, the shift in dianion absorption spectrum has been set as the main spectroscopic signature of these impurities. Methylimidazole and imidazole were shown to reproduce some of the features seen in voltammetry, while not having similar effects to RTIL on the dianion absorption spectrum.

In contrast, addition of lithium salt in the electrolysis experiments enabled to reproduce the spectroscopic changes seen in RTIL solutions. Presence of lithium led to a blue shift of the dianion absorption spectrum. This observation was a key factor in understanding the mechanism of the chemical reaction involving the dianion with Li^+ cation. Where the lithium cation complexed with the dianion as follow:

$$2Li^+ + TCNQ^{2-} \rightarrow Li_2TCNQ_{(solid)}$$

The shift in cyanide vibrations of the dianion to higher frequencies was also consistent with a complexation reaction. Lipin and Xiangqin have reported a shift of the 2107cm^{-1} to higher frequencies. While the shift was shown to be dependent on the lithium concentration, the average frequency of 2130 cm^{-1} was consistent with our results 2125cm^{-1}.[84] Adsorption of Li_2TCNQ complex on electrode surface could be also seen in the reoxidation reaction within the voltammetric timescale. Interestingly, this complexation reaction had no measurable stabilization of the second reduction in acetonitrile. However, addition of RTIL to acetonitrile solution of TCNQ, in the presence of lithium salt, revealed two major changes on the voltammetry (*Figure 95*).

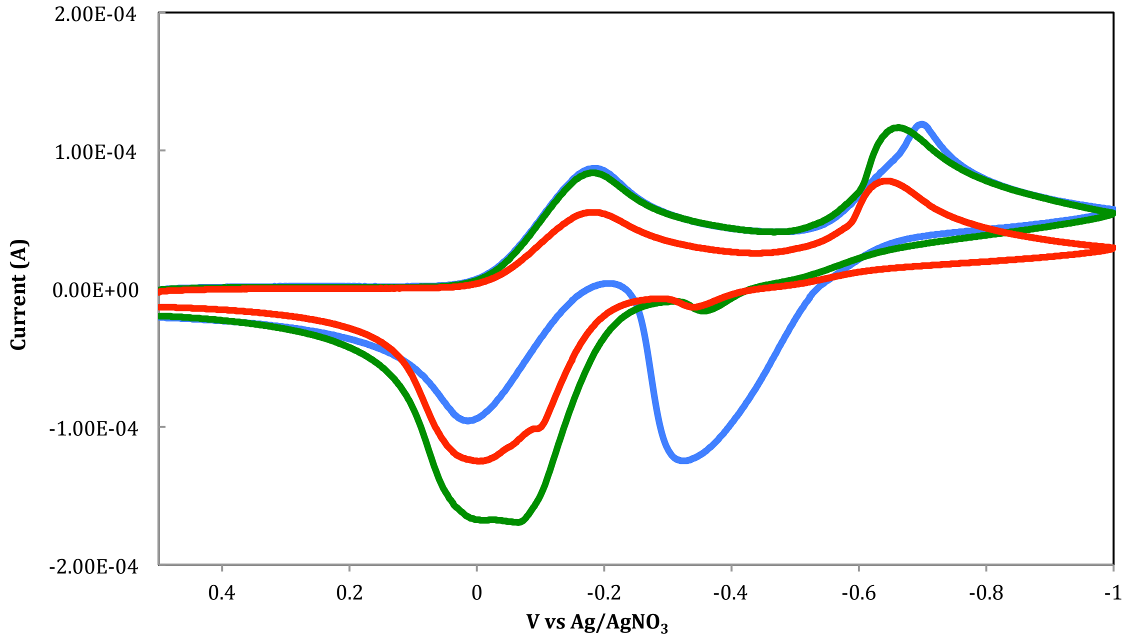

Figure 95: Voltammograms of TCNQ reduction in ACN with added $LiClO_4$, before (blue), after addition of 5%$BMImNTF_2$ (green) and 10%$BMImNTF_2$ (red). 500mV/s

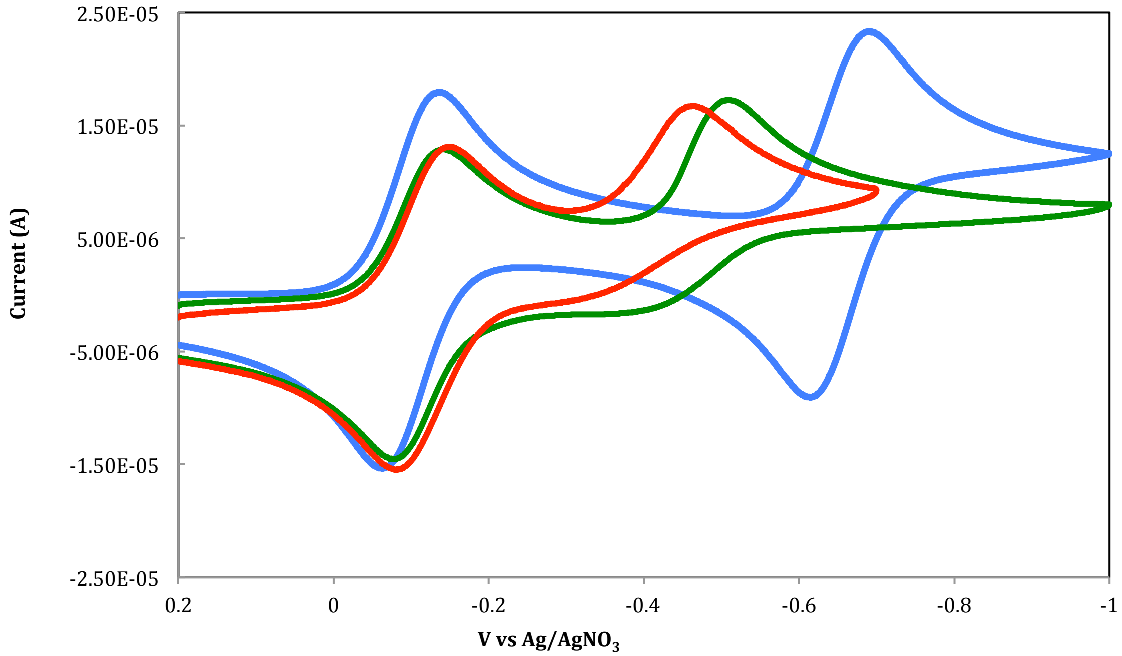

Figure 96: Voltammograms of TCNQ reduction in ACN (blue), 20%$BMImNTF_2$ (green) and in 100%$BMImNTF_2$ (red). 100mV/s

As expected, the second reduction wave was stabilized by introduction of the RTIL. Increasing the RTIL fraction reduced the adsorption of the Li_2TCNQ complex on the electrode surface. These two effects were mimicking the voltammetry seen in contaminated RTIL solutions. Hence, the driving forces for the large shift in RTIL solutions can be envisioned as the combination of two factors: the complexation reaction of dianion with lithium cation and solvation of the complex by RTIL environment. The latter conclusion was also consolidated by the voltammetric results in mixtures of contaminated RTILs (*Figure 96*). The complete disappearance of the actual reduction wave at 20%RTIL indicated that enough lithium content was present to complex all electrogenerated dianion. In this mixture, the voltammogram looked quite similar to the one in 100% RTIL. However, larger stabilization was observed in the 100% ionic liquid than at 20%RTIL mixture. Such additional stabilization implied that the complexation reaction was indeed taking place within the RTIL domain. This was consistent with slow diffusion of the complex during the oxidation (backward) reaction. Hence, in the mixture, the lithium impurities do stay within the ionic liquid domains where the chemical reaction takes place. Consequently, the partitioning of the dianion into RTIL domains is marked by its complexation with the impurities.

Figure 97 summarizes the observed processes for the TCNQ reduction in ACN-RTIL media. While the impurity could lead to change in electronic structure of the dianion in molecular solvent, it had no significant effect on the thermodynamics of the reduction wave.

However, the presence of impurities within the RTIL solvents led to significant stabilization of the reduction wave. In addition, the formation of ionic liquid nano-domains in mixtures has powered the chemical reaction at very small fractions of RTIL and reduced the adsorption of the product on the electrode surface.

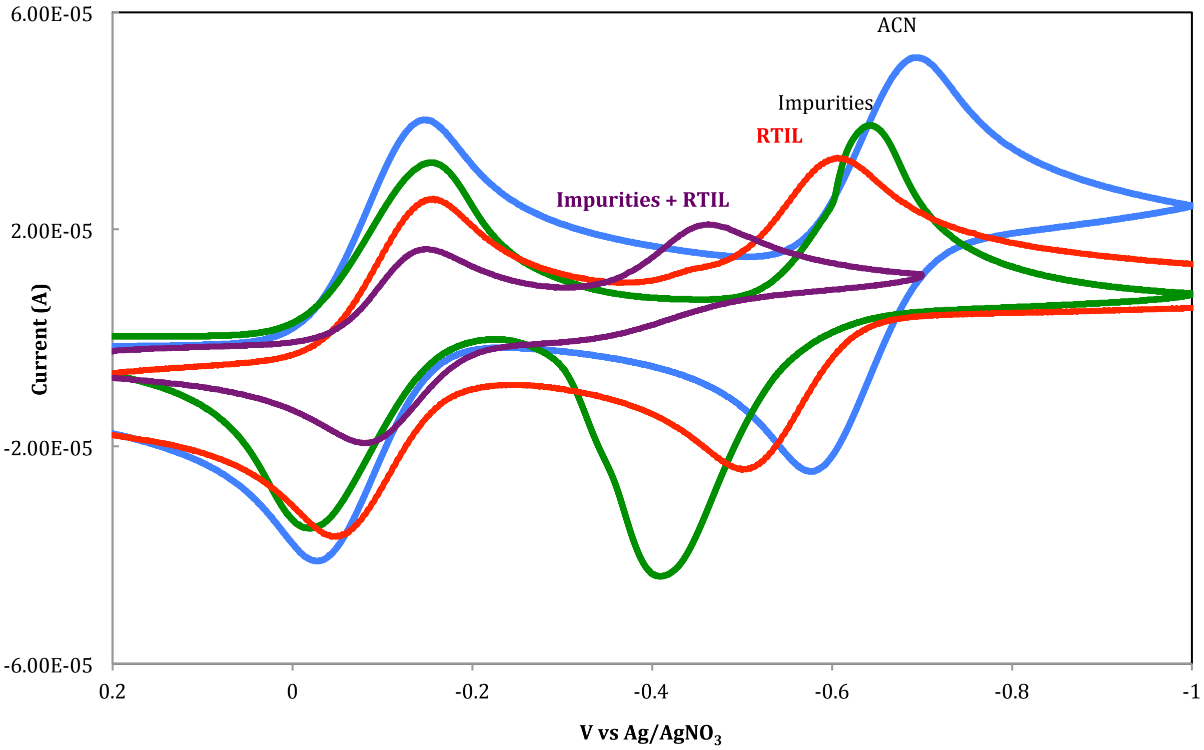

Figure 97: Different reduction processes of TCNQ reduction in ACN-RTIL media.

Finally, it should be pointed out that the voltammetry of TCNQ in ACN-RTIL mixtures led to deconvolution of the effects of nano-domains formation from the impurities in imidazolium RTILs. The coalescence of the two waves into one wave in case of DNB reductions has precluded this deconvolution.

Chapter 5 Voltammetry and Spectroelectrochemistry of Fullerene C_{60} in Benzonitrile/RTIL Mixtures

The previous investigation on DNB and TCNQ reductions indicated that nanostructures of molecular and RTIL domains were present in the mixed solvents systems. In order to investigate the factors that control the partitioning of solutes into nano-domains, the electrochemistry of C_{60} in similar mixed solvent systems was studied. The structure of C_{60} (*Figure 98*) and its redox products are spherical in nature and the charge is diffusely distributed.

Two types of RTILs were used in this investigation. The first type contained the planar $BMIm^+$ cation, which contains an ionic environment where ion pairing with the spherical redox species is expected to be poor. The second type contained a tetraalkylammonium cation, where the flexibility of the cation would provide better ionic interaction.

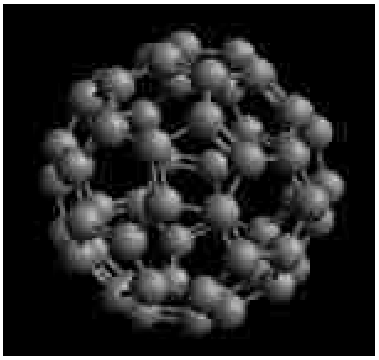

Figure 98: Fullerene C_{60}

5.1 Voltammetry

5.1.1 Voltammetry in BzCN-RTIL

Voltammetry of C_{60} was first carried out in benzonitrile, at the solubility limit (about 0.5mM). In the molecular solvent, the first three reversible reduction waves were observed, respectively, at -0.76, -1.17 and -1.66V versus $Ag/AgNO_3$ (*Figures 99-100*). These potentials were in agreement with reported values in molecular solvents.[91] Previous works have reported up to six waves, but only three were accessible in mixed benzonitrile/RTIL solutions.

As the neutral C_{60} was insoluble in pure ionic liquids, voltammetric measurements of the first three reduction waves were carried out in mixtures with benzonitrile up to 60% (v/v) in RTIL. The addition of $BMImPF_6$ to benzonitrile solution of C_{60} shifted the reduction potentials to more positive values. In these mixtures, the three waves were reversible in voltammetric scale. While the first wave did not shift significantly with the presence of the RTIL, the second and third waves exhibited larger shifts. Similar to imidazolium RTIL, the reduction waves were reversible and shifted to more positive potentials with increase of $AmNTF_2$ fraction in the mixture. Higher stabilization was observed for the third wave compared to the second wave. Due to its wider electrochemical window and low viscosity, voltammograms in ammonium RTIL mixtures exhibited better reoxidation for the third wave.

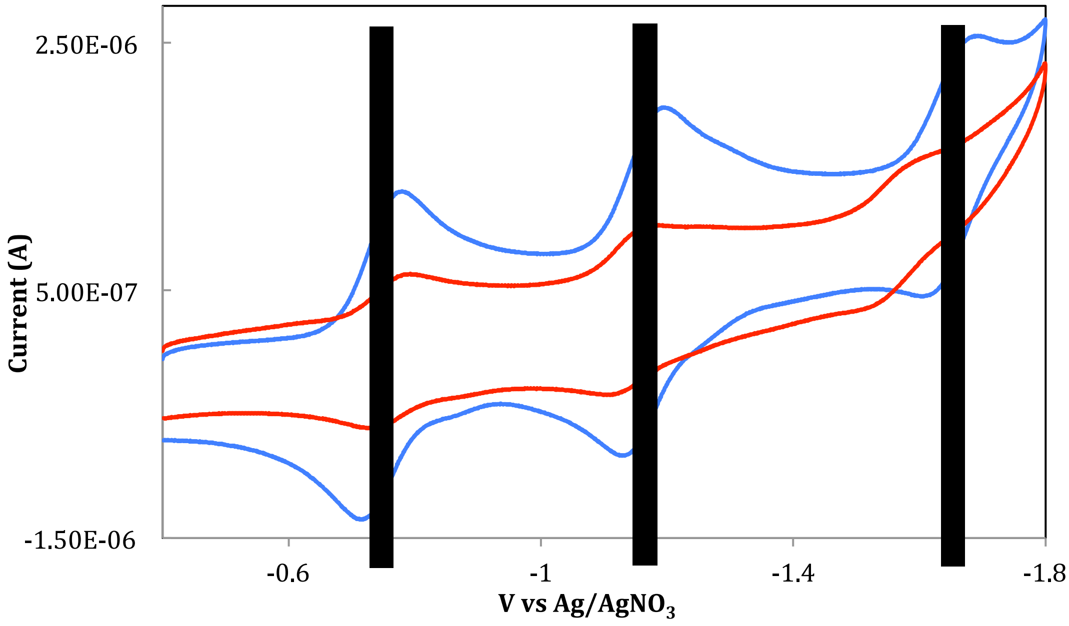

Figure 99: Cyclic voltammetry of 0.48 mM C_{60} *in BzCN (blue) and 40 %BMImPF*$_6$ *(red). 100 mV/s*

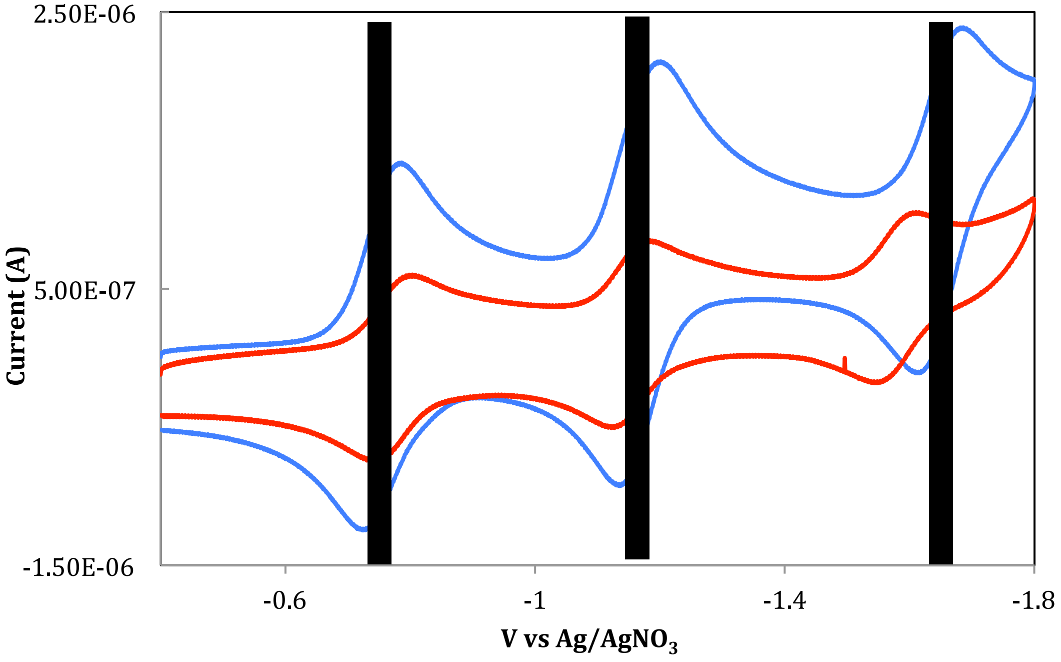

Figure 100: Cyclic voltammetry of 0.48 mM C_{60} *in BzCN (blue) and 33%AmNTF*$_2$ *(red). 100 mV/s*

5.1.2 Voltammetry in RTIL

Attempts were made to carry out the voltammetry in pure $AmNTF_2$ because of its large electrochemical window, reasonable viscosity and lower impurities content. Extensive electrolysis of C_{60} in pure $AmNTF_2$ formed fullerides that had significant solubility in the RTIL. It was then possible to carrying out the cyclic voltammetry in pure RTIL. While C_{60}^{-}/C_{60}^{2-} and C_{60}^{2-}/C_{60}^{3-} waves were reversible, the first wave C_{60}/C_{60}^{-} wave was not, very likely due to the insolubility of C_{60} in the pure ionic liquid. Voltammograms in pure $AmNTF_2$ showed significant stabilization of the second and third waves. Features of a fourth reduction wave could be observed at -1.85V (*Figure 101*).

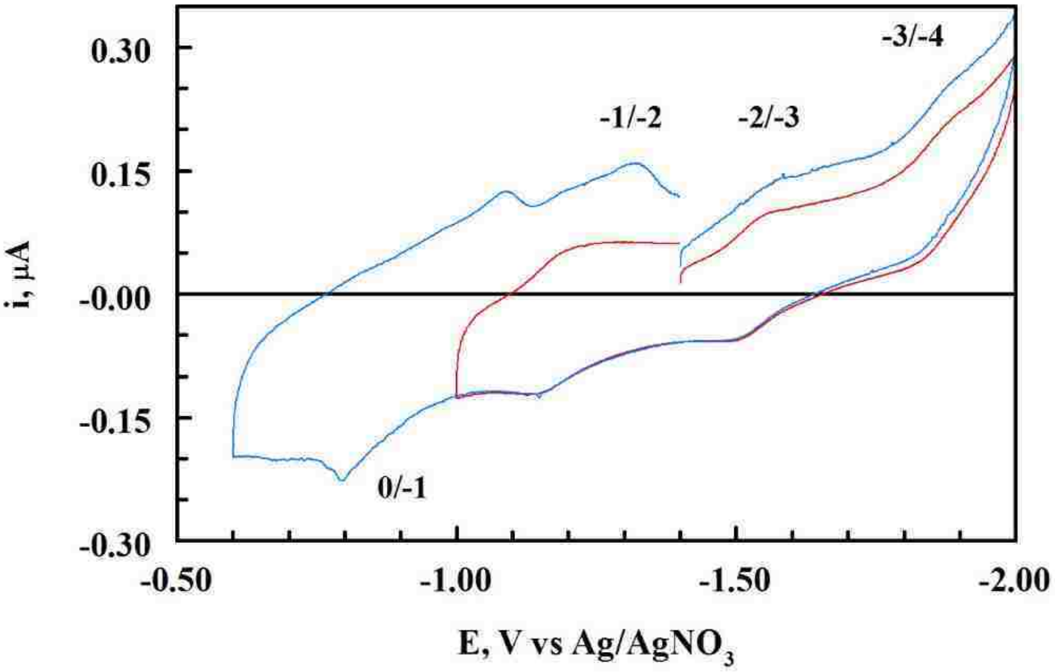

Figure 101: Cyclic voltammetry of C_{60}^{2-} in $AmNTF_2$. Red line: positive scan switched at -1.0 V; Blue line: positive scan switched at -0.60 V.

5.2 Potential shifts vs %RTIL

Due to possible drift of the reference potential, upon change in liquid-electrode junction potential, the measured $E_{1/2}$ potentials were referenced to the internal reference $DmFc^+/DmFc$. *Figure 102* shows the shift in $E_{1/2}$ values (vs DmFc) of the first three waves for mixtures of benzonitrile with $BMImPF_6$, $BMImBF_4$ or $AmNTF_2$. In these mixtures, the first three waves of C_{60} shifted to positive potentials as the %RTIL increased. The shifts were small for the first waves, but became more significant for the second and third waves. For a given %RTIL, larger shifts were observed for $BMIm^+$ containing RTILs as compared to $AmNTF_2$ mixtures.

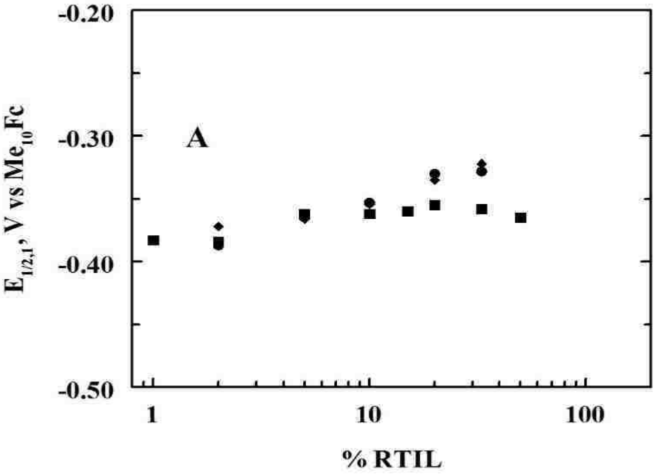

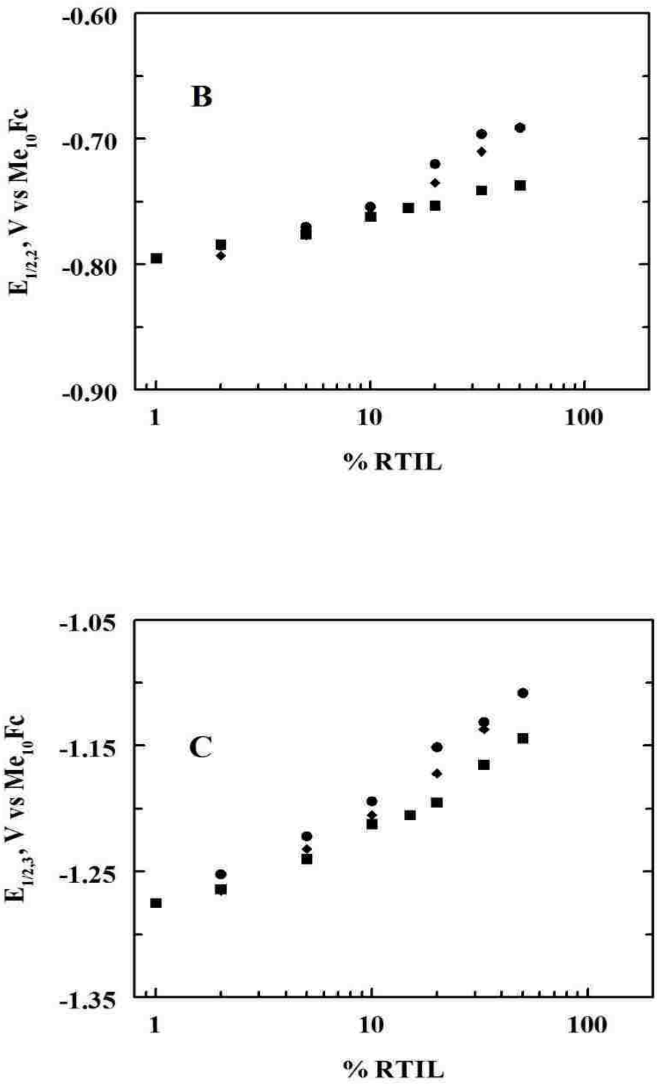

Figure 102: Variation in the $E_{1/2}$ values for the first three waves of C_{60} in mixtures of benzonitrile and $BMImPF_6$ (circles), $BMImBF_4$ (diamonds), or $AmNTF_2$ (squares). A: first wave; B: second wave; C: third wave.

5.3 Potential shifts vs Guttmann AN

In order to evaluate the correlation of the potential shifts of C_{60} in RTIL solutions with the acceptor properties of the solvents, the Gutmann AN for RTIL mixtures were measured by the method of Schmeisser et al.[136] (see Chapter 2). Variation in the Gutmann AN with %RTIL showed a non-linear trend. Similar non-linear behavior between %RTIL in molecular solvent mixtures and the polarity parameter π^* has already been reported.[35] A typical plot was shown in the Chapter 2 for %$AmNTf_2$ mixtures.

Potential shifts obtained in our mixtures, along with data obtained in molecular solvents[94], were plotted in respect to Gutmann AN of the solvents (*Figure 103*). While no clear correlation was observed for change in $E_{1/2,1}$ with AN for molecular solvents, a good linear relationship with positive slope was observed for benzonitrile/RTILs. For the second wave, a similar positive slope was observed for both the molecular and the mixed benzonitrile/RTIL solutions. In our mixtures, larger shifts were observed for the $BMIm^+$ mixtures as compared to the $AmNTf_2$ mixtures. This is mostly due to larger Gutmann AN of $BMIm^+$ mixtures at a given volume ratio. A better correlation, with higher positive slope, was observed for the third wave.

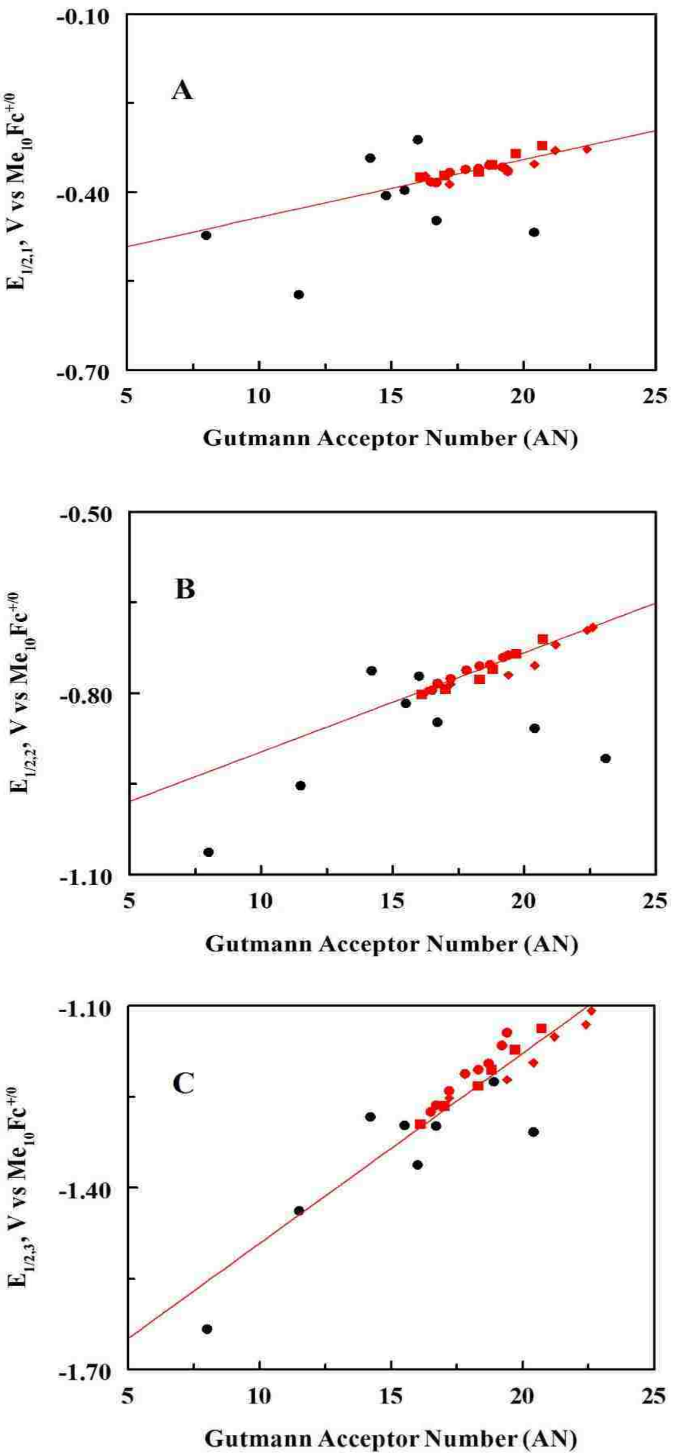

Figure 103: Variation in the $E_{1/2}$ values for C_{60} in BzCN/RTIL mixtures. Black symbols are molecular solvents.[94] *Red symbols are for BzCN/RTIL mixtures: AmNTF$_2$ (circles), BMImPF$_6$ (diamonds), BMImBF$_4$ (squares). Least square fit slopes for BzCN/RTIL mixtures only: $E_{1/2,1}$: 1.0 x 10^{-2}, (R^2 = 0.90), $E_{1/2,2}$: 1.6 x 10^{-2}, (R^2 = 0.95), $E_{1/2,3}$: 2.6 x 10^{-2} (R^2 = 0.93).*

Figure 104 shows variation of potential differences ($\Delta E_{12} = E_1 - E_2$ and $\Delta E_{23} = E_2 - E_3$) as a function of Gutmann AN. At lower concentrations of the RTIL, the ΔE_{12} and ΔE_{23} values correlated well with AN, with slopes of -6 and -10mV, respectively. Higher stabilization was observed at higher concentrations of RTILs, beyond what would be expected from the AN.

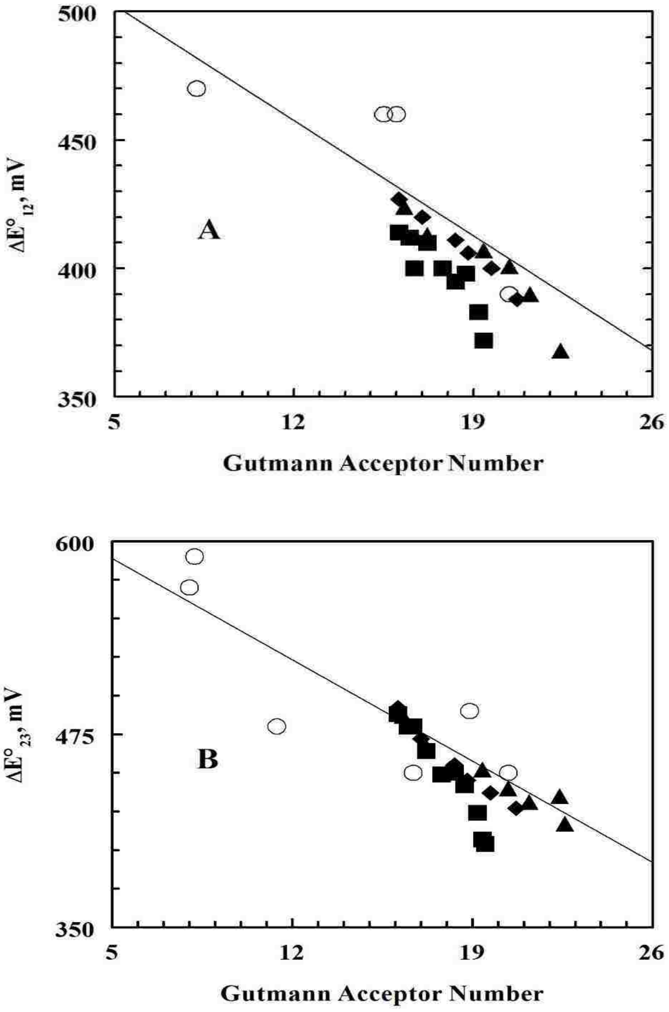

Figure 104: Variation in ΔE_{12} (A) and ΔE_{23} (B) values as a function of the Gutmann AN; benzonitrile/AmNTf$_2$ mixtures (■); benzonitrile/BMImPF$_6$ (▲); benzonitrile/BMImBF$_4$ (♦). The trend lines are based on the molecular solvent data (○)[94].

5.4 Potential shifts vs ion pairing

The effect of the physical state of the salt on the reduction potentials was evaluated by carrying out the voltammetry in both RTILs and salts that are solid a room temperature. A total concentration of TBAP and the added salt was kept constant at 0.50 M, to maintain a constant ionic strength. For the first wave, two ion pairing equilibria can occur for mixtures of TBAP/BMIm$^+$ salts:

$$C_{60}^{-} + TBA^{+} \rightarrow (TBA^{+})(C_{60}^{-}) \qquad K_{IP1,TBA^{+}C_{60}^{-}}$$

$$C_{60}^{-} + BMIm^{+} \rightarrow (BMIm^{+})(C_{60}^{-}) \qquad K_{IP1,BMIm^{+}C_{60}^{-}}$$

Similar reactions can be written for C_{60}^{2-}, and C_{60}^{3-}, with the subscript after IP indicating the number of cations ion paired with the C_{60} anionic species. A detailed analysis for the first three waves of C_{60} for mixtures of TBAP/BMIm$^+$ salts is shown in the Appendix. The results are summarized in *Table 13*. A similar approach was used for the analysis of other salt mixtures. The $E_{1/2}$ values as a function of the salt concentration for the first three waves of C_{60} are shown in *Figure 105*, along with the theoretical lines based on the constants in *Table 5-1*.

For the first wave, while there was no significant ion pairing between BMIm$^+$ (as solid salt) and C_{60}^-, the THA$^+$ ion paired more strongly with C_{60}^- than TBA$^+$, very likely due to larger alkyl chains. For the RTILs, a negative shift in the $E_{1/2,1}$ values with the increased concentration of salts indicated that TBA$^+$ ion paired more strongly with C_{60}^- than the RTILs cations. The smaller interaction of Am$^+$ (RTIL cation) with C_{60}^- compared to TBA$^+$, indicated that the physical structure of the salts was the predominant parameter, over ion paring effects, shifting $E_{1/2,1}$ values.

Table 13: Ion Pairing Equilibrium Constants for C_{60}-Anionic Species

C_{60}-Species	Salt	K_{IP1}	K_{IP2}	K_{IP3}
C_{60}^{-}	TBAP	1.5	—	—
	THAP	5	—	—
C_{60}^{2-}	TBAP	13	2.5	—
	THAP	35	1.3	—
	$AmNTf_2$	3	—	—
	$BMImPF_6$	2	—	—
C_{60}^{3-}	TBAP	36	20	0.5
	THAP	60	5	—
	$AmNTf_2$	650		
	$BMImBF_4$	500	—	—
	$BMImPF_6$	800	—	—

For the second wave, similar trends to $E_{1/2,1}$ were observed, with smaller shifts for the RTILs compared to BMImCl salt. The small shifts for $E_{1/2,2}$ for the RTILs were consistent with small K_{IP1} between the cations and C_{60}^{2-}, with no measurable value for K_{IP2}. For THAP salt, the larger size of the cation had less effect on the shifts in the $E_{1/2,2}$, consistent with comparable K_{IP} values for TBA^+ and THA^+.

For the third wave, addition of $BMIm^+$ (as BMImCl) shifted the potential to more negative values, indicating weaker ion pairing of C_{60}^{3-} with $BMIm^+$. Interestingly, the $E_{1/2,3}$ shifted positively for the three RTILs, indicating a strong interaction of the cations with C_{60}^{3-}, even though $BMIm^+$ and Am^+ do not ion pair with C_{60}^{3-} stronger than TBA^+. In addition, while a large K_{IP1} was observed for the ion pairing of the RTIL salts with C_{60}^{3-}, no measurable values were obtained for K_{IP2} and K_{IP3}.

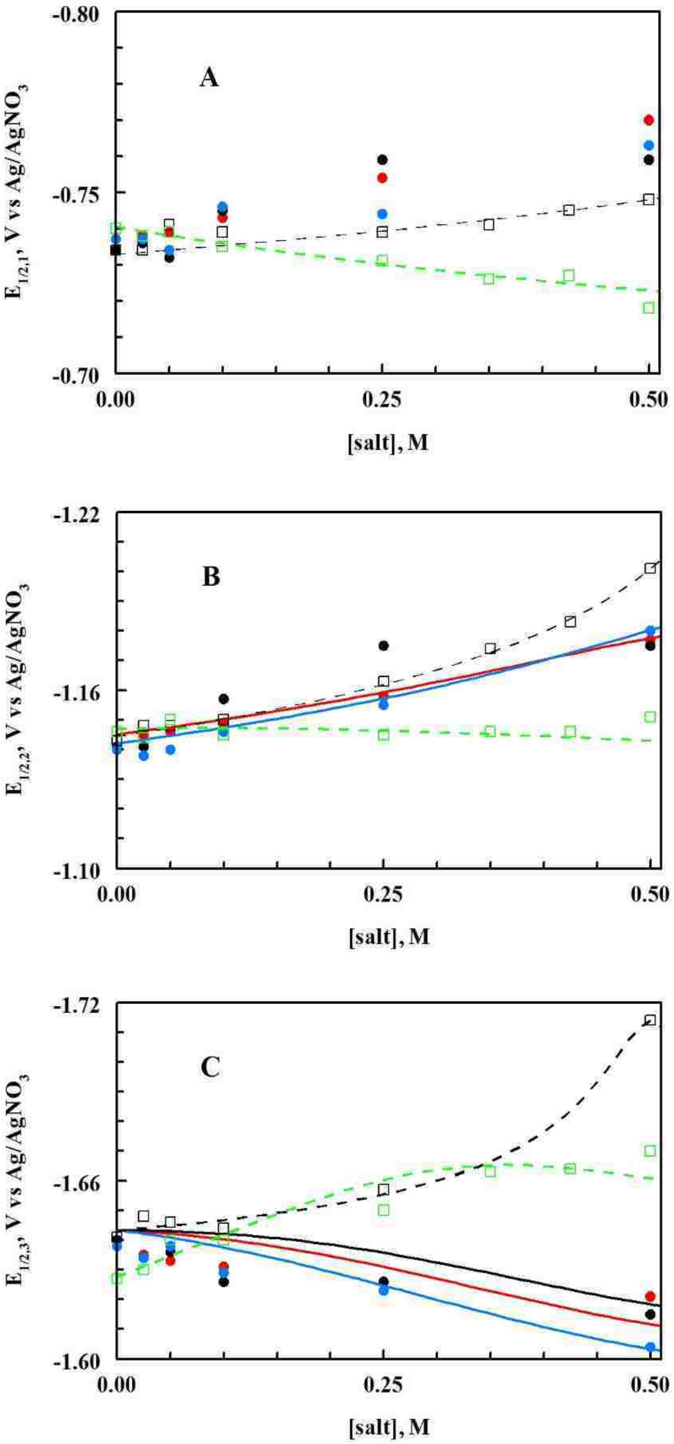

Figure 105: $E_{1/2}$ as a function of the salt concentration in benzonitrile. Salts: BMImCl (□, black), THAP (□, green), AmNTf$_2$ (•, red), BMImBF$_4$ (•, black), BMImPF$_6$ (•, blue). C_{TBAP} + C_{salt} = 0.50 M. Theoretical lines correspond to the predicted shifts in $E_{1/2}$ values based on K_{IP} values.

Figure **106** shows the variation of experimental and predicted ΔE_{23} values as a function of the salts concentrations, using the equilibrium constants in *Table 13*. While BMImCl had no significant effect on the ΔE_{23} values, addition of RTILs (including $BMImPF_6$ and $BMImBF_4$) significantly decreased the ΔE_{23} values.

Further differences between the solid and the RTILs salts could be observed through the magnitude of calculated ion paring constants. As for the solid salts, the potential shifts were well described by successive ion pairing constants (K_{IP1}, K_{IP2}, K_{IP3}), leading to first, second and third power relationships between the salt concentration and the $E_{1/2}$. However, in case of RTILs, the potential shifts could be explained by only one large K_{IP} value and a first order concentration relationship between the half potential and the RTIL concentration. It is unlikely that a single $BMIm^+$ cation would displace 2-3 TBA^+ cations, given that $BMIm^+$ forms weaker ion pairs. This implies that the RTIL salts interact with C_{60}^{3-} as a unit rather than individual free cations (like TBA^+ in TBAP), which is consistent with the formation of nano-domains in these mixtures. The more likely explanation is that anionic C_{60} species are extracted into RTIL domains, where they are solvated by 2-3 cations of the RTIL. It is worth noticing that this latter effect could be also observed to smaller extent for the potential shift of the second wave.

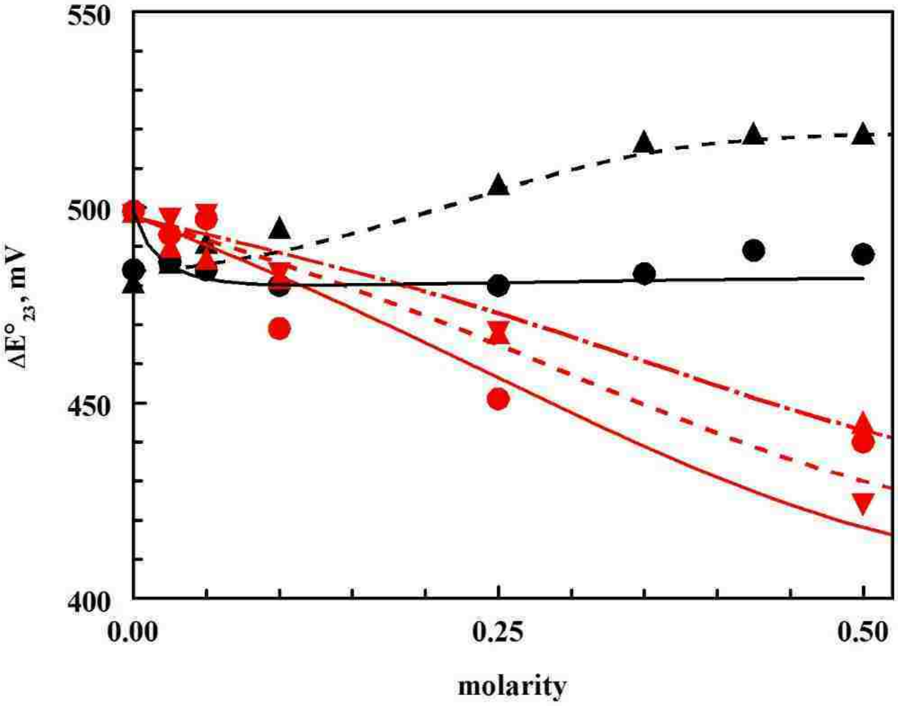

Figure 106: Dependence of the $\Delta E°_{23}$ values in the concentration of the electrolyte concentration in benzonitrile. Electrolyte: BMImCl (• balck), THAP (▲ balck), $BMImBF_4$ (• red), $BMImPF_6$ (▼red), $AmNTF_2$ (▲ red). Solid line is for ion pairing between TBA^+ and anionic C_{60} species: $K_{IP1,C60-} = 15$, $K_{IP1,C60(2-)} = 80$, $K_{IP2,C60(2-)} = 80$, where K_{IP1} and K_{IP2} are for the ion pairing of the first and second TBA^+ cation with the anion. For all the electrolytes: $M_{added\ salt} + M_{TBAP} = 0.50$ M.

5.5 DFT calculations

Preliminary work has been done using DFT calculations to understand the solvation of the C_{60} anions with $BMIm^+$ and Am^+ cation (for simplicity, TBA^+ was used instead of the ethyldimethylpropylammonium cation). The ΔG_{disp} could be calculated from the disproportionation reactions. Where Cat^+ is the cation of the salt:

$$2\ Cat^+C_{60}^- \rightarrow C_{60} + (Cat^+)_2C_{60}^{2-}$$

$$2\ (Cat)_2C_{60}^{2-} \rightarrow (Cat^+)C_{60}^- + (Cat^+)_3C_{60}^{3-}$$

Using this value, the ΔE_{12} and ΔE_{23} values could be theoretically calculated. The changes in the ΔE_{12} and ΔE_{23} values without ion pairing (but solvated) to the values with ion pairing is shown in *Table 14*. Ion pairing of reduced species with Na^+ cations resulted in stabilization of ΔE_{12} and ΔE_{23} by 268 and 203mV, respectively. Interestingly, a larger stabilization was observed for $BMIm^+$ (238 and 228 mV) and TBA^+ (359 and 267 mV) cations, as one would expect less interaction of reduced species with big cations compared to the small acidic Na^+ cation. Such stronger interactions could be due to significant hydrogen bonding contribution. Hydrogen bonding of reduced species with imidazolium cation was reported in literature.[65] In the case of the dianion and trianion, particularly, such hydrogen-bonding network may be a template of clusters formation of cations around the reduced species. In comparing the difference between ion pairing by $BMIm^+$ with Am^+, the tetraalkylammonium ion was able to reduce the ΔE_{12} value by 121 mV and the ΔE_{23} value by 39 mV. Comparing the experimental ΔE_{12} and ΔE_{23} with the same acceptor numbers, we obtain differences of 30 and 48 mV, respectively. The predicted stabilization overestimated the ΔE_{12} value, while the ΔE_{23} value was reasonably close to predicted value. The better correspondence with the ΔE_{23} as compared to the ΔE_{12} values was probably due to the stronger ion pairing with the more negatively charged species. In both cases, better stabilization was observed for the more flexible tetraalkylammonium ion with the spherical C_{60} species, than with the planar $BMIm^+$ cation (*Figure 107*). More detailed calculations are needed to account for the presence of the anion in the cluster in order to simulate the more realistic nano-domains that are present in the RTIL solutions. The absence of the counter anions is probably the source of the underestimation of the ΔE values, as compared to the experimental values.

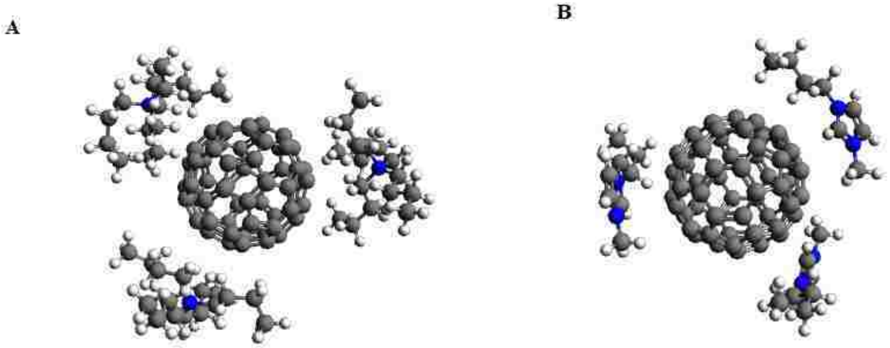

Figure 107: Structures of $(TBA^+)_3C_{60}^{3-}$ *(A) and* $(BMIm^+)_3C_{60}^{3-}$ *(B) used in DFT calculation.*

Table 14: Effect of ion pairing on calculated disproportionation energies

DFT: m06/6-31G	No ion paring		Na^+		$BMIm^+$		TBA^+	
	First	Second	First	Second	First	Second	First	Second
Δ***G*** (kJ/mol)	65.21	44.45	39.39	24.86	42.25	22.50	30.61	18.73
Δ***E*** (V)	0.676	0.461	0.408	0.258	0.438	0.233	0.317	0.194

5.6 Mass transport vs viscosity

In order to evaluate the effect of nano-domains on the transport properties of the mixtures solution, variations of C_{60} diffusion were compared with changes in viscosity of mixtures. The diffusion coefficient ratios were calculated based on the peak current for the first wave in benzonitrile/RTIL mixtures. The current in cyclic voltammetry at a macro-electrode is proportional to the square root of the diffusion coefficient:

$$i_{p,BzCN} = \text{constant x } D_{BzCN}^{1/2} = \text{constant}/\eta_{BzCN}^{1/2}$$

$$i_{p,mixture} = \text{constant x } D_{mixture}^{1/2} = \text{constant}/\eta_{mixture}^{1/2}$$

Therefore,

$$\frac{D_{mixture}}{D_{BzCN}} = \left(\frac{i_{p,mixture}}{i_{p,BzCN}}\right)^2 = \frac{\eta_{BzCN}}{\eta_{mixture}}$$

As shown in *Figure 108*, the viscosity ratio of the solution ($\eta_{BzCN}/\eta_{mixture}$, red line) decreased in an exponential manner as a function of the %AmNTf$_2$. The diffusion coefficient ratios of C_{60} though decreased much more modestly, indicating that the change in diffusion kinetics was not inversely proportional to the change in viscosity. One way to envision this non-proportionality between diffusion and viscosity would be through the preferential solubility of C_{60} in nano-domains of mixtures. As the neutral C_{60} is poorly soluble in the RTILs, it will be expected to partition mostly into benzonitrile nano-domains of the mixed solvent. In mixtures, diffusion of C_{60} would be exclusively through the molecular solvent domains, which will probably have a micro-viscosity less than the measured viscosity.

Assuming that the obstruction of the diffusion by the RTIL nano-domains is proportional to the %RTIL, the diffusion of C_{60} through the benzonitrile nano-domains would be proportional to % benzonitrile: $D_{mixture} = D_{BzCN}$ x %BzCN. This relationship reasonably predicted the diffusion coefficient ratios for the RTIL/benzonitrile mixtures better than the viscosity for at least mixtures up to 20%. Above 50% $AmNTf_2$, C_{60} ceases to be soluble in the solution, and the current abruptly drops to near zero.

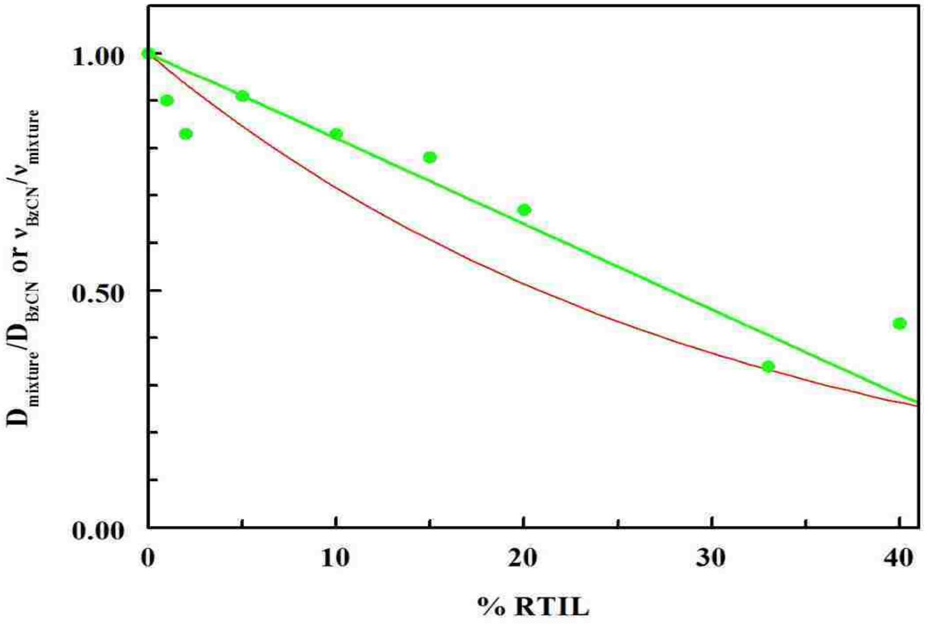

Figure 108: Variation of viscosity of the solution at a function of %$AmNTF_2$ (red line), normalized to the viscosity of benzonitrile at 25°C. The green filled circles are the ratio of the diffusion coefficients between the RTIL mixtures and pure benzonitrile based on the first peak current. The green line is the best fit to the ratio of $D_{mixture}/D_{BzCN}$.

5.7 Spectroelectrochemistry

In order to evaluate the effect of RTIL on the electronic structures of C_{60} redox products, UV-visible and NIR spectroelectrochemistry of C_{60} was carried out in benzonitrile and mixed RTIL/benzonitrile solution.

5.7.1 UV-visible Spectroelectrochemistry

The UV-visible spectroelectrochemistry of C_{60} in benzonitrile showed spectral features of reduced species, with λ_{max} values of 332 (330), 338 (339), 340 (340) and 340 nm for C_{60}, C_{60}^{-}, C_{60}^{2-} and C_{60}^{3-} (*Figure 109*). These features were consistent with the work of Dubois et al.[88]

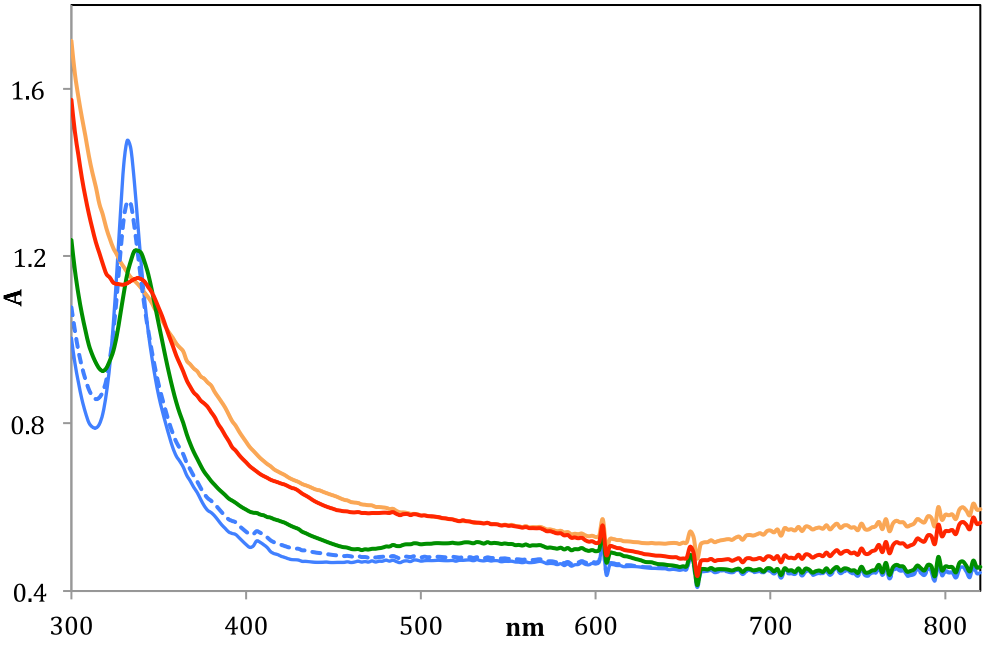

Figure 109: UV-vis spectroelectrochemistry of C_{60} in benzonitrile C_{60} (blue), C_{60}^{-} (Green), C_{60}^{2-} (Red) and C_{60}^{3-} (Orange). Dashed blue line is the final spectrum after reoxidation.

The reduction waves were well separated, making it easier to extract spectra of the fullerides. Upon reduction, the spectra became broader with a new shoulder appearing around 380 nm and a broad band in the 700-800 nm regions.

Electrolysis in 20% BMImPF$_6$/benzonitrile showed very similar behavior with some small differences (*Figure 110*). For C$_{60}$, the spectra were identical in benzonitrile and 20% BMImPF$_6$, consistent with the poor solubility of C$_{60}$ in RTILs nano-domains. The spectra of reduced species show some differences between benzonitrile and 20% RTIL mixture. In the mixture, the bands were blue shifted, with λ_{max} C_{60}^{-}: 334 (338), C_{60}^{2-}: 336 (340), C_{60}^{3-}: 338 (340) nm (in benzonitrile), and sharper than for pure benzonitrile. These small shifts in the UV-visible were difficult to interpret and a need to look at longer wavelengths in the near infrared region was essential.

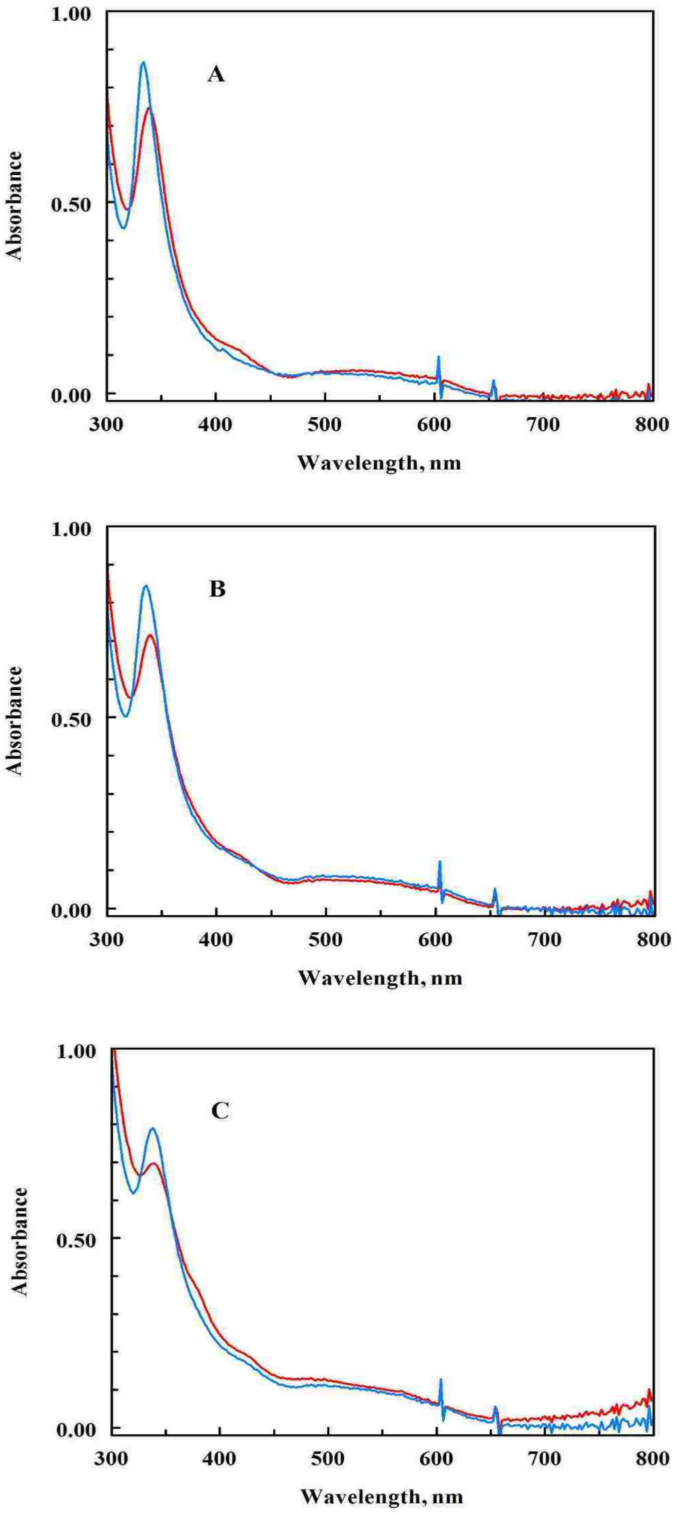

Figure 110: UV-vis spectra of C_{60}^{-} *(A),* C_{60}^{2-} *(B) and* C_{60}^{3-} *(C) in benzonitrile (Red), 20%BMImPF*$_6$ *(Blue).*

5.7.2 Near-IR Spectroelectrochemistry

Figure 111 shows NIR spectra of C_{60} electrolysis at the reduction potentials of the first three waves in benzonitrile. Because the starting material doesn't exhibit any significant spectral feature in the NIR region, its spectrum was subtracted from other spectra. Spectral features of reduced species C_{60}^{-} (936, 1006 and 1082nm), C_{60}^{2-} (841, 954, 1318nm) and C_{60}^{3-} (791, 879, 956, 1372nm) were consistent with reported values.[103]

Electrolysis in 33%$AmNTF_2$ revealed important changes on the absorbance spectra of reduced species (*Figure 112*). The reduction was reversible in electrolysis time scale as shown by the complete bleaching of spectral features in the final spectrum.

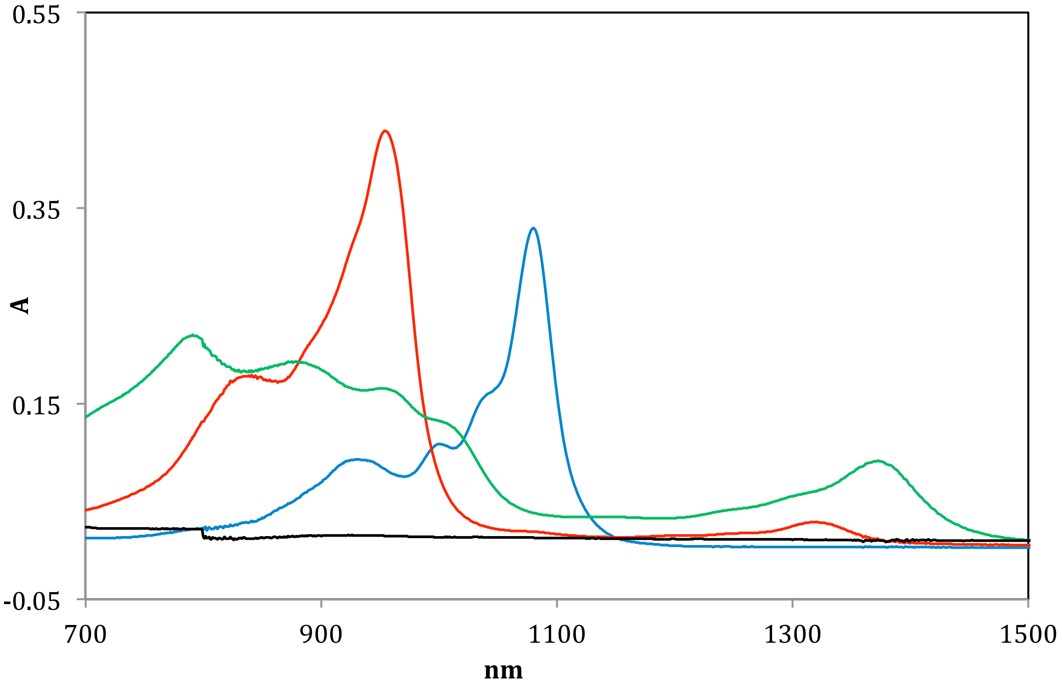

Figure 111: NIR spectroelectrochemistry of C_{60} in benzonitrile, C_{60}^{-}(blue), C_{60}^{2-}(Red), C_{60}^{3-} (Green) and background (black)

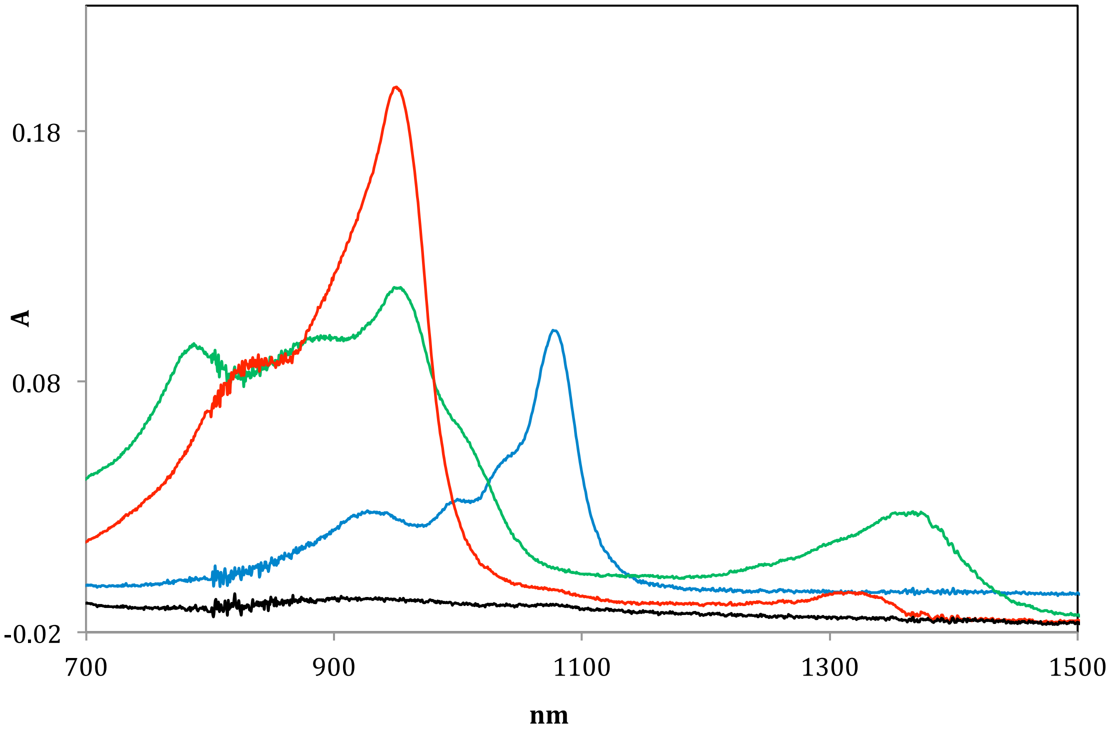

Figure 112: NIR spectroelectrochemistry of C_{60} *in 33%AmNTF*$_2$ C_{60}^{-}*(blue),* C_{60}^{2-}*(red),* C_{60}^{3-} *(Green) and background (black)*

Comparison of individual spectra of reduced species obtained in benzonitrile and 33%AmNTF$_2$ mixture enabled the evaluation of the effect of RTIL on the absorption spectra. The C_{60}^{-} (*Figure 113*: 936, 1005 and 1076nm) and C_{60}^{2-} (*Figure 114*: 836, 950, 1318nm) spectra were fairly similar to observed ones in benzonitrile, with minimal shifts in the presence of the RTIL.

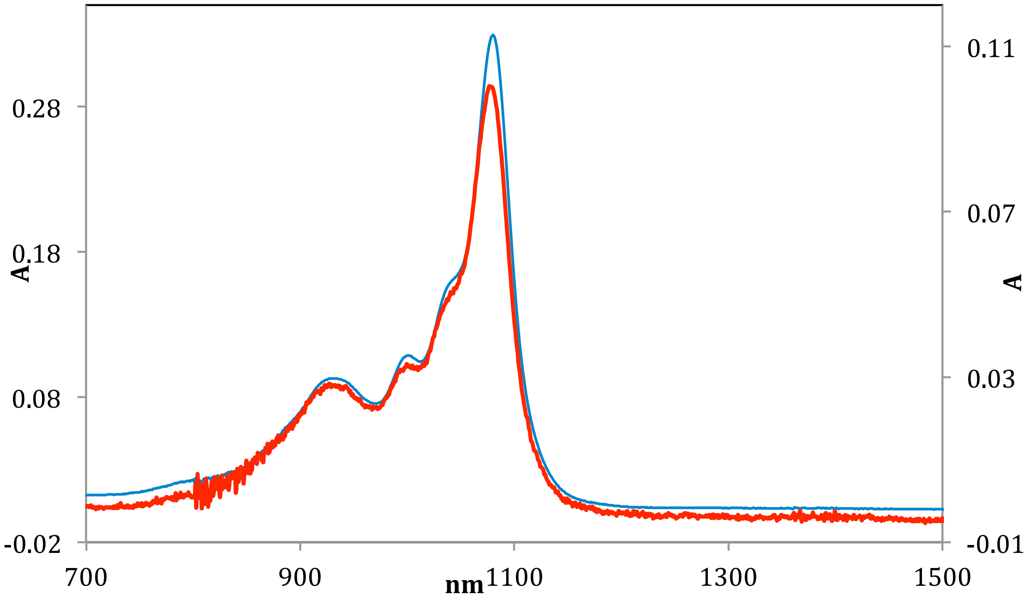

Figure 113: NIR spectra of C_{60}^{-}: benzonitrile (blue), 33%AmNTF$_2$ (Red).

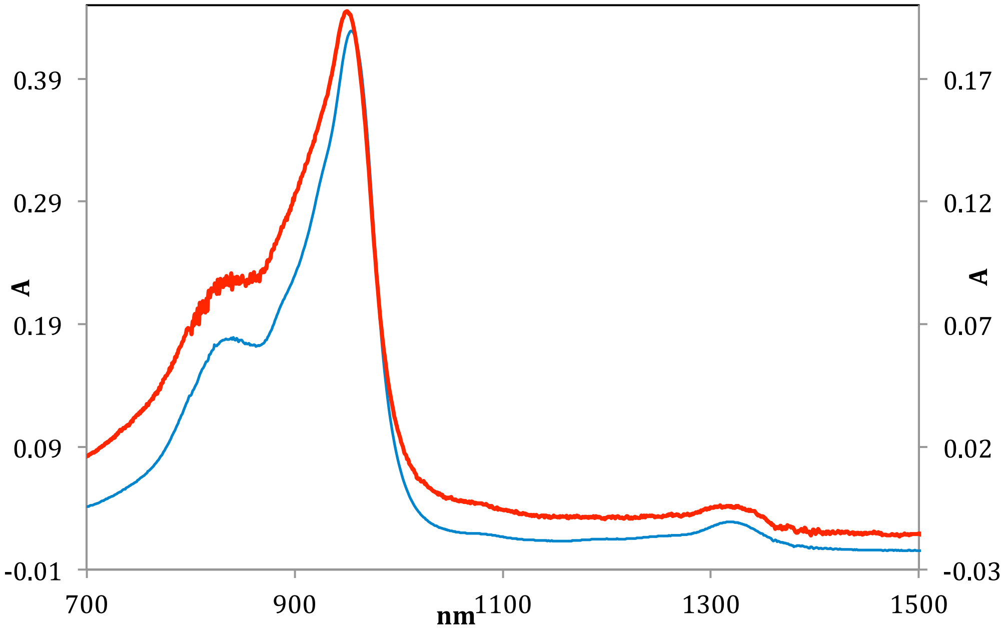

Figure 114: NIR spectra of C_{60}^{2-}: benzonitrile (blue), 33%AmNTF$_2$ (Red).

The presence of the RTIL had an important impact on the trianion C_{60}^{3-} spectrum (787, 878, 951, 1368nm). While the shifts in the λ_{max} values were relatively small (956 to 951 nm, 791 to 787 nm, 878 nm band became a shoulder), the molar absorptivity changed significantly with 951 nm band having the strongest absorbance, as compared to the 791 nm band in benzonitrile alone (*Figure 115*). The 1368 nm band appeared to be blue-shifted, but the overlap with the solvent/electrolyte made it difficult to measure accurately. These results were consistent with the voltammetric data, where the strongest interaction in the voltammetry was observed between the RTIL nano-domains and C_{60}^{3-}. Similarly the most significant changes in the visible/near infrared spectra were observed with the C_{60}^{3-} spectrum.

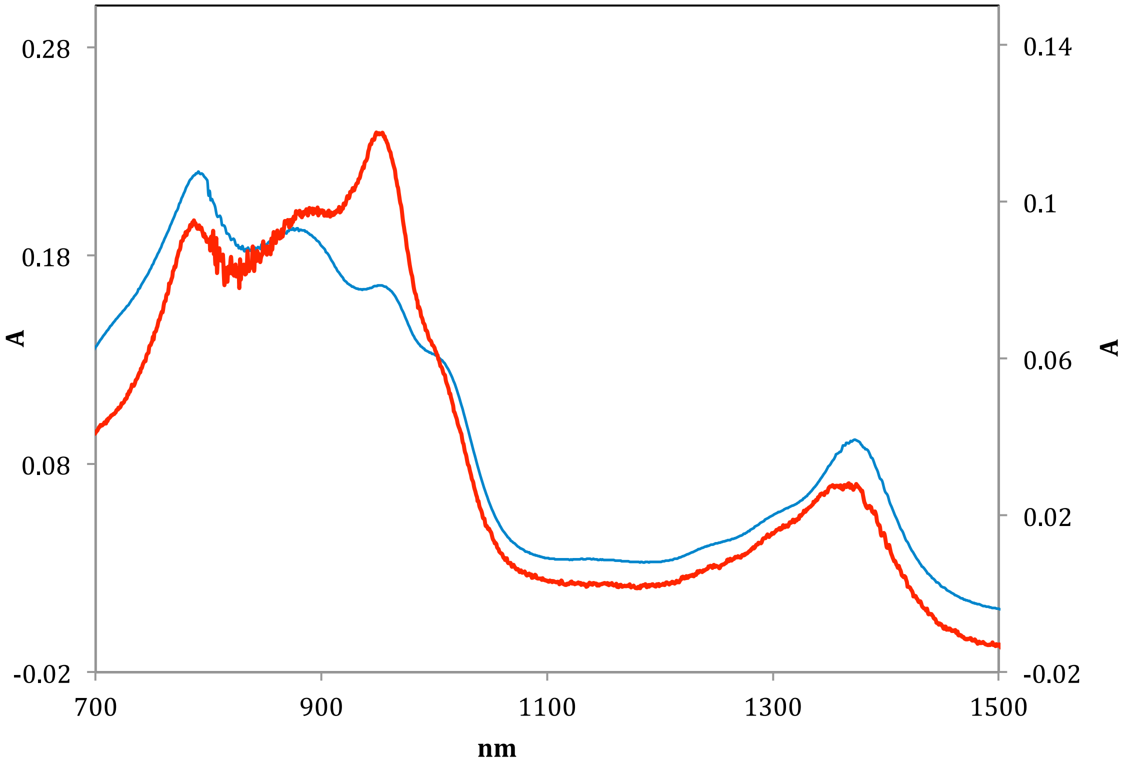

Figure 115: NIR spectra of C_{60}^{3-}: benzonitrile (blue), 33%AmNTF$_2$ (Red).

5.8 Summary

The electrochemistry of fullerene C_{60} was successfully investigated in mixed benzonitrile-RTIL solvents. The spherical structure of fullerides was able to highlight further aspects of RTIL interactions with redox products. Large stabilization was observed for the trianion compared to anion and dianion, upon introduction of RTIL in the mixture solutions.

Correlation of potential shifts with Gutmann acceptor number of solvents allowed the deconvolution of the ion-paring interactions from structural effects of RTILs in the mixtures solutions. At lower concentrations of the RTIL, the redox potentials in the mixed solvents were correlated well with the Gutmann acceptor number. At higher RTIL concentrations, the shifts exceeded the amounts expected from the stabilization for the redox products on the basis of Gutmann acceptor numbers. This effect was more clear in the curvature of ΔE_{23} as a function of AN, which was observed at higher concentrations of RTIL. Higher stabilization was observed for $AmNTF_2$ as compared to $BMImPF_6$ or $BMImBF_4$, mainly due to flexibility of the alkyl chains of the AmN^+ cation, leading to a stronger aggregation around the reduced species. This higher stabilization with ammonium compared to imidazolium cations, was also predicted by DFT calculations of clustering cations around the reduced species. One major aspect of RTIL nano-clusters is its ability to act as a single unit rather than successive ion pairing as observed for non-RTIL salts.

The insolubility of starting material C_{60} in RTILs was a key feature which highlighted a unique physical characteristic, local versus bulk viscosity of mixture solvents. Subtle change in diffusion coefficients compared to the viscosity of the mixture was consistent with the structural effects of RTILs on the transport properties in mixtures. The insolubility of C_{60} in RTILs led to a preferential solvation within molecular domains, which resulted in an enhancement of diffusion kinetics, beyond what would be expected by the increase in the viscosity of the more rich RTIL mixtures. Finally, UV-visible and NIR spectroelectrochemical analyses showed significant effects of the RTIL nano-domains on the electronic structures of fullerides, especially on the trianion.

The impact of RTIL nanodomains on the electrochemistry of fullerenes may have more interesting implications on the chemistry of other fullerene types. Endohedral fullerene with non-isolated pentagon rule (non-IPR) cage such as $Sc_2S@C_{72}$ have been reported by Chen et al.[147] It was demonstrated that the non-IPR structure of the cage is stabilized by strong ion pairing of the host-guest, leading to the transfer of four electrons from the cluster to the cage. The electronic configuration was then predicted as an ionic structure $(Sc_2S)^{4+}@(C_{72})^{4-}$. As a result of the establishment of a negative charged on the surface of the fullerene cage, the solubility of the fullerene is expected to improve in RTILs. Hence, introduction of RTIL into a molecular solution of $(Sc_2S)^{4+}@(C_{72})^{4-}$ would result in strong interactions with RTIL cations, leading to significant partitioning of the endohedral solute into RTIL domains in the mixture solution. As a result of this partitioning, the electronic configuration of the solute may change. This can be directly probed by UV-visible-NIR spectroscopy. In other words, the change of the electronic structure of the non-IPR endohedral upon strong interactions with RTIL would represent a further evidence of the internal charge transfer between the cluster and the fullerene cage.

Chapter 6 Spectroelectrochemical and Voltammetric Study of Nickel Porphyrins in THF-RTILs Mixtures

In the previous studies, investigation of RTIL effects on the redox products has been mainly directed toward the effects on the electrogenerated anions. As introduced in Chapter 1, few works have been dedicated to study the interactions of positively charged species with RTILs.

The goal of this work is the evaluation of the effect of RTILs on oxidation/reduction processes of Ni(OEP) and Ni(OEPone) (*Figure 116*) and the assessment of the ability of RTILs to interact with cationic and anionic substrates. Voltammetry of nickel(II) octaethylporphyrin (NiOEP) exhibits two reductions and two oxidations waves that would fit within the RTILs electrochemical windows. FTIR spectroelectrochemistry was additionally carried out on Ni(OEPone) in order to study the interaction of metalloporphyrins with the RTIL nano-domains.

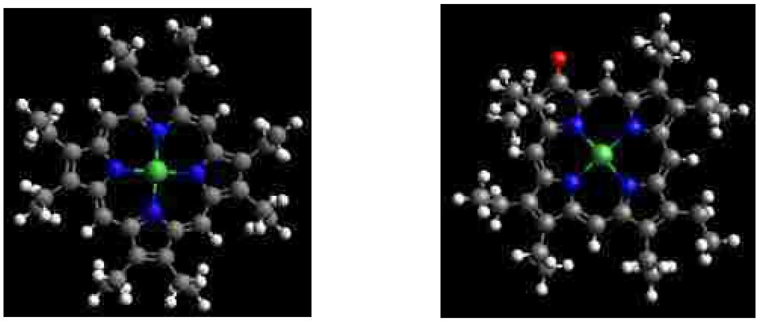

Figure 116: NiOEP (left) and NiOEPone (right) structures

6.1 Electrochemistry of Ni(OEP)

6.1.1 Cyclic voltammetry

The cyclic voltammetry of Ni(OEP) in pure THF is shown in *Figure 117*. Four reversible waves were observed under the conditions of the experiment: two reversible reduction waves at -1.75 and -2.47 V, and two oxidation waves at +0.54 V and +0.79 V versus Ag/AgNO$_3$. These potentials were in agreement with reported values in molecular solvents by Kadish.[110]

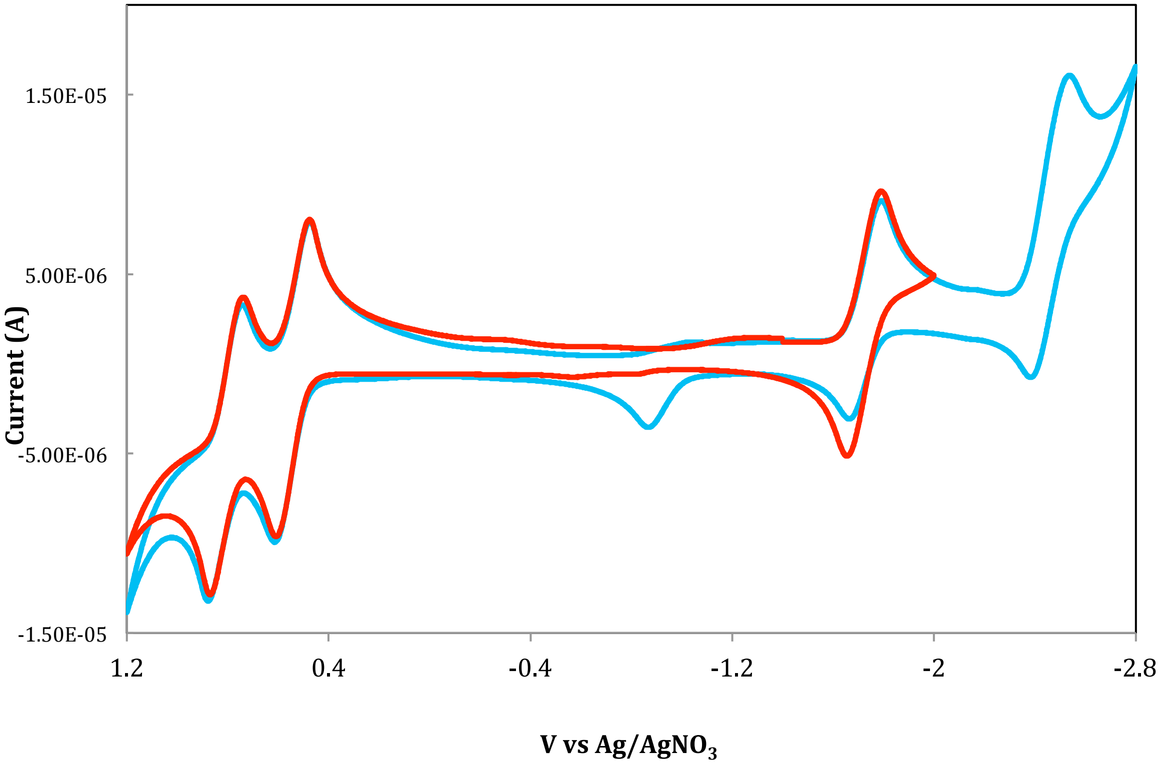

Figure 117: Cyclic voltammetry of NiOEP in THF/0.10 M TBAP. Scan rate = 100 mV/s.

$E_{initial}$ = -1.40 V, initial scan is negative.

The product of the second reduction was not completely stable on the voltammetric time scale, and an additional oxidation peak was observed on the reverse scan. When the potential was reversed after the first wave, this new oxidation peak was not observed. Such processes, which may be due to a decomposition product, were reported previously by Kadish et al. for nickel porphyrins reductions.[110] The study of this reaction was beyond the scope of the present investigation, but the second wave was chemically reversible enough to measure the $E_{1/2,2}$ for the reduction.

Figure 118 shows cyclic voltammetry of NiOEP in THF and 33%$BMImPF_6$ mixture. In this mixture, the second reduction wave disappeared at only 5% RTIL. This is very likely due to decomposition (deprotonation) of $BMIm^+$ cation at very negative potentials, which narrowed the electrochemical window of this RTIL. Addition of the RTIL led to significant stabilization of the first reduction wave to more positive potentials, while smaller shifts of the oxidation waves were observed in the mixtures.

The cyclic voltammetry of Ni(OEP) in mixtures of THF/$AmNTF_2$ is shown in *Figure 119*. In these mixtures, the four waves could be observed, indicating higher stability of the ammonium ionic liquid compared to the imidazolium at very negative potentials. In the presence of $AmNTF_2$, the two oxidation waves were shifted to more negative potentials, but larger shifts in the positive direction were observed for the reduction waves, especially the second wave. The two oxidation potentials shifted about the same amount as was observed for $BMIMPF_6$, and a significantly larger shift was seen for the first reduction wave. The shifts were comparable in both RTILs.

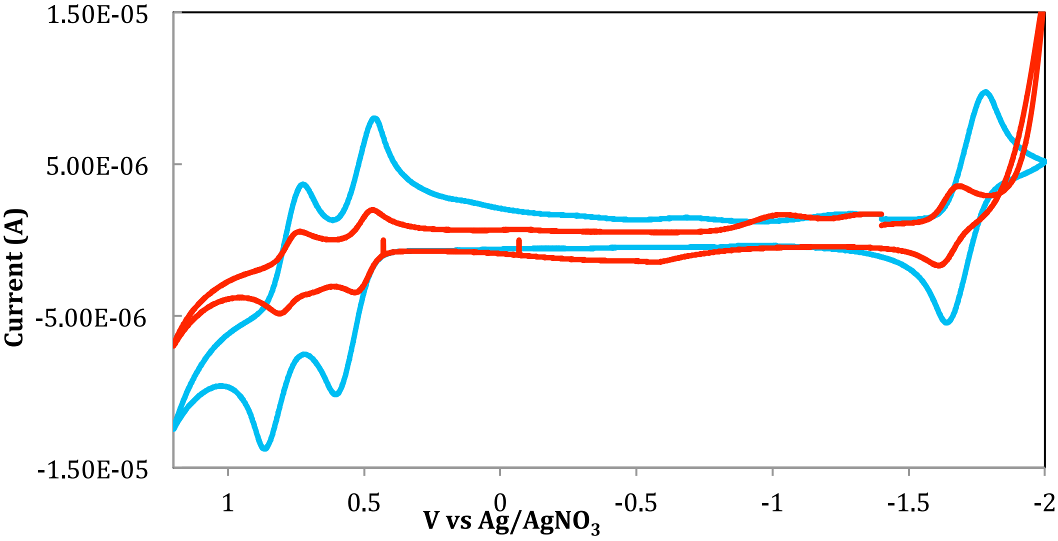

Figure 118: Cyclic voltammetry of NiOEP in THF- and 33%BMImPF$_6$ mixtures. Scan rate = 100 mV/s. E$_{initial}$ = -1.40 V, initial scan is negative.

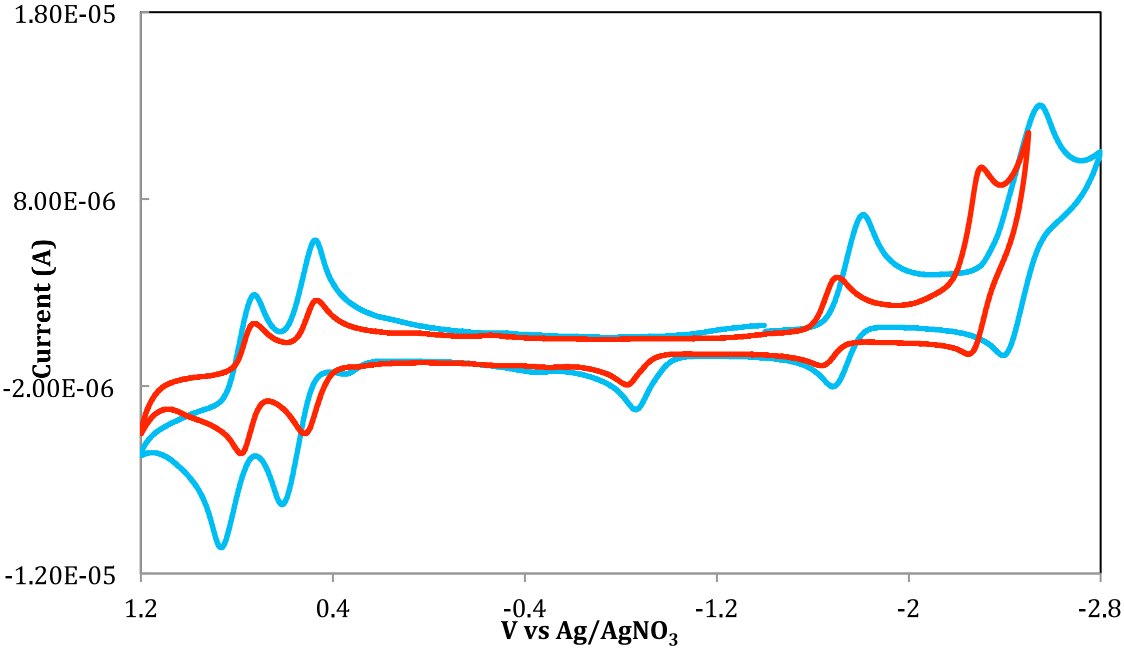

Figure 119: Cyclic voltammetry of NiOEP in THF and 33%AmNTF$_2$ mixtures. Scan rate = 100 mV/s. E$_{initial}$ = -1.40 V, initial scan is negative.

The shifts in the second oxidation (E_{Ox2}) and the first reduction (E_{Red1}), compared to first oxidation potential (E_{Ox1}), as a function of $BMImPF_6$ fraction are shown in *Figure 120*. While the shifts in the potentials were large for the reduction wave, the difference between the two oxidation waves was almost independent of %RTIL. These shifts would not be completely due to changes in the reference potential (E_{Ox1}), as the oxidation waves and the reduction waves shifted in opposite directions (the ΔE values were plotted so that values were positive). This indicated that the RTIL stabilized the reduced species, while there was no additional stabilization of the dicationic species in the RTIL.

In the case of $AmNTF_2$, the absolute difference between the two reduction and oxidation waves were plotted in *Figure 121*. Because these were differences in two potentials, possible shifts in the reference potential were minimized. The differences in oxidation potentials were nearly independent of %$AmNTF_2$ as was seen for $BMImPF_6$. Interestingly, the reduction potential differences showed a large stabilization of the dianionic species by the RTIL.

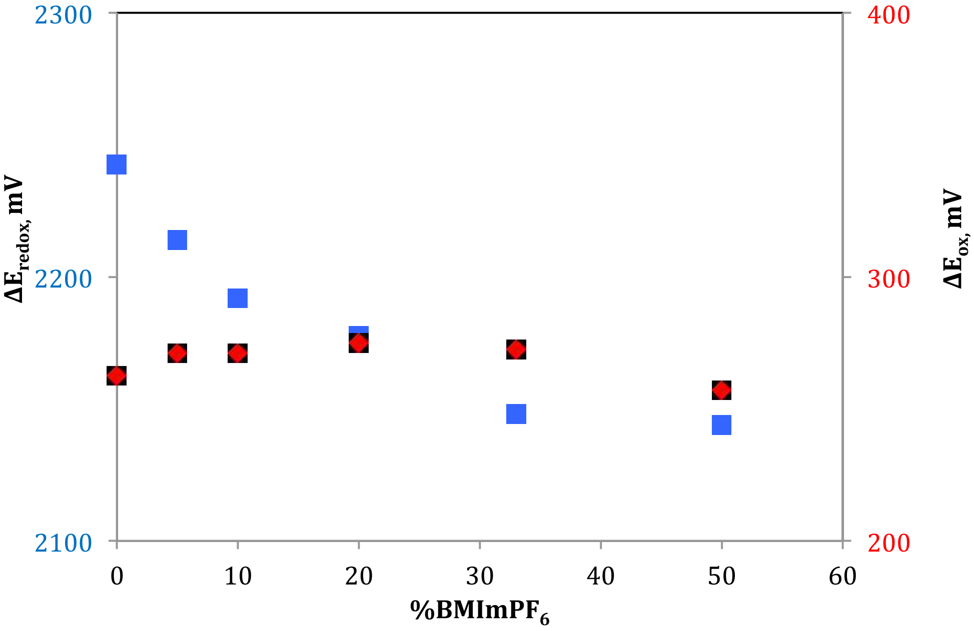

Figure 120: Potential difference values for Ni(OEP) in THF/BMIMPF$_6$ mixtures as a function of %RTIL. Red diamonds: ΔE_{12} oxidation; blue squares: $\Delta E_{redox} = E_{1Ox} - E_{1Red}$

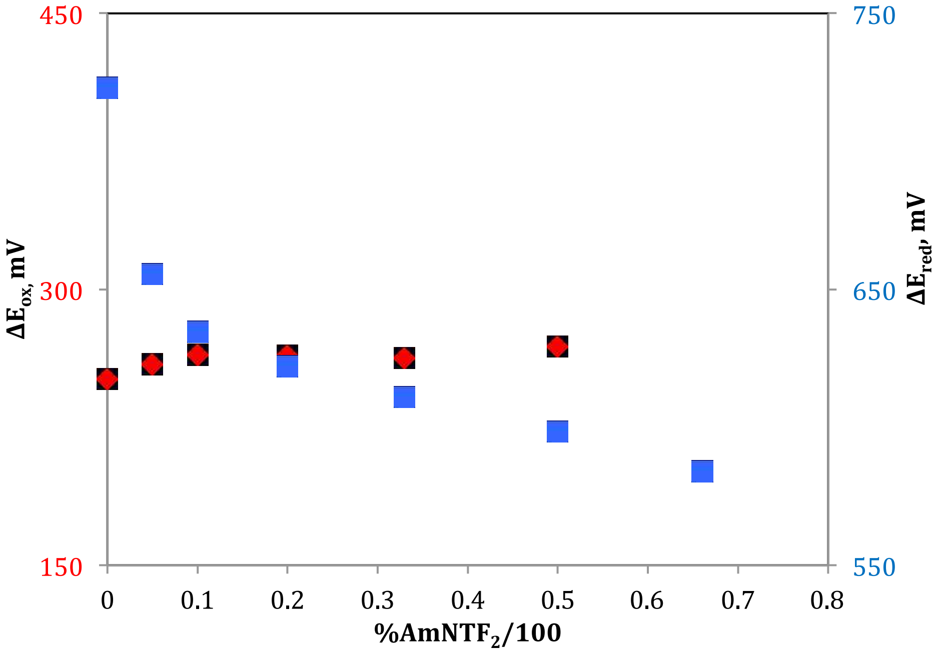

Figure 121: Potential difference values for Ni(OEP) in THF/AmNTF$_2$ mixtures as a function of %RTIL. Red diamonds: ΔE_{12} oxidation; blue squares: ΔE_{12} reduction

6.1.2 Potential shifts vs Gutmann AN

As was addressed in the previous chapter, a more direct measure of the ability of the mixtures to solvate the electroactive species is the Gutmann acceptor number (AN). The Gutmann AN of THF-RTILs mixtures were measured as described earlier. The relationship between the Gutmann AN and the %RTIL was non-linear, as shown in *Figure 122* for mixtures of THF and $AmNTF_2$ or $BMImPF_6$.

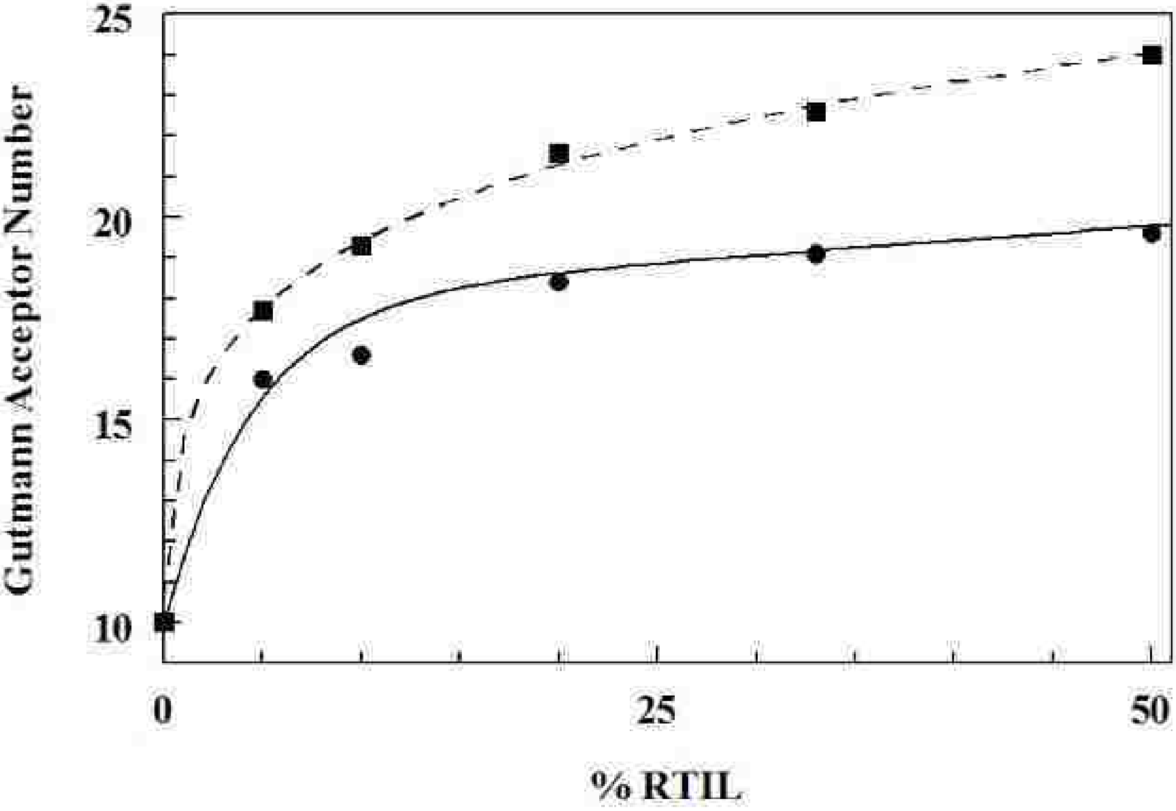

Figure 122: Variation in the Gutmann Acceptor number as a function of %RTIL.

AmNTF₂: •, solid line. BMImPF₆: ■, dashed line.

As with previous studies, the potentials shifts were referenced to DmFc$^+$/DmFc reference system. Because the Gutmann AN of pure THF was quite far from the mixtures, only observed potentials in the mixtures were considered. While this exclusion did not affect the trend of potential shifts, it enabled to obtain better correlation factor (R^2) of the linear relationships. This approach was essential for an accurate comparison of the shifts of oxidation and reduction processes in mixture solvents. *Figure 123* shows the $E_{1/2}$ values for Ni(OEP) in mixtures of THF with $AmNTF_2$ and $BMImPF_6$ as a function of the Gutmann AN.

In these mixtures, the potential shifts were linearly correlated with the acceptor properties of the mixtures. The reduction waves were shifted to more positive potentials with the addition of the RTILs. Higher shifts were observed for the second reduction (slope of 0.049 V/AN) compared to the first wave (slope of 0.032 V/AN for $AmNTF_2$ and 0.021 V/AN for $BMImPF_6$). Interestingly, the oxidation waves were shifted to more positive potentials with the increase of Gutmann AN. In contrast to reduction processes, the shifts were comparable in both first (0.014 V/AN for $AmNTF_2$ and 0.012 V/AN for $BMImPF_6$) and second (0.015 V/AN for $AmNTF_2$ and 0.01 V/AN for $BMImPF_6$) oxidation waves, for the same RTIL. For both reduction and oxidation processes, larger slopes were observed for ammonium compared to imidazolium mixtures.

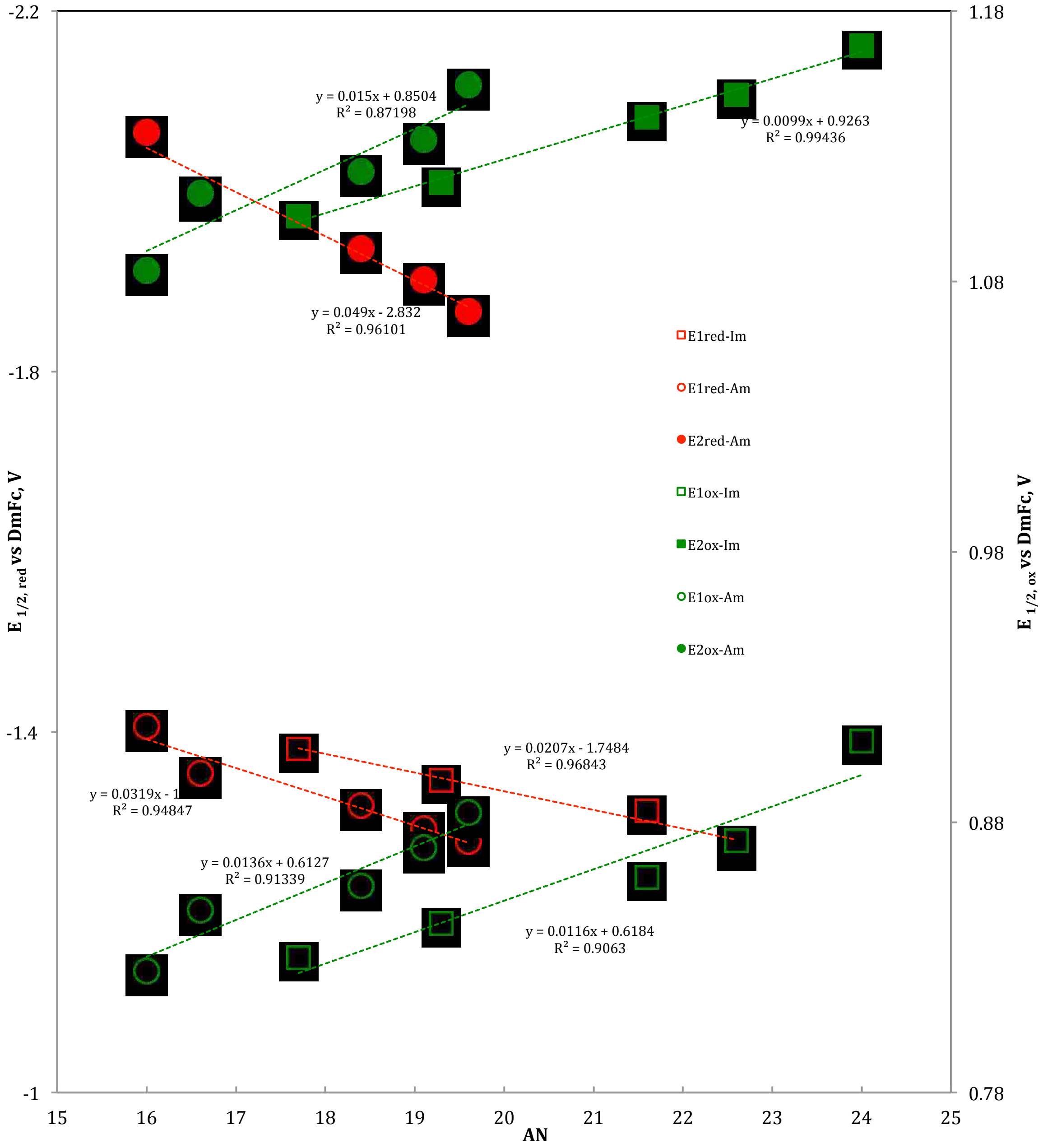

Figure 123: $E_{1/2}$ values for Ni(OEP) in THF/RTIL mixtures as a function of the Gutmann AN. Red symbols/lines are for the reduction waves; green symbols/lines are for the oxidation waves. Open symbols are the first wave; closed symbols are the second wave. $AmNTF_2$: circles; $BMImPF_6$: squares.

As was observed for other redox systems, stabilization of the reduction waves by the RTIL was expected, due to strong interactions of the negatively charged products with RTIL cations. This is consistent with the partitioning of reduced species into RTIL nano-domains in the mixture. For similar AN mixtures, the higher ability of the ammonium cation to solvate the reduced species led to better stabilization of the reduced species compared to imidazolium cation. The large shifts of the oxidation waves to more positive potentials indicated a strong repulsion between the oxidized species and RTIL components. This repulsion was more pronounced in the $AmNTF_2$ as compared to $BMImPF_6$ mixtures.

From these results, it was quite apparent that, while reduction products were solvated by RTIL domains, the oxidation products were very likely partitioned into the molecular solvent domain in mixture solutions. Moreover, the cation identity had a significant effect on the extent of these interactions. In comparison to the imidazolium cation, the ammonium cation showed a stronger interaction with reduced products and larger repulsion toward oxidized products. Trends for stronger interactions, going beyond the AN, could also be detected at higher RTIL fractions.

This effect became clearer when the shifts were examined using the difference between the first and second waves ($\Delta E_{12} = E_1 - E_2$) as a function of the Gutmann acceptor number. The results are shown in *Figure 124* for both RTILs (the second reduction wave was not observable for $BMImPF_6$). For $\Delta E_{12,\,red}$, the difference decreased linearly (slope = -17.1 mV/AN) as the Gutmann acceptor number increased. This result was consistent with significantly higher solvation of the dianion by the RTIL as compared with the mono-anion.

On the other hand, the $\Delta E_{12,\ ox}$ had a positive slope as expected, showing that the dication was less stabilized than the mono-cation in higher Gutmann AN solutions. The slope though was quite small (1.5 mV/AN for $AmNTF_2$ and 0.9mV/AN for $BMImPF_6$), showing relatively comparable repulsion of the cation and dication with the RTIL in mixed solutions.

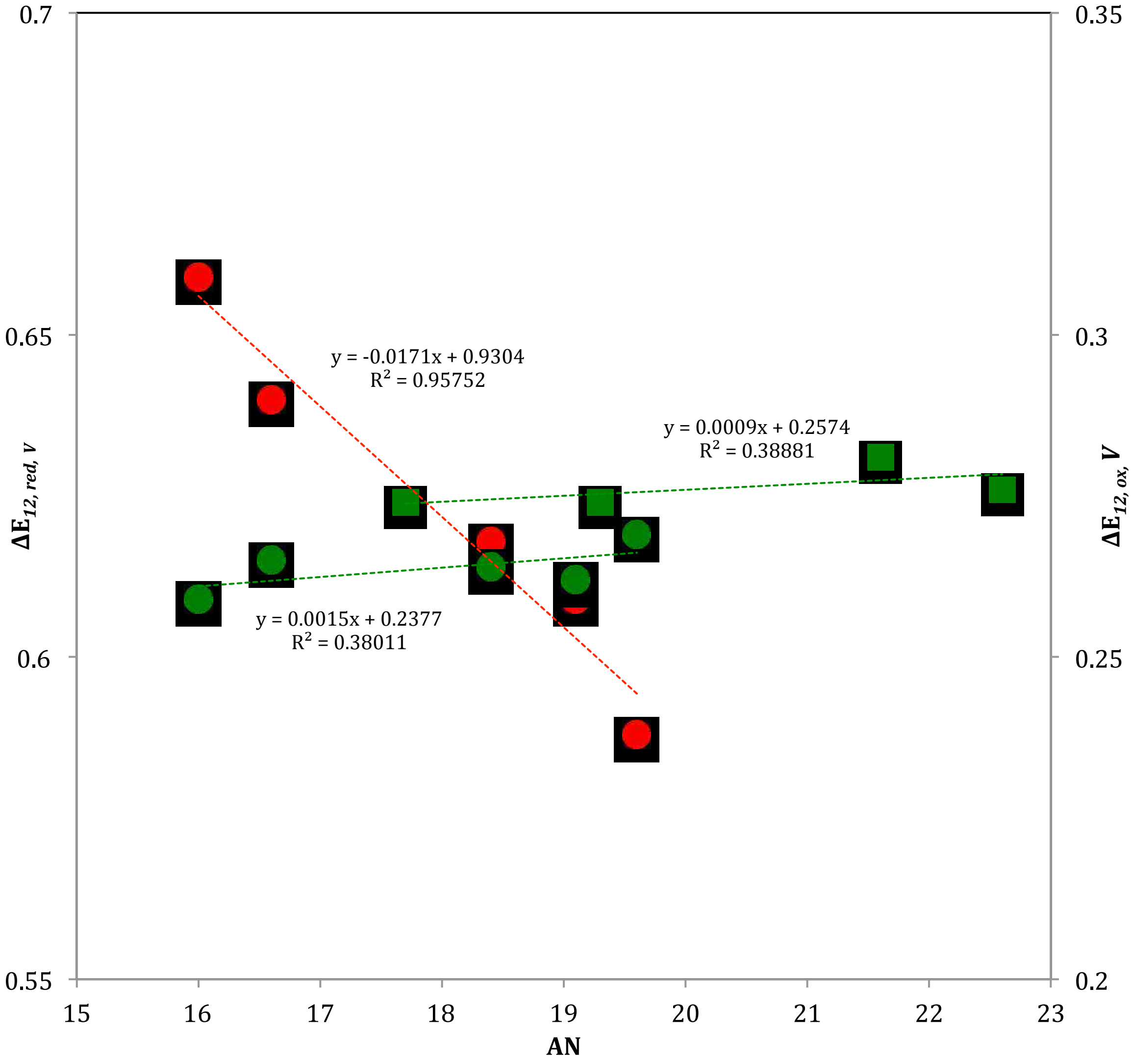

Figure 124: ΔE_{12} values versus AN for the reduction (red) and oxidation (green) for the voltammetry of Ni(OEP) in THF/RTIL mixtures. Squares: $BMImPF_6$ and Circles: $AmNTF_2$.

6.1.3 Diffusions in THF-RTILs

Similar to the previous study in benzonitrile-RTILs mixtures, the changes of diffusion coefficient were compared with the variation in solution viscosity in THF-RTILs mixtures. The results are shown in *Figure 125*. The viscosity ratios were also plotted on the graph. The viscosity ratios for both $AmNTf_2$ and $BMImPF_6$ were nearly identical for solutions that were mostly molecular solvents (even at 50% RTIL, the mole fraction of RTIL was around 0.22). Up to about 50% RTIL, the diffusion coefficient ratios were larger than the viscosity ratio, but trended to the same values for high concentration of the RTIL. This indicated that the diffusion was faster than predicted by the Stokes-Einstein equation for mixtures where the %RTIL was less than 50%. Unlike the viscosity ratio which followed an exponential relationship, the diffusion coefficient ratio decreased linearly with %RTIL. As with the viscosity ratios, the diffusion coefficient ratios depended on the %RTIL and not the identity of the RTIL.

These results were consistent with the presence of molecular solvent and RTIL domains within the mixed solvent systems and that the electroactive species diffuses mostly within the molecular solvent region. The results parallel the voltammetry of C_{60} in benzonitrile/$AmNTf_2$ seen in the previous chapter. The dashed line in the figure is a linear fit to the data.

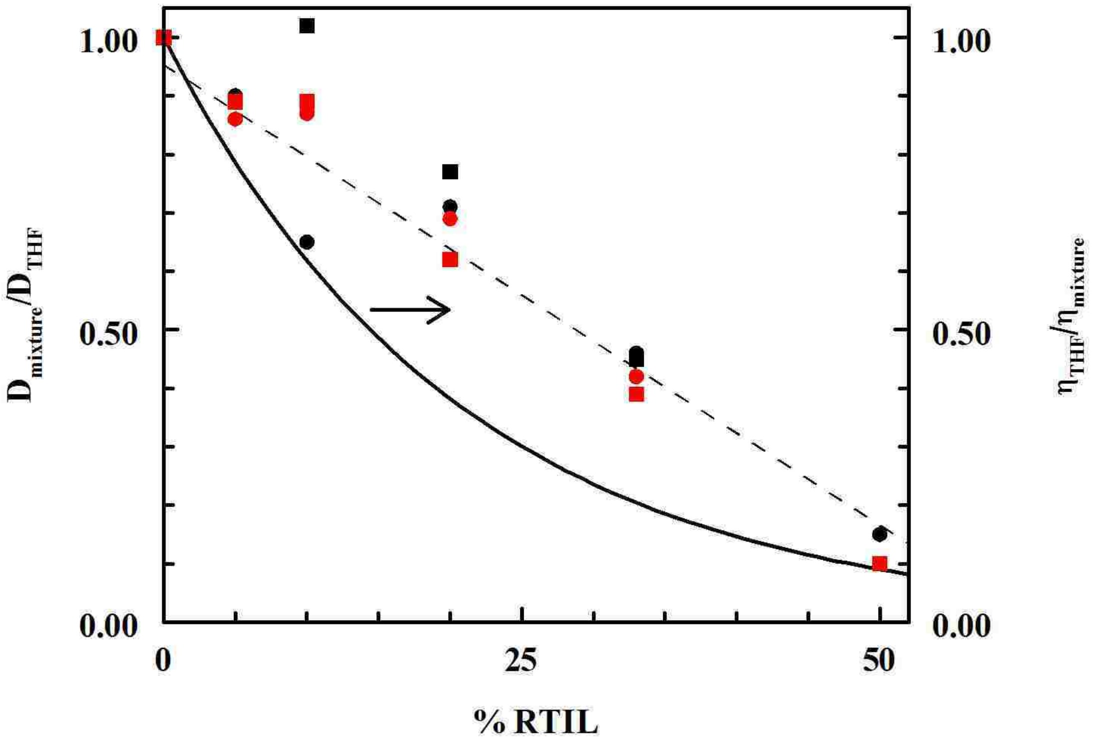

Figure 125: Plot of the viscosity ratio/diffusion coefficient ratio as a function of %RTIL. The viscosity and diffusion coefficients are normalized to the values in THF. Line is the viscosity ratio ($\eta_{THF}/\eta_{mixture}$). Diffusion coefficient ratios: Ni(OEP) first reduction couple ($AmNTF_2$: •, $BMImPF_6$: •), Ni(OEPone) first reduction couple ($AmNTF_2$: ■, $BMImPF_6$: ■)

6.1.4 UV-visible Spectroelectrochemistry

The UV-visible spectroelectrochemistry was carried out for the first reduction and the two oxidation waves in THF. The first reduction product Ni(OEP)$^-$ in THF gave the same spectrum as previously reported in literature (*Figure 126*). This species has been previously described by Lexa et al. as a Ni(I) complex.[122] The reoxidation scan allowed for the complete recovery of the Ni(OEP) spectrum. The instability of the product of the second wave precluded the acquisition of a spectrum for the two electron product.

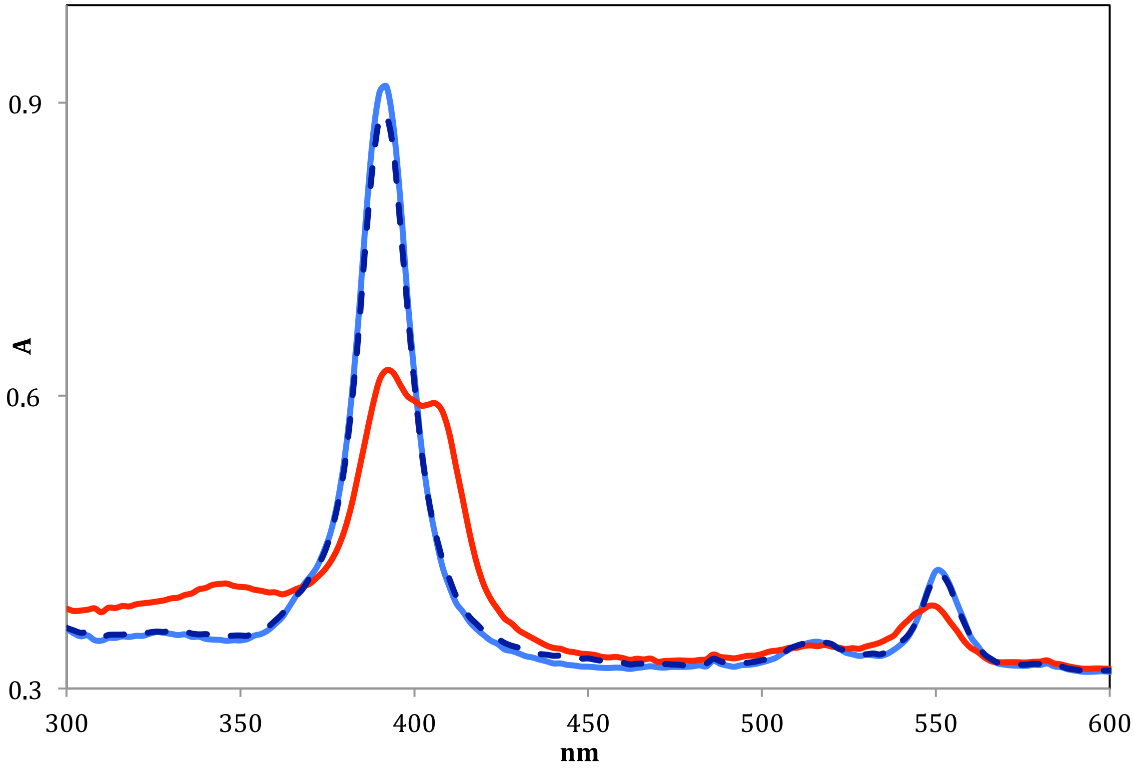

Figure 126: UV-vis spectroelectrochemistry of 0.5 mM Ni(OEP) reduction in THF. Blue line: initial spectrum; Red lines: spectrum after stepping at -2 V for 100s; dashed dark blue: reoxidation spectrum after stepping at -1.4V for 100s.

The spectroelectrochemistry of Ni(OEP) was carried out in THF-%AmNTF$_2$ mixture. The spectral features for the starting material and reduction product of the first wave in 20%AmNTF$_2$ are shown in *Figure 127*.

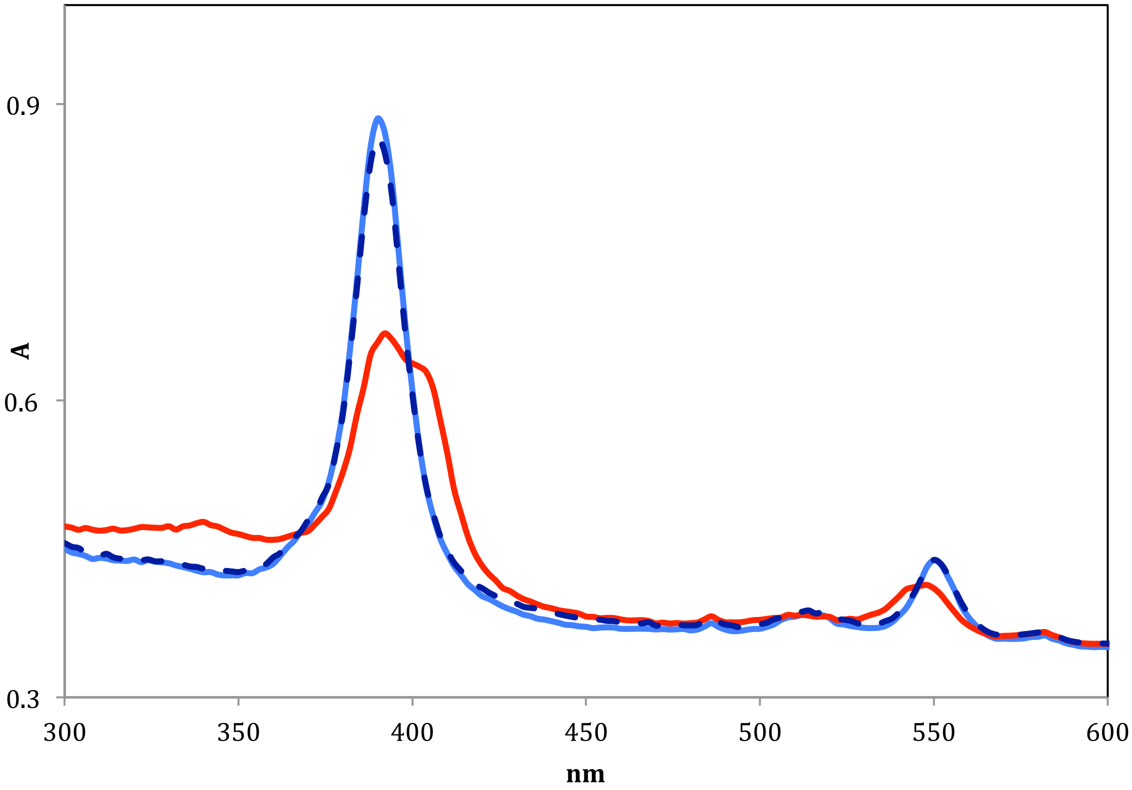

Figure 127: Spectroelectrochemistry of 0.5 mM Ni(OEP) reduction in THF-20%AmNTF$_2$. Blue line: initial spectrum. Red lines: spectrum after stepping at -1.8V for 150s. Dashed dark blue: reoxidation spectrum after stepping at -1.4V for 150s.

No changes were observed in the visible spectra of Ni(OEP) in THF or mixed solvents (*Figure 128*). Small shifts were observed for the two major bands in Ni(OEP)$^-$ when AmNTF$_2$ was added to the solution. The Soret band shifted from 406 to 404 nm, while the Q band shifted from 546 to 542 nm. Overall the spectrum was consistent with a Ni(I) complex in the presence or absence of the RTIL.

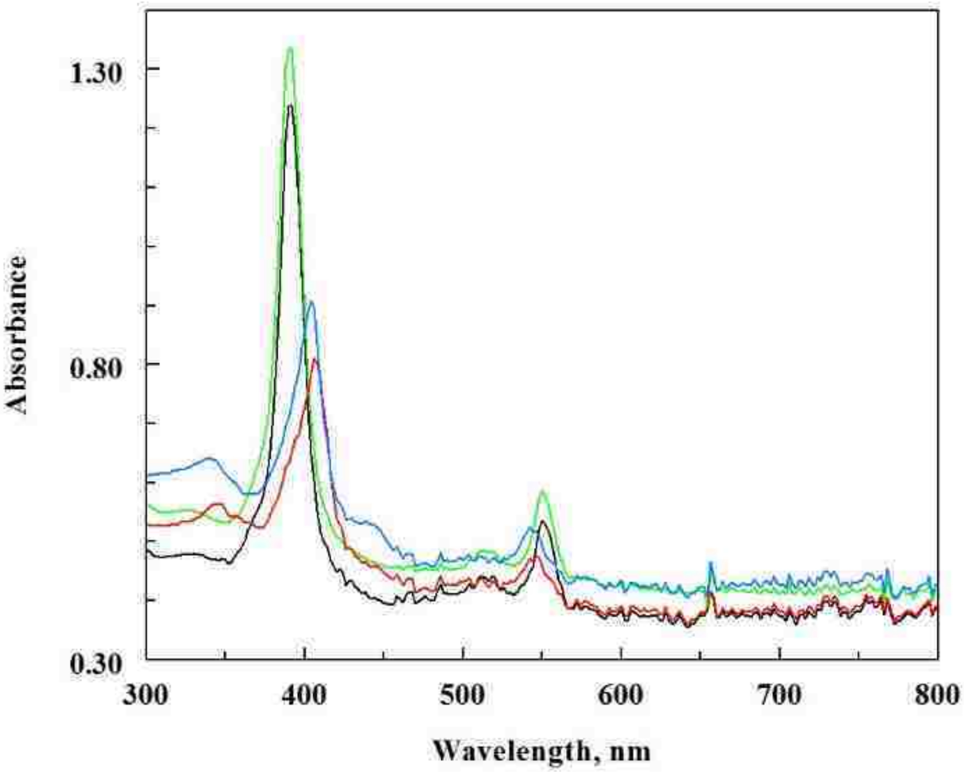

Figure 128: UV-vis spectroelectrochemical reduction of Ni(OEP) in THF and THF/AmNTF$_2$ mixtures. Ni(OEP) in THF: black line, Ni(OEP)$^-$ in THF: red line, Ni(OEP) in THF/10% AmNTF$_2$: green line, Ni(OEP)$^-$ in THF/10% AmNTF$_2$: blue line.

Spectra taken during the first oxidation of NiOEP in THF are shown in Figure 129. The Soret band decreased significantly in molar absorptivity, which was consistent with reports by previous workers.[116,117] While isosbestic points were observed from the initial spectrum to +740 mV, the isosbestic points were lost at more positive potentials. Based on previous work[118,119], the spectra in this potential range are probably a dimer of Ni(OEP) and Ni(OEP)$^+$, [Ni(OEP)]$_2^+$. When about half of the Ni(OEP) was converted to Ni(OEP)$^+$, three species would be present in solution, leading to the loss of the isobestic points (*Figure 130*). The complete oxidation of Ni(OEP) yielded a spectrum for Ni(OEP)$^+$ (black line, *Figure 131*) that was consistent with the spectrum for Ni(OEP)$^+$ in methylene chloride (*Figure 132*).

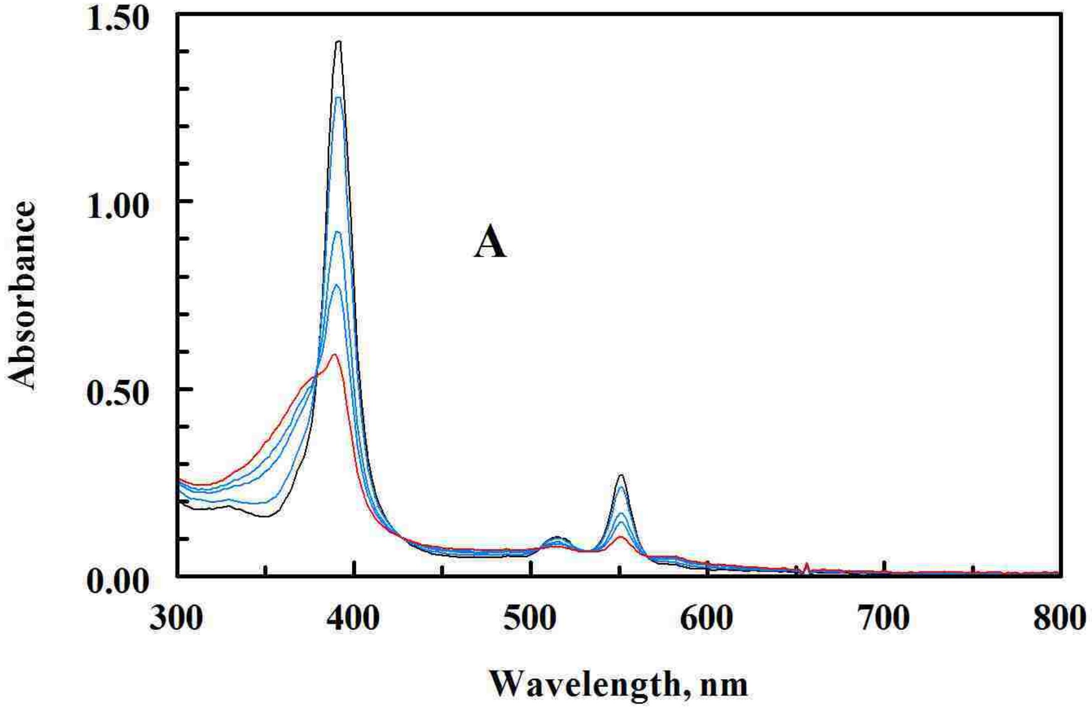

Figure 129: UV-vis spectroelectrochemistry of 0.5 mM Ni(OEP) in THF. Black line: initial spectrum; blue lines: intermediate spectra; red line: spectrum at +0.74 V.

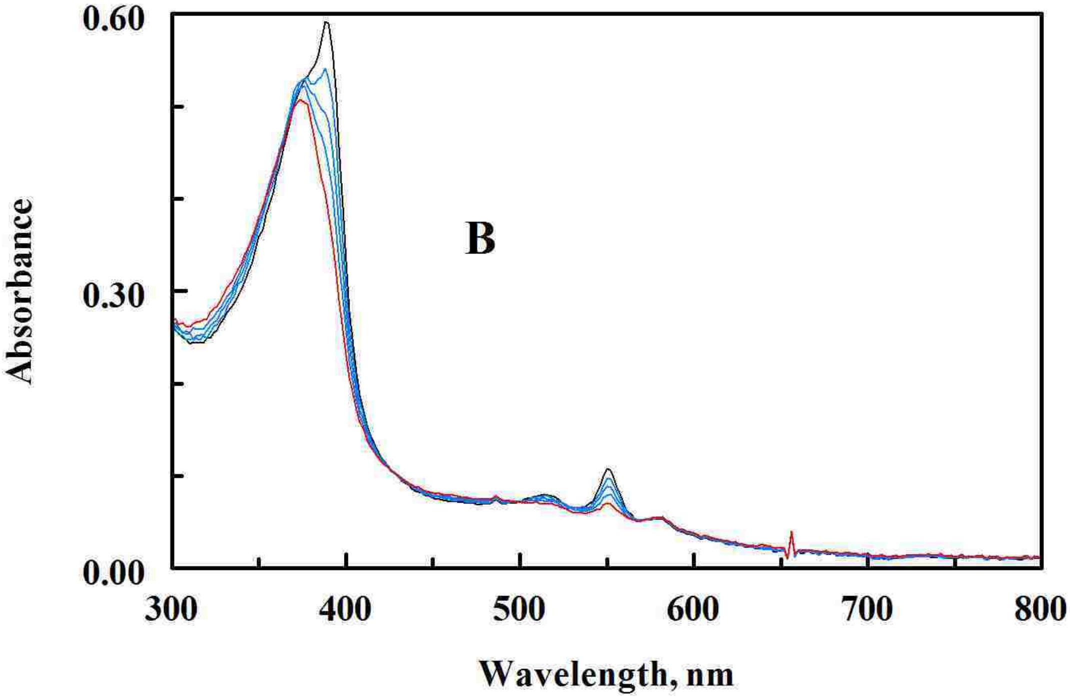

Figure 130: UV-vis spectroelectrochemistry of 0.5 mM Ni(OEP) in THF. Spectra from +0.74 V (black line) to +0.83 V (red line). Blue lines: intermediate spectra

Further oxidation of $Ni(OEP)^+$ to $Ni(OEP)^{2+}$ is also shown in *Figure 131*. The broad dication spectrum (red line in *Figure 131*) was consistent with previous reports, though some $Ni(OEP)^+$ could still be observed in the final spectrum. While evidence of the cation dimer was observed in the THF electrolysis, there was no evidence of this species in the spectroelectrochemistry of Ni(OEP) in methylene chloride (*Figure 132*).

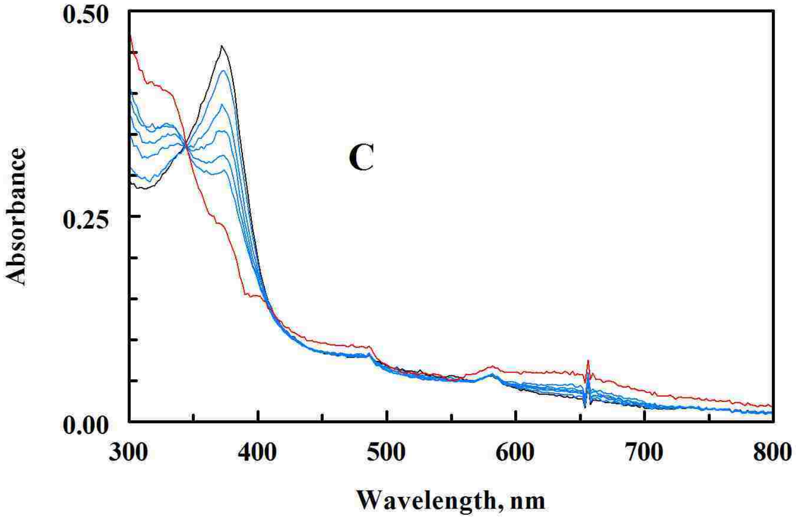

Figure 131: UV-vis spectroelectrochemistry of 0.5 mM Ni(OEP) in THF. Spectrum of Ni(OEP)$^+$ (black line, +0.83 V). Blue lines: intermediate spectra (forward scan: +0.95, +1.02 V, +1.15 V; reverse scan: +1.17 V, +1.07 V, +0.91 V). Spectrum of Ni(OEP)$^{2+}$ (red line, calculated after removal of residual Ni(OEP)$^+$).

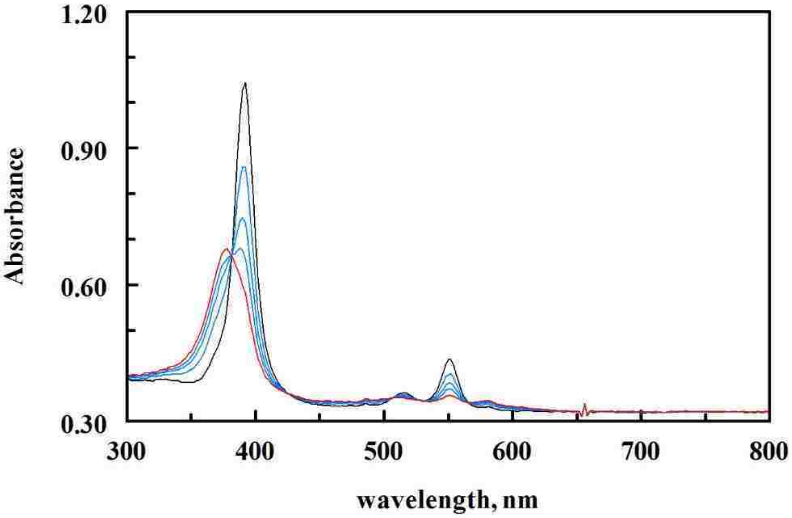

Figure 132: UV-vis spectroelectrochemical oxidation of Ni(OEP) to Ni(OEP)$^+$ in 0.10 M TBAP/methylene chloride. Black line: initial spectrum of Ni(OEP). Red line: final spectrum, Ni(OEP)$^+$. Blue lines: intermediate spectra.

Because there were no significant shifts in the oxidation potentials, not much effort has been done on the electrolysis in mixtures. However, preliminary results of Ni(OEP) spectroelectrochemical oxidation in %RTIL mixtures showed that spectral features were quite similar to THF. No noticeable shifts were observed in the Soret band for the cation and dication. The dimer cation appeared to be more stable than in pure THF, making it more difficult to see Ni(OEP)$^+$ before the second oxidation occurs. Typical changes upon the oxidation in mixtures are shown in the *Figure 133*.

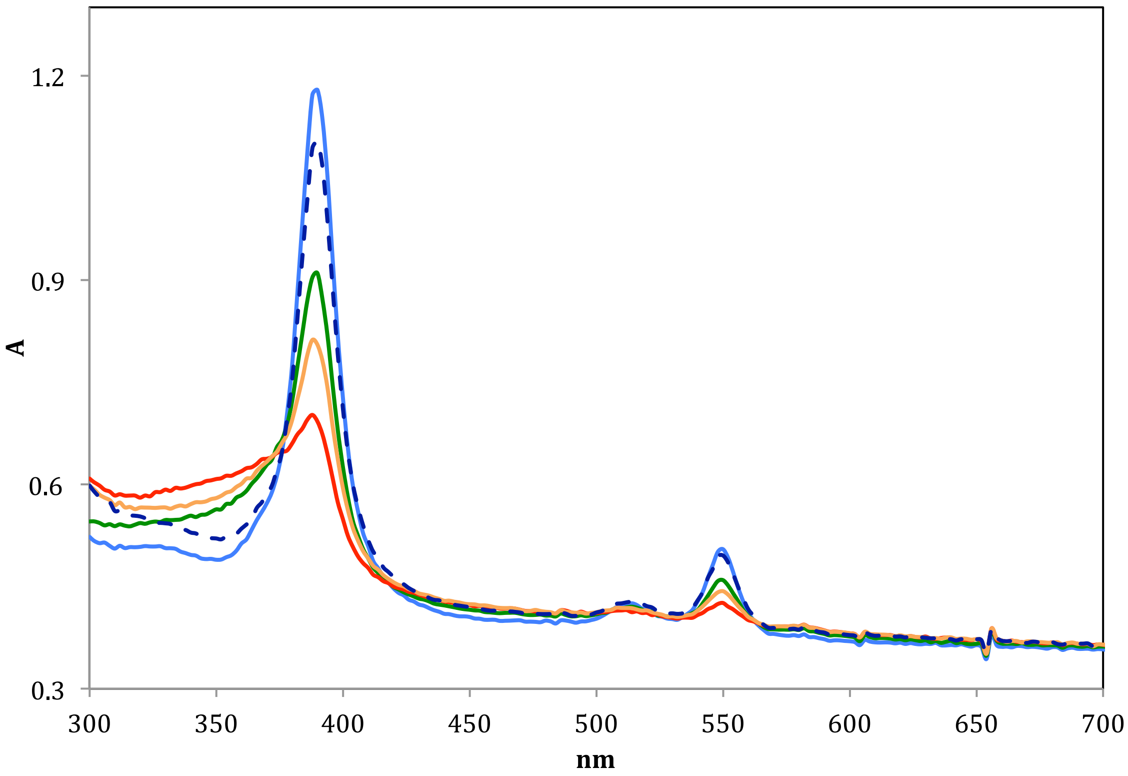

Figure 133: UV-vis spectroelectrochemistry of 0.5 mM Ni(OEP) in 50%AmNTF$_2$. Spectra obtained by stepping potentials at oxidation waves for 500s. Blue line: initial spectrum; Green line: +0.65V; Red line: +1V. Orange line: backward +0.65V. Dashed line: backward +0.3V.

6.2 Electrochemistry of Ni(OEPone)

UV-visible spectroelectrochemistry of NiOEP showed some spectral shifts due to the RTIL, but these shifts were difficult to interpret on a molecular level. In order to interpret these interactions more directly, NiOEPone was studied. The porphinone ligand in NiOEPone has a carbonyl group that can be readily observed using infrared spectroelectrochemistry, and this group creates a polar moiety on the ring that may interact strongly with the RTIL cation.

6.2.1 Cyclic voltammetry

The cyclic voltammetry of Ni(OEPone) is shown in *Figure 134*. At lower scan rates, the two oxidation waves and the first reduction wave remained reversible, but the second reduction wave was chemically irreversible. Similar to NiOEP, decomposition of the second reduction products is observed, resulting an additional oxidation peak on the reverse scan. At higher scan rates (using ultra micro electrode), the three reduction waves become chemically reversible, with features of a fourth reversible reduction wave at more negative potentials.

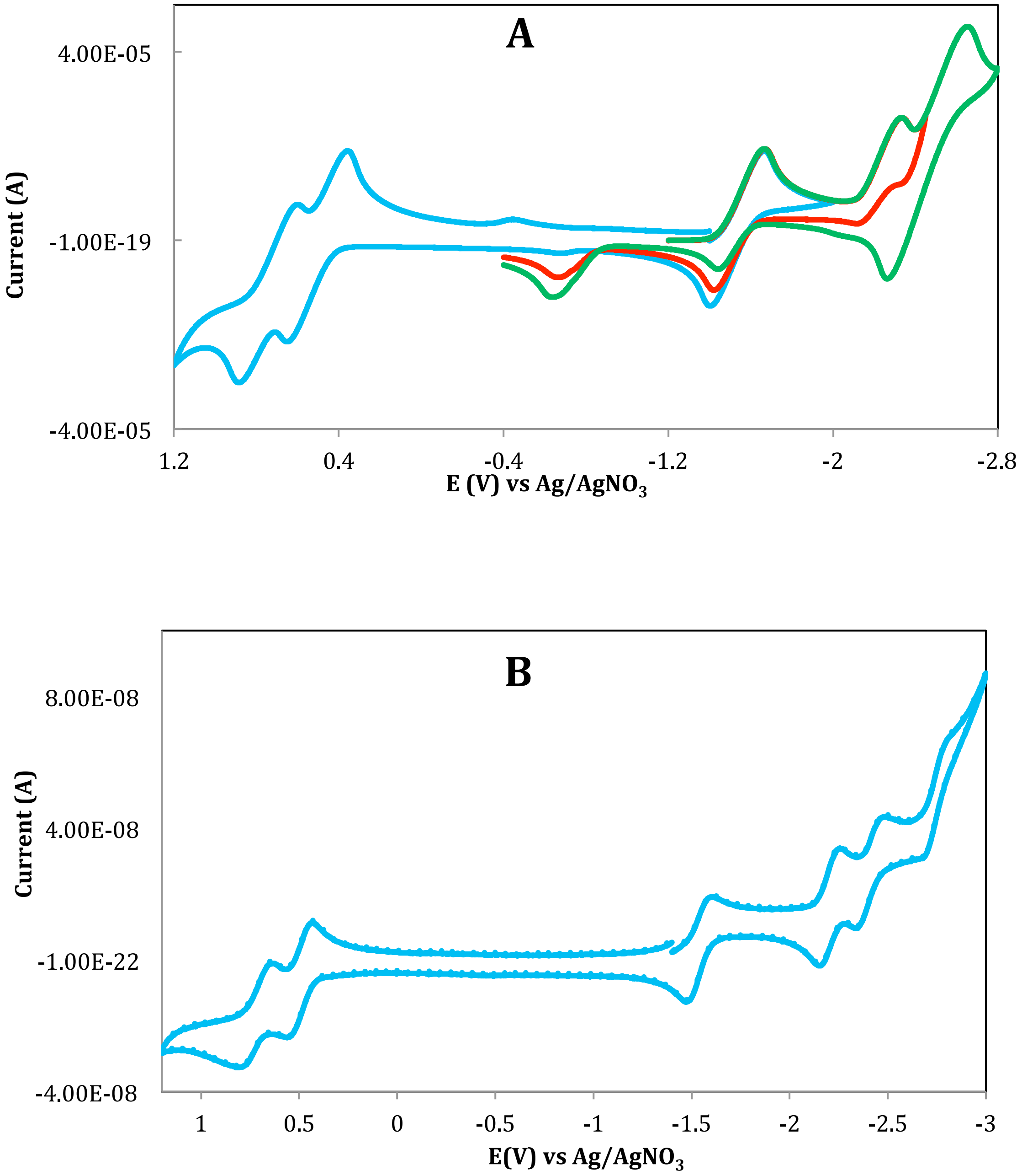

Figure 134: Cyclic voltammetry of 2.0 mM Ni(OEPone) in THF/0.10 M TBAP. A: Scan rate = 100 mV/s. $E_{initial}$ = -1.40 V, initial scan is negative. Working electrode: Pt (r = 1.6mm). B: Scan rate = 20 V/s. $E_{initial}$ = -1.40 V, initial scan is negative. Working electrode: Pt (r = 10μm)

In THF, the first reduction wave of Ni(OEPone) was shifted by 163 mV to more positive potentials, as compared to Ni(OEP). Similar shifts were observed by Stolzenberg and Stershic.[148] Shifts of 94 mV for ZnOEP/ZnOEPone and 367 mV for MnOEP/MnOEPone have been observed for reductions that have been assigned to the formation of π-anion radicals. Smaller shifts were observed for FeOEP/FeOEPone (30 mV) and CoOEP/CoOEPone (20 mV) where M(I) species were formed.[135] The second wave was shifted by 210 mV positive of the Ni(OEP) wave.

Both oxidation waves of Ni(OEPone) were shifted negative of the Ni(OEP) waves, the first wave by 50 mV and the second wave by 75 mV. This compares with a 20 and 30 mV shift of the first wave in acetonitrile and methylene chloride, respectively, and a 60 (acetonitrile) and 100 mV (methylene chloride) shift of the second oxidation wave.[113] The third wave for the reduction of Ni(OEPone) has not been previously reported.

Upon the addition of $AmNTF_2$, the reduction waves shifted to more positive potentials while the oxidation potentials relatively shifted to more negative potentials (*Figure 135*). Increasing the RTIL fraction in the mixture reduced the reversibility of the second reduction wave. While the second wave was not affected as much by the RTIL, significant stabilization was observed for the third wave in the mixture.

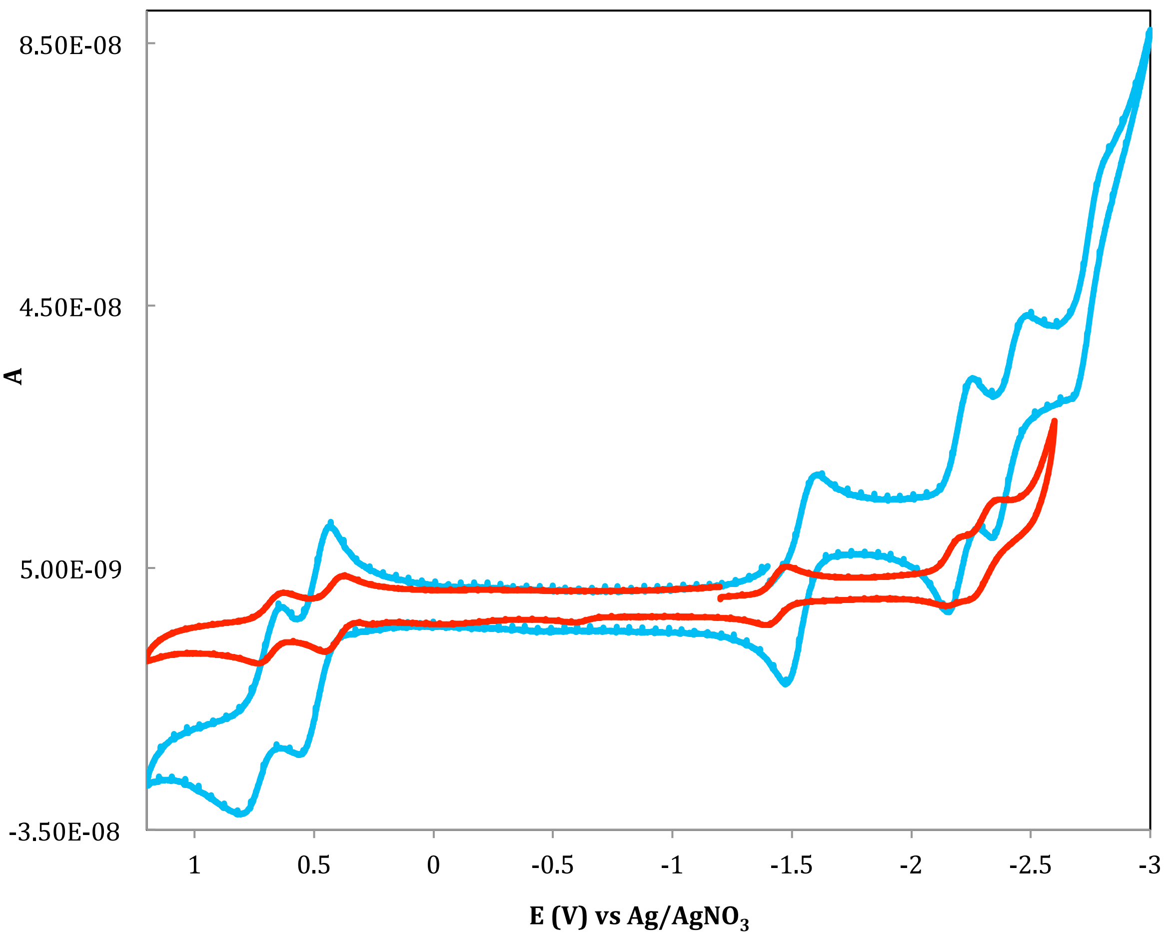

Figure 135: Cyclic voltammetry of 2.0 mM Ni(OEPone). Blue line: THF/0.10 M TBAP. Red line: 33% AmNTF$_2$. Scan rate = 20 V/s. $E_{initial}$ = -1.40 V, initial scan is negative. Working electrode: Pt (r = 10μm)

The shifts in half wave potentials, referenced to $DmFc^+/DmFc$, as a function of Gutmann AN are shown in *Figure 136*. While the potentials were linearly correlated with the Gutmann AN as with Ni(OEP), there were important differences. The slope of the first wave for Ni(OEPone) (0.049 V/AN) was much higher than the slope observed for Ni(OEP) (0.032 V/AN). The slope of the second wave of Ni(OEPone), by contrast, dropped to 0.033 V/AN compared to 0.049 V/AN for Ni(OEP). A large slope of 0.050 V/AN was observed for the third wave. As was observed for Ni(OEP), the oxidation potentials shifted to more positive values with comparable slopes of 0.012 V/AN and 0.014 V/AN for the first and second wave, respectively. Differences in the observed slopes for the reduction potentials of the two complexes are very likely due to change in reduction centers. The presence of the carbonyl band in the porphyrin ring is expected to delocalize the charge onto the ligand, upon the first reduction. Such delocalization of the negative charge onto the polar moiety of the porphyrin ligand would lead to higher interactions with RTIL cation. This is consistent with large shift of 160mV for the first reduction wave of NiOEPone versus NiOEP. As result, a higher slope was observed for the first wave of the NiOEPone compared to NiOEP. This also reflected significant interactions between the RTIL and $Ni(OEPone)^-$ as compared to Ni(OEPone). Upon the addition of a second electron, the double charge was equivalently distributed over the metal and ligand centers, leading to slightly higher interactions of $Ni(OEPone)^{2-}$ with RTIL compared to $Ni(OEPone)^-$. These comparable interactions with RTIL components resulted in smaller slope of the second wave versus the first wave. The third reduction, where the charge is mostly localized on the ligand, will lead to strong interactions with the RTIL cations, resulting in a much higher shift. Similar trends were observed for radical anion versus dianion of DNB and TCNQ.

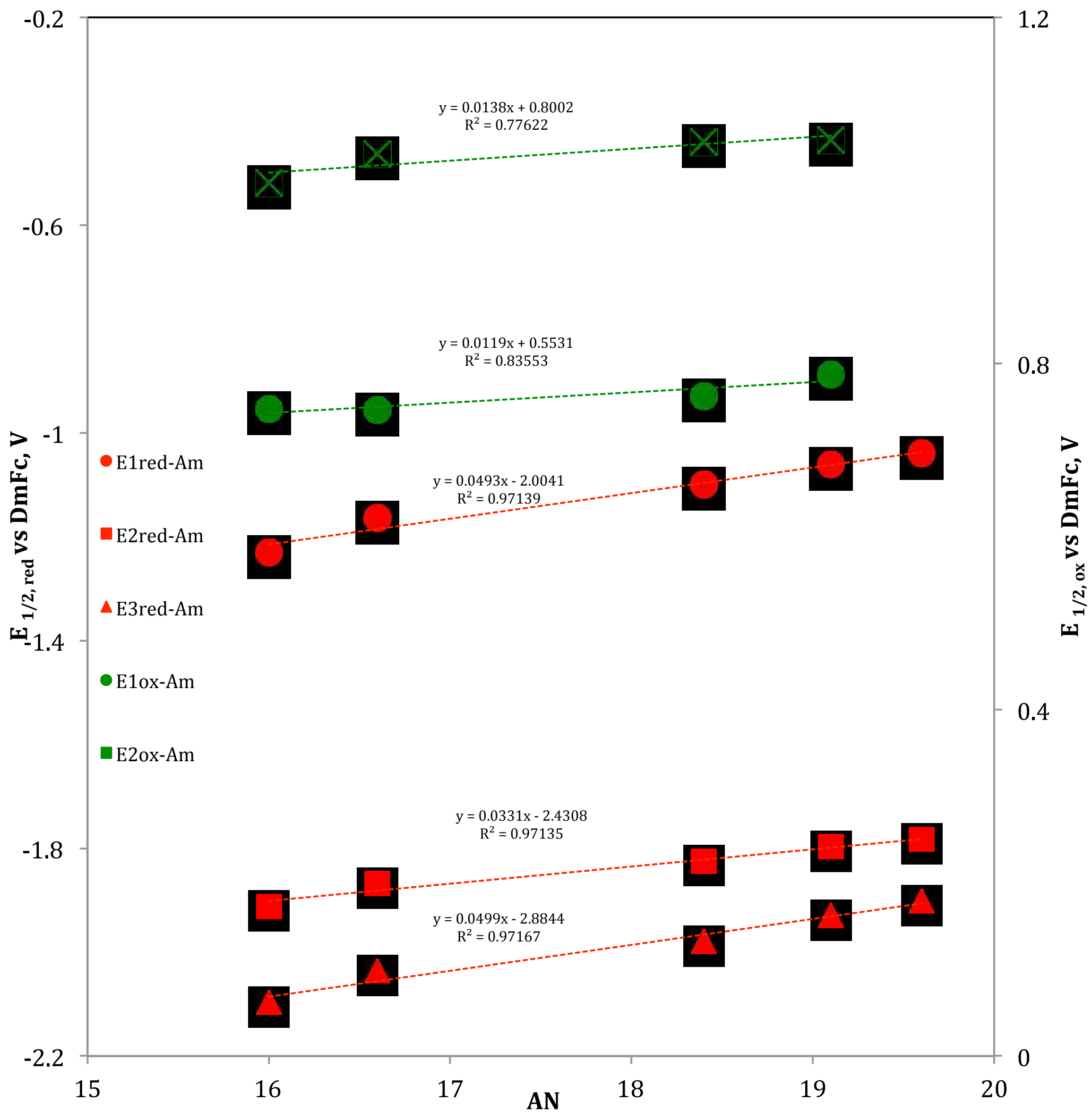

Figure 136: Potential shifts $E_{1/2}$ values for Ni(OEPone) in THF/$AmNTF_2$ mixtures as a function of the Gutmann AN. Red symbols/lines are for the reduction waves; green symbols/lines are for the oxidation waves. Circles are the first wave; Squares are the second wave; Triangles is the third wave.

As result of differences in the shifts of the reduction potentials, the ΔE_{12} for the reduction waves increased as the Gutmann AN increased (*Figure 137*), which was the opposite of the results for Ni(OEP). The above rationale on the reduction center will be assessed in the following discussions, through spectroelectrochemical investigations.

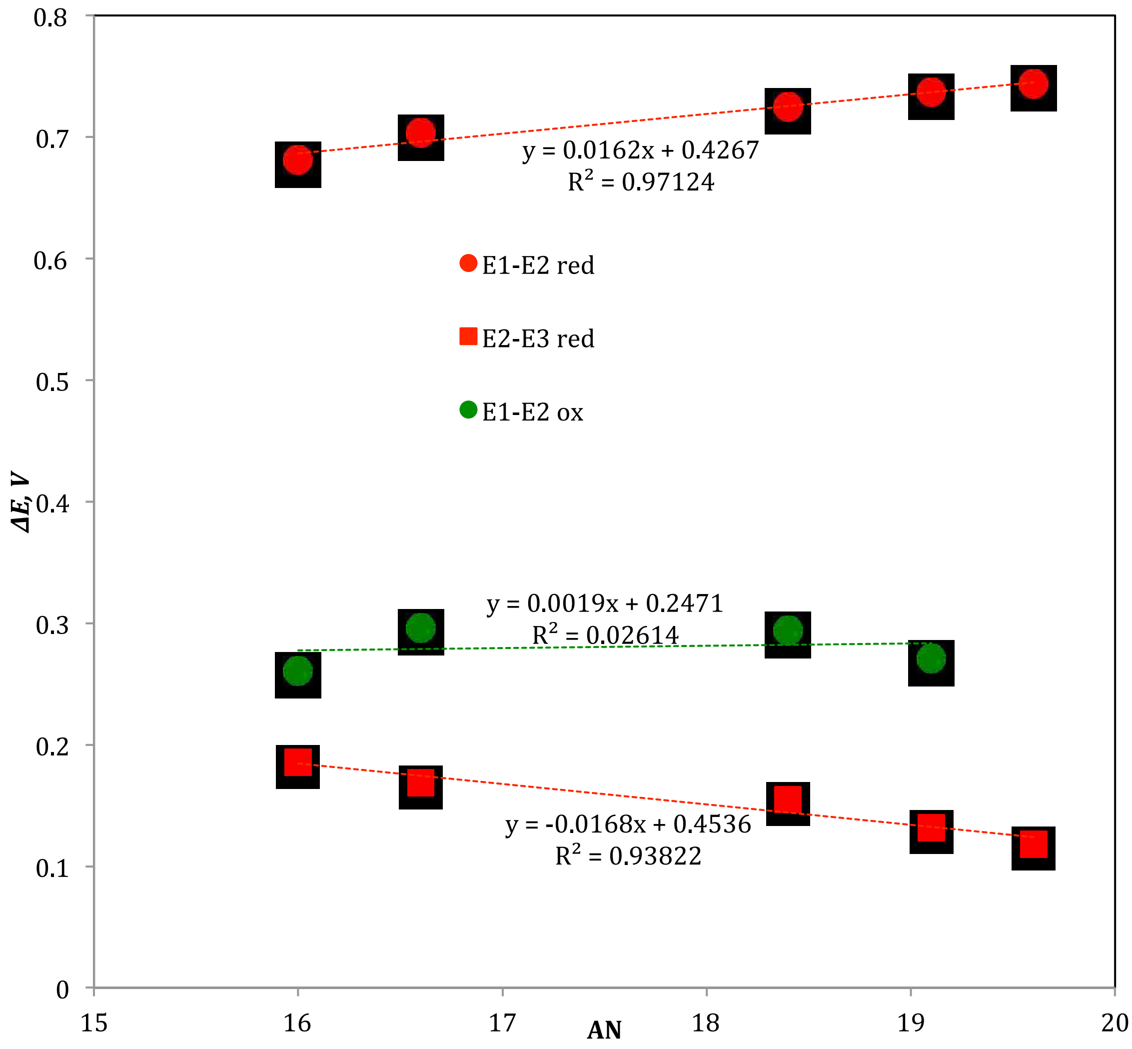

Figure 137: Potential shifts ΔE values for Ni(OEPone) in THF/AmNTF$_2$ mixtures as a function of the Gutmann AN. Red is for reduction. Green is for oxidation. Circles are ΔE_{12}; Squares are ΔE_{23}

6.2.2 UV-visible Spectroelectrochemistry

The UV-visible spectroelectrochemical reduction of Ni(OEPone) in THF (first wave) is shown in *Figure 138*-A. Upon reduction, the Soret band was significantly bleached with new split Soret bands at 418 and 467 nm. In addition, a broad weak band was observed between 600 and 750 nm. Bleaching of the Soret band and a broad band between 600 and 750 nm is frequently an indication of a π-anion radical.[121] While Zn(OEPone)$^-$ has a broad band at 452 nm, the Soret band was not split as in the nickel complex. However, reduction of both complexes led to bleaching of the 621 nm band. Thus there are characteristics of metal and ring reduction for Ni(OEPone)$^-$.

Electrolysis of NiOEPone in 33%AmNTF$_2$ showed more bleaching of the Soret band in the mixture than in THF, indicating more delocalization of the charge in the porphyrin ligand in the presence of the RTIL (*Figure 138*-B). This is consistent with stronger interactions of the negatively charged, reduced species, upon partitioning into RTIL nano-domain. These results were in agreement with higher shift of the reduction potential of Ni(OEPone), compared to Ni(OEP), with increase of RTIL fraction in mixtures.

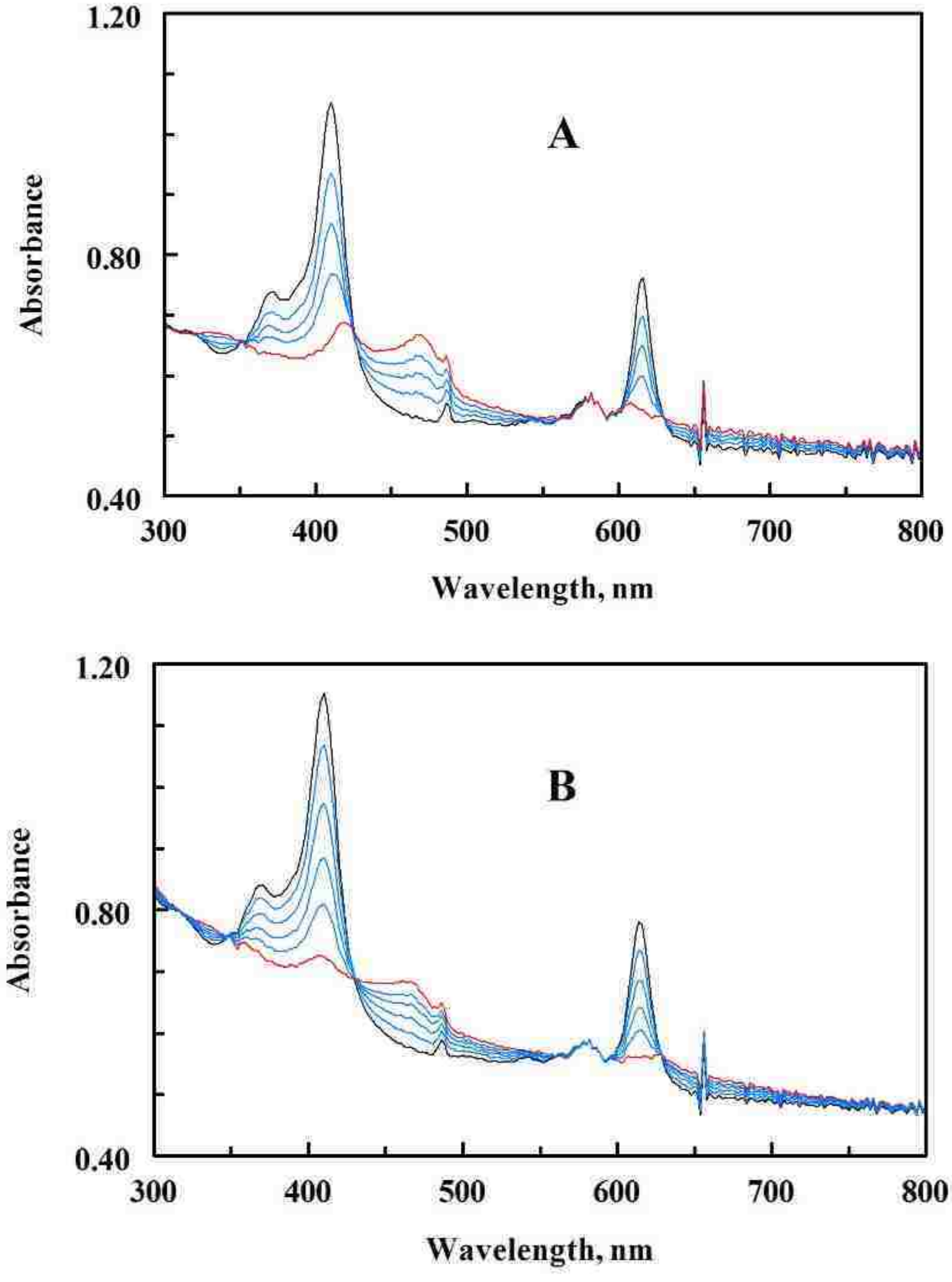

Figure 138: UV-vis spectroelectrochemical Reduction of Ni(OEPone) to Ni(OEPone)$^-$ in THF (A) 33%AmNTF$_2$ (B). Black line: initial Ni(OEPone) spectrum. Red line: Ni(OEPone)$^-$ spectrum after removal of residual Ni(OEPone). Blue lines: intermediate spectra. Potential stepped from -1.0 V to -1.8 V vs Ag/AgNO$_3$ for 300s.

6.2.3 FTIR Spectroelectrochemistry

The effect of the RTIL on the carbonyl vibration of NiOEPone complex in both solvents THF and RTIL is shown in *Figure 139*. The carbonyl band, ν_{CO}, for Ni(OEPone) was observed at 1718 cm^{-1} in THF, but was downshifted by about 4 cm^{-1} when the substrate was dissolved in AmNTF$_2$. The interaction between the ionic solvent and Ni(OEPone) had a small but measureable effect on the carbonyl band.

The FTIR spectroelectrochemistry of Ni(OEPone) was carried in order to see if similar shifts can be observed in the reduction product. The FTIR difference spectrum is shown in *Figure 140* for the first reduction of Ni(OEPone) in THF (blue line). The ν_{CO} at 1718 cm^{-1} band for the carbonyl disappeared while new bands at 1682, 1608, 1573 and 1541 cm^{-1} appeared. The band at 1682 cm^{-1} is consistent with the carbonyl band of Ni(OEPone)$^{-}$. The additional bands were typical of reduced metalloporphinones.[149,150] While not a definitive indicator of the electronic structure of the M(OEPone)$^{-}$ species, formation of M(I) species generally shows a smaller decrease in the ν_{CO} than the M(II)(OEPone$^{\cdot-}$) species. For example, the ν_{CO} for π-anion radicals such as Zn(OEPone)$^{-}$ and Mn(OEPone)$^{-}$ are 1662 and 1657 cm^{-1}, respectively, while the ν_{CO} for M(I) complexes such as Fe(OEPone)$^{-}$ and Co(OEPone)$^{-}$ were 1671 and 1674 cm^{-1}.

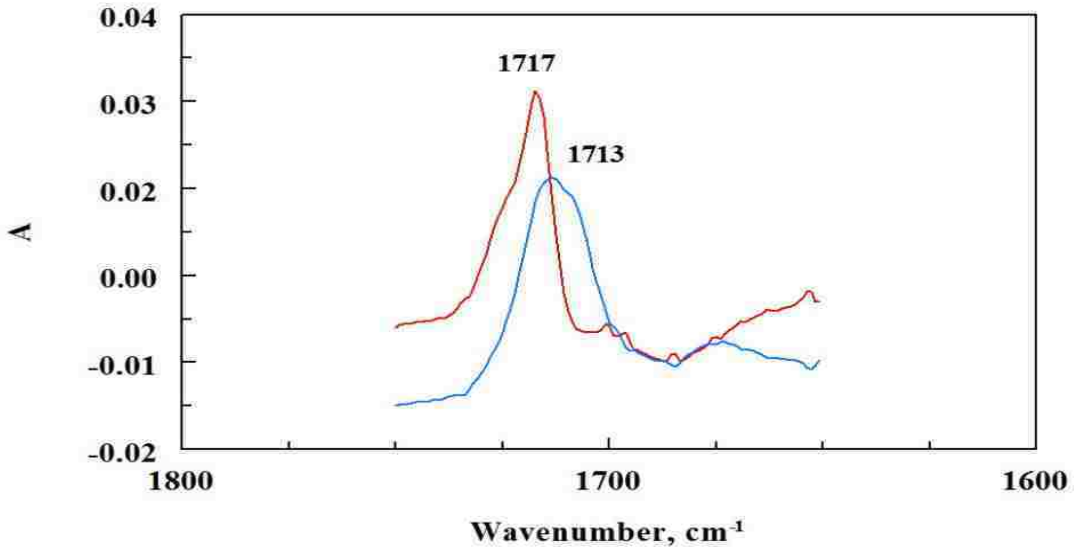

Figure 139: FTIR spectra of Ni(OEPone) in THF (red line) and AmNTF$_2$ (blue line).

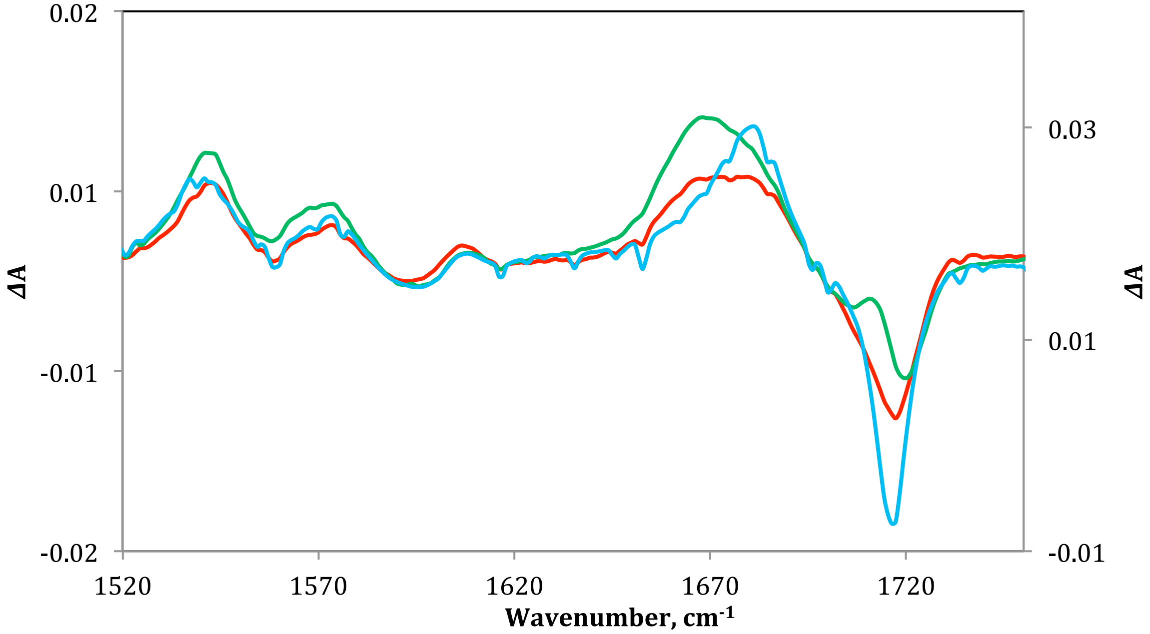

Figure 140: Difference spectra of FTIR spectroelectrochemical reduction at the first wave of Ni(OEPone) in THF/0.10 M TBAP (Blue line), THF-33% AmNTF$_2$ (Red line) and THF-50% AmNTF$_2$ (Green line).

The FTIR spectroelectrochemical experiment was then repeated in THF-%AmNTF$_2$ mixtures. In the presence of the RTIL, there was a small but measurable shift in the ν_{CO} band for Ni(OEPone) (from 1717 to 1715 cm^{-1} for 33%RTIL, red line) consistent with what was observed in pure AmNTF$_2$. Upon reduction in mixtures, though, the difference spectra showed a broadening of the ν_{CO}, indicating that there were probably two ν_{CO} bands for Ni(OEPone)$^-$. As the %RTIL increased, the second band grew at the expense of the original band. On the other hand, the bands at 1608 and 1573 cm^{-1} were unaffected, but there was a small upshift in the 1541 cm^{-1} band. At higher RTIL fractions (50%RTIL, green line) the ν_{CO} is sharpened at the lower frequencies.

The difference spectrum for the ν_{CO} band was analyzed using GRAMS in order to deconvolute the bands. Because of the small shift in the ν_{CO} for Ni(OEPone), there may have also been two bands for the starting material. The deconvolution of the ν_{CO} bands is shown in *Figure 141* for 33%AmNTF$_2$. The results were consistent with two bands for Ni(OEPone)$^-$ at 1682 and 1666 cm^{-1}. Similarly two bands were observed for Ni(OEPone) with the 1718 cm^{-1} being the dominant species, but a small difference band at 1707 cm^{-1} was observed (it is not unusual for the difference bands to be shifted from the absorbance spectrum when the bands are close together).

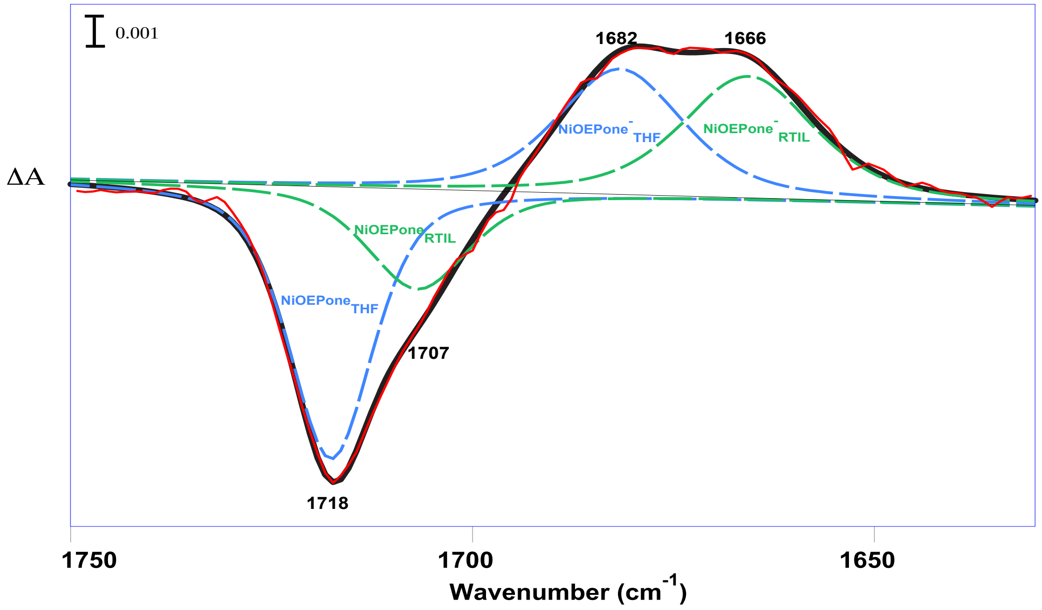

Figure 141: Deconvolution of the difference spectra for the reduction of Ni(OEPone) in THF/33% AmNTF$_2$. Red line: experimental difference spectrum. Black line: calculated difference spectrum. Green lines: bands for Ni(OEPone) species in AmNTF$_2$. Blue lines: bands for Ni(OEPone) species in THF. Pink line: residual

From the deconvolution, the difference peak areas were nearly equal for the 1682 and 1666 cm^{-1} bands for this mixture. The experiment was then repeated at different concentrations of the RTIL. The two bands at 1666 and 1682 cm^{-1} indicated that Ni(OEPone)$^-$ experienced two different types of solvation environment in the mixed RTIL/THF solutions. The band at 1682 cm^{-1} was attributed to the THF domain, while the 1666 cm^{-1} band was assigned to the RTIL domain.

The distribution of Ni(OEPone) and Ni(OEPone)$^-$ between the THF and RTIL nano-domains could be estimated from the difference peaks. By integrating the area under the difference bands shown in *Figure 141*, the distribution constant could be calculated assuming that there are two nano-phases: RTIL nano-domain and the THF nano-domains. The distribution constant, D, is equal to:

$$D = \frac{M_{RTIL}}{M_{THF}} = \frac{\#mol_{RTIL} / V_{RTIL}}{\#mol_{THF} / V_{THF}}$$

Where M = molarity of Ni(OEPone)$^-$ in the RTIL or THF phase, #mol is the number of moles of Ni(OEPone)$^-$ in the RTIL or THF phase, V_{RTIL} is the total volume of added RTIL and V_{THF} is the total volume of added THF. If $mol_{total} = \#mol_{RTIL} + \#mol_{THF}$, then, dividing the top and bottom of the right hand side by mol_{total}, we obtain,

$$D = \frac{(\#mol_{RTIL} / mol_{total}) / V_{RTIL}}{(\#mol_{THF} / mol_{total}) / V_{THF}} = \frac{X_{Ni,RTIL} V_{THF}}{X_{Ni,THF} V_{RTIL}} = \frac{X_{Ni,RTIL} V_{THF}}{(1 - X_{Ni,RTIL}) V_{RTIL}}$$

Where $X_{Ni,RTIL}$ is the mole fraction of Ni(OEPone)$^-$ in the RTIL phase and $X_{Ni,THF}$ is the mole fraction of Ni(OEPone)$^-$ in the THF phase. Rearranging this equation, we can obtain,

$$\frac{V_{RTIL}}{X_{Ni,RTIL}} = V_{RTIL} + \frac{V_{THF}}{D}$$

For V_{THF} = 1.00 mL, the equation becomes:

$$\frac{1}{X_{Ni,RTIL}} = V_{RTIL} + \frac{1}{D} = \frac{DV_{RTIL} + 1}{DV_{RTIL}}$$

A value of D = 2.8 was obtained from our results (*Figure 142*). For Ni(OEPone), the distribution into the RTIL layer was small, making the calculation more difficult, but, for the highest concentration of RTIL, a value of D = 0.5 could be estimated. This is consistent to the expectation that the anionic species are more soluble than the neutral within the RTIL domain.

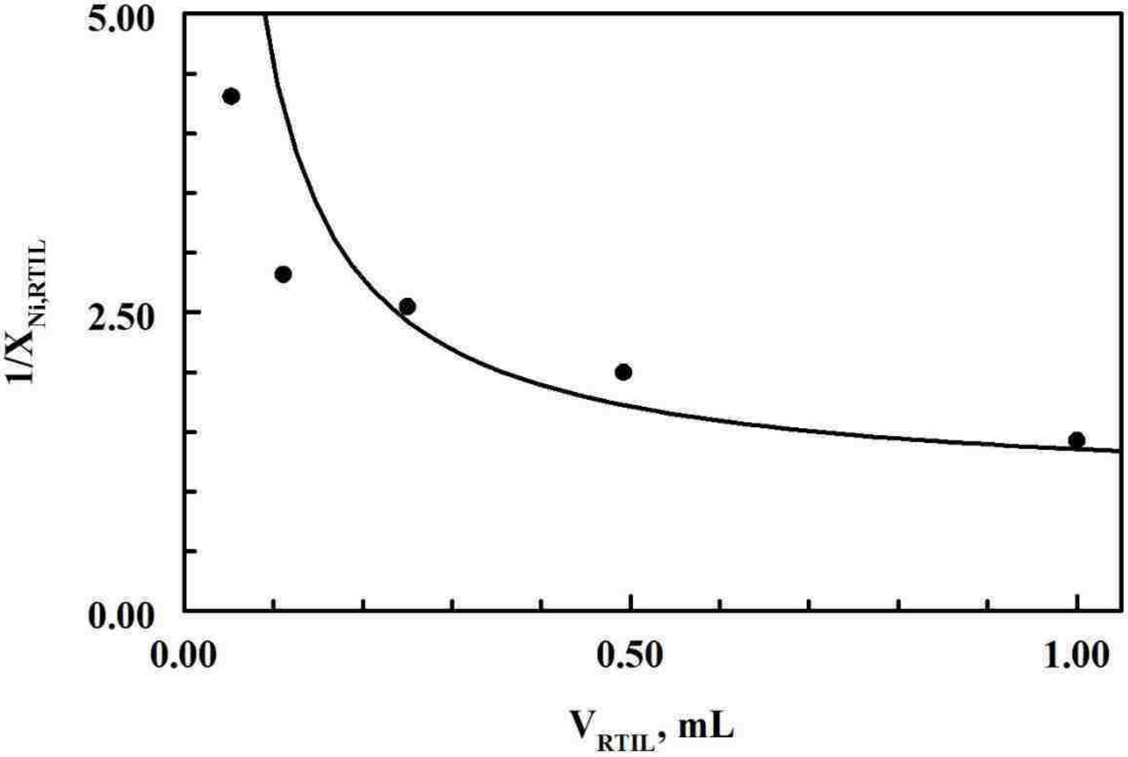

Figure 142: Plot of the reciprocal of the mole fraction of Ni(OEPone)$^-$ in RTIL ($X_{Ni,RTIL}$) versus V_{RTIL}. Line is the best fit for Eq. 6 with D = 2.8, where D is the distribution coefficient between the RTIL and THF nanodomains. V_{THF} = 1.0 mL.

The experiment was also repeated with the oxidation of Ni(OEPone) (*Figure 143*). As before, two bands were observed for Ni(OEPone) but only one band for Ni(OEPone)$^+$. This is very likely due to the fact that the ν_{CO} for Ni(OEPone)$^+$ was the same in both THF and the RTIL, or that Ni(OEPone)$^+$ favors the THF nano-domains over the RTIL nano-domain. Given that the neutral, Ni(OEPone), shifted in going from THF to the RTIL, the second explanation is the most likely the one. These results were in agreement with voltammetric analysis, which indicated strong repulsions between the oxidized products and RTIL components in mixture solutions.

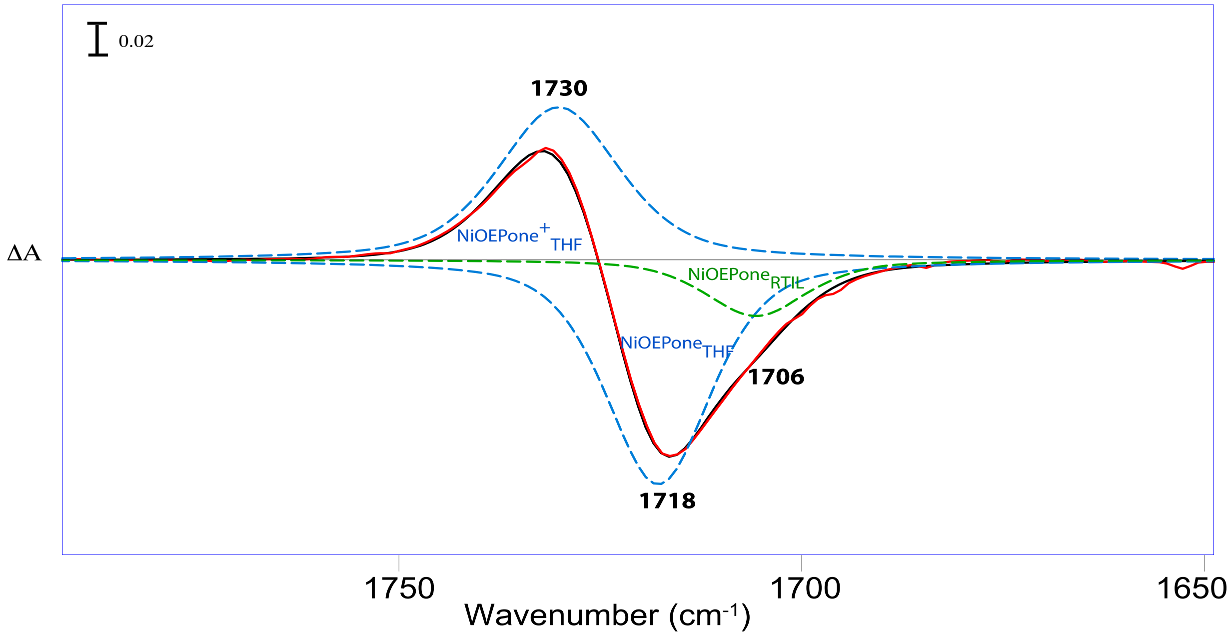

Figure 143: Deconvolution of the difference spectra for the oxidation of Ni(OEPone) in THF/33% AmNTF$_2$. Red line: experimental difference spectrum. Black line: calculated difference spectrum. Green line: bands for Ni(OEPone) species in AmNTF$_2$. Blue lines: bands for Ni(OEPone) species in THF. Pink line: residual

6.3 Discussion

The results of the voltammetric and spectroscopic data were consistent with the formation of nano-domains in the RTIL within the THF/RTIL mixtures. The partitioning between the THF and RTIL domains was shown to be controlled by both electrostatic and electronic factors. A comparison of the voltammetry and spectroelectrochemistry for Ni(OEP) and Ni(OEPone) indicated the complexity of the interactions between the RTIL and charged substrates. One main conclusion was that RTILs preferentially solvate electrogenerated anions over electrogenerated cations. The large electrogenerated anions were able to interact strongly with the RTIL cation without increasing repulsion between the ions of the RTIL.

The shifts in the $E_{1/2,1}$ and $E_{1/2,2}$ values for Ni(OEP) could be understood mostly on the basis of electrostatics. As expected, larger shifts were observed for the dianion $\mathrm{Ni(OEP)}^{2-}$ than for the mono-anion $\mathrm{Ni(OEP)}^{-}$. Similar results were also observed for C_{60} in molecular solvent/RTIL mixtures for the electrochemical formation of C_{60}^{3-}. Because C_{60} is spherical and Ni(OEP) is mostly planar, it would be easier for the dianion of Ni(OEP) to incorporate into the RTIL nano-domains than C_{60}^{2-}. Moreover, delocalization of the second electron over the porphyrin ligand, compared to the first metal centered reduction, led to higher stabilization of the second reduction wave.

In addition to the charge on the substrate, the presence of polar moieties within the substrates increased the interactions between the substrates and the RTIL. The latter effect was more prominent in the voltammetry of NiOEPone, where the shifts of $E_{1/2,1}$, $E_{1/2,2}$ and $E_{1/2,3}$ values were more complex, and could not be explained simply on the basis of overall charge.

The introduction of a polar group into the ligand had significantly delocalized the charge onto the ligand, leading to stronger interactions with RTIL components. As result, the first reduction wave of NiOEPone was highly stabilized by RTIL compared to NiOEP. While the second wave was less sensitive to RTIL, the voltammetry showed high stabilization of the third wave, which was almost merging with the second wave at 33%RTIL. With two charges distributed over the porphyrin ligand, the Ni(I) porphyrin trianion would be highly partitioned into RTIL nano-domains, similarly to DNB^{2-}.

The exchange between the two nano-domains was slow enough to observe the two solvation environments, using FTIR for Ni(OEPone) and $Ni(OEPone)^-$. The FTIR spectroelectrochemical data clearly showed a strong interaction between $Ni(OEPone)^-$ and the RTIL phase, causing a significant downshift in the ν_{CO} band. The visible spectra (broad weak Soret band) already showed that there was significant ring delocalization of the negative charge in $Ni(OEPone)^-$, indicating that the $Ni(OEPone)^-$ complex was more like a π-radical anion than a Ni(I) complex. The weakening of the ν_{CO} bond in the presence of the RTIL showed that the RTIL environment favors additional electron density on the CO group, which previous DFT calculations for other metalloporphinones have shown that the HOMO orbital is anti-bonding at the C=O moiety.[149,150] The downshift in the ν_{CO} band was not simply the effect of ion pairing. The Am^+ cation is very similar in size and ion pairing ability to TBA^+, which was present in the THF solution. Had it been simply ion pairing interactions, the band at 1666 cm^{-1} would have been observed in the THF/TBAP solution. Indeed, the presence of RTIL nano-domains allowed for a more powerful interaction between the substrate and the ions of the RTIL.

Because the RTIL cation is larger than the RTIL anion, incorporation of the electrogenerated cations would cause significant cation-cation repulsion. As result the positively charged products were mostly partitioned into the molecular domain. This was indicated by the shift of the oxidation potentials to more positive values upon addition of RTIL in the mixtures. Further evidence of such partitioning could be observed by FTIR spectroscopy, where the carbonyl vibration of the oxidized product was insensitive to RTIL introduction in the mixture.

Finally, the diffusion of electroactive species in mixed molecular solvent/RTIL solutions was shown to occur mostly within the molecular solvent domain. The RTIL decreased the diffusion coefficient of the electroactive species, but not nearly as much as predicted by the Stokes-Einstein equation.

Chapter 7 Spectroelectrochemical and Voltammetric Study of Iron Fluorinated Porphyrins in THF-RTILs Mixtures

In this chapter, the influence of RTIL nano-domains on the redox chemistry of iron porphyrin will be investigated in THF-RTILs mixtures. One major complexity of such system emerges from changes of the axial ligation to the metal center upon redox reactions.

In this work, we have used two different ligands, chloride and perchlorate, as counter anions of the iron porphyrin. In addition, we used a fluorinated porphyrin to enhance the solubility of these complexes in the RTIL solution and to allow the probing of changes in the electronic structures by ^{19}F-NMR (*Figure **144***). This investigation was carried out in the two regions of the binary THF-RTIL: molecular solvent rich mixtures (THF-%RTIL) and the RTIL rich mixtures (RTIL-%THF).

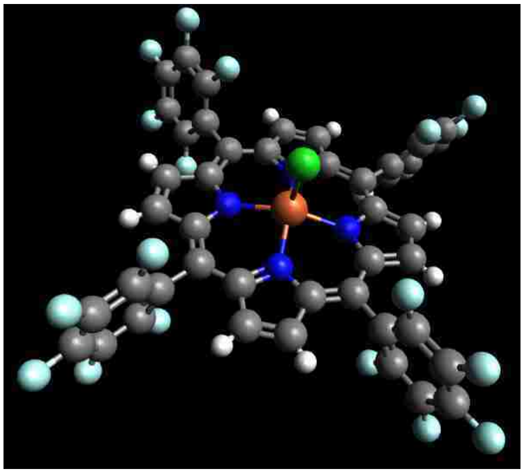

Figure 144: Structure of $FeF_{20}TPPCl$

7.1 Electrochemistry in THF rich mixtures

7.1.1 Cyclic voltammetry

The cyclic voltammetry of $FeF_{20}TPPCl$ and $FeF_{20}TPPClO_4$ in pure THF is shown in *Figure* ***145***. Three reversible waves were observed, respectively, at -0.44 V for the chloride and +0.05V for the perchlorate, -1.22 V and -1.68 V versus $Ag/AgNO_3$. The reported half potentials for FeTPPCl in THF were -0.7 V, -1.54 V and -2.11V, respectively for the three reduction waves.[151,152] Fluorination of the phenyl arms stabilized the three waves, by 0.26, 0.32 and 0.42, respectively. While the first electron reduction is metal centered resulting in a ferrous complex, the second electron is also believed to form mostly a metal centered reduction products (some delocalization to the porphyrin ligand could be also observed), followed by ligand reduction forming a radical dianion.[153] In case of the perchlorate complex, the weak anion may be displaced by the solvent for the ferric species. This solvent coordination shifts the first reduction to more positive potentials by about 0.5V. The electrochemical reactions are described as follow:

$$\mathbf{Fe^{III}F_{20}TPPCl + e- \rightarrow Fe^{II}F_{20}TPP + Cl^-}$$

$$\mathbf{Fe^{II}F_{20}TPP + e- \rightarrow Fe^{I}F_{20}TPP^{-}}$$

$$\mathbf{Fe^{I}F_{20}TPP^- + e- \rightarrow Fe^{I}F_{20}TPP^{2-}}$$

For the perchlorate complex, the counter anion is displaced by the THF:

$$\mathbf{Fe^{III}F_{20}TPPClO_4 + 2\,THF \rightarrow Fe^{III}F_{20}TPP(THF)_2^+ + ClO_4^-}$$

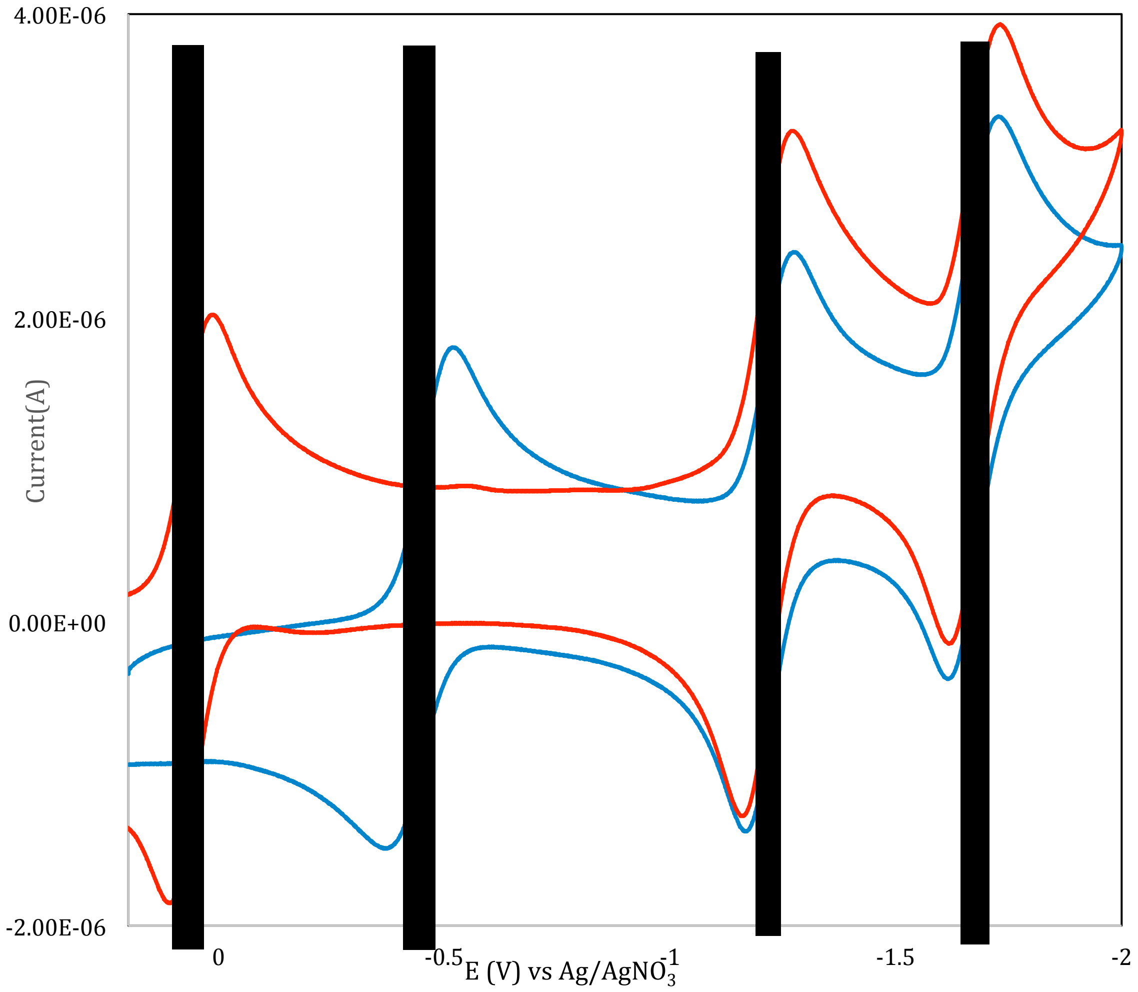

[redacted] [redacted] [redacted] [redacted]

Figure 145: Voltammogram of three reduction waves of $FeF_{20}TPPCl$ *(blue) and* $FeF_{20}TPPClO_4$ *(red) in THF/0.1M TBAP*

Cyclic voltammetry of $FeF_{20}TPPCl$ was also carried out in THF-%RTIL mixtures. *Figure* ***146*** shows that the introduction of RTILs shifted the three reduction waves to more positive values. Higher stabilization was observed for the third wave compared to first two waves. Addition of the imidazolium ionic liquid slows down the chloride coordination to the ferric species upon re-oxidation. At higher RTIL concentrations, the solvent coordination to the metal center becomes more dominant.

To eliminate possible drifts of the reference electrode, due to change of liquid junction potential between mixtures, the potential shifts were referenced to the oxidation potential of the internal reference $DmFc^+/DmFc$ (-0.26 V vs $Ag/AgNO_3$ in THF). The plots of DmFc-referenced potentials versus RTIL fraction shows that most of the stabilization occurs at 20% of the ionic liquids (Figures 147-148). At 40%RTIL, the three waves were shifted, respectively, by 300, 196 and 314 mV in imidazolium mixtures and by 288, 187 and 211 mV in ammonium mixtures. The larger shifts of the first and the third waves, compared to the second one, resulted in increasing the ΔE_{12} value and reducing the ΔE_{23} value.

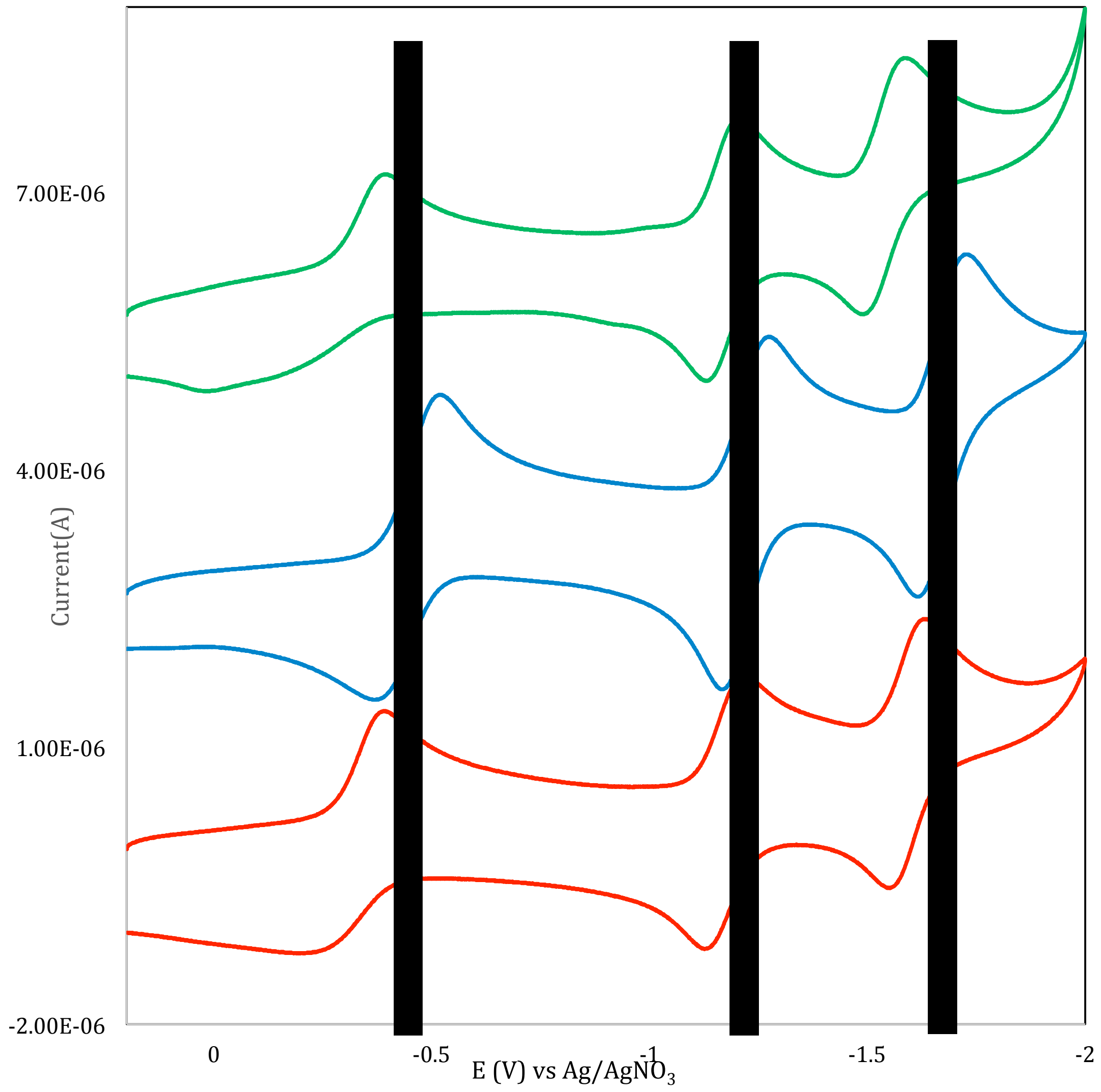

Figure 146: Voltammogram of three reduction waves of $FeF_{20}TPPCl$ *in THF (blue), 20%*$AmNTF_2$ *(red) and 20%*$BMImPF_6$ *(green).*

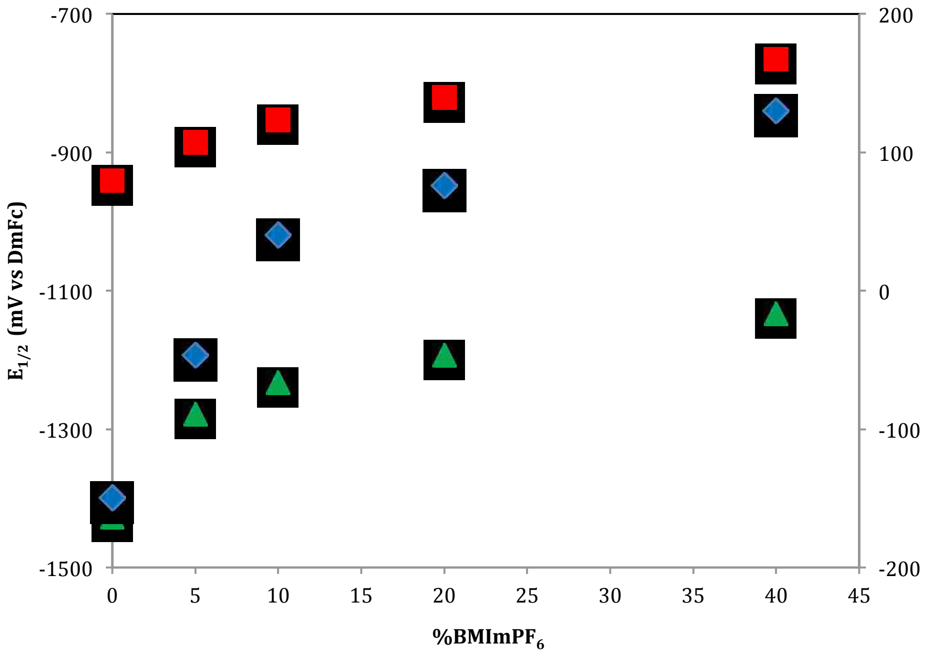

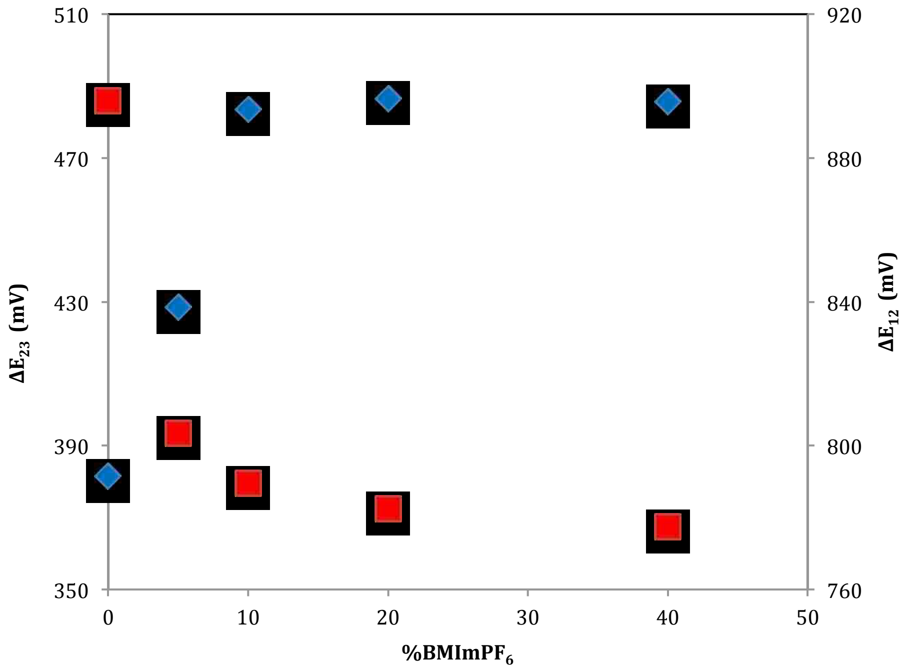

Figure 147: Variation of $E_{1/2,1}$ (diamonds), $E_{1/2,2}$ (squares), $E_{1/2,3}$ (triangles) and ΔE_{12} (diamonds) and ΔE_{23} (squares) for $FeF_{20}TPPCl$ in THF-%$BMImPF_6$ mixtures.

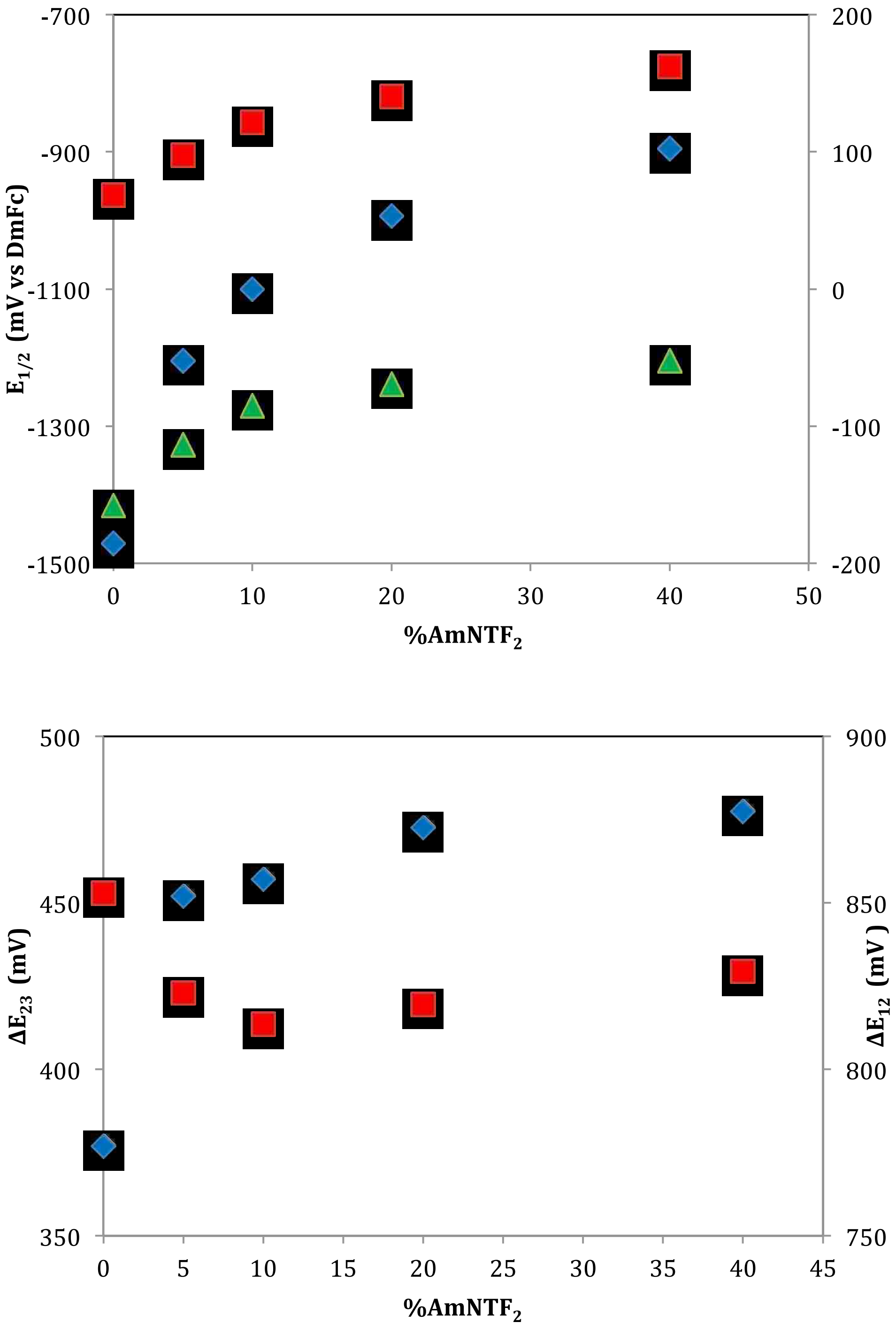

Figure 148: Variation of $E_{1/2,1}$ (diamonds), $E_{1/2,2}$ (squares), $E_{1/2,3}$ (triangles) and ΔE_{12} (diamonds) and ΔE_{23} (squares) for $FeF_{20}TPPCl$ in THF-%$AmNTF_2$ mixtures as a function of %RTIL.

Cyclic voltammetry of $FeF_{20}TPPClO_4$ was also carried out in mixtures of up to 40% RTILs (*Figure* ***149***). Shifts of the corrected potentials showed that at 40%RTIL, the three waves were shifted, respectively, by 62, 194 and 283 mV in imidazolium mixtures and by 53, 188 and 218 mV in ammonium mixtures (Figures 150-151). Displacement of the perchlorate anion by the solvent made the $E_{1/2,\,1}$ value less sensitive to the presence of the RTIL in mixtures and reduced the ΔE_{12} value.

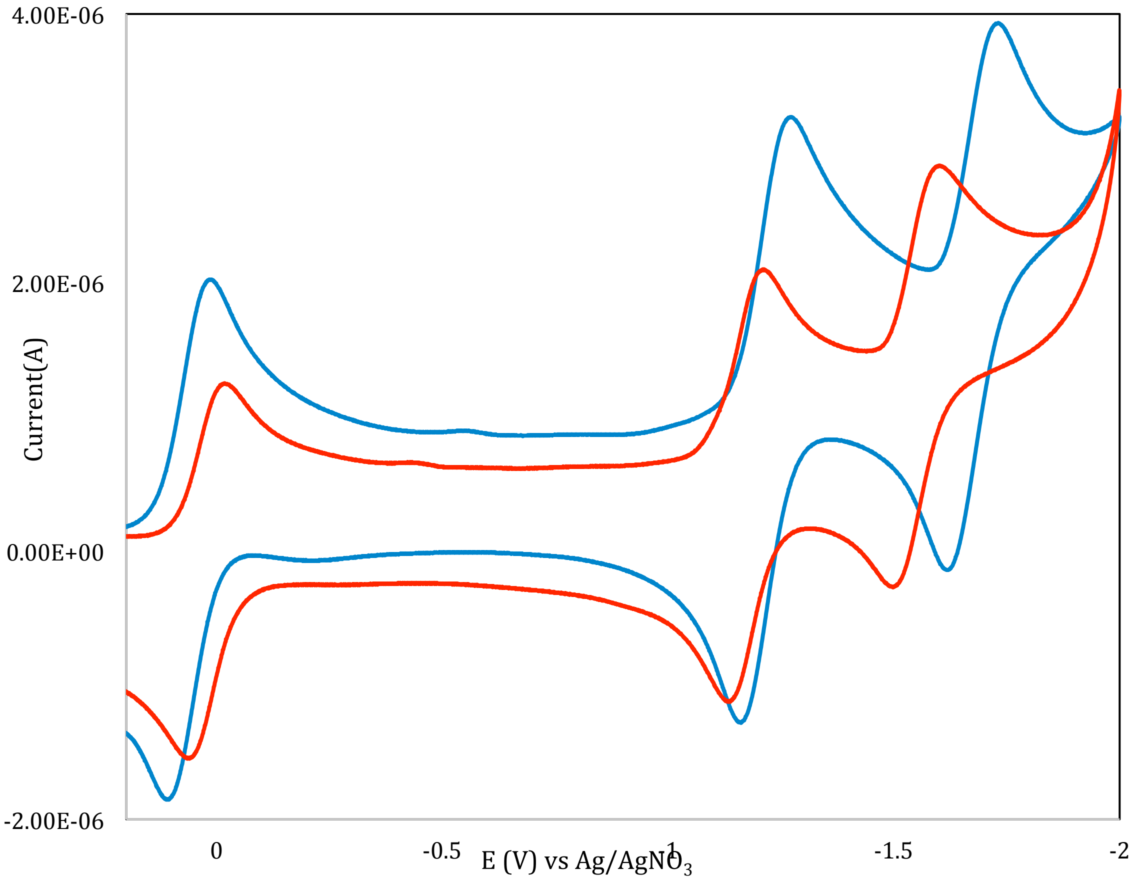

Figure 149: Voltammogram of three reduction waves of $FeF_{20}TPPClO_4$ in THF and 20%$BMImPF_6$.

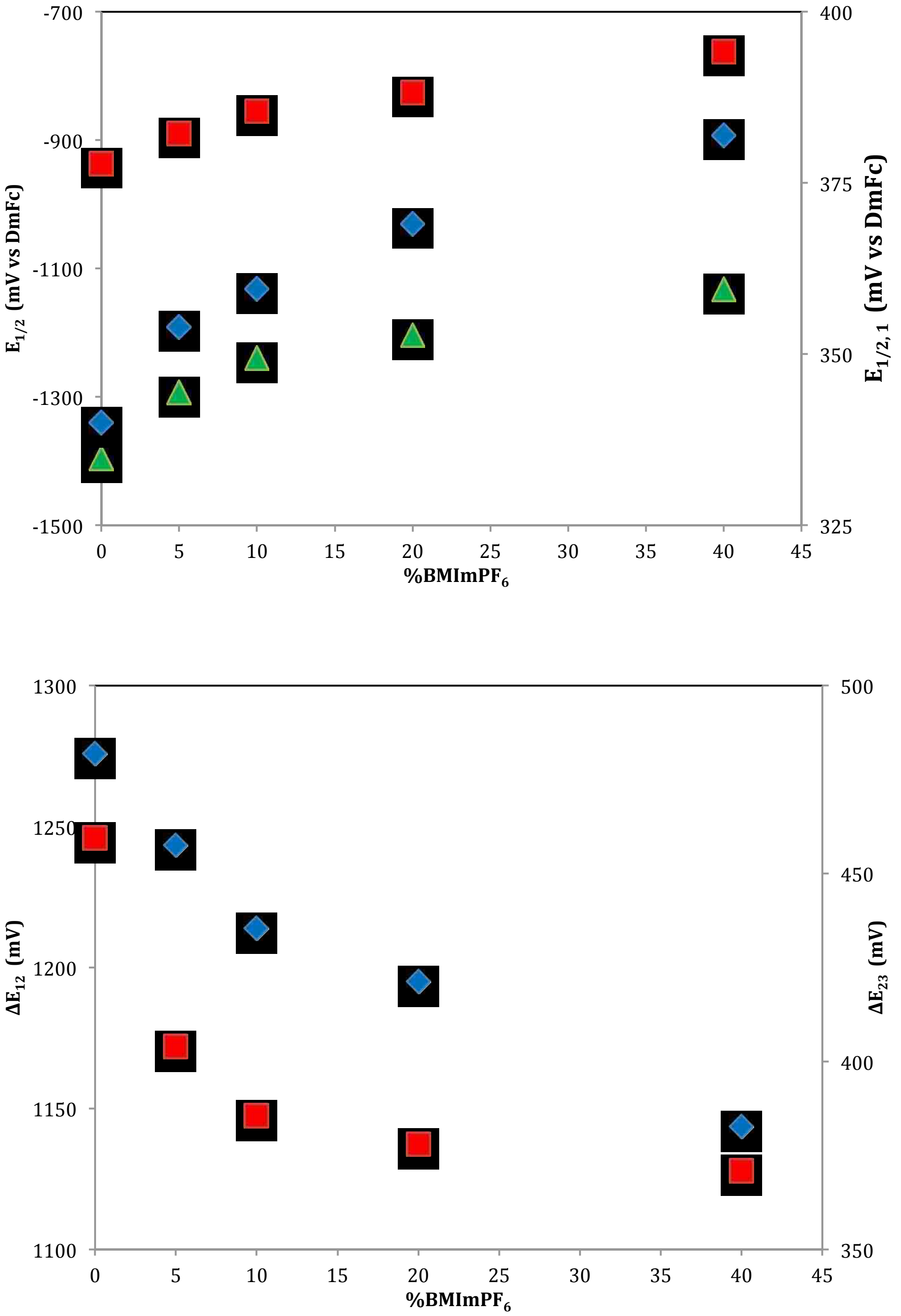

Figure 150: Variation of $E_{1/2,1}$ (diamonds), $E_{1/2,2}$ (squares), $E_{1/2,3}$ (triangles) and ΔE_{12} (diamonds) and ΔE_{23} (squares) for $FeF_{20}TPPClO_4$ in THF-%$BMImPF_6$ mixtures.

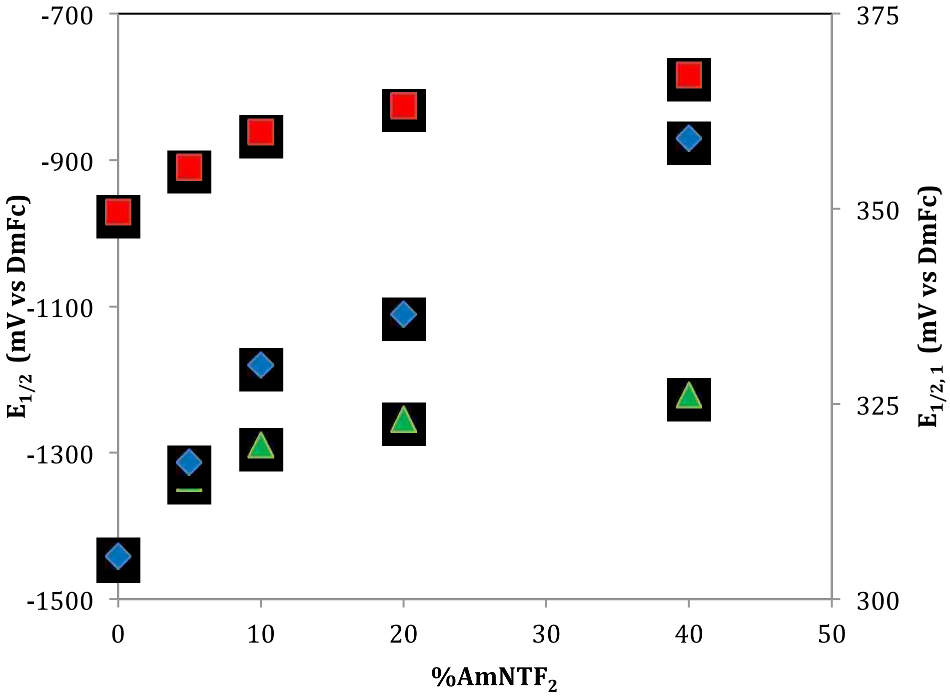

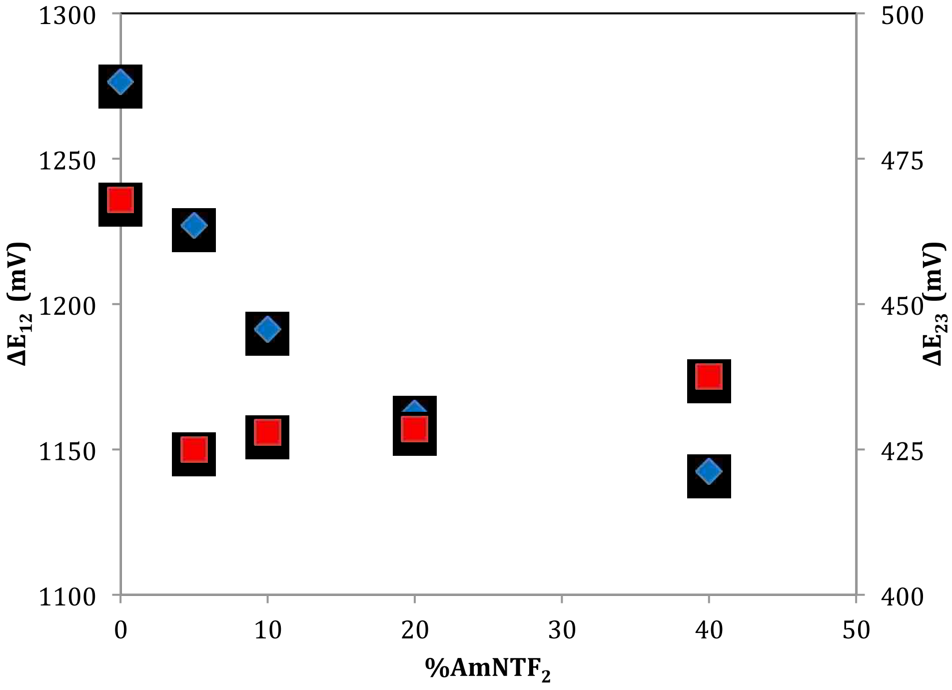

Figure 151: Variation of $E_{1/2,1}$ (diamonds), $E_{1/2,2}$ (squares), $E_{1/2,3}$ (triangles) and ΔE_{12} (diamonds) and ΔE_{23} (squares) for $FeF_{20}TPPClO_4$ in THF-%$AmNTF_2$ mixtures.

7.1.2 Potential shifts vs Gutmann AN

As was done for the previous redox systems, the potential shifts were assessed with respect to the acceptor properties of the mixture. *Figure **152*** shows shifts of half potentials as a function of Gutmann AN of the mixtures. The excellent correlation of $E_{1/2}$ values with AN showed that the potential shifts can be predicted by the acceptor properties of the mixture. Such linear relationship appeared to be more consistent than the correlations with solvent donicity, reported by Kadish.[151] In that work, the first reduction potential of FeTPPCl was about 200mV more negative than the values predicted by donor number of THF.

A small slope of 2.9 mV/AN was observed for the first reduction of the $FeF_{20}TPPClO_4$, showing weak and/or equivalent interactions of both oxidized and reduced species with RTIL components

In contrast, exchanging the perchlorate with chloride counter anion resulted in larger slope of 20.8 mV/AN for the first reduction wave of $FeF_{20}TPPCl$, indicating higher stabilization of the reduction products over the reactants by the RTIL. The largest slope 21.5 mV/AN was observed for the third wave, consistent with a strong interaction of the negatively charged species with the RTIL. It is worth noting that, at similar AN, the potentials were slightly more stabilized by the ammonium ionic liquid compared to the imidazolium RTIL. The higher shifts observed in imidazolium mixtures, at same RTIL fractions, were mainly due to rise of the solution AN.

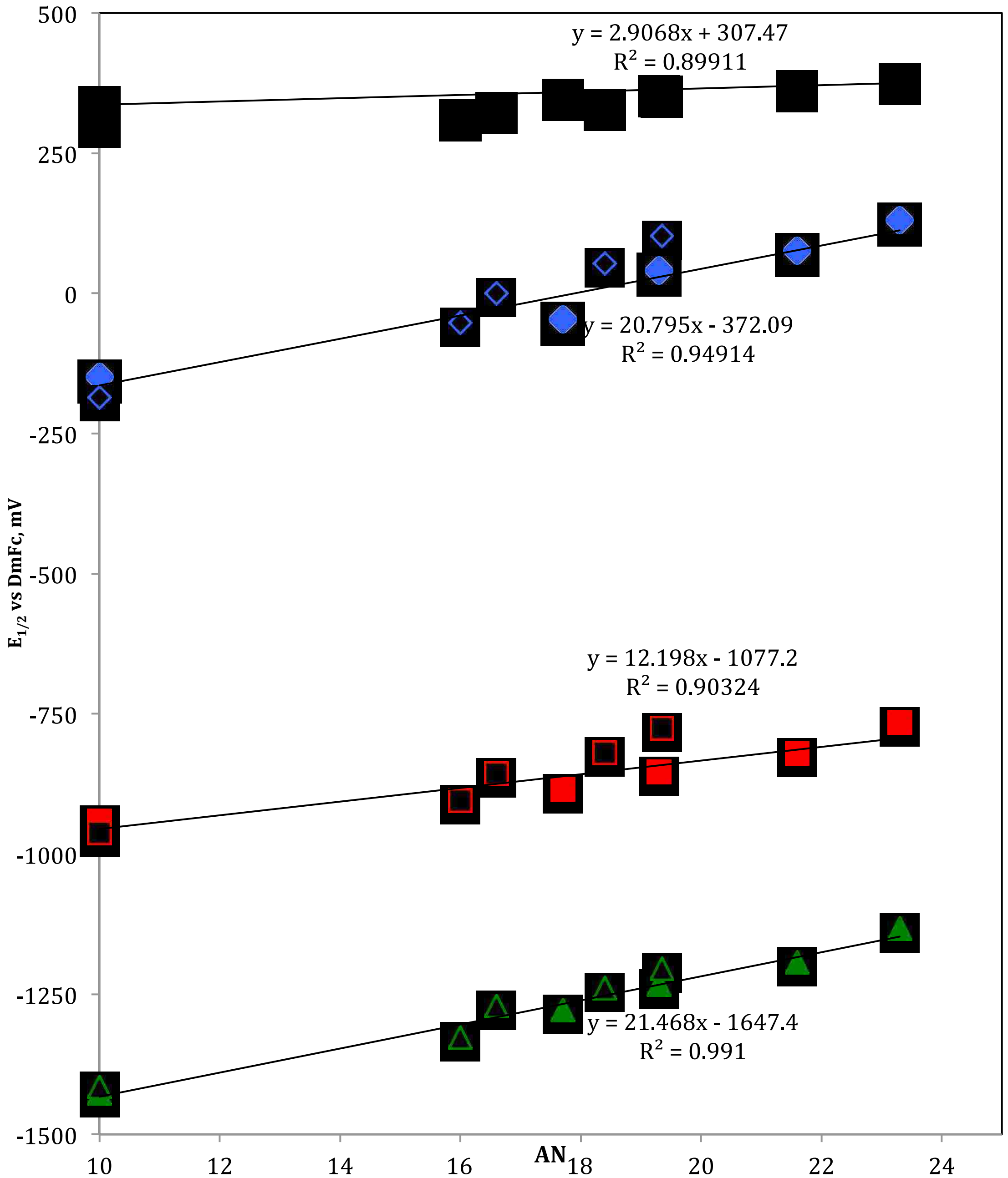

Figure 152: Variation of $E_{1/2}$ with AN of THF-%RTIL: BMImPF$_6$ (filled) and AmNTF$_2$ (empty) FeF$_{20}$TPPCl: $E_{1/2,\ 1}$ (diamonds), $E_{1/2,\ 2}$ (squares), $E_{1/2,\ 3}$ (triangles). FeF$_{20}$TPPClO$_4$: $E_{1/2,\ 1}$ (circles)

7.1.3 UV-visible Spectroelectrochemistry

Figure ***153*** shows the UV-visible spectroelectrochemistry of $FeF_{20}TPPCl/ClO_4$ for the three reduction waves in THF. The three reductions were reversible in the electrolysis time scale. The change in axial ligation from Cl^- to ClO_4^- shifted the Soret band of the ferric species from 412 to 394 nm. A similar shift (from 407 to 390 nm) was observed, when the chloride was displaced by methanol in acetonitrile solution of $FeF_{20}TPPCl$.[127] Here, the weak perchlorate counter anion was displaced by THF solvent.

The first reduction shifted the Soret band from 412 to 418nm, forming the metal reduced ferrous species. A red shift of 1 nm was observed for FeTPPCl in methylene chloride, which was attributed the intermediate spin ferrous species, whereas a 21nm shift was characteristic for the formation of low spin ferrous species in THF.[154,155] The second reduction product exhibited significant bleaching of the Soret band with spectral features at 318, Soret 376 and 458nm, 516, 580 and 700nm at the Q band region. These features were comparable with a metal centered reduction product, the low valent $Fe^{I}TPP^-$ in THF.[153] Strong bleaching of the Soret band was consistent with a withdrawing effect of the fluorinated phenyls, which tend to delocalize the charge onto the ligand moiety. Hence, the spectrum of the second reduction product $FeF_{20}TPP^-$ can be attributed to low valent $Fe^{I}F_{20}TPP^-$ with significant delocalization to the ring. The third reduction with spectral features at 350, 450nm, 520nm and a small broad band above 700nm can be reasonably attributed to $Fe^{I}F_{20}TPP^{2-}$ dianion.[153] Spectra of the reduction products were similar for both complexes, indicating no coordination of the counter anions to the reduced metal centers in THF.

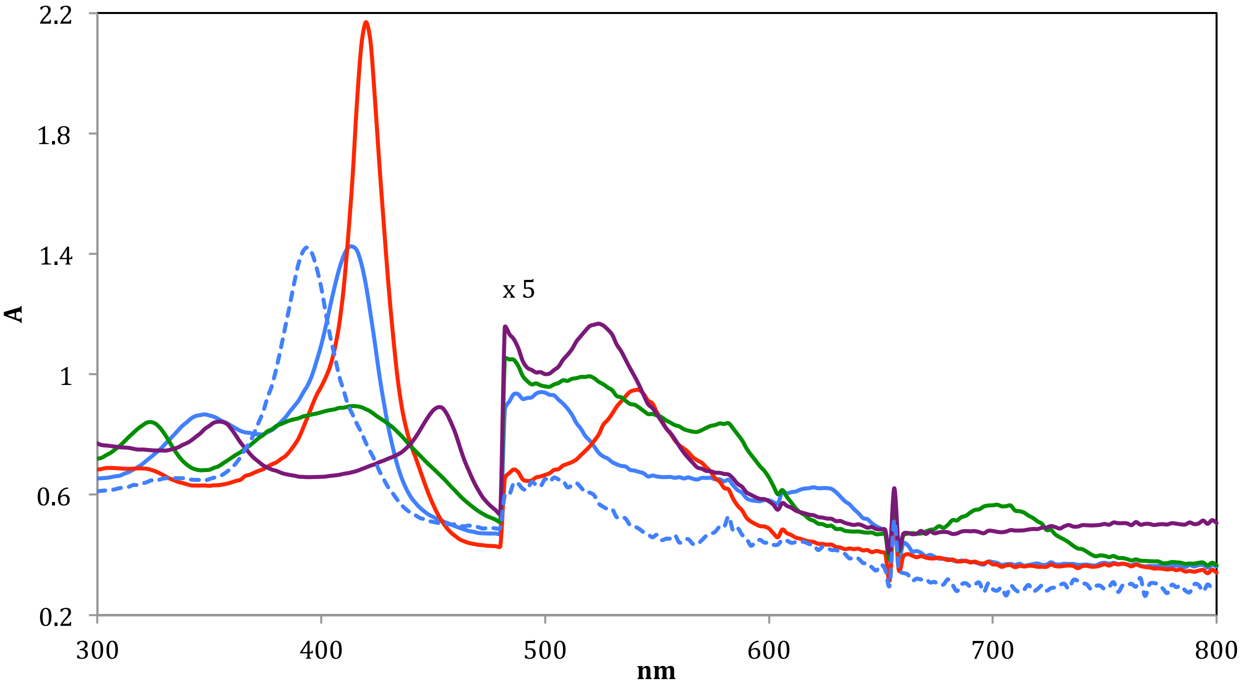

Figure 153: UV-vis spectroelectrochemistry of 0.2 mM $FeF_{20}TPPCl$ *(solid blue) in THF.* $FeF_{20}TPP$ *(red),* $FeF_{20}TPP^{-}$ *(green),* $FeF_{20}TPP^{2-}$ *(violet),* $FeF_{20}TPPClO_4$ *(dashed blue).*

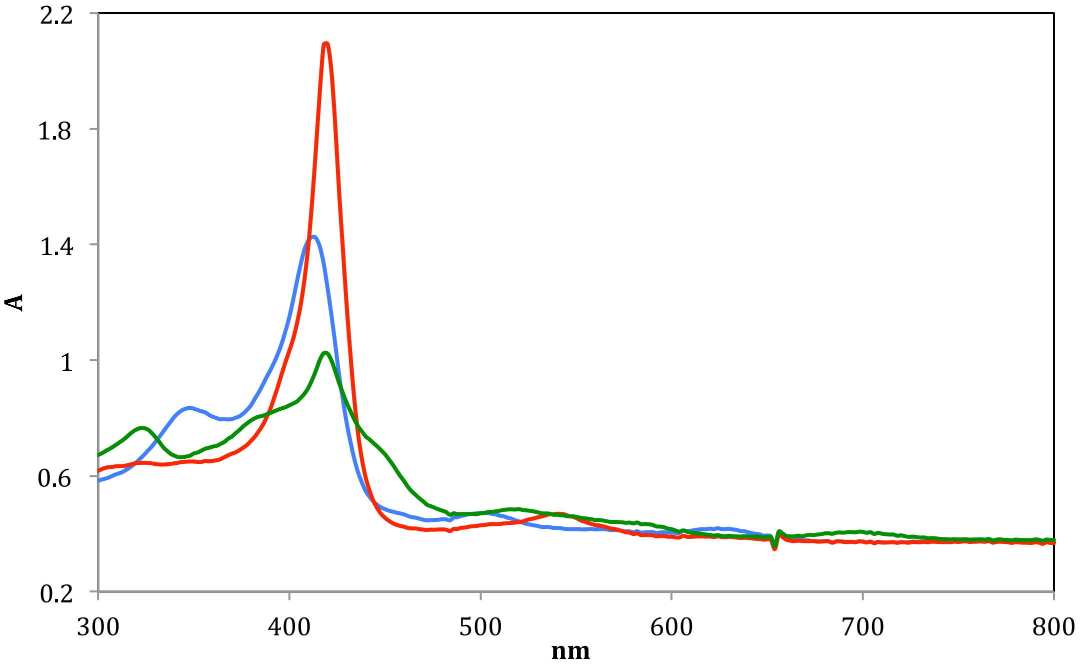

Figure 154: UV-vis spectroelectrochemistry of 0.2 mM $FeF_{20}TPPCl$ *(blue) in THF-20%RTIL.* $FeF_{20}TPP$ *(red),* $FeF_{20}TPP^{-}$ *(green).*

The UV-visible spectroelectrochemistry was carried out for the two first reductions of $FeF_{20}TPPCl$ in mixtures THF-%RTIL (*Figure **154***). For both complexes, the reductions were reversible in the electrolysis time scale. At higher RTIL fractions, the increase in solution viscosity resulted in slow diffusion, which required long electrolysis time.

Comparison of the spectra of each species, as a function of RTIL concentration, reveals important observations. Upon addition of the RTIL to the THF solution, the Soret band of the ferric species became significantly broader with a shoulder around 406nm. This broadness may indicate some change on the ligation of the metal center (*Figure **155***). In these mixtures, the ferrous species showed similar spectra, with few changes in the Q band region (*Figure **156***). Due to its low absorptivity, the spectral features of second reduction product were obtained from difference spectra with the ferrous species. Interestingly, addition of RTIL blue shifted the spectrum of $FeF_{20}TPP^-$, where the Soret band was moved by almost 18nm (458 to 440nm), when going from 0 to 50%RTIL (*Figure **157***).

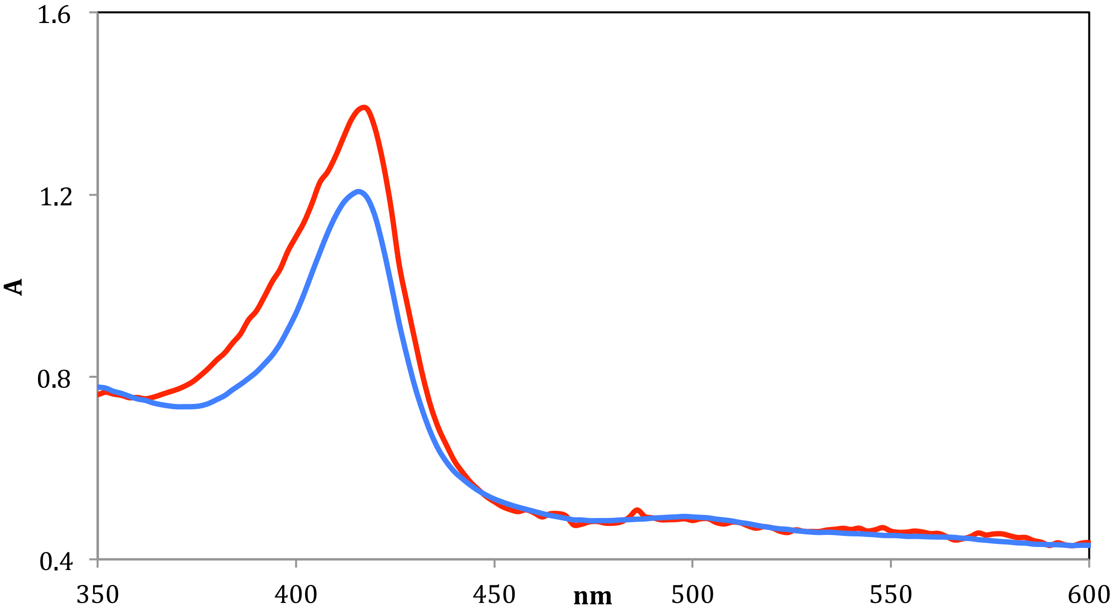

Figure 155: $FeF_{20}TPPCl$ in THF (blue) and 50%RTIL (red)

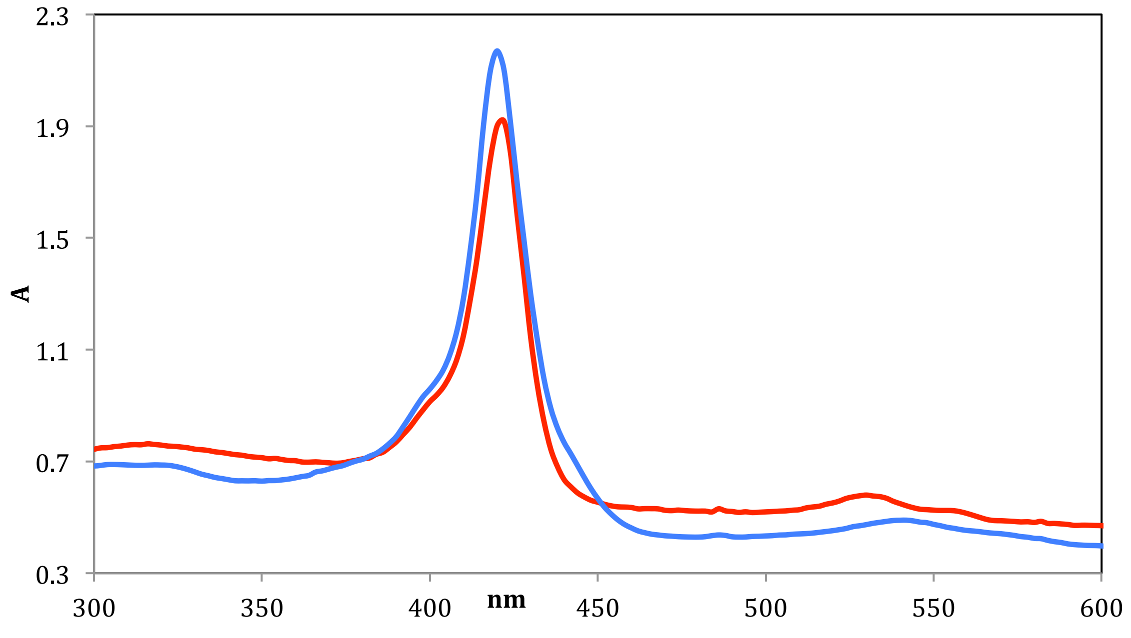

Figure 156: FeF$_{20}$TPP in THF (blue) and 20%RTIL (red).

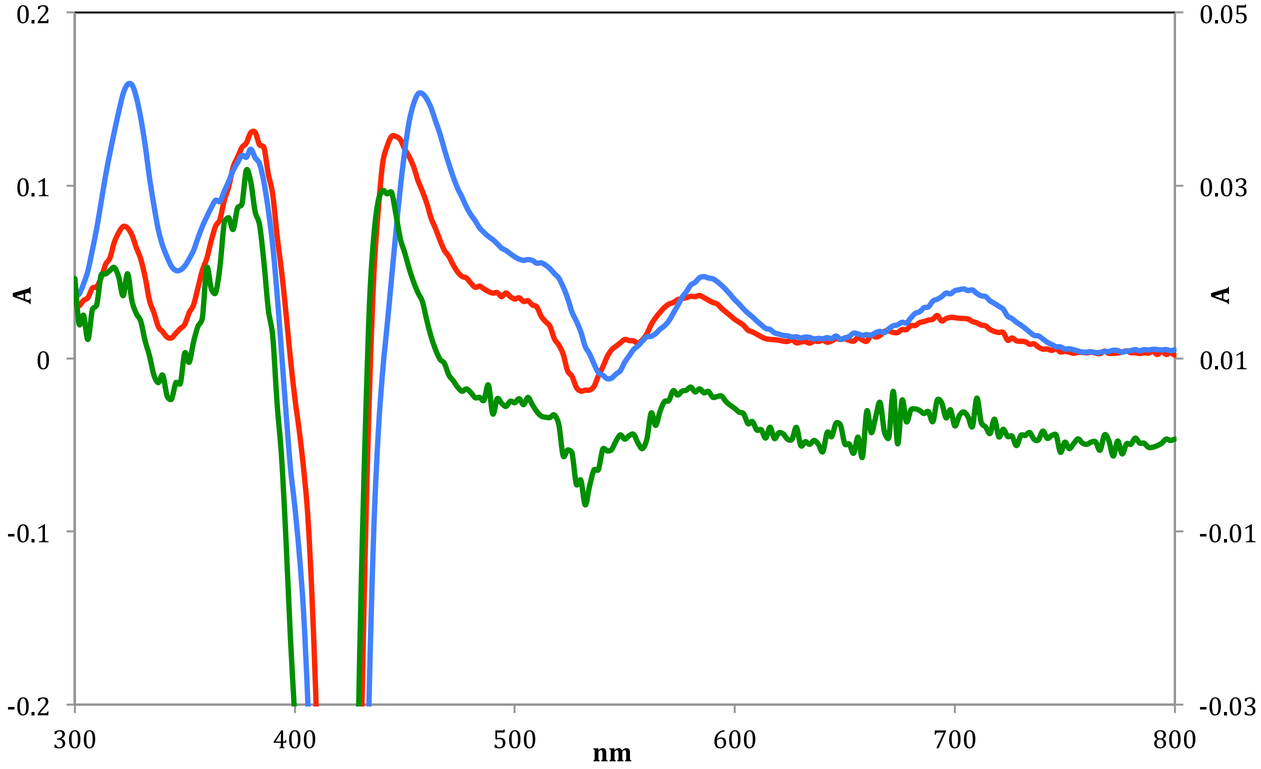

Figure 157: FeF$_{20}$TPP^{-} in THF (blue), 20 (red) and 50% (green) RTIL.

7.1.4 ^{19}F-NMR

In order to probe changes in the solvation environment and/or the electronic structures of solutes upon RTIL introduction, ^{19}F-NMR of the redox products was carried out in mixtures. The two first reductions products of our complex were chemically prepared as described in the experimental part (*Chap. 2*). It is worth noting that the lower potentials of the first two waves enabled us to obtain the one and the two electrons reduced products using same reducing agent $TBABH_4$. The use of this reducing agent kept the ionic environment similar to the spectroelectrochemical experiments. These features further justified our choice of fluorinated porphyrin compared to other ligands. In THF, the perchlorate ClO_4^- anion was mostly displaced by the solvent, resulting in a positively charged six coordinated ferric species. Hence, the three prepared complexes had three distinct total charges, positive, neutral and negative. This charge difference will be important to understand the interactions solute-solvent in an ionic environment. The ^{19}F-NMR spectrum of the positively charged ferric species shows three resonances, *o*: -135ppm, *m*: -162ppm and *p*: -153ppm (*Figure **158***). This spectrum was consistent with reported spectrum of positively charged ferric species $FeF_{20}TPP(MeOH)^+$ in acetonitrile.[127] First electron reduction downshifted the fluorine resonance to *o*:-142ppm, *m*: -167ppm and *p*: -159ppm for the neutral ferrous species. This spectrum was similar to the reported high spin ferrous species in THF.[130] Upon the second reduction, the signals were shifted to o: -141ppm, m: -173ppm and p: -162ppm for the negatively charged $FeF_{20}TPP^-$. No spectrum has been reported for this species in literature.

The ^{19}F-NMR spectra of the three redox products in mixtures THF-%RTIL are shown in Figures 159-161. In general, the signals obtained in the mixtures were slightly broader than in THF. This broadness would be due to less tumbling in the more viscous media, resulting in faster relaxation. For the positively ferric species, the addition of the RTIL showed the presence of only one species, having comparable spectral features to that in THF. Similar to the ferric species, addition of RTIL to THF solution of the neutral ferrous species had no significant effect on the spectrum, and one species could be observed in the mixture. Slight shifts of 1ppm were observed though, when going from THF to the mixtures.

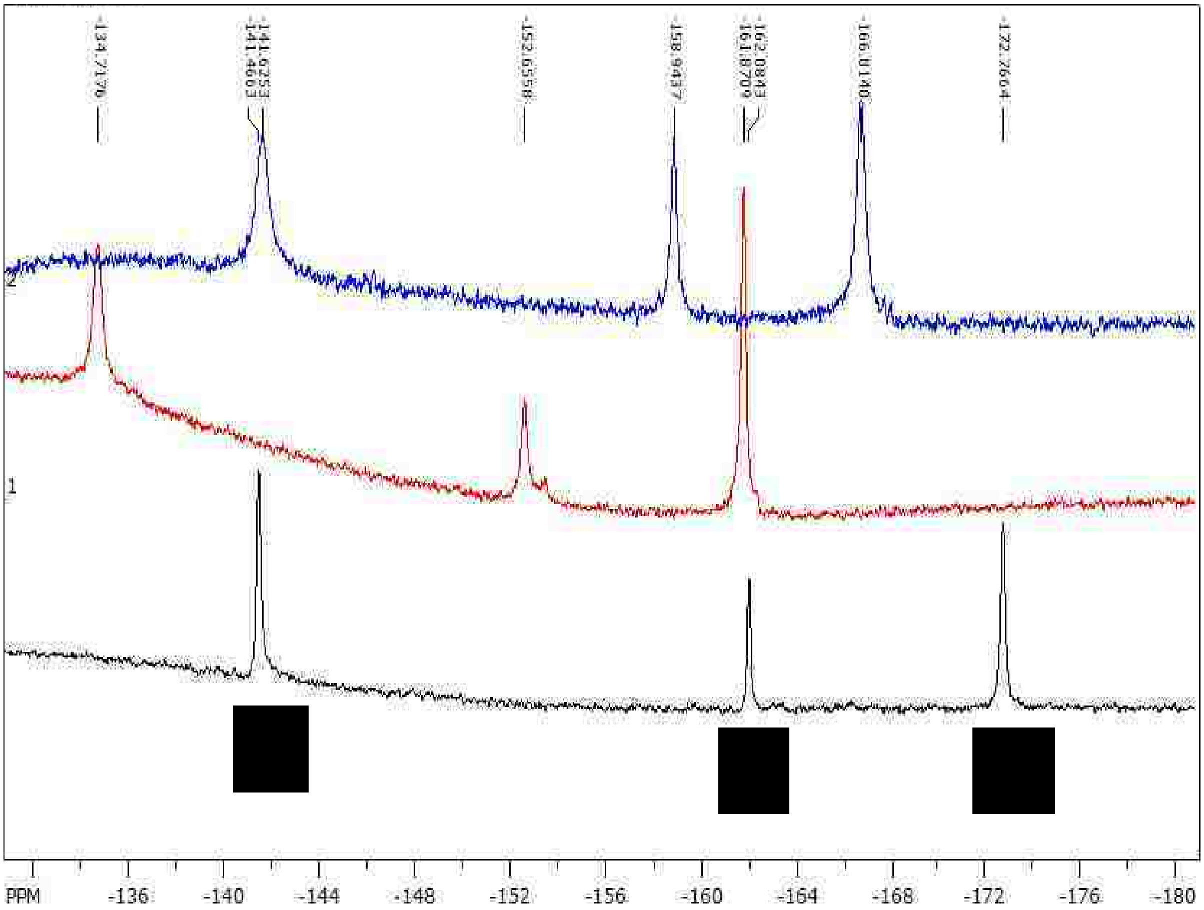

Figure 158: ^{19}F-NMR of $FeF_{20}TPPClO_4$ (red), $FeF_{20}TPP$ (blue) and $FeF_{20}TPP^-$ (black) in THF

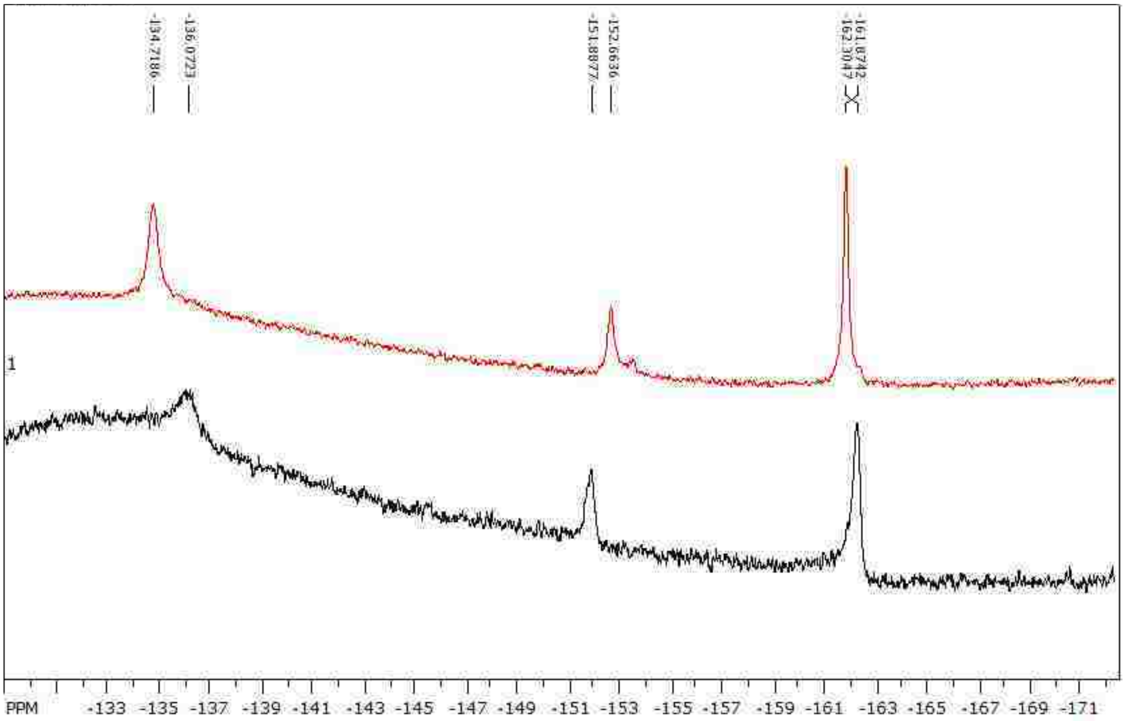

Figure 159: ^{19}F-NMR of FeFe$_{20}$TPPClO$_4$ in THF (red) and 70%RTIL (black)

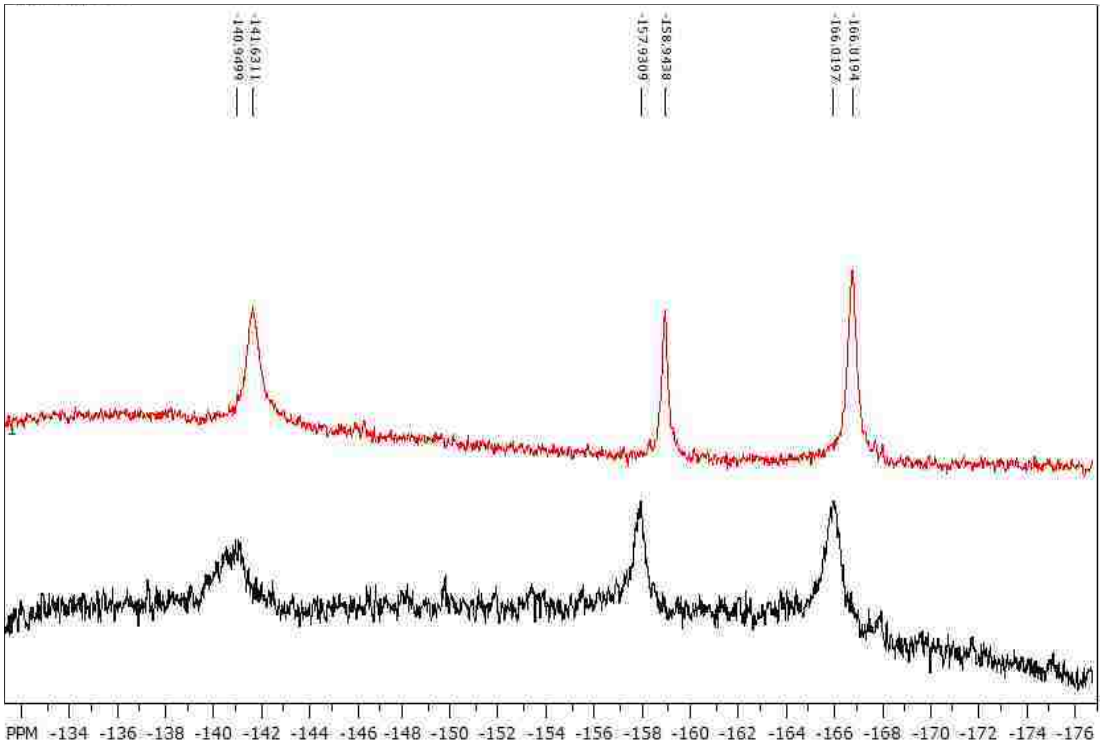

Figure 160: ^{19}F-NMR of FeFe$_{20}$TPP in THF (red) and 50%RTIL (black)

Due to the observed shift in the UV-visible spectrum for the negatively charged $FeF_{20}TPP^-$, the RTIL fraction was increased to 90% in the ^{19}F-NMR experiments (*Figure **161***). The results showed that even at these high RTIL fractions, only one species was observed. A single species may be due to the complex in one phase, or rapid exchange between the phases. While the shape of $FeF_{20}TPP^-$ spectrum didn't change much, significant shifts of the fluorine signals were observed in the mixture. A shift of 3ppm was observed for the *m* and *p* resonances, when going from 0 to 90%RTIL.

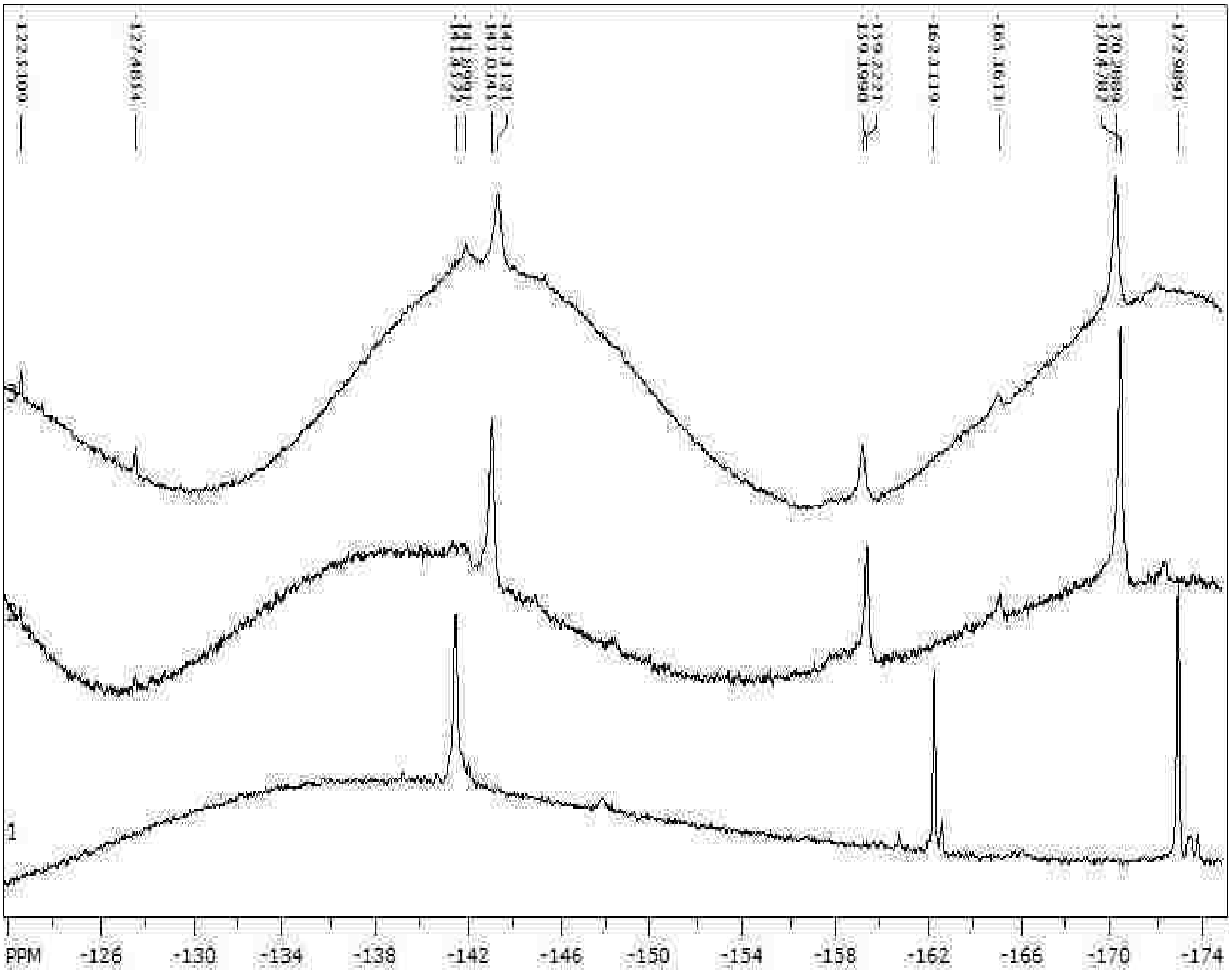

Figure 161: ^{19}F-NMR of $FeFe_{20}TPP^-$ in THF, 80 and 90%RTIL from bottom to top, respectively.

7.1.5 Discussion

The voltammetry of $FeF_{20}TPPCl(ClO_4)$ in the molecular rich mixtures showed a large stabilization of the first three reduction waves with the introduction of an RTIL. These shifts may be correlated with changes in the charge of the redox products. For $FeF_{20}TPPClO_4$, displacement of the weak ligand ClO_4^- anion by solvent, resulted in the formation of a positively charged ferric species in solution. This displacement made the first wave less sensitive to the RTIL and shifted the potential only by 50mV at 40%RTIL. Such a small shift also indicated weak interactions of the positively charged ferric species with RTIL components. The small slope of the $E_{1/2}$ vs AN plot further indicated weak interactions of both ferric (reactant) and ferrous (product) species with RTIL components. This weak interaction was also consistent with the results of UV-visible spectroelectrochemistry and ^{19}F-NMR, where the addition of the RTIL had no significant effect on the electronic structure of the ferric/ferrous species.

In contrast, a large stabilization of the first reduction wave of $FeF_{20}TPPCl$ by about 300mV at 40%RTIL was observed. While the cationic ferric and neutral ferrous species had more affinity to THF, the large shift is mainly attributed to the strong solvation of the reduction by-product, Cl^- anion, by the RTIL. This preferential partitioning of ferric/ferrous complexes in THF domain and the counter anion into the RTIL domain could be also observed at the voltammetric reoxidation reaction of the first wave. Although it was reasonable to expect a slow coordination of the chloride anion in a very viscous media (due to slow diffusion), this feature was observed at small concentrations (10 to 20%) of RTIL.

These effects were quite indicative of the presence and impact of nano-domains on the solvation of solutes in the mixture.

As was mentioned, the UV-visible and NMR analysis showed that the electronic structure of the ferrous species was not significantly affected by the RTIL introduction. This is expected for a neutral species to be mostly solvated in the molecular domain in the mixture. However, the voltammetry shows a large stabilization (200mV at 40%RTIL) of the second wave by introduction of the ionic liquid. This shift was attributed to stronger interactions of the RTIL with the second reduction product $FeF_{20}TPP^-$, a negatively charged species. The slope of 12.2 mV/AN for $E_{1/2,\,2}$ vs AN was consistent with RTIL stabilization of the negatively charged species compared to the neutral ferrous product. Such strong interactions blue shifted the UV-visible spectrum by about 18nm at only 40%RTIL. Although the NMR analysis at very high concentrations of RTIL showed the presence of only one species, the shift (3ppm) of the fluorine resonance in the mixture indicated strong interactions of this negatively charged species with RTIL. This feature will be further studied in the second part of this investigation.

At this stage, not much effort has been dedicated to the study of the RTIL effect on the third wave product, a doubly charged radical dianion. However, the voltammetric results showed a large stabilization (about 300mV) of this wave upon RTIL additions, consistent with the partitioning of this species into the RTIL domain in the mixture. This stabilization could be also predicted by Gutmann AN, which exhibited a large slope of 21.2 mV/AN for $E_{1/2,\,3}$. Finally, the stronger interactions of ammonium over imidazolium ionic liquid with redox products, in mixtures with similar AN, is very likely due to the structural flexibility of the ammonium over the planar imidazolium cation.

7.2 Electrochemistry in RTIL rich mixtures

7.2.1 Cyclic voltammetry

In this part, we have restricted our analysis to the first two reduction waves in $AmNTF_2$-%THF mixtures. The choice of the $AmNTF_2$ RTIL arises from the higher solubility of our complex, lower impurities content and faster diffusion (lower viscosity) in this ionic liquid compared to imidazolium RTIL.

The two reductions waves of $FeF_{20}TPPCl$ in pure $AmNTF_2$ appear reversible, with half potentials at -0.23V and -1.15V versus $Ag/AgNO_3$ (*Figure **162***). The second reduction shows two reoxidation pathways, which indicated a chloride coordination to the metal center.

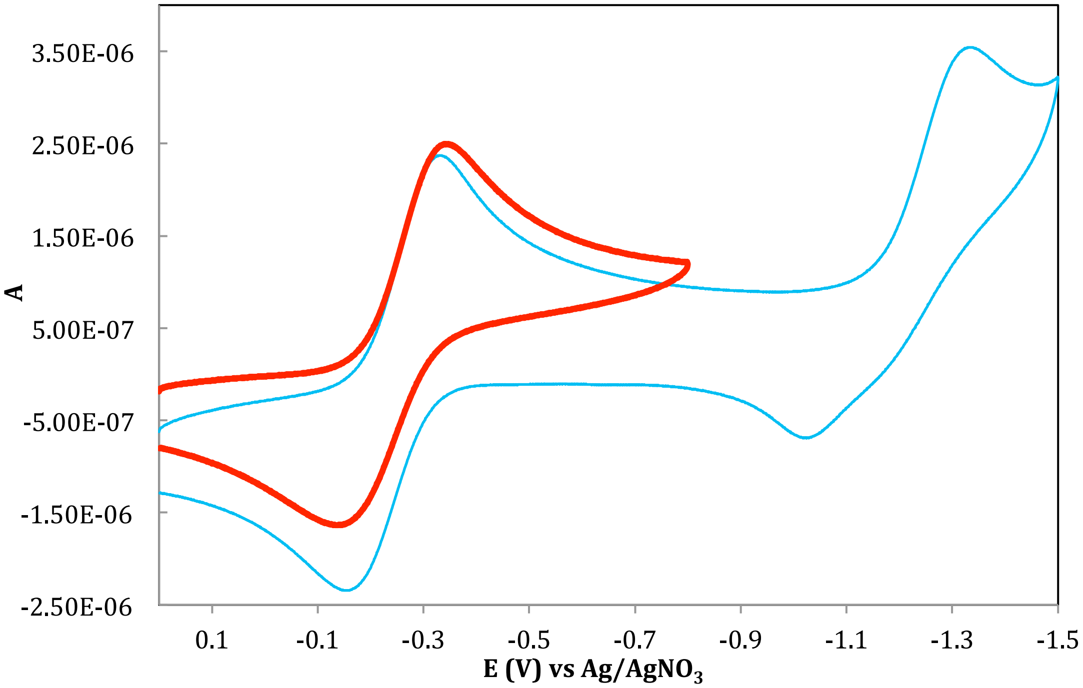

Figure 162: Cyclic voltammetry of $FeF_{20}TPPCl$ in pure $AmNTF_2$. 100mV/s

As expected, the addition of THF to $AmNTF_2$ solution of $FeF_{20}TPPCl$ shifted the first wave to more negative values, while the second wave was significantly stabilized (*Figure **163***). In these mixtures, the competition of solvent/counter anion to coordinate with the metal center was observed at the first wave.

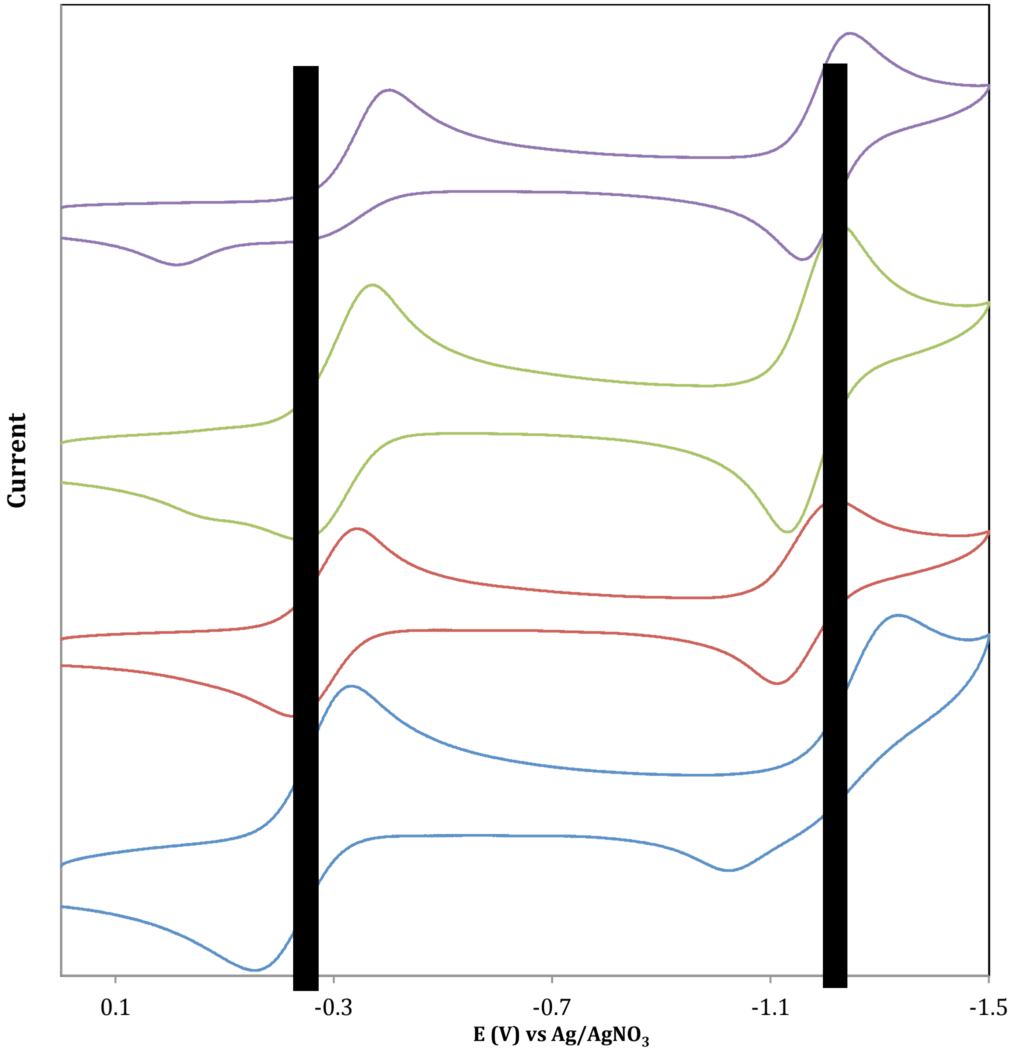

Figure 163: Cyclic voltammetry of $FeF_{20}TPPCl$ in RTIL, 20, 50 and 80%THF, from bottom to top, respectively.

Further addition of THF has completely switched the coordination of the ferric metal center to the solvent, THF. Repetitive voltammetry or scanning through the second wave didn't affect the course of the first reoxidation (*Figure **164***).

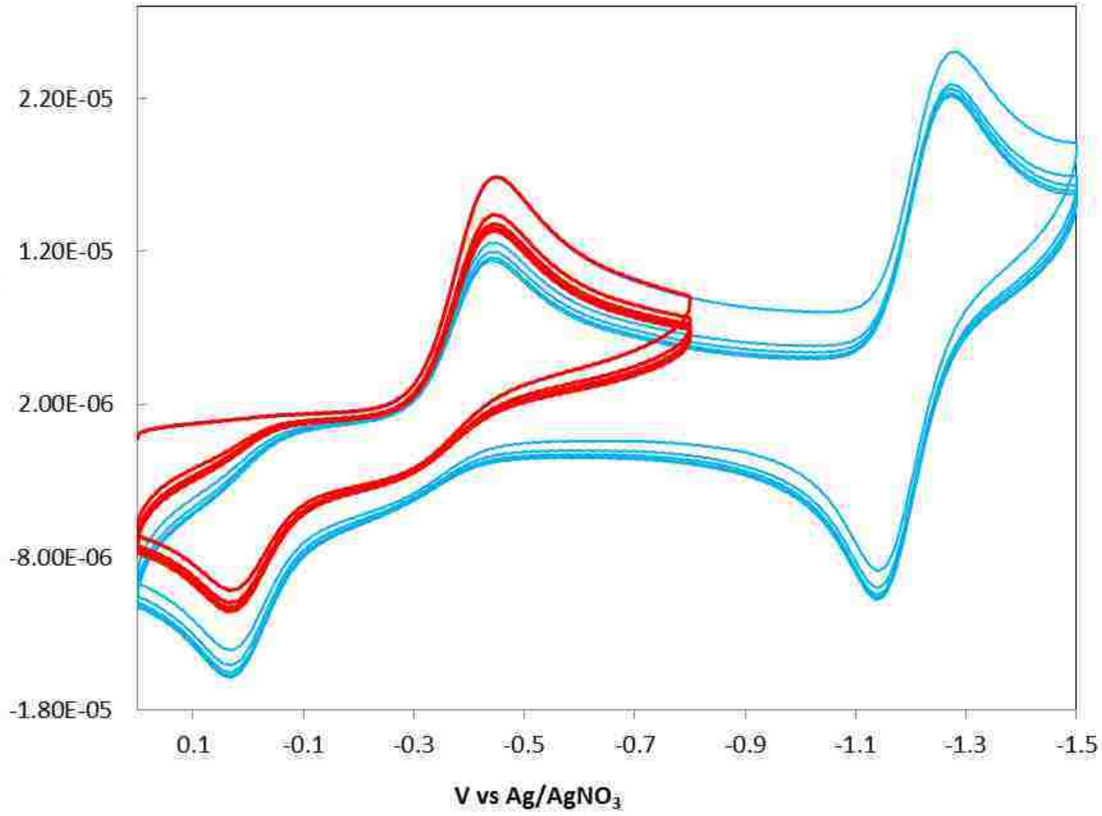

Figure 164: Repetitive cyclic voltammetry of FeF$_{20}$TPPCl in RTIL-80%THF

7.2.2 UV-visible Spectroelectrochemistry

7.2.2.1 In pure RTIL

The spectroelectrochemistry of $FeF_{20}TPPCl$ was carried out in pure $AmNTF_2$ and in mixtures, at the first and second reduction waves. *Figure* ***165*** shows the spectral changes upon first reduction of $FeF_{20}TPPCl$ in pure RTIL. The results showed a reduction product with a Soret band at 434nm, exhibiting a red shift of about 14nm compared to one seen in THF (420nm). Larger shifts (21nm), with the Soret band at 445nm, were reported for the imidazole coordinated low spin ferrous species in THF.[154] Reoxidation regenerated the ferric species. More interestingly, scanning through the potential of the second reduction led to a continuous increase of the 434nm band, without significant change in the isosbestic points (*Figure* ***166***). Reverse electrolysis enabled a complete reoxidation to a ferric species, with a slight shift (406nm) of the Soret band compared to the starting material (410nm). From these results, the spectral features of the reduced species in the RTIL were quite different from the one observed in THF. More surprising, it looks that the spectra of both first and second reductions products had similar features, Soret band at 434 and Q band at 558nm in RTIL.

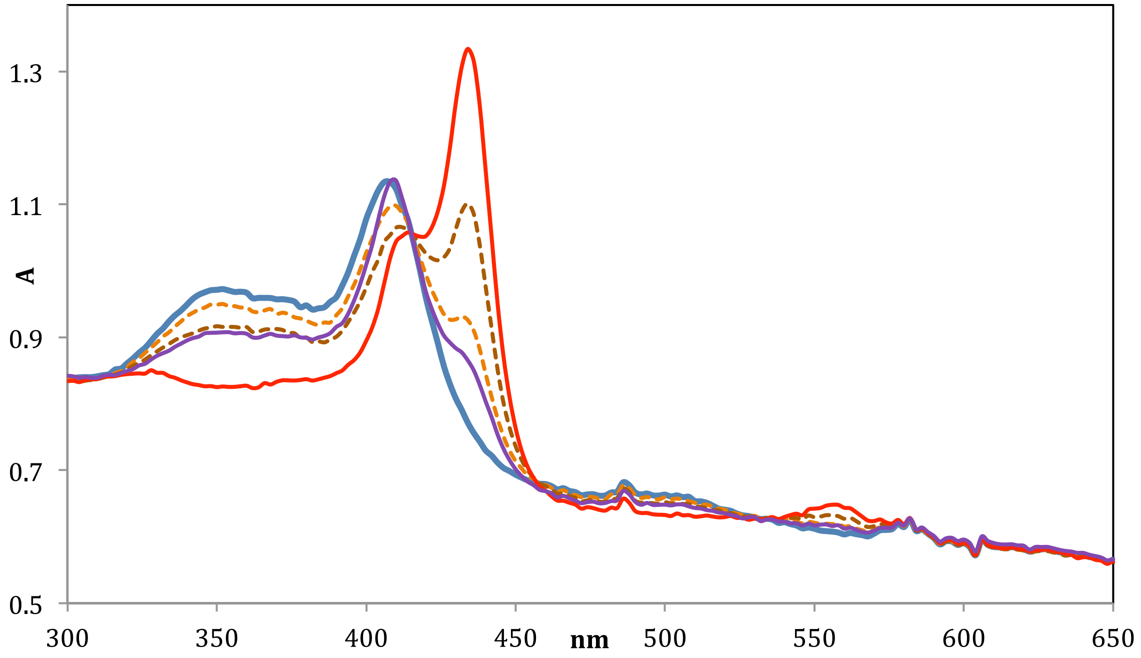

Figure 165: UV-visible SEC of FeF$_{20}$TPPCl in AmNTF$_2$. Starting material (blue), first reduction product (red, -0.6V vs Ag/AgNO$_3$) and intermediate spectra (dashed)

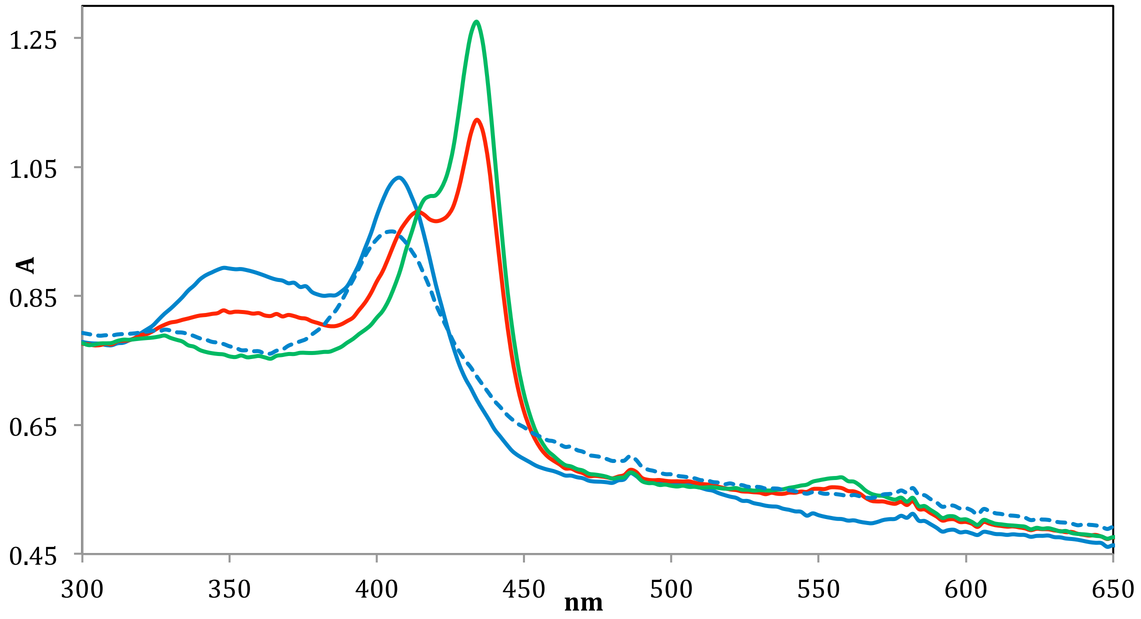

Figure 166: UV-visible SEC of FeF$_{20}$TPPCl in AmNTF$_2$. Starting material (blue), first reduction (red, -0.4V), second reduction (green, -1.2V) and reoxidation (dashed, +0.2V) products. Potentials are versus Ag/AgNO$_3$.

In order to verify out the spectral features of the two reduction products, the spectroelectrochemistry of the chemically prepared ferrous species was carried out in pure RTIL. *Figure **167*** shows the electrolysis of $Fe^{II}F_{20}TPPCl^-$ in $AmNTF_2$, at the first (oxidation) and the second (reduction) wave. As was seen for the reduction of $Fe^{III}F_{20}TPPCl$, the starting material exhibits a Soret band at 434nm with a shoulder around 418nm. Oxidation of this ferrous species gave a ferric species with 406nm, while its reduction showed formation of 434nm species. At the end of this electrolysis experiment, where the final potential was set to the starting material range, the ferrous species exhibited a Soret band mostly at 418nm with a shoulder at 434nm. *Figure **168*** shows the results when the electrolysis was repeated, by starting from the end solution of the first experiment. This time, the oxidation product had a Soret band at 394nm, the reduction product at 434nm and the final product 418nm.

These repetitive electrolysis experiments showed clearly the effect of the chloride coordination to metal center of the ferrous species. When the chloride is coordinated, the ferrous species exhibits a Soret band at 434nm. Upon reoxidation, the spectra showed different coordinations to the ferric 410nm (Cl^-), 394nm (solvent) and a 406nm species. As the increase of 434nm band was highly potential dependent, upon reduction of the ferrous species, this feature can be reasonably attributed to the formation of the second reduction product $FeF_{20}TPP^-$ (more details below).

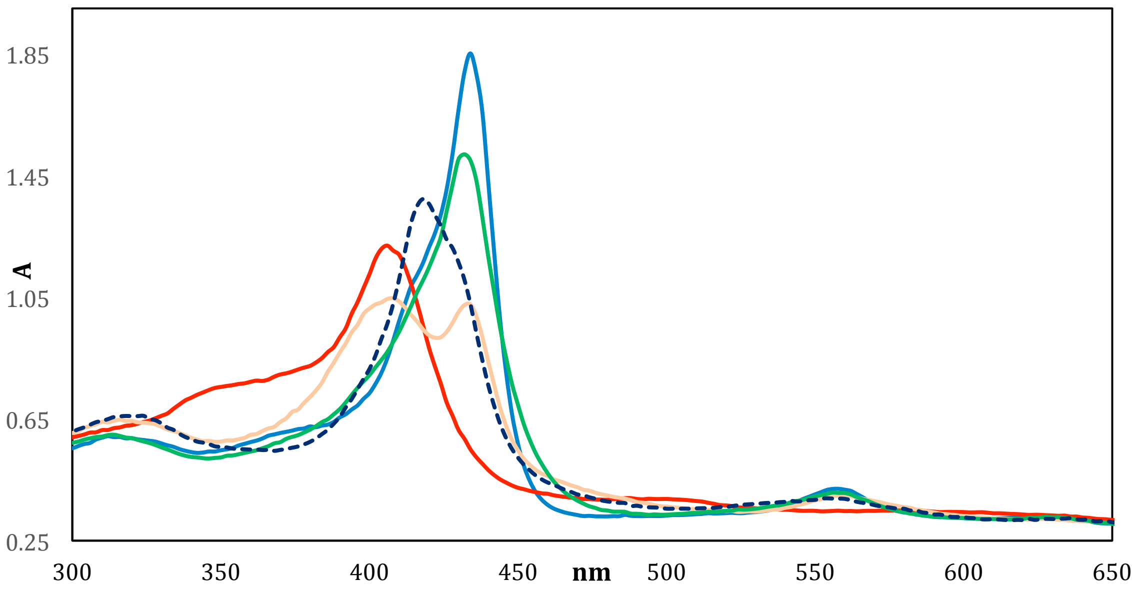

Figure 167: UV-visible SEC of Fe^{II}F$_{20}$TPPCl$^-$ in AmNTF$_2$. Starting material (blue), oxidation (red, +0.2V), first reduction (orange, -0.6V), second reduction (green, -1.3V) and final reoxidation (dashed, -0.6V) products. Potentials are versus Ag/AgNO$_3$.

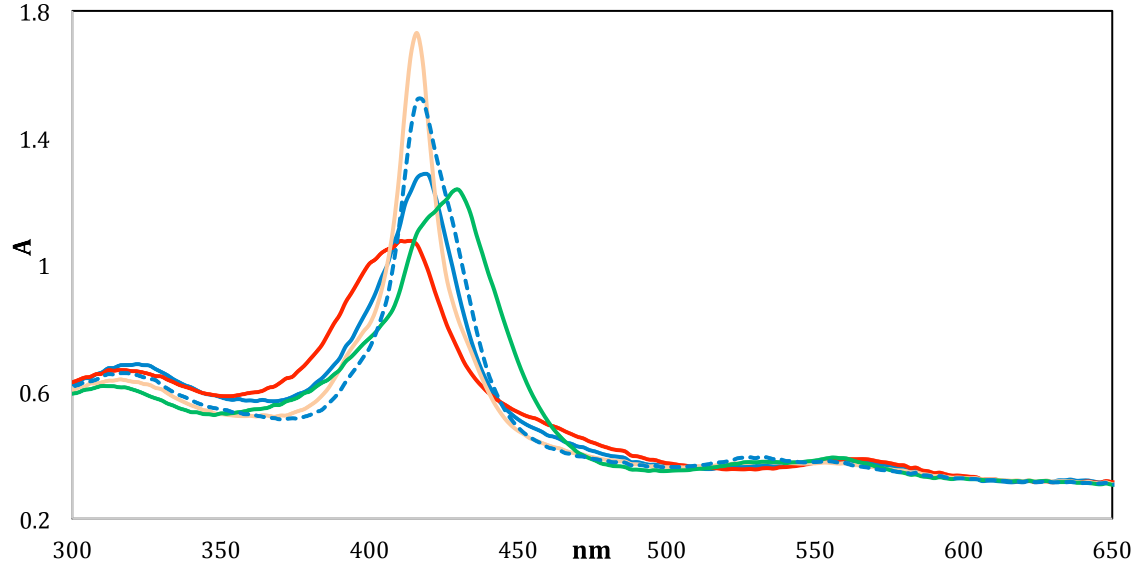

Figure 168: UV-visible SEC of Fe^{II}F$_{20}$TPP in AmNTF$_2$. Starting material (blue), oxidation (red, +0.2V), first reduction (orange, -0.6V), second reduction (green, -1.3V) and final reoxidation (dashed, -0.6V) products. Potentials are versus Ag/AgNO$_3$.

7.2.2.2 In RTIL rich mixtures

As was done for low %RTIL mixtures, spectroelectrochemistry was also carried in mixtures RTIL rich mixtures. The electrolysis of $Fe^{III}F_{20}TPPCl$ has been carried out at the first and second reduction waves. Addition of THF (50%) to an RTIL solution showed presence of more than one species in the mixture (*Figure **169***). The broad spectrum of the starting material clearly shows presence of three species: two ferric (394 and 410nm) and one ferrous species (418nm). Starting the scan at very positive potentials led to oxidation of the ferrous species to 394nm. Reversibly, at a potential before the actual first wave of $Fe^{III}F_{20}TPPCl$, the 394nm species was completely reduced to the ferrous product, giving a mixture of two species. The complete reduction of the 410nm to the ferrous species is observed at more negative potentials in the range of the first wave.

Addition of higher fraction of THF (66%) led to more partitioning of the starting material (410nm) into the 394nm and 418nm (*Figure **170***). Similarly, the ferrous species was completely oxidized to 394nm ferric one at positive potentials, followed by a reversible reduction to 418nm ferrous product. Interestingly, even at a high fraction of THF (2/3 v/v), the second reduction led to 434nm species, similar to the one observed in pure RTIL solution. The reoxidation led to a complete oxidation to the starting material with a shoulder at 394nm.

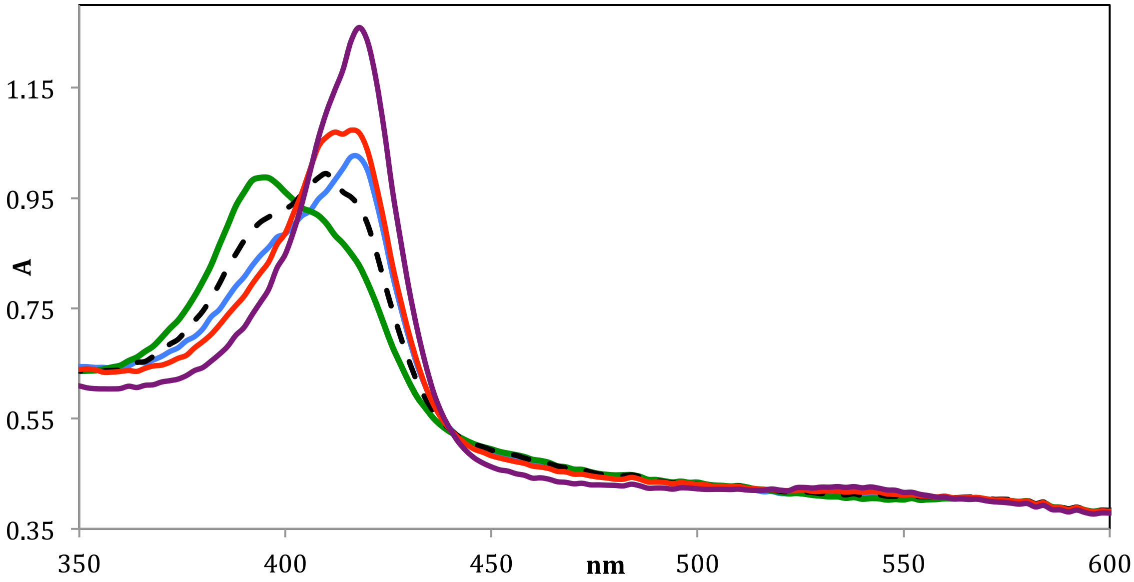

Figure 169: UV-visible spectroelectrochemistry of FeF$_{20}$TPPCl in RTIL-50%THF. Starting spectrum (blue), oxidation (green, +0.2V), intermediate (dashed, -0.2V), reduction (red, -0.4V) and reduction (violet, -0.8V) products. Potentials are versus Ag/AgNO$_3$.

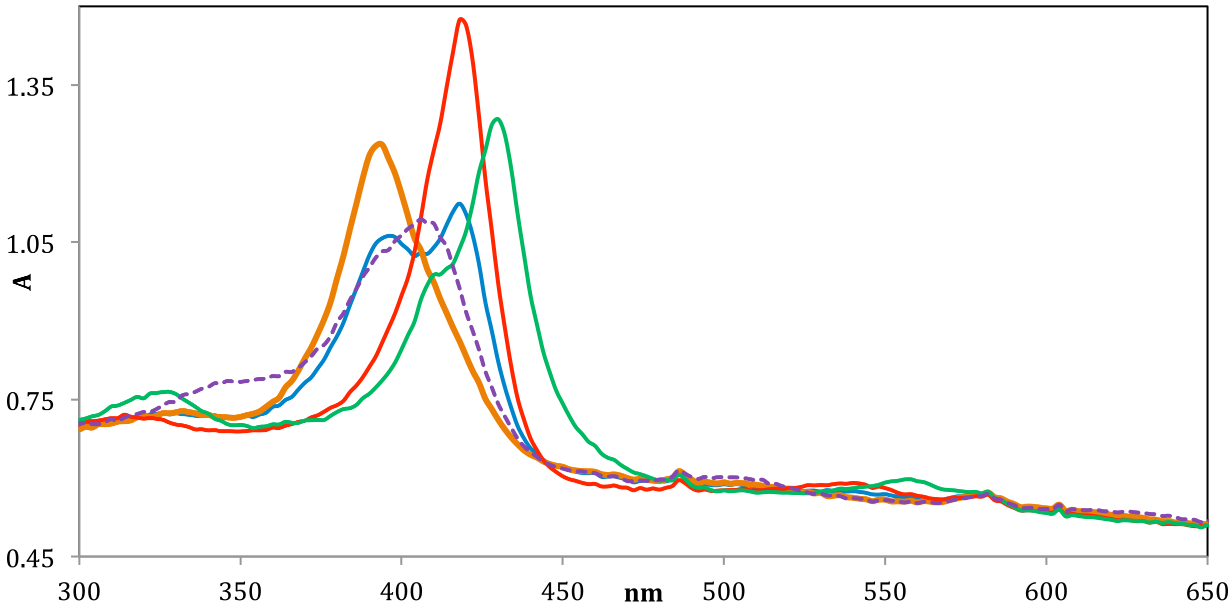

Figure 170: UV-visible spectroelectrochemistry of FeF$_{20}$TPPCl in RTIL-66%THF. Starting spectrum (blue), oxidation (green, +0V), first reduction (red, -0.8V), second reduction (green, -1.2V), reoxidation (dashed, +0.4V) products. Potentials are versus Ag/AgNO$_3$.

To evaluate the effect of axial ligand nature, spectroelectrochemistry of $Fe^{III}F_{20}TPPClO_4$ was carried out in pure RTIL and in mixture solutions. *Figure* ***171*** shows results of the electrolysis in pure $AmNTF_2$. The product of the first reduction in the RTIL showed mainly a Soret band at 418nm, while the second reduction led to 434nm species, seen previously. It is worth noting that at longer electrolysis time and in the potential range of the first reduction wave, formation of the 434nm species could be also observed.

Electrolysis of $Fe^{III}F_{20}TPPClO_4$ in the mixture showed 418nm and 434nm, respectively, for the first and second reduction products (*Figure* ***172***). These spectral features were quite similar to those observed for the reduction of $Fe^{III}F_{20}TPPCl$ in the mixture solution.

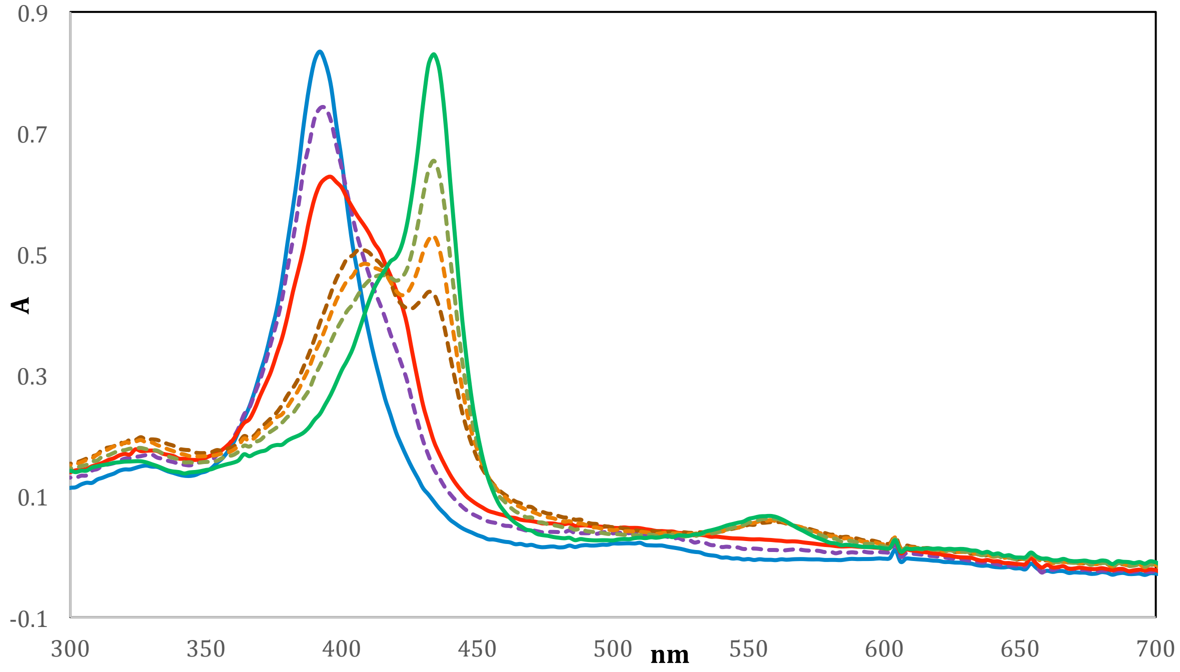

Figure 171: UV-visible spectroelectrochemistry of $FeF_{20}TPPClO_4$ in $AmNTF_2$. Starting spectrum (blue), first reduction (red, -0.6V), second reduction (green, -1.25V) and intermediate (dashed) products. Potentials are versus $Ag/AgNO_3$.

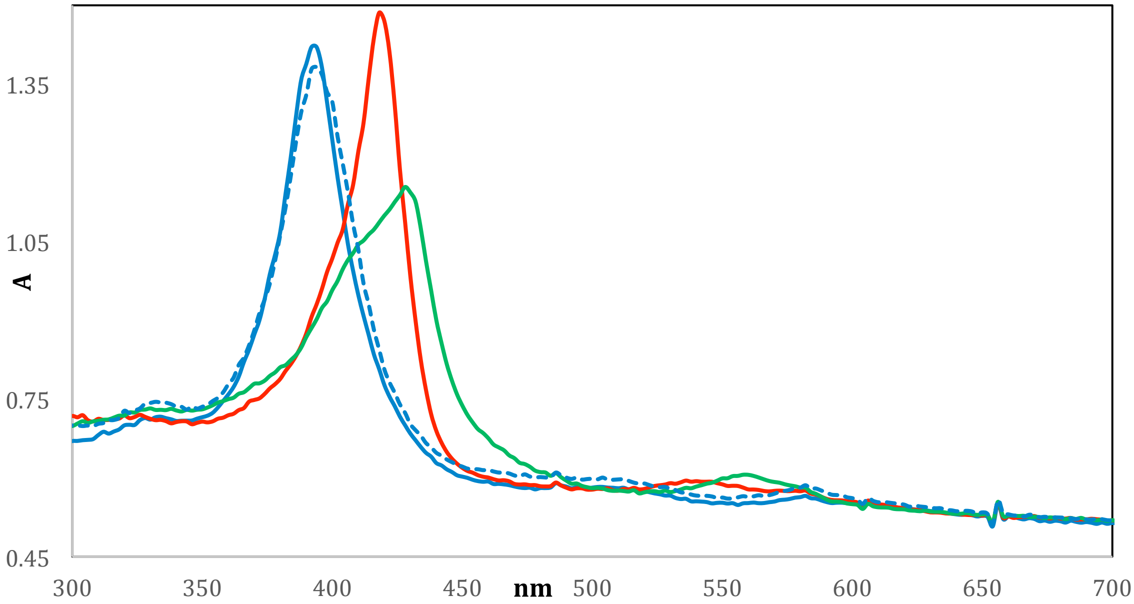

Figure 172: UV-visible spectroelectrochemistry of $FeF_{20}TPPClO_4$ in $AmNTF_2$-50%THF. Starting spectrum (blue), first reduction (red, -0.65V), second reduction (green, -1.0V), reoxidation (dashed, +0.2V) products. Potentials are versus $Ag/AgNO_3$.

Figure ***173*** shows spectra of $FeF_{20}TPPCl$ in different mixtures, where the Soret band of the starting material splits into 408, 394 and 418nm bands upon THF addition to an RTIL solution. These features correspond to the chloride coordinated ferric complex (408), solvent coordinated ferric complex (394nm) and the solvent coordinated ferrous species (418nm). *Figure* ***174*** shows that addition of as little as 2% of THF to an RTIL solution of ferrous complex shifted the Soret band from 434nm to 418nm. This later species correspond to the ferrous complex that is observed in pure molecular solvent.

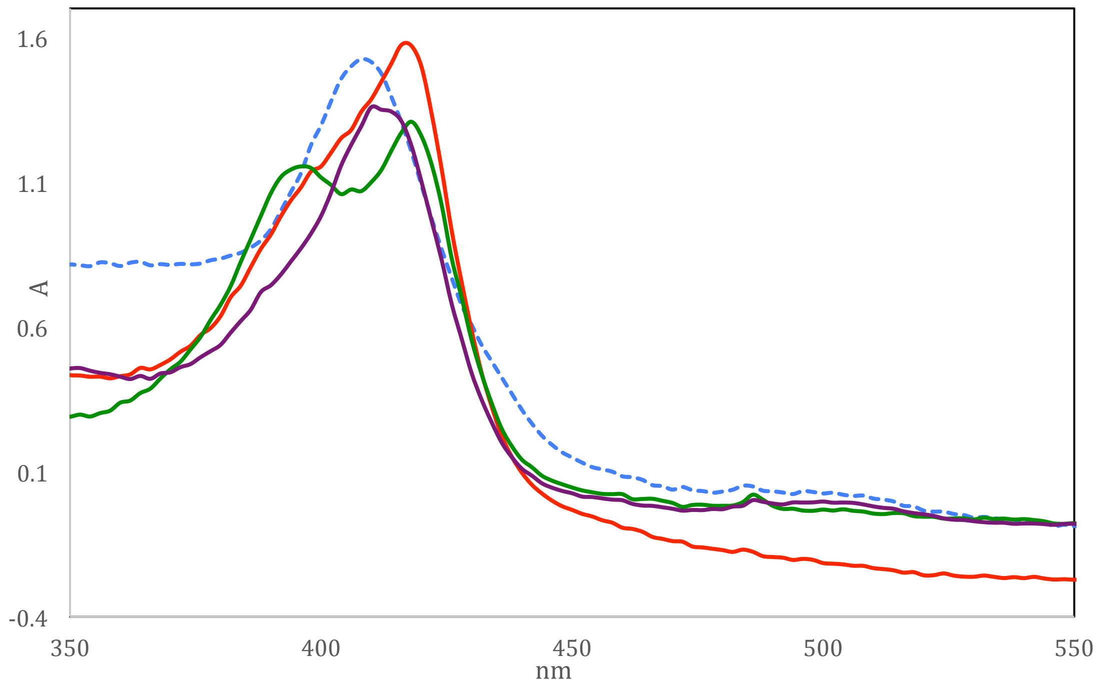

Figure 173: UV-visible spectra of $Fe^{III}F_{20}TPPCl$ in $AmNTF_2$ (dashed), 50% (red), 66% (green) and 90% (violet) THF.

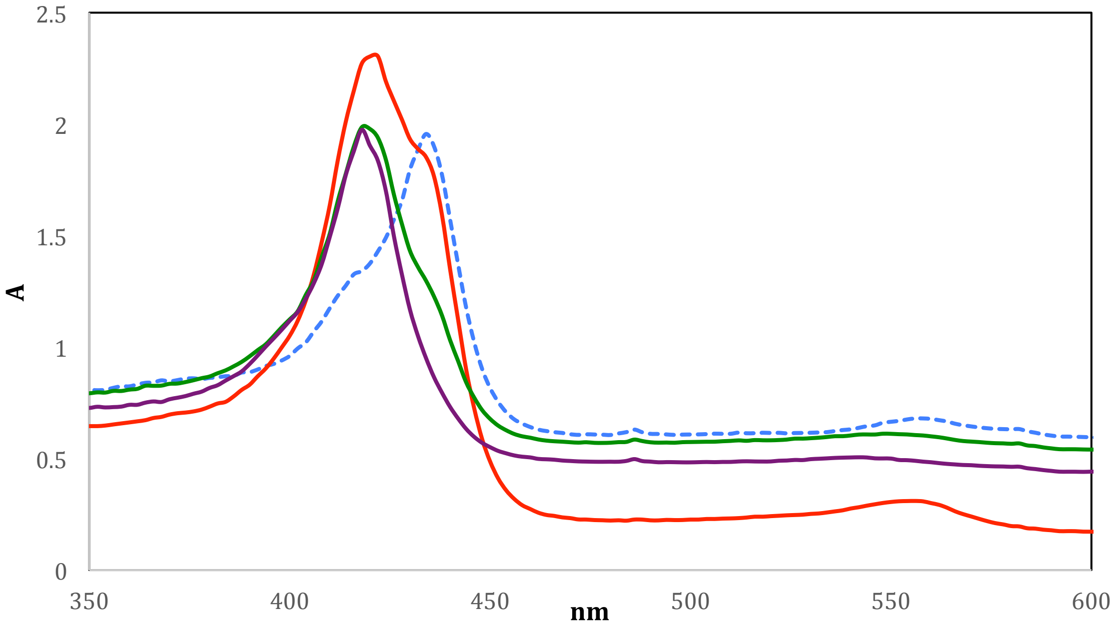

Figure 174: UV-visible spectra of $Fe^{II}F_{20}TPPCl^{-}$ in $AmNTF_2$ (dashed), 2% (red), 7% (green) and 20% (violet) THF.

7.2.3 ^{19}F-NMR

^{19}F-NMR was also carried out for the chemically prepared complexes in RTIL rich mixtures. Due to the high viscosity of RTIL, the NMR spectra were generally broader than the ones in the molecular solvent. The shape of $Fe^{III}F_{20}TPPCl$ spectrum in RTIL was little different from the one seen in THF, with a significant upshift of the fluorine signals in the ionic liquid. Regardless the shift due to change of solvent environment, both species can be attributed to high spin ferric complex.[130]

Addition of up to 80%THF onto an RTIL solution of $Fe^{III}F_{20}TPPCl$ shows presence of only one species, where the *ortho* resonance were singlets in all mixtures (*Figure **175***). In case of $Fe^{III}F_{20}TPPClO_4$ complex, the spectrum was similar to the one seen in THF (*Figure **176***). In addition to the symmetric feature of the spectrum, the very small shifts of the fluorine resonances in all mixtures indicate that the solvent coordination to the ferric center was not much affected by change in solvent composition.

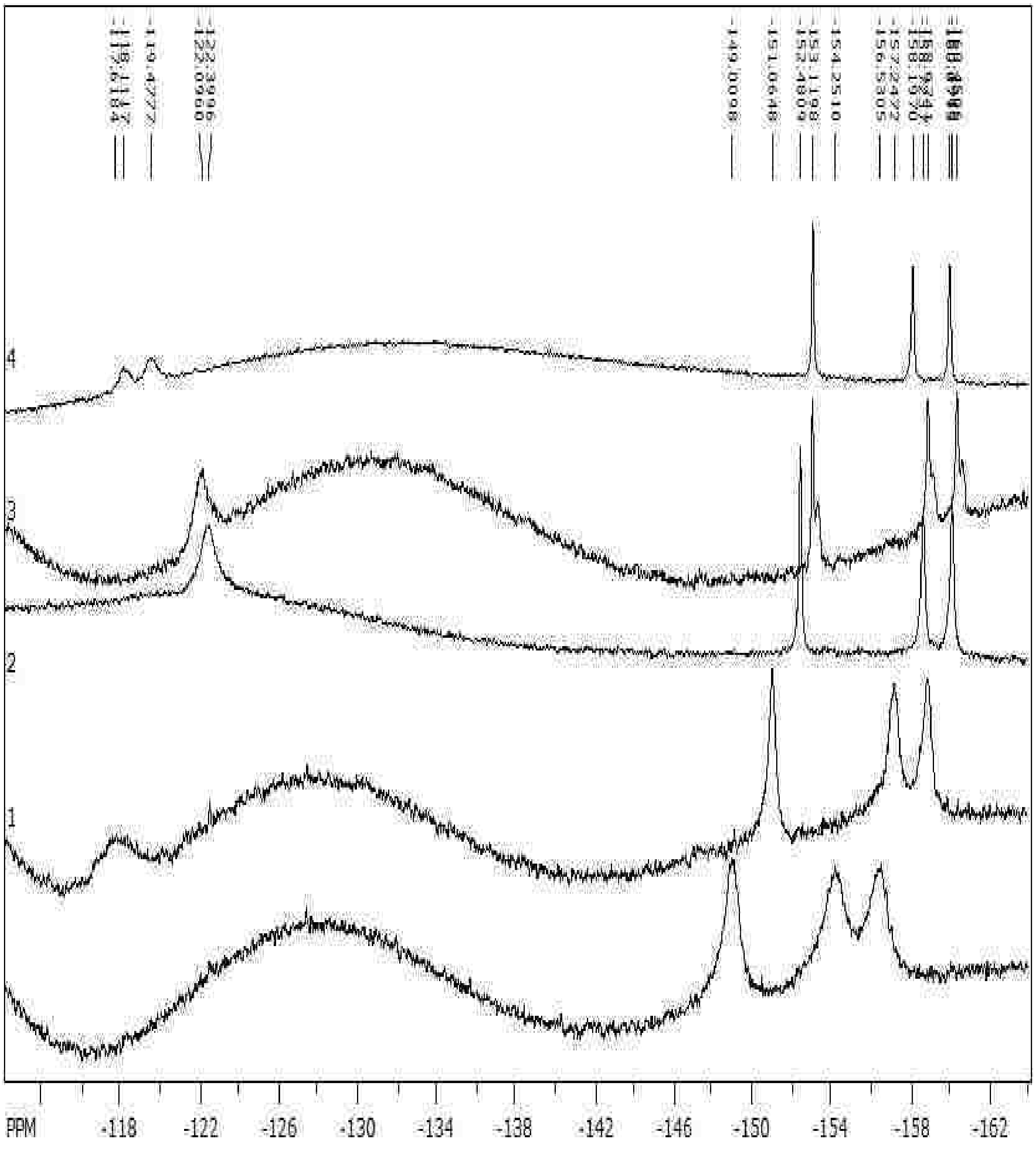

Figure 175: ^{19}F-NMR of Fe^{III}F$_{20}$TPPCl in AmNTF$_2$, 10, 50, 80 and 100%THF, from bottom to top, respectively.

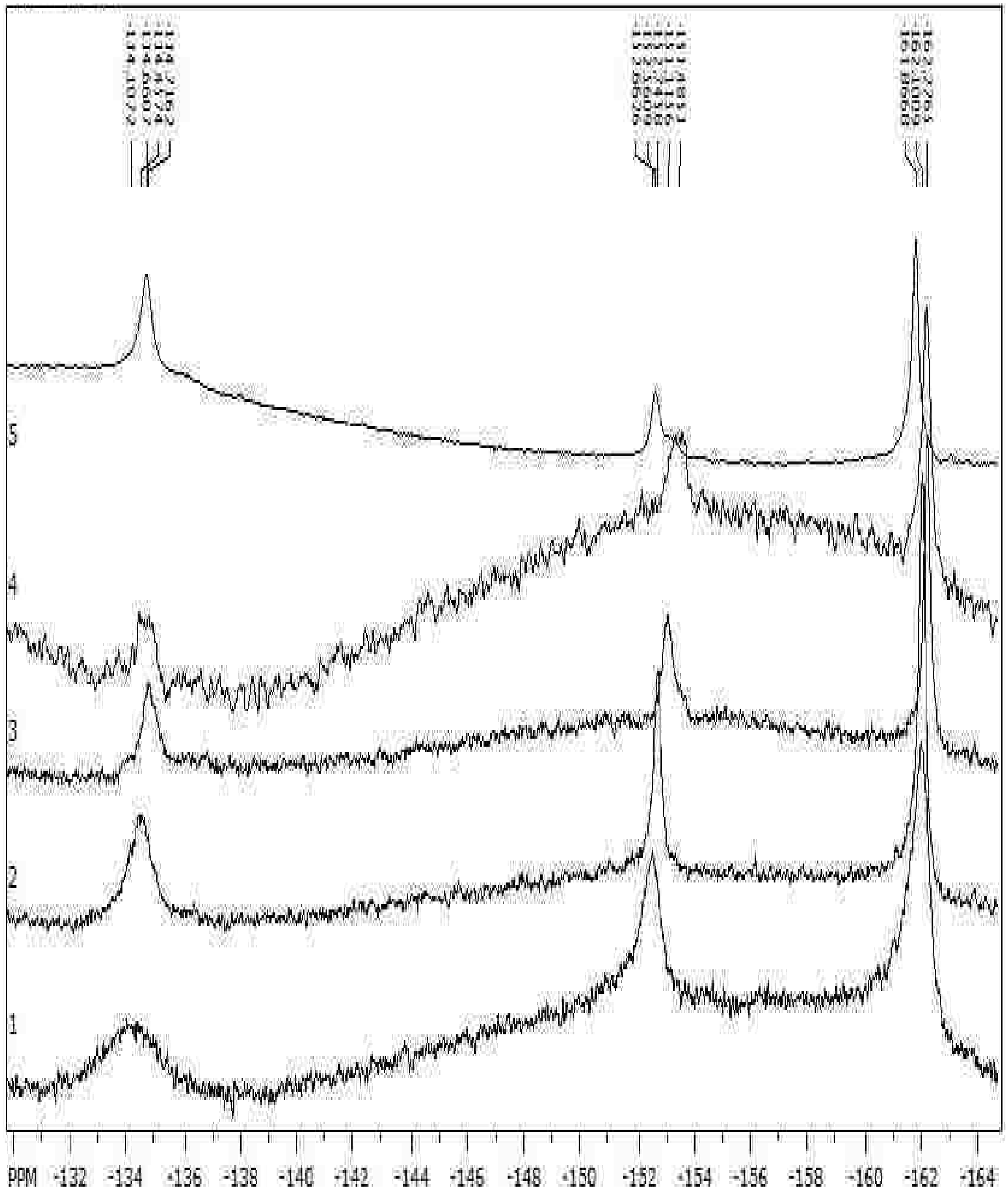

Figure 176: ^{19}F-NMR of Fe^{III}F$_{20}$TPPClO$_4$ in AmNTF$_2$, 20, 66, 85 and 100%THF, from bottom to top, respectively.

Figure ***177*** shows the ^{19}F-NMR spectrum of the ferrous complex $Fe^{II}F_{20}TPPCl^-$, isolated from the chemical reduction of $Fe^{III}F_{20}TPPCl$, in RTIL-%THF mixtures. In pure RTIL, the spectrum of this complex (*o*: -128 and -131ppm, *p*: -154ppm, *m*: -161ppm) looked quite different from the one in molecular solvent. While in THF the fluorine resonance exhibited a symmetric coordinated species, in RTIL the signals showed a non-symmetric complex. This is very likely due to the chloride coordination to the metal center in the ionic liquid. It is worth noting that the fluorine resonance in the RTIL were comparable to reported shifts *o*: -131 and -132.2ppm, *p*: -157.9ppm, *m*: -165 and -166ppm for chloride coordinated high spin ferrous species in toluene. An intermediate spin, with shifts of *o*: -135.5 and *p*: -152.2ppm, *m*: -161.4ppm, has been assigned to the four coordinated ferrous species in toluene.[130] Interestingly, a gradual addition of THF to an RTIL solution of this species led to growing signals at the expense of the starting spectrum, indicating the presence of more than one species in the mixture. The new resonance looked more like the spectrum of the ferrous species in the molecular solvent. At 50%THF, all the starting material was converted to the new species and only one species was present in the mixture. This last spectrum corresponded very well to the observed one for ferrous species in the pure molecular solvent. Similarly, *Figure* ***178*** showed the ^{19}F-NMR spectrum of the ferrous complex $Fe^{II}F_{20}TPPClO_4^-$, isolated from the chemical reduction of $Fe^{III}F_{20}TPPClO_4$, in RTIL-%THF mixtures. The starting spectrum of the complex in ionic liquid showed an asymmetry and looked similar to the $Fe^{II}F_{20}TPPCl^-$ spectrum in RTIL. This is again an indication of the perchlorate coordination to the metal center. In the same manner, addition of THF switched the starting material from perchlorate coordinated to THF coordinated ferrous complex in the mixture.

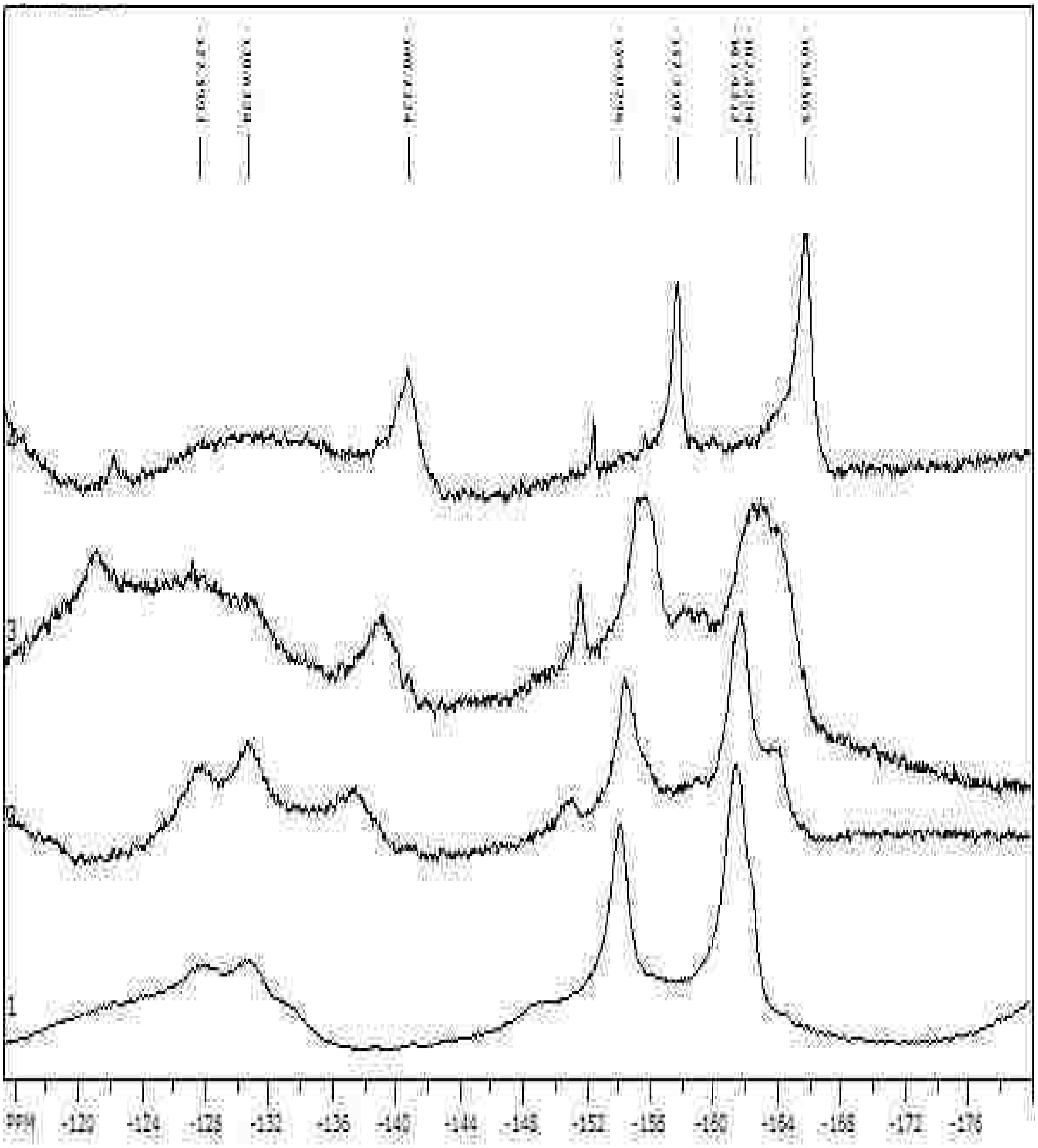

Figure 177: ^{19}F-NMR of $Fe^{II}F_{20}TPPCl^{-}$ in $AmNTF_2$, 10, 20, 50%THF, from bottom to top, respectively.

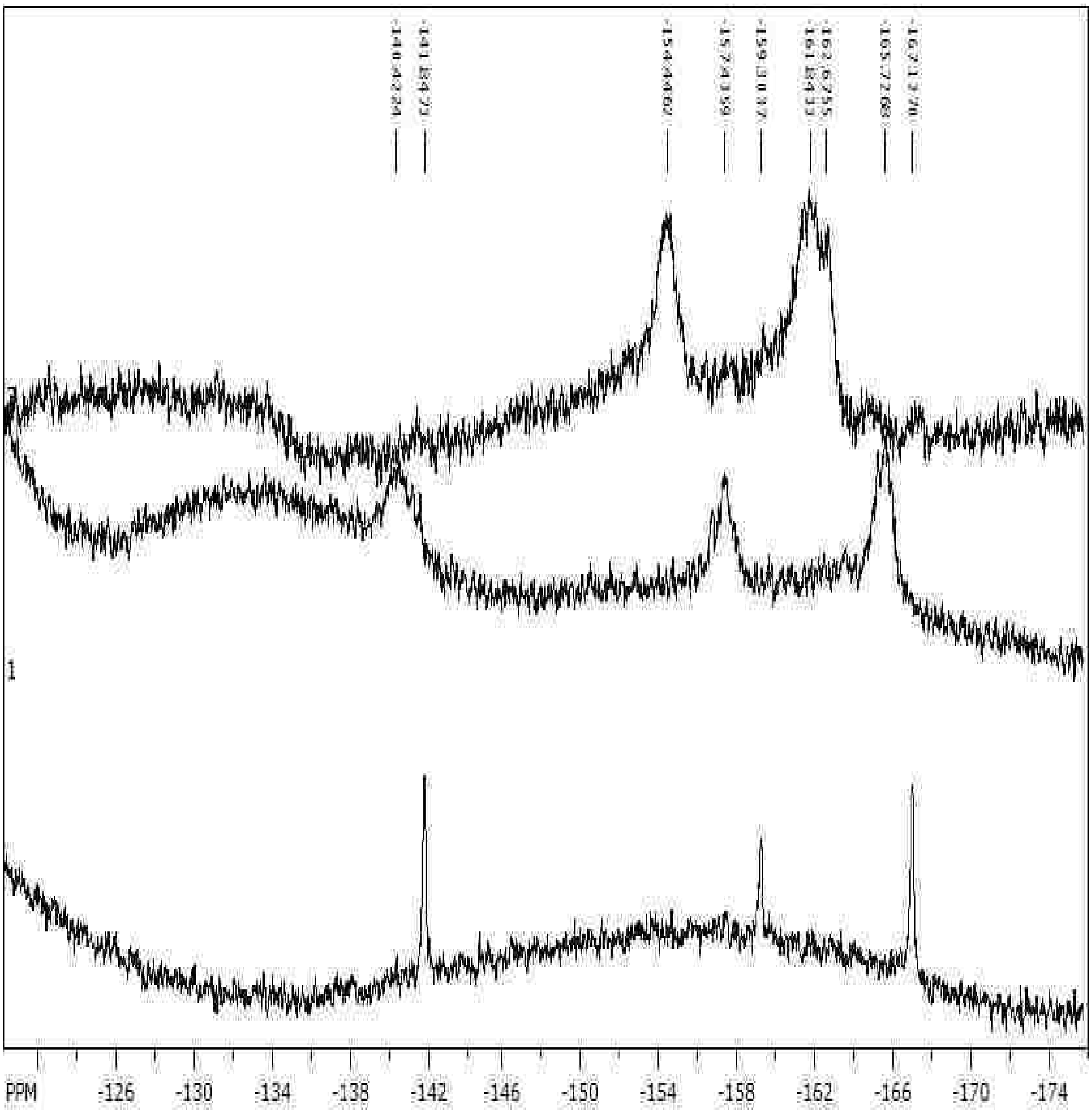

Figure 178: ^{19}F-NMR of Fe^{II}F$_{20}$TPPClO$_4^-$ in AmNTF$_2$, 33 and 100%THF, from top to bottom, respectively.

Figure ***179*** shows the ^{19}F-NMR spectrum of $FeF_{20}TPP^{-}$, isolated from the chemical two electrons reduction of $Fe^{III}F_{20}TPPClO_4$, in RTIL-%THF mixtures. The spectrum of this species in RTIL was completely different from the one observed in THF. It is worth noting that in RTIL solution, the chemical shifts of the fluorine resonance (*o*: -128 and -131ppm, *p*: -154ppm, *m*: -161ppm) of this complex were quite similar to those of the ferrous species.

More interesting, addition of THF to an RTIL solution of this species switched the spectrum of the $FeF_{20}TPP^{-}$ that is observed in the molecular solvent (*o*: -128 and -141ppm, *p*: -162ppm, *m*: -173ppm. Here again, intermediate spectra containing the two species could be also observed in the mixtures. At 66%THF, the spectrum looked mostly like the one in the molecular solvent. This substitution of the starting spectrum by changing the solvent composition of the mixture ruled out the possibility of a chemical oxidation of the complex by the RTIL, and that it is indeed stable in the pure ionic liquid.

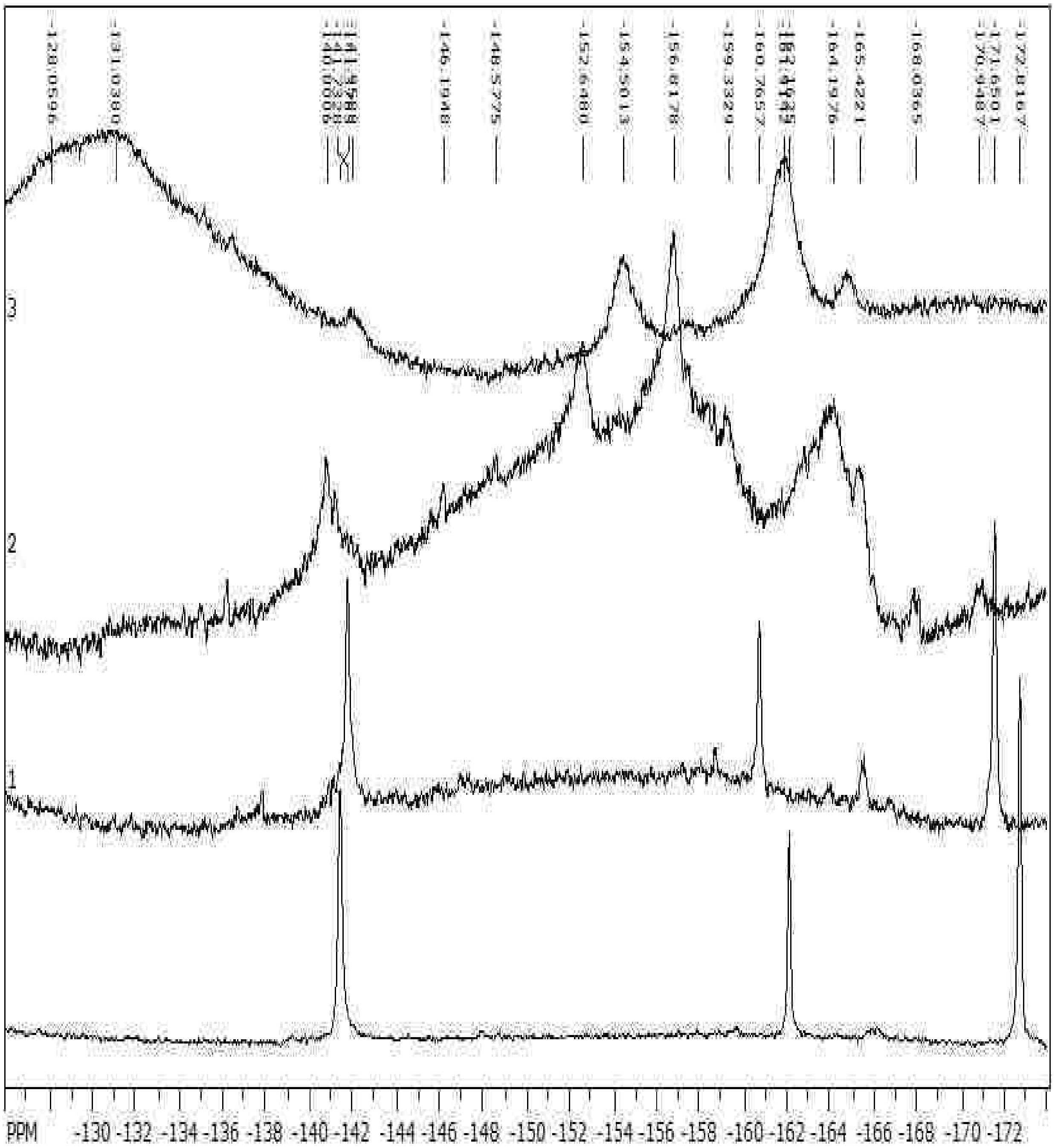

Figure 179: ^{19}F-NMR of $FeF_{20}TPP^-$ in $AmNTF_2$, 50, 66 and 100%THF, from top to bottom, respectively.

7.2.4 EPR

A further indication about the stability of the reduced *$FeF_{20}TPP^-$* in the ionic liquid could be obtained through EPR measurements. *Figure 180* shows the EPR spectrum of *$FeF_{20}TPP^-$* in the pure molecular and the RTIL solvents. The spectrum in the molecular solvent showed a g value of 2.28, consistent with reported values for this species in THF.[153] In the RTIL, the spectral features were fairly similar to the one in the molecular solvent, with an increase of the g value to 2.65.

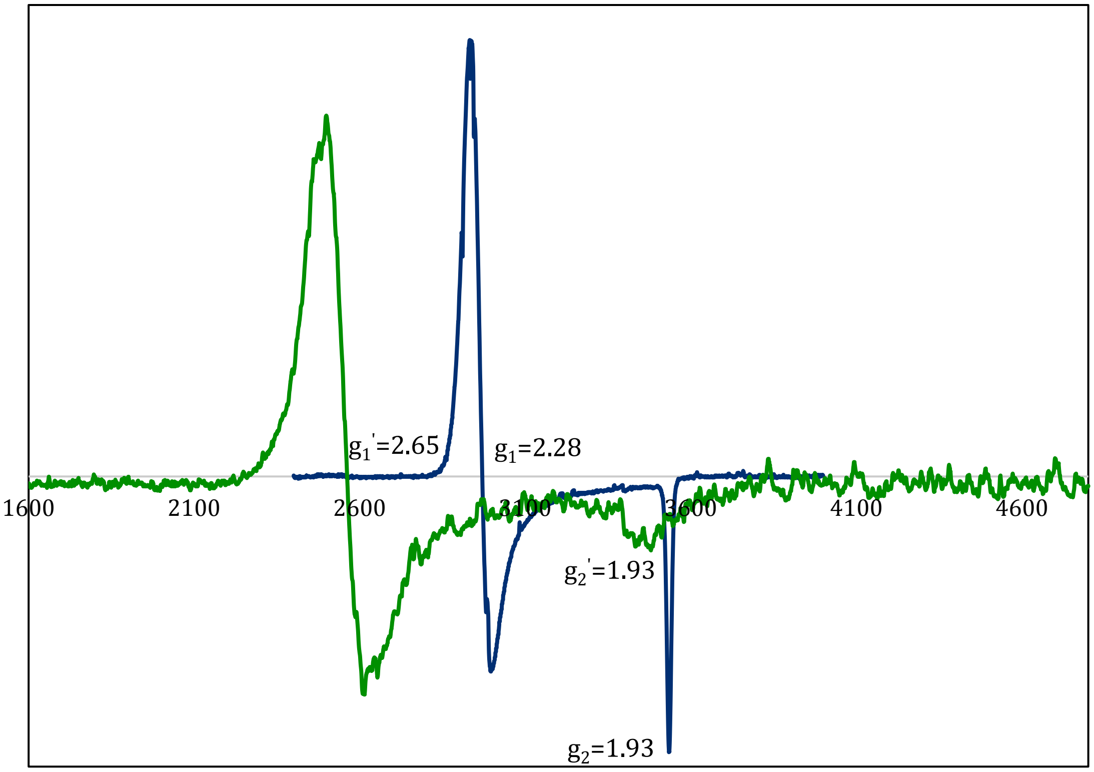

Figure 180: EPR spectra of $FeF_{20}TPP^-$ in THF (blue) and $AmNTF_2$ (green). Frequency is 9.5MHz. Temperature: 77 K.

7.3 Discussion

Cyclic voltammetry of $FeF_{20}TPPCl$ in RTIL rich mixtures indicated the displacement of the chloride anion upon addition of THF to ionic liquid solution. Consistent with the voltammetric results, the UV-visible spectra also showed partitioning of the ferric species into the molecular solvent (394nm) and RTIL domains (408nm), when going from pure RTIL to the mixture. Whereas the ferric complex is chloride coordinated in both pure solvents, the partitioning into domains appeared to be strong enough to dissociate the covalent bonding of the metal center and the counter anion. Two complementary driving forces that may contribute to generate such dissociation would be the preferential solvation of the small basic chloride anion by the RTIL and the positively charged ferric complex by THF. In addition to the two ferric complexes, the partitioning generated a partial self-reduction of the complex to ferrous species. This partial reduction can be result of the established negatively charged environment, due to excess of the chloride anion within the RTIL domain. Further additions of THF diminished the partitioning effect and one species was observed in the mixture, $FeF_{20}TPPCl$. Of note, reoxidation reaction of the first wave also showed a shift of the Soret band to 406nm. Such small shift, from 410 to 406nm, is very likely an indication of solvent coordination to the ferric chloride species. The first reduction wave in pure RTIL indicated an axial ligation of the counter anion to the ferrous metal center. This coordination red shifted the Soret band of the complex by about 14nm, when going from the molecular solvent to the ionic liquid. The NMR shifts of fluorine resonances were consistent with reported spectrum of high spin $Fe^{II}F_{20}TPPCl^-$ in toluene.[130]

The addition of a small amount of THF to the pure solution of $Fe^{II}F_{20}TPPX(Cl^{-}/ClO_4^{-})$ in RTIL changed the electronic structure to the one seen in the pure molecular solvent. As a result, the second voltammetric wave was stabilized, due to easier reduction of $Fe^{II}F_{20}TPP(THF)_2$ compared to $Fe^{II}F_{20}TPPX^{-}$, and the reoxidation was more reversible. These results were confirmed by UV-visible and ^{19}F-NMR analysis in the mixtures, where addition of THF gradually switched the signals from an axial ligand coordinated to solvent coordinated ferrous species. A similar switch was observed when exchanging the counter anion from chloride to perchlorate, where the reduction product had mostly a Soret band at 418nm. Possible coordination to the weak perchlorate anion could be also observed at long electrolysis time in pure RTIL. As an alternative to THF addition, scanning through the second reduction wave released the counter anion of the ferrous/ferric species, and were mainly solvent coordinated species upon the reoxidation reaction.

The spectroelectrochemistry of our complexes in pure RTIL showed that the second reduction product had spectral features quite different from those in THF. While the spectrum in the molecular solvent exhibited a bleached Soret band, the spectrum of the reduced species showed a very sharp band at 434nm. This change in the electronic structure can be rationalized on the basis of the reduction center, where the fluorinated porphyrin arms would significantly delocalize the charge on the porphyrin core leading to the bleach of the Soret band in THF. In contrast, strong ion paring of the RTIL cation with a negatively charged species resulted in higher localization of the charge on the metal center.

The feature of a mainly metal centered reduction product could be seen even after addition of 50%THF to an ionic liquid solution, indicating a strong partitioning of this species into RTIL domain in this mixture. These results were also consistent with the ^{19}F-NMR analysis, which confirmed the chemical stability of the product in the pure RTIL solution. Addition of large THF fractions to the ionic liquid solution led to the product observed in the molecular solvent.

Interestingly, the UV-visible and ^{19}F-NMR analysis showed that both first and second reduction products had quite similar electronic structures in the RTIL. Such similarity is very likely due to charge localization on the metal moiety for both products. Although both species have same overall charge, their interactions with the RTIL should be rationalized through two distinct pathways. Interaction with the first reduction product was mostly by driving an axial coordination of the neutral ferrous complex with accessible counter anions in RTIL solution. The effect on the second reduction product was mainly through strong ion paring with the RTIL cation, which changed the electronic structure of the complex in an intramolecular level.

The EPR results also showed a significant change of the proportionality factor (g) of the second reduction product, when going from molecular to RTIL solvent. The non-coordination of the RTIL to the metal center was illustrated by a larger g value, whereas the smaller g value in the molecular solvent indicated significant coordination of THF to low valent metal center. Such coordination could prevent the partition of $FeF_{20}TPP^-$ into RTIL domain in the molecular solvent rich mixtures. No partition of $FeF_{20}TPP^-$ could be observed when 90% RTIL was added to THF solution (THF-%RTIL mixtures). This indicated the impact of the direction of mixture preparation on the partition of solutes into RTIL domain.

Throughout this investigation, the effects of RTIL nano-domains on the redox processes of $FeF_{20}TPPX$ was demonstrated. The *Figure 181* and *Table 15* summarize the observed redox pathways and the spectral features of the redox products in the studied solvent system. The potential shifts were correlated to acceptor properties of the mixture system and solvent-counter anion interactions. The partitioning into nano-domains and its impact on electronic structures of reduced species were shown from UV-visible and NMR analysis. Finally, it should be noted that the schema in *Figure 181* might be restricted to solvent systems and counter anions used in this work. Further investigation, using more coordinating molecular solvents and stronger counter anions, may provide more insight on the impact of RTIL on the redox processes of metalloporphyrins.

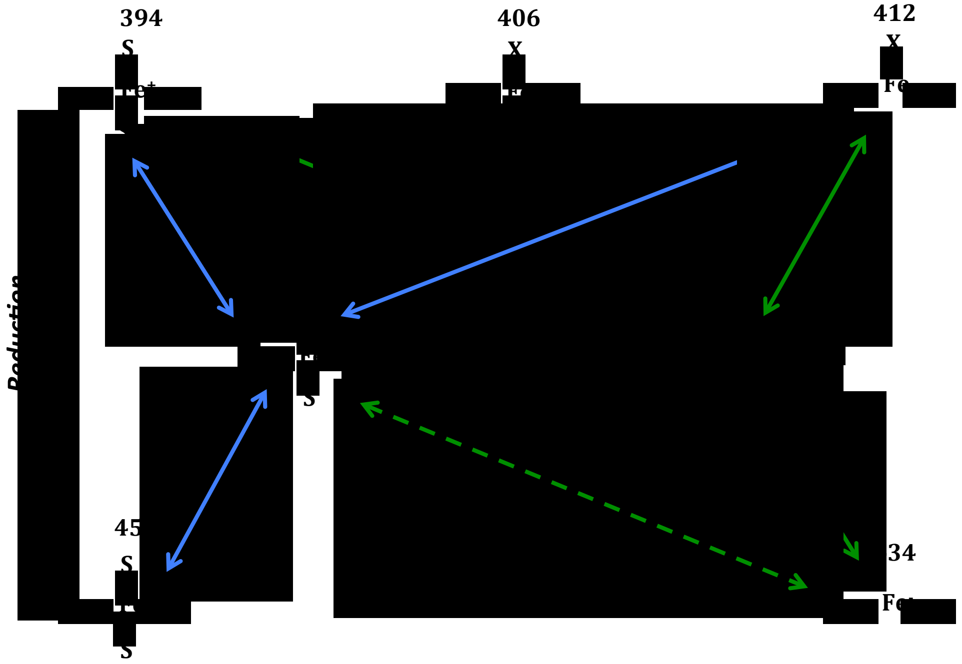

Figure 181: Observed redox species and pathways of $FeF_{20}TPPX$ in THF (solid blue), RTIL (solid green) and RTIL-%THF (dashed green) solvents.

Table 15: Spectral features of the fluorinated iron porphyrin complexes in THF and RTIL solvents

Species/Solvent	UV-vis (nm)		^{19}F-NMR (ppm)	
	THF	RTIL	THF	RTIL
$\mathrm{Fe^{III}F_{20}TPPCl}$	350, 412, 506, 632 [155] H.S S 418 [127] 407 [154]* L.S S 424 Q 442, 555, 602 [155]* H.S S 416	410, 504, 632	-118, -119, -153, -158, -160 [130a] H.S -102, -105.1, -147.2, -152.1, -154.6	-116, -117, -149, -154, -156
$\mathrm{Fe^{III}F_{20}TPPClO_4}$	394, 506, 632 [127] 390	394, 506, 630	-135, -153, -162 [127] -134.6, -152.2, -160.1	-134, -152, -162
$\mathrm{Fe^{II}F_{20}TPP(Cl^-/ClO_4^-)}$	420, 542 [154]* L.S S 445 Q 504, 547, 580	434, 558	-142, -159, -167 [130b] H.S -140.4, -157.7, -165.3	-128, -131, -154, -161 [130c1] H.S -131, -132.2, -157.9, -165.1, -166 [130c] I.S -135.5, -152.2, -161.4
$\mathrm{FeF_{20}TPP^-}$	328, 384, 458, 518, 584, 700 [153]* 390, 423, 510, 575, 605	434, 558	-141, -162, -173	-128, -13, -154, -161
$\mathrm{FeF_{20}TPP^{2-}}$	360, 456, 530, 750 [153]* 358, 448, 515, 710, 778	-	-	-

** Data for FeTPPX. Used solvents in references were: CH_2Cl_2 in Ref[155], THF with imidazole coordination in Ref[154], ACN with triflate in Ref[127], THF in Ref[153], CD_2Cl_2 in Ref[130a], THF in Ref[130b] and toluene in Ref[130c] (for Ref[130c1]: X=Cl^-).*

Chapter 8 Conclusion

Room temperature ionic liquids (RTIL) have been very attractive as replacement for molecular solvents (MS) in many areas in chemistry. However, their application has been often prevented due to their high cost and high viscosity. The use of RTIL in electrochemical applications might be boosted by mixing with MS. The use of the mixed solvents as reaction media will reduce the cost and viscosity of RTILs. In addition, the solvation properties of the mixture can be tailored over a wider range of MS and RTILs. When ionic species are dissolved in molecular solvents, they can either mix homogeneously with the solvents or aggregate to form nano-domains similar to micelles. With the formation of nano-domains in the mixture, molecular and ionic solutes can partition between the MS and the RTIL phases. In RTIL domains, the properties and reactivity of the solute would be more like those in pure ionic liquids.

In the present work, analytical approaches have been employed to probe the presence and RTIL nano-domains and their effects on multi-electron redox processes in mixture solvents. With the correlation of the potential shifts with acceptor properties of the mixture, it was possible to evaluate the extent of ion paring interactions within the molecular and RTIL domains. The impact of RTIL domains on the electronic structures of redox products was examined using several spectroscopic methods, including UV-visible, infrared and NMR. Computational tools such as chemometrics, voltammetric simulations and DFT calculations were used to complement the experimental analysis.

Throughout our investigation, there was strong evidence showing that mixed molecular/RTIL solution were not homogeneous, creating RTIL and MS domains within the solution. Potential shifts and changes in electronic configurations of the studied redox systems were indicative of the charge/structure effects of RTIL nano-domains.

Upon the first reduction of DNB, TCNQ and C_{60}, the charge was significantly delocalized over the entire molecule, minimizing the interactions between the RTIL and the substrate. A similar effect probably occurred for $NiOEP^-$ due to backbonding of the Ni(I) electron density to the porphyrin ring. As result, the electrostatic interaction between the anion and the RTIL was not strong. For NiOEP, DNB and TCNQ the most significant shifts were observed for the second reduction wave. With the formation of DNB^{2-}, $TCNQ^{2-}$ and $NiOEP^{2-}$, the mostly planar complexes could incorporate easily into the RTIL domain, leading to significant potential shifts in $E_{1/2,2}$. On the other hand, $C_{60}{}^{2-}$ is a spherical species with a diffuse charge, causing it to be poorly incorporated into the RTIL domain. Inclusion of the highly charged trianion, $C_{60}{}^{3-}$, into RTIL domain led to a large stabilization of the reduction potential in the mixture.

For $NiOEPone^-$, the electron density was already significantly localized on the ring, and the presence of the RTIL concentrated that electron density on the polar C=O moiety, allowing for a significant electrostatic interaction between the RTIL and $NiOEPone^-$. This interaction was probably not significantly strengthened with the formation of the dianion, $NiOEPone^{2-}$ (presumed to be a Ni(I) π-radical anion structure) because the $NiOEPone^-$ species was already incorporated into the RTIL nano-domain. The formation of a Ni(I) complex would not significantly increase the interaction with the RTIL.

While the reduction potentials were strongly affected by the presence of RTILs, the oxidation potentials were not. Most RTILs consist of large cations with small anions. RTILs are already formed by the weak electrostatic interaction between the cations and anions, mostly caused by steric effects. Large anions such as $NiOEP^{-/2-}$ can be readily solvated by the large RTIL cations without introducing electrostatic repulsion between the cations of the RTILs. On the other hand, cations such as $NiOEP^{+/2+}$ would not be well incorporated into the RTIL nano-domains because of cation-cation repulsion in the RTIL nanodomains. The neutral NiOEPone species could interact to some extent with the RTIL nanodomains, though equilibrium favors their presence in the THF nanodomains.

The presence of nano-domains in the THF-RTIL mixture had significant impact on the metal coordination and electronic structures of iron porphyrin redox products. Due to change in axial ligation to the metal center, the RTIL interactions were more complex than for other systems. However, with the above background on RTIL interactions with redox products, the voltammetry of $FeF_{20}TPPCl$ in THF-RTIL mixtures could be understood to a great extent.

Similar to $NiOEP^{+/2+}$, the uncoordinated $FeF_{20}TPP^+$ showed strong partitioning into the MS domains. Solvation of the small basic Cl^- by RTIL domain led to its displacement from the ferric center by THF solvent. In pure ionic liquid though, coordination of the ferrous center to the counter anion changed its electronic configuration. Addition of small amount of THF displaced the counter anion and the uncoordinated neutral $FeF_{20}TPP$ was dissolved by the molecular domain.

In contrast to DNB^-, $TCNQ^-$, C_{60}^- and $NiOEP^-$, solvation of $FeF_{20}TPP^-$ by the ionic liquid led to strong interactions with the RTIL cation. This resulted in high localization of the charge on the metal center. Such effect was analogous to $NiOEPone^-$, where the RTIL localized the charge on the polar moiety of the ligand. For both $FeF_{20}TPP^-$ and $NiOEPone^-$, the exchange between the two nano-domains was slow enough to observe the two solvation environments.

Our investigation showed a high solubility of the fluorinated porphyrin in pure RTIL, making it a powerful candidate for homogeneous catalysis of CO_2 reduction. In this case, the fluorination of the porphyrin delocalized the charge onto the ligand over the metal center in the molecular solvent. However, partition of $FeF_{20}TPP^-$ into RTIL domains in the mixture solutions has remarkably switched the reduction site to the metal center. This change would enhance the catalytic reduction of CO_2 by $Fe^{I}F_{20}TPP^-$. The RTIL solvation is expected to increase the nucleophilicity of the low valent iron(I) to reduce CO_2, lowering the energetic barrier of the catalytic reaction. Such coordination chemistry of metalloporphyrins for the activation of carbon dioxide in RTIL was reported by Quezada et al.[156] In their work, the CO_2 was reduced to CO at the modified electrode by cobalt(I) center at -0.8V vs Ag/AgCl. The overall rate of the catalytic reaction can be then tuned by the mixture composition. Indications of change in the reactivity and reaction course were observed in the reduction of CO_2 in mixed MS-RTIL solutions. The presence of $EMImNTF_2$ in acetonitrile switched the reaction course from the oxalate anion to CO.[157] The stabilization of CO_2^- in mixed DMF/RTIL solutions has been demonstrated both experimentally and by DFT calculations for the electroreduction of CO_2 in DMF solutions with low concentrations of RTIL.[158] Shi et al. used mixed RTIL/propylene carbonate solutions for the electrochemical reduction of CO_2 to CO.[15] The reduction of CO_2 to CO could be efficiently achieved at -1.5 V vs Ag/AgCl in mixed $EMImBF_4$/water solutions, based on complexation of the intermediate CO_2^- with the RTIL cation.[159] These studies confirm the importance of mixed RTIL/MS in electro-catalytic systems.

Another major impact of RTIL nano-domains could be observed on the mass transport in the mixture. The limited solubility of non-polar substrates by RTIL domains would enhance their transport beyond what would be expected by the mixture viscosity. In such cases, the diffusion would be mostly through molecular channels in the mixture. Partitioning of reduced products into the RTIL domains was shown to slow their diffusion in the mixture.

Presence of impurities in RTILs may have dramatic effects on the reduction potentials and the electronic structure of redox products. These effects could be empowered at low RTIL fraction mixtures, upon partitioning of both impurities and reduction products into RTIL domains. This implies that impurities could be envisioned as a signature for RTIL nano-domains in the mixture solvents.

Not much effort was dedicated to study the impact of direction for the mixture preparation, %RTIL versus MS% mixtures. Preliminary analysis though in both regions of the binary RTIL-MS indicated that the dilution direction might be very critical for the formation and the impact of RTIL nano-domains. For instance, the electronic structure of $FeF_{20}TPP^-$ was not much affected by the addition of up to 90% of RTIL to the MS solution. By contrast, this same configuration could be only observed after addition of more than 50% of the molecular solvent into RTIL solution. This difference could be attributed to the ability of the MS to break apart the RTIL clusters, and vice-versa, the

RTIL to aggregate at low fractions. This is also consistent with observed changes in the conductivity in the RTIL-MS mixture, where maxima were observed between 20-50% RTIL fractions. For a more detailed description of these equilibria, extended investigations over a wider range of RTIL and polar/nonpolar MS mixtures, are needed.

Thus, our results broadly suggested that an RTIL environment could be maintained upon the addition of up to 50%MS to ionic liquid solution. Presence of highly charged solutes might eventually help to maintain the RTIL solvation, by templating the nano-clusters formation at higher %MS in the mixture. While the cost could be reduced by half in using the 50%MS mixture, the viscosity would drop by 1 order of magnitude, enhancing the mass transport in solution. In addition, the solvation ability is expected to rise by a couple orders of magnitude.

Through the outcome of this work on RTIL nano-domains, new avenues on the use of these solvents as reaction media for many areas in chemistry (i.e., nanotechnology, catalysis, energy conversion, sensors…) can be explored. A systematic interpretation of the experimental results obtained in ionic liquids may require the consideration of the impact of RTIL nano-structures on chemical reaction pathways. Finally, this work may represent a milestone for theoretical investigations in modeling the solvation environment of solutes in RTILs.

Appendix

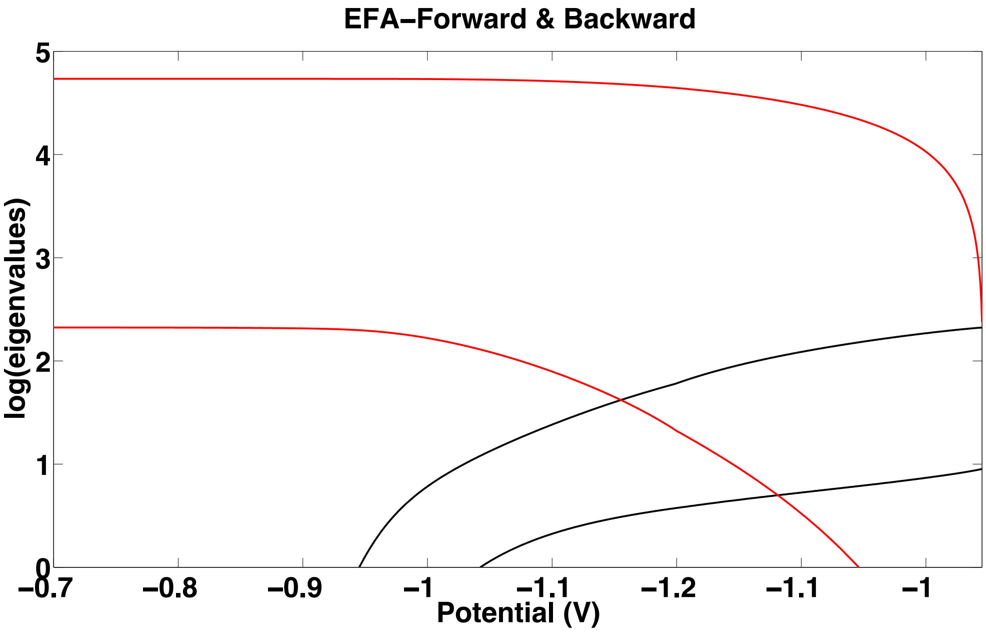

Figure 182: EFA of DNB reduction in $BMImPF_6$

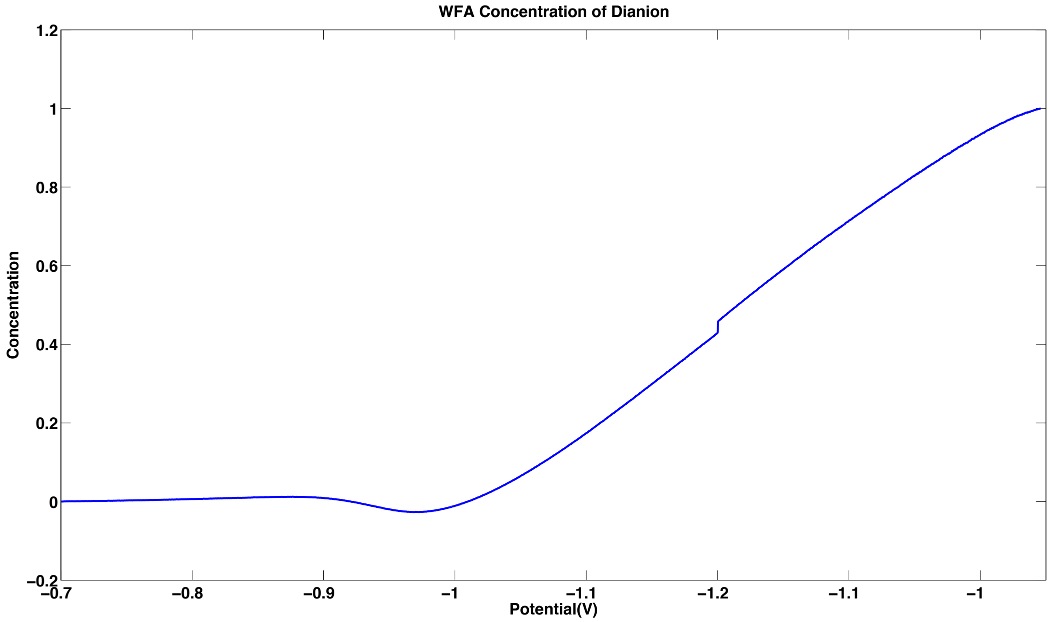

Figure 183: Concentration of DNB dianion in the forward scan in $BMImPF_6$

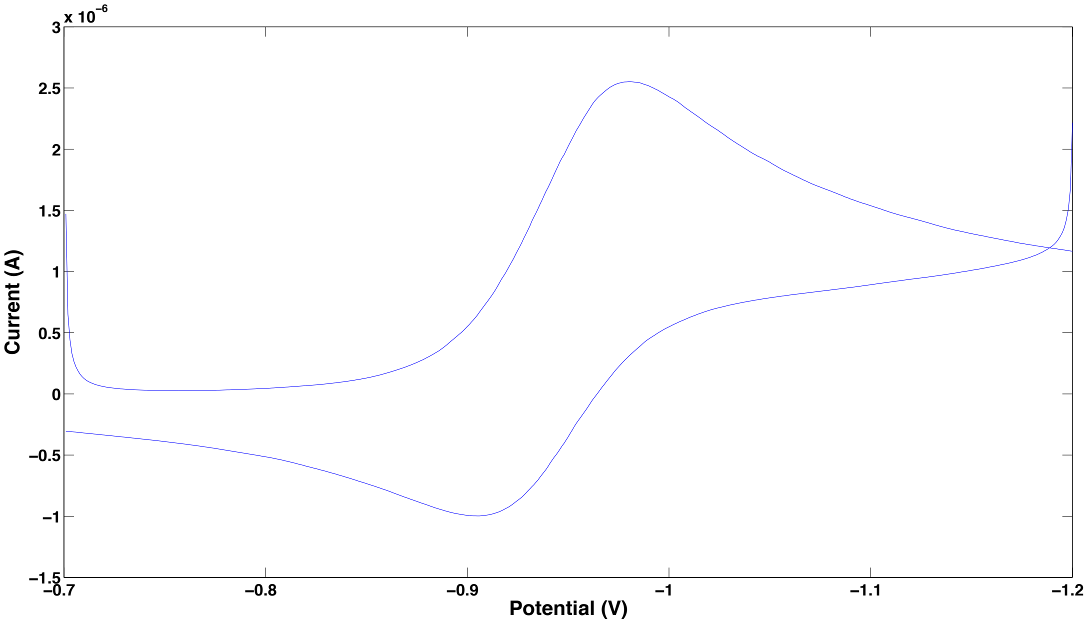

Figure 184: Recorded current during 0.1mM DNB electrolysis in $BMImPF_6$ at 0.1mV/s. Potentials are versus $Ag/AgNO_3$

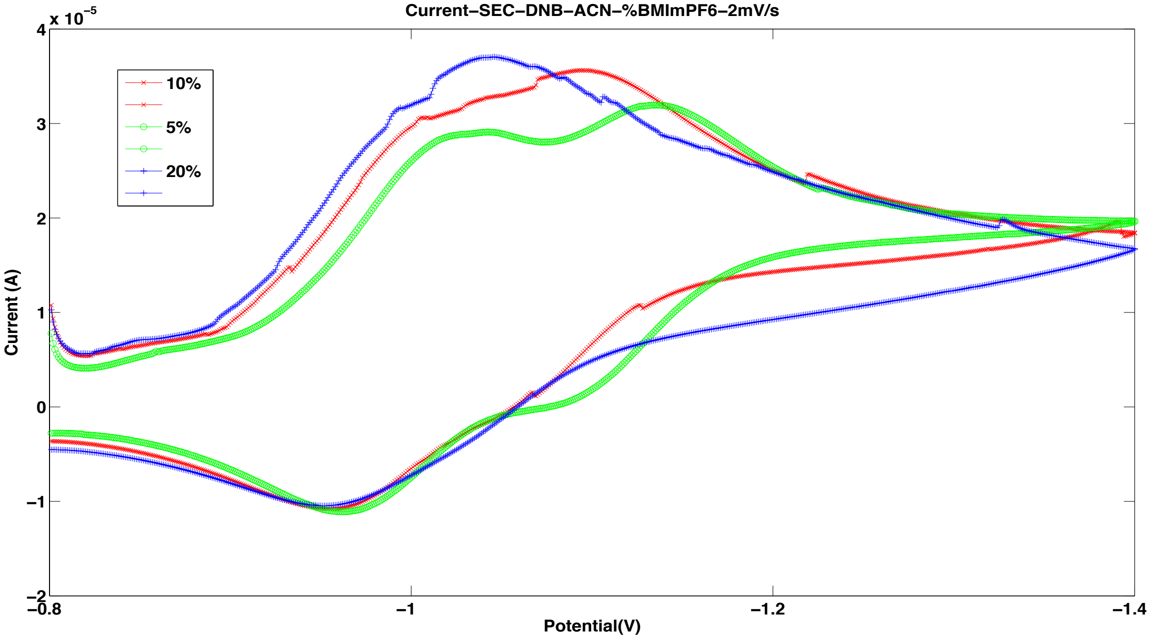

Figure 185: Recorded current during 0.1mM DNB electrolysis in ACN with 5, 10 and 20% $BMImPF_6$ mixtures. Potentials are versus $Ag/AgNO_3$

Table 16: Potential shifts of DNB reduction in ACN-RTILs

% RTIL	E_1 V vs Ag/AgNO$_3$	E_2 V vs Ag/AgNO$_3$	ΔE_{12} (mV)
0	-1.004	-1.228	224
5% BMImPF$_6$	-1.002	-1.118	116
10% BMImPF$_6$	-0.982	-1.082	100
20% BMImPF$_6$	-0.966	-1.048	82
32% BMImPF$_6$	-0.956	-1.004	48
58% BMImPF$_6$	-0.962	-0.994	32
2% EDMPAmNTf$_2$	-0.990	-1.109	159
5% EDMPAmNTf$_2$	-0.977	-1.072	134
10% EDMPAmNTf$_2$	-0.964	-1.079	115
5% BMImNTf$_2$	-0.991	-1.115	125
10% BMImNTf$_2$	-0.989	-1.075	86

Table 17: ΔE$_{12}$ (mV) of DNB reduction in ACN-Solid/liquid Salts

Log(%RTIL)	BMImPF$_6$	AmNTF$_2$	BMImNTF$_2$	BMImCl	dried BMImNTF$_2$
-1.3	116				
-1	100				
-0.7	82				
-0.495	48				
-0.236572	32				
0	24				
-1.7		159			
-1.3		134			
-1		115			
0		39			
-1.3			125		
-1			86		
-2.2239199				178.5	
-1.9254756				160.5	
-1.5352015				123.5	
-1.2466547				112.5	
-0.9695636				101	
-0.6364145				99.5	
-2					185
-1.7					163
-1.3					129
-1					96

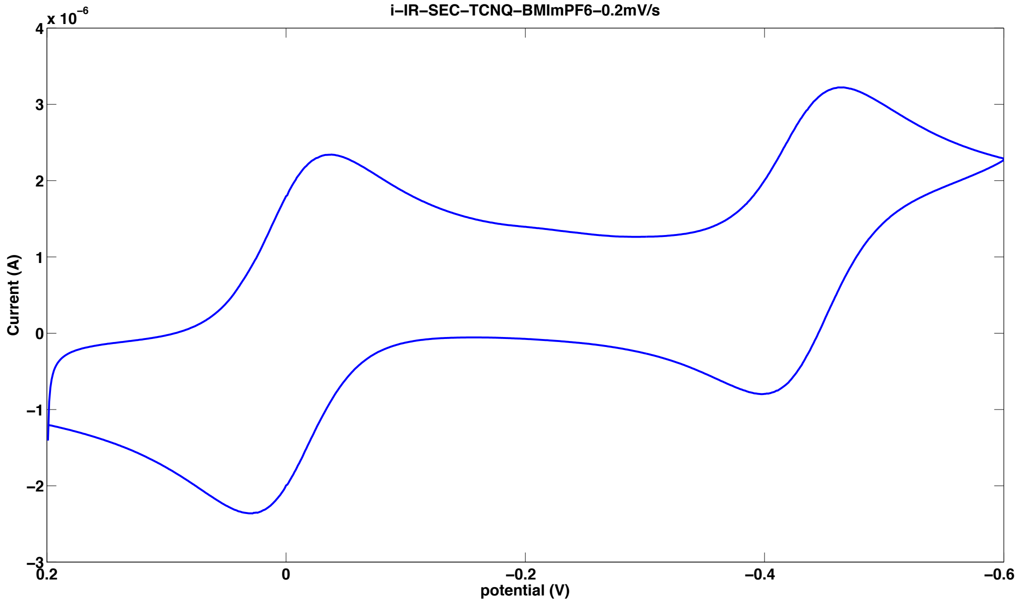

Figure 186: Recorded current during FTIR-SEC electrolysis of reduction of 2mM TCNQ in BMImPF$_6$. Potentials are versus Ag/AgNO$_3$

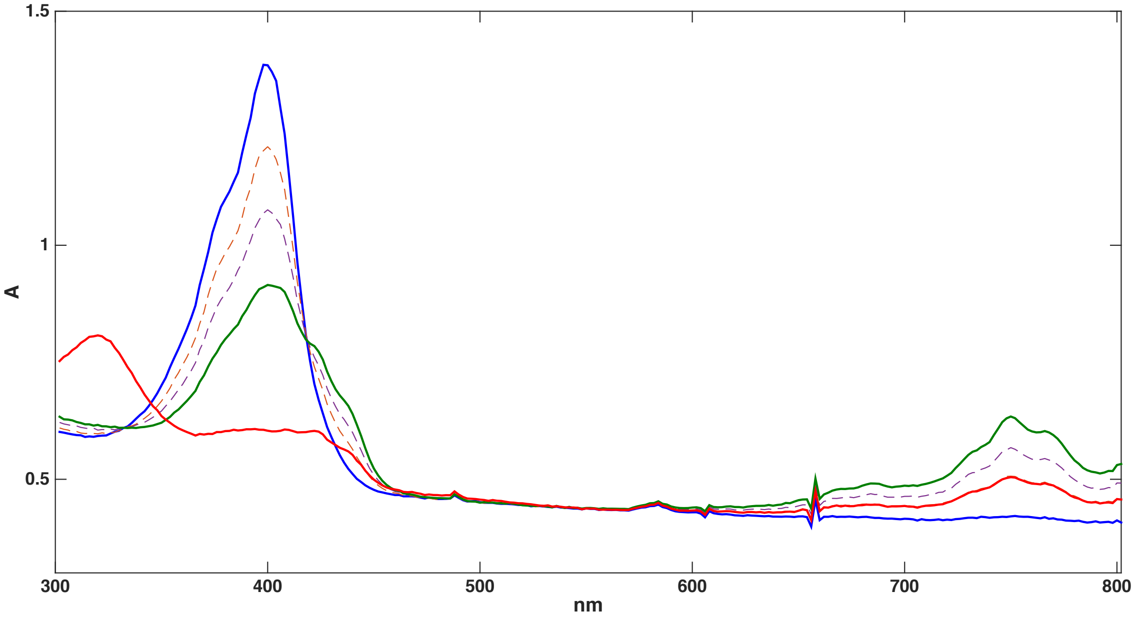

Figure 187: UV-visible spectral profiles of the neutral, radical anion and dianion TCNQ in BMImPF$_6$

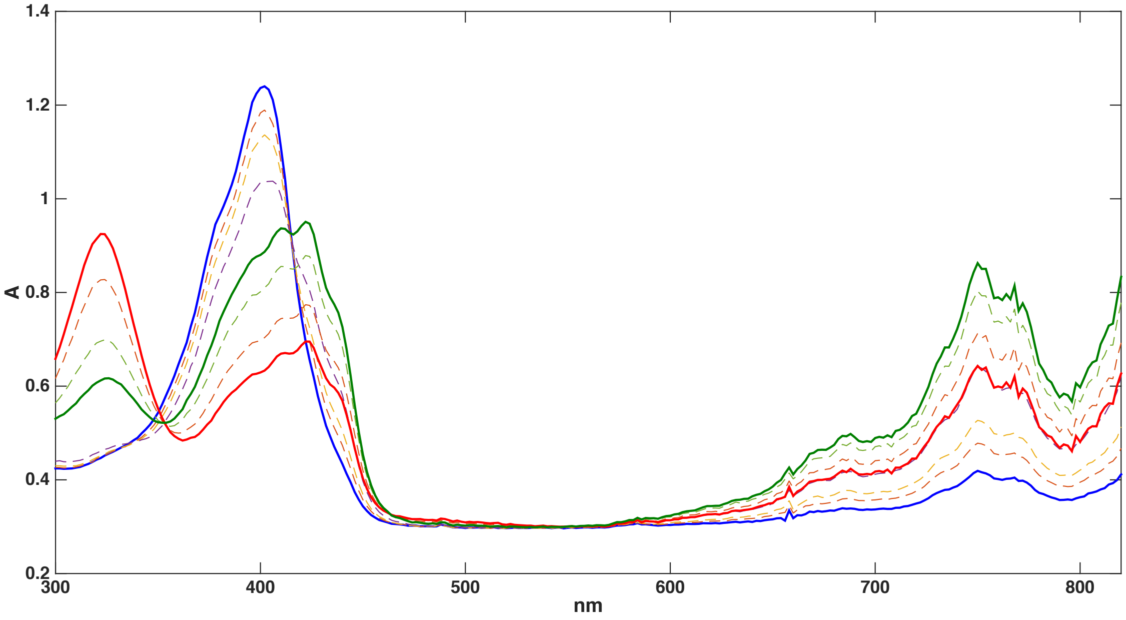

Figure 188: UV-visible spectral profiles of the neutral, radical anion and dianion TCNQ in $BMImBF_4$

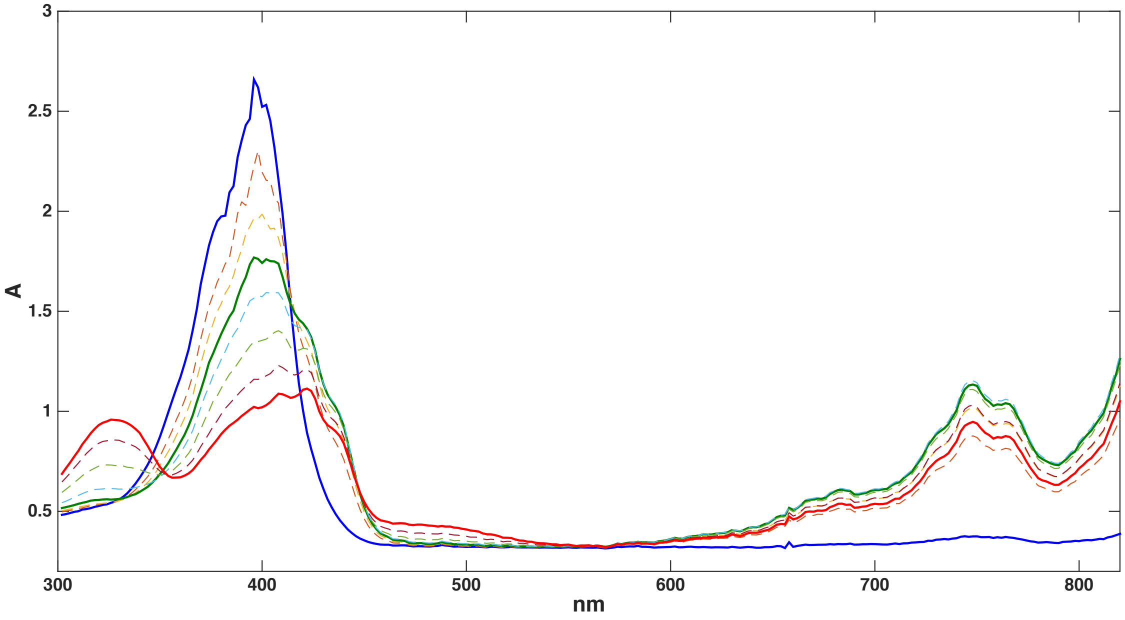

Figure 189: UV-visible spectral profiles of the neutral, radical anion and dianion TCNQ in $AmNTF_2$

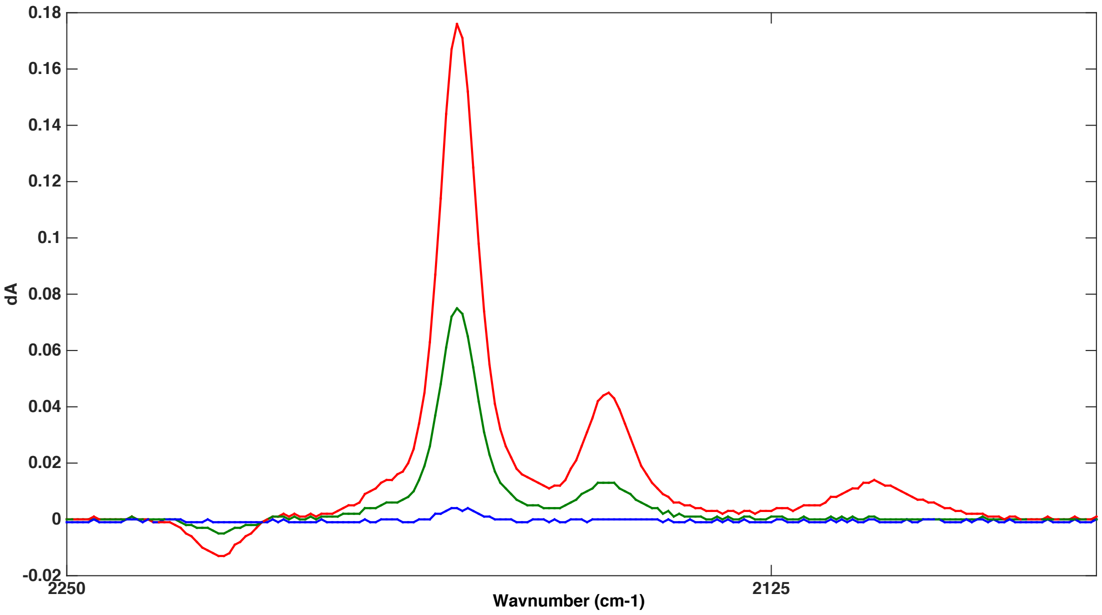

Figure 190: IR features of TCNQ, TCNQ$^-$ and TCNQ^{2-} obtained by electrolysis of 2 mM TCNQ in BMImPF$_6$ at scan rate of 0.2mV/s.

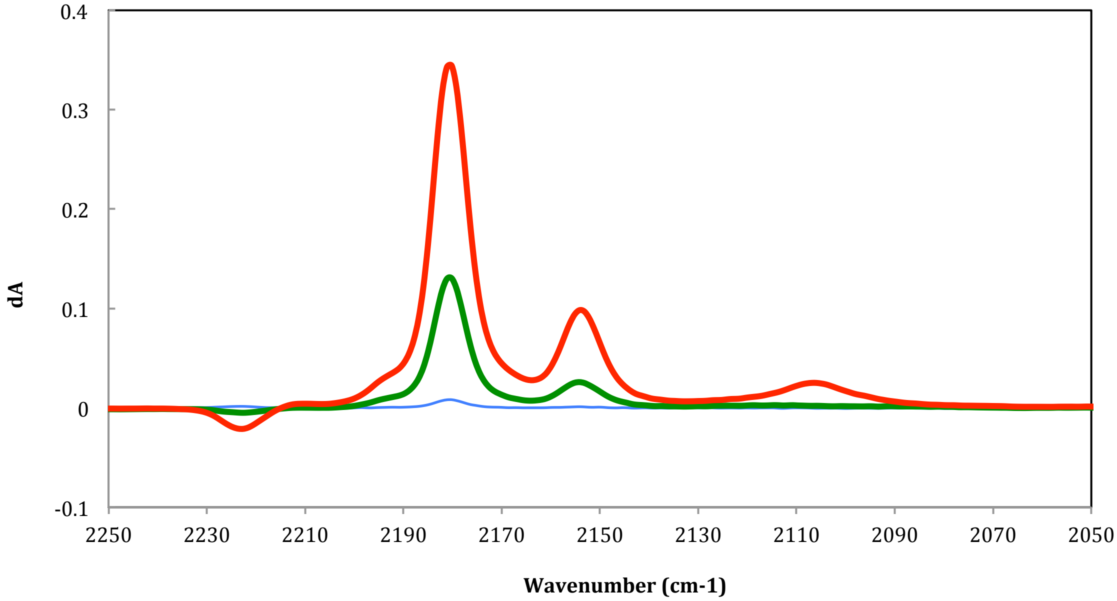

Figure 191: IR features of TCNQ, TCNQ$^-$ and TCNQ^{2-} obtained by electrolysis of 2 mM TCNQ in BMImBF$_4$

Table 18: Experimental NMR shifts versus Guttmann AN of molecular solvents

Molecular Solvent	Shift (ppm)	AN
THF	-2.72	8
ClBz	-4.165	11.6
BzCN	-6.33	15.5
DMF	-6.18	16
ACN	-7.5325	18.9
DCM	-7.81	20.4
$CHCl_3$	-9.615	23.1
Isopropanol	-14.34	33.5

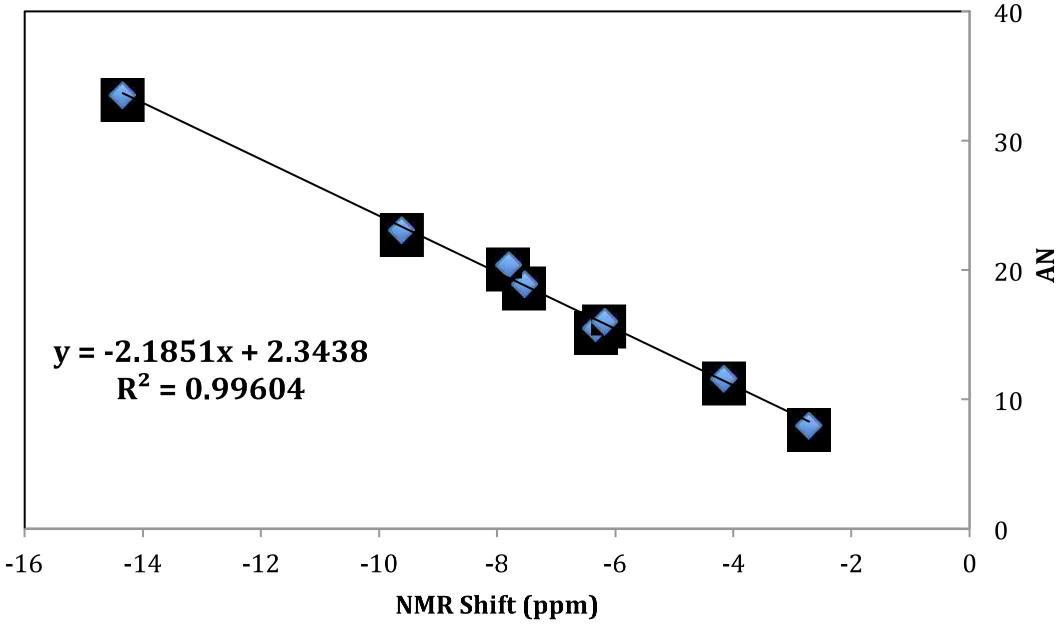

Figure 192: Correlation of our experimental NMR shifts versus Guttmann AN of molecular solvents

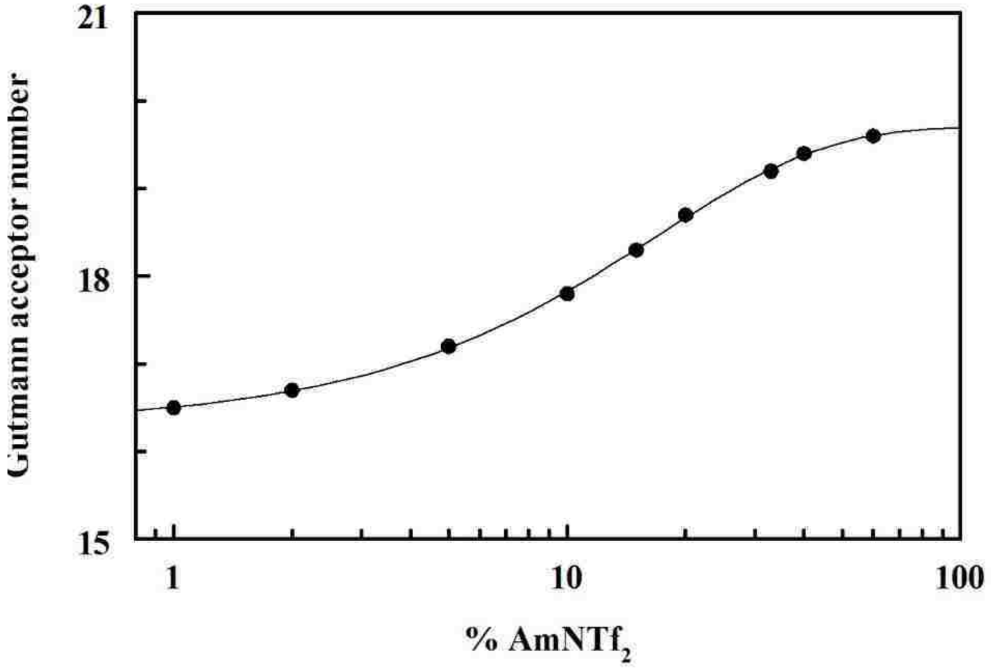

Figure 193. The relationship between the Gutmann acceptor number and the %AmNTF$_2$ in benzonitrile. The line is the best fit line for the following equation:

$$AN = 19.70 - 3.387 \exp(-\%AmNTF_2/16.85)$$

Table 19: Guttmann AN versus reduction potentials of C_{60} in molecular solvents (A) and (B) Benzonitrile-RTIL mixtures. Potentials are versus $Ag/AgNO_3$

(A) Molecular solvents			
AN	E1	E2	E3
8 (THF)	-0.473	-1.063	-1.633
11.5 (Chlorobenzene)	-0.573	-0.953	-1.438
14.2 (Pyridine)	-0.343	-0.763	-1.283
14.8 (Nitrobenzene)	-0.406	-	-
15.5 (Benzonitrile)	-0.397	-0.817	-1.297
16 (DMF)	-0.312	-0.772	-1.362
16.7 (Dicholoroethane)	-0.448	-0.848	-1.298
20.4 (Dicholoromethane)	-0.468	-0.858	-1.308
23.1 (Chloroform)	-	-0.908	-

(B) BzCN%RTIL	AmNTF$_2$				BMImPF$_6$				BMImBF$_4$			
	AN	$E^1_{1/2}$	$E^2_{1/2}$	$E^3_{1/2}$	AN	$E^1_{1/2}$	$E^2_{1/2}$	$E^3_{1/2}$	AN	$E^1_{1/2}$	$E^2_{1/2}$	$E^3_{1/2}$
0	16.5	-0.383	-0.795	-1.275	16.3	-0.373	-0.797	-1.28	16.1	-0.375	-0.802	-1.295
5	16.7	-0.384	-0.784	-1.264	17.2	-0.387	-0.785	-1.252	17	-0.372	-0.793	-1.265
10	17.2	-0.367	-0.776	-1.24	19.4	-0.362	-0.77	-1.222	18.3	-0.366	-0.777	-1.232
20	17.8	-0.362	-0.762	-1.212	20.4	-0.353	-0.754	-1.194	18.8	-0.354	-0.76	-1.205
40	18.3	-0.36	-0.755	-1.205	21.2	-0.33	-0.72	-1.151	19.7	-0.335	-0.735	-1.172
60	18.7	-0.355	-0.753	-1.195	22.4	-0.328	-0.696	-1.131	20.7	-0.322	-0.71	-1.137

Determination of Ion Pairing Constants from the Shifts in $E_{1/2}$ Values:

The approach used in this work for the calculation of ion pairing constants is based on the shift in the $E_{1/2}$ values as the salt concentration is varied. In order to maintain the ionic strength, the total salt concentration was maintained at 0.50 M. Assuming the C_{60} does not ion pair with cations, the shift in the $E_{1/2,1}$ values for C_{60} is given by the following equilibria for mixtures of TBA^+ with cation, C^+. For the first wave,

$$C_{60}^- + TBA^+ \rightarrow (TBA^+)(C_{60}^-) \qquad K_{IP1,TBA^+C_{60}^-} \tag{1}$$

$$C_{60}^- + C^+ \rightarrow (C^+)(C_{60}^-) \qquad K_{IP1,C^+C_{60}^-} \tag{2}$$

This can be repeated for each anionic C_{60} species with the number following IP indicating the number of cations paired and the C_{60} species indicated in the subscript. The K values are successful K values. If K_{IP} is large, this would actually be a displacement reaction, but this approach would equally apply in that case. The fraction of C_{60}^- that is uncomplexed (unpaired) is given by the following equation:

$$[C_{60}^-] = M_{C60}/(1 + K_{IP1,TBA^+C_{60}^-}[TBA^+] + K_{IP1,C^+C_{60}^-}[C^+]) \tag{3}$$

and the shift in $E_{1/2,1}$ in the presence of TBA^+ is given by:

$$E_{1/2,1c} = E_{1/2,1u} + 0.059\log\left(1 + K_{IP1,TBA^+C_{60-}}\left[TBA^+\right] + K_{IP1,C^+C_{60-}}\left[C^+\right]\right) \tag{4}$$

Since $[TBA^+] + [C^+] = 0.50$,

$$\Delta E = E_{1/2,1c} - E_{1/2,1u} = 0.059\log\left(1 + K_{IP1,TBA^+C_{60-}}\left[TBA^+\right] + K_{IP1,C^+C_{60-}}(0.50 - \left[TBA^+\right]\right) \tag{5}$$

$$\Delta E = 0.059\log\left(1 + 0.50K_{IP1,C^+C_{60-}} + \left(K_{IP1,TBA^+C_{60-}} - K_{IP1,C^+C_{60-}}\right)\left[TBA^+\right]\right) \tag{6}$$

Rearranging,

$$10^{\frac{\Delta E}{0.059}} = Y_1 = \left(1 + 0.50K_{IP1,C^+C_{60}^-}\right) + \left[K_{IP1,TBA^+C_{60}^-} - K_{IP1,C^+C_{60}^-}\right]\left[TBA^+\right] \tag{7}$$

A plot of Y_1 versus $[TBA^+]$ should be linear with an intercept of ($1+0.50\,K_{IP1,C^+C_{60}^-}$) and a slope equal to ($K_{IP1,TBA^+C_{60}^-} - K_{IP1,C^+C_{60}^-}$). The plot is shown in *Figure **194*** for mixtures of TBAP/BMImCl. The intercept in *Figure **194*** was close to unity indicating that the ion pairing of $BMIm^+$ with C_{60}^- was at most 0.08, and $K_{IP1,TBA^+C_{60}^-}$ was 1.5. The value of $E_{1/2,1u}$ in Eq. 5 was determined from solutions where no TBA^+ was present, with the assumption that C^+ ion pairs much weaker with C_{60}^- than TBA^+. This assumption can be verified from the plot of Eq. 7. If $K_{IP1,C^+C_{60}^-}$ is small enough so that C^+ does not ion pair significantly with C_{60}^-, then Eq. 7 will be linear with an intercept of 1. That was the case in Figure S-13. For other mixtures, the $E_{1/2,1}$ from 0.50 $\underline{M}$ BMImCl was used for $E_{1/2,1u}$.

Three equilibria need to be considered for the second wave of C_{60}: $K_{IP1,TBA^+C_{60}^-}$, $K_{IP1,TBA^+C_{60}^{2-}}$ and $K_{IP2,TBA^+C_{60}^{2-}}$, where IP1 and IP2 refer to the first and second cation ion pairing with C_{60}^{2-}, respectively. From the shift in the first wave, it is clear that TBA^+ ion pairs stronger than $BMIm^+$. Therefore, for ion pairing with C_{60}^{2-} and C_{60}^{3-}, only ion pairing with TBA^+ will be considered. Using the mass balance equation, the concentrations of C_{60}^- and C_{60}^{2-} is given by:

$$\left[C_{60}^-\right] = \frac{M_{C_{60}}}{1 + K_{IP1,TBA^+C_{60}^-}\left\|TBA^+\right\|}$$

$$\left[C_{60}{}^{2-}\right]=\frac{M_{C_{60}}}{1+K_{IP1,TBA^+C_{60}^{2-}}\left[TBA^+\right]+K_{IP1,TBA^+C_{60}^{2-}}K_{IP2,TBA^+C_{60}^{2-}}\left[TBA^+\right]^2}$$

Substituting these equations into the Nernst equation, the shift in $E_{1/2,2}$ with the concentration of TBA^+ is given by:

$$\Delta E=E_{1/2,2c}-E_{1/2,2u}=0.059\log\left(\frac{1+K_{IP1,TBA^+C_{60}^{2-}}\left[TBA^+\right]+K_{IP1,TBA^+C_{60}^{2-}}K_{IP2,TBA^+C_{60}^{2-}}\left[TBA^+\right]^2}{1+K_{IP1,TBA^+C_{60-}}\left[TBA^+\right]}\right)$$

Or,

$$\Delta E=0.059\log\left(\frac{1+K_{IP1,TBA^+C_{60}^{2-}}\left[TBA^+\right]+K_{IP1,TBA^+C_{60}^{2-}}K_{IP2,TBA^+C_{60}^{2-}}\left[TBA^+\right]^2}{1+1.5\left[TBA^+\right]}\right)$$

Rearranging,

$$Y_2=\frac{\left(1+1.5\left[TBA^+\right]\right)10^{\Delta E/0.059}-1}{\left[TBA^+\right]}=K_{IP1.TBA^+C_{60}^{2-}}+K_{IP1.TBA^+C_{60}^{2-}}K_{IP2.TBA^+C_{60}^{2-}}\left[TBA^+\right]$$

When Y_2 is plotted versus the concentration of TBA^+, the intercept is equal to $K_{IP1.TBA^+C_{60}^{2-}}$ and $K_{IP2.TBA^+C_{60}^{2-}}$ can be calculated from the slope. The results are shown in ***Figure 195*** for the second wave of C_{60} for mixtures of TBAP/BMImCl. The intercept is equal to 12.8 ($K_{IP1.TBA^+C_{60}^{2-}}$) and the slope is equal to 31.4, yielding $K_{IP2.TBA^+C_{60}^{2-}}=2.5$.

Using a similar approach for the third wave, the concentration of $C_{60}{}^{3-}$ is given by:

$$\left[C_{60}{}^{3-}\right] = \frac{M_{C_{60}}}{1 + K_{IP1,TBA^+C_{60}^{3-}}\left[TBA^+\right] + K_{IP1,TBA^+C_{60}^{3-}}K_{IP2,TBA^+C_{60}^{3-}}\left[TBA^+\right]^2 + K_{IP1,TBA^+C_{60}^{3-}}K_{IP2,TBA^+C_{60}^{3-}}K_{IP3,TBA^+C_{60}^{3-}}\left[TBA^+\right]^3}$$

and the shift in $E_{1/2,3}$ is equal to:

$$\Delta E = 0.059\log\left(\frac{1 + a\left[TBA^+\right] + b\left[TBA^+\right]^2 + c\left[TBA^+\right]^3}{1 + 12.8\left[TBA^+\right] + 31.4\left[TBA^+\right]^2}\right)$$

Where,

$$a = K_{IP1,TBA^+C_{60}^{3-}},\ b = K_{IP1,TBA^+C_{60}^{3-}}K_{IP2,TBA^+C_{60}^{3-}},\ c = K_{IP1,TBA^+C_{60}^{3-}}K_{IP2,TBA^+C_{60}^{3-}}K_{IP3,TBA^+C_{60}^{3-}}$$

Rearranging,

$$Y_3 = a + b\left[TBA^+\right] + c\left[TBA^+\right]^2$$

and Y_3 is equal to:

$$Y_3 = \frac{\left(1 + 12.8\left[TBA^+\right] + 31.4\left[TBA^+\right]^2\right)10^{\Delta E/0.059} - 1}{\left[TBA^+\right]}$$

A plot of Y_3 versus [TBA$^+$] would yield a quadratic fit, as shown in *Figure **196*** for TBAP/BMImCl mixtures. From the best fit quadratic equation, $K_{IP1.TBA^+C_{60}^{3-}}$ = 35; $K_{IP2.TBA^+C_{60}^{3-}}$ = 21; $K_{IP3.TBA^+C_{60}^{3-}}$ = 0.5. This approach was used for the other TBAP/salt mixtures.

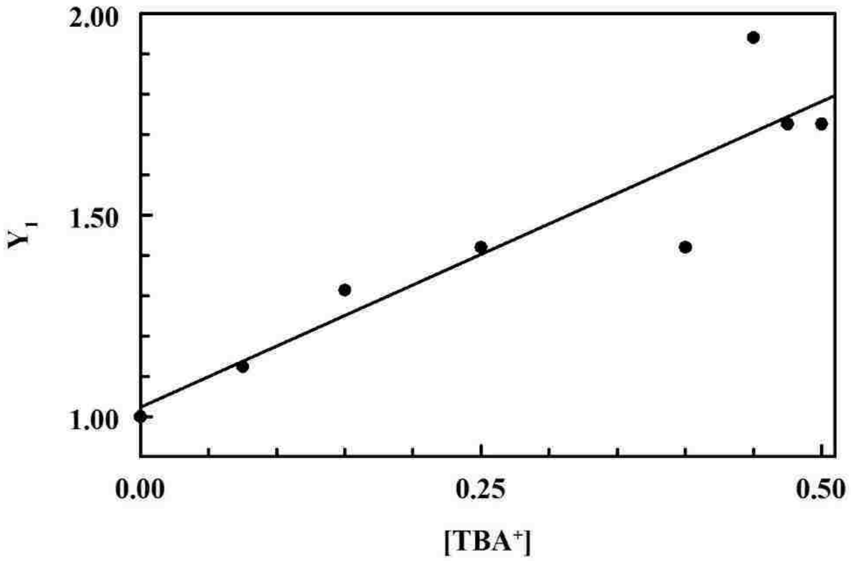

Figure 194: Plot of Y_1 versus [TBA$^+$] for first wave of C_{60} for TBAP/BMImCl mixtures. Slope = 1.47; Intercept = 1.04

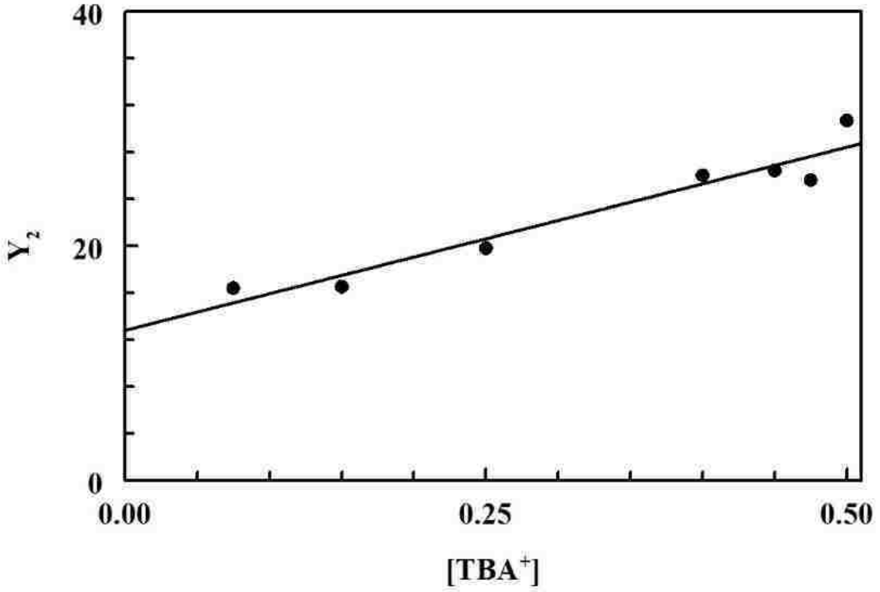

Figure 195: Plot of Y_2 versus the concentration of TBA$^+$ for the second wave of C_{60} for TBAP/BMImCl mixtures. Slope = 31.4; Intercept = 12.8

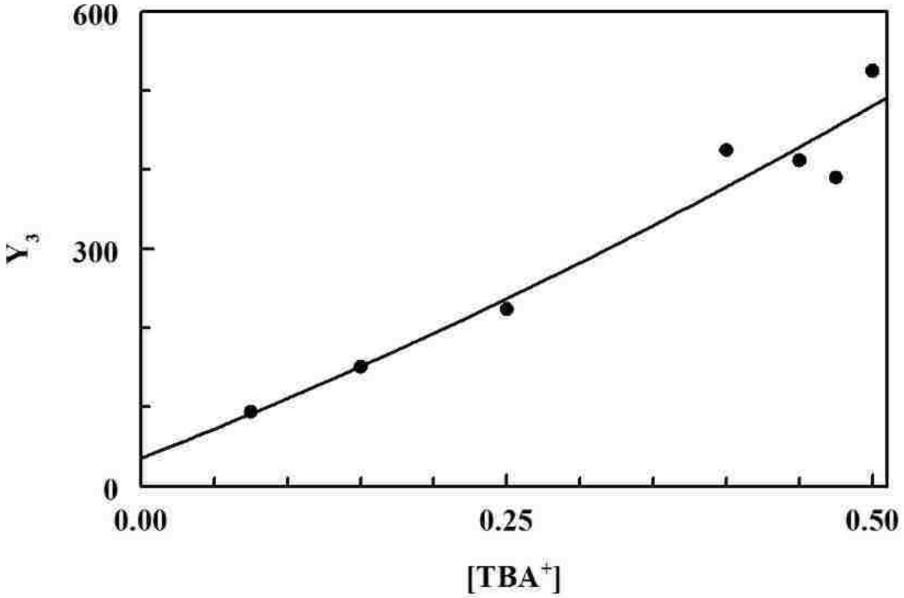

Figure 196: Plot of Y_3 *versus* [TBA$^+$] *for the third wave of* C_{60} *for TBAP/BMImCl mixtures. The best fit quadratic equation is:* $336\,[TBA^+]^2 + 722\,[TBA^+] + 35.4$.

Table 20: Guttmann AN versus Potential shifts of NiOEP in THF-RTIL mixtures

Acceptor Number	%BMImPF$_6$	Versus Ag/AgNO$_3$, V			DmFc	Versus DmFc, V		
		Reduction	Oxidation			Reduction	Oxidation	
		$E^1_{1/2}$	$E^1_{1/2}$	$E^2_{1/2}$		$E^1_{1/2}$	$E^1_{1/2}$	$E^2_{1/2}$
10	0	-1.71	0.529	0.796	-0.279	-1.431	0.808	1.075
17.7	5	-1.683	0.528	0.802	-0.302	-1.381	0.83	1.104
19.3	10	-1.671	0.518	0.792	-0.3245	-1.3465	0.8425	1.1165
21.6	20	-1.658	0.514	0.795	-0.3455	-1.3125	0.8595	1.1405
22.6	33	-1.647	0.498	0.774	-0.375	-1.272	0.873	1.149
24	50	—	0.502	0.759	-0.408	-	0.91	1.167

Acceptor Number	% AmNTF$_2$	Versus Ag/AgNO$_3$, V				DmFc	Versus DmFc, V			
		Reduction		Oxidation			Reduction		Oxidation	
		$E^1_{1/2}$	$E^2_{1/2}$	$E^1_{1/2}$	$E^2_{1/2}$		$E^1_{1/2}$	$E^2_{1/2}$	$E^1_{1/2}$	$E^2_{1/2}$
10	0	-1.742	-2.47	0.542	0.793	-0.2565	-1.4855	-2.2135	0.7985	1.0495
16	5	-1.698	-2.357	0.533	0.792	-0.292	-1.406	-2.065	0.825	1.084
16.6	10	-1.682	-2.322	0.52	0.785	-0.3275	-1.3545	-1.9945	0.8475	1.1125
18.4	20	-1.671	-2.289	0.504	0.768	-0.3525	-1.3185	-1.9365	0.8565	1.1205
19.1	33	-1.669	-2.278	0.494	0.756	-0.3765	-1.2925	-1.9015	0.8705	1.1325
19.6	50	-1.68	-2.268	0.482	0.751	-0.4015	-1.2785	-1.8665	0.8835	1.1525

Table 21: Guttmann AN versus Potential shifts of NiOEPone in THF-RTIL mixtures

Acceptor Number	% AmNTF$_2$	Versus Ag/AgNO$_3$, V					DmFc	Versus DmFc, V				
		Reduction			Oxidation			Reduction			Oxidation	
		$E^1_{1/2}$	$E^2_{1/2}$	$E^3_{1/2}$	$E^1_{1/2}$	$E^2_{1/2}$		$E^1_{1/2}$	$E^2_{1/2}$	$E^3_{1/2}$	$E^1_{1/2}$	$E^2_{1/2}$
10	0	-1.549	-2.209	-2.415	0.492	0.718	-0.2565	-1.2925	-1.9525	-2.1585	0.7485	0.9745
16	5	-1.523	-2.204	-2.3895	0.456	0.717	-0.292	-1.231	-1.912	-2.0975	0.748	1.009
16.6	10	-1.492	-2.195	-2.364	0.419	0.715	-0.3275	-1.1645	-1.8675	-2.0365	0.7465	1.0425
18.4	20	-1.452	-2.177	-2.332	0.41	0.704	-0.3525	-1.0995	-1.8245	-1.9795	0.7625	1.0565
19.1	33	-1.437	-2.174	-2.306	0.411	0.682	-0.3765	-1.0605	-1.7975	-1.9295	0.7875	1.0585
19.6	50	-1.441	-2.185	-2.303	--	--	-0.4015	-1.0395	-1.7835	-1.9015	-	-

Table 22: Half potentials (mV) of the three reduction waves of $FeF_{20}TPPX$ in THF-%RTILs

Solvent	THF-%$BMImPF_6$								THF-%$AmNTF_2$							
Species	$FeF_{20}TPPCl$			$FeF_{20}TPPClO_4$			DmFc	AN	$FeF_{20}TPPCl$			$FeF_{20}TPPClO_4$			DmFc	AN
%RTIL	$E^1_{1/2}$	$E^2_{1/2}$	$E^3_{1/2}$	$E^1_{1/2}$	$E^2_{1/2}$	$E^3_{1/2}$	E_{ox}		$E^1_{1/2}$	$E^2_{1/2}$	$E^3_{1/2}$	$E^1_{1/2}$	$E^2_{1/2}$	$E^3_{1/2}$	E_{ox}	
0	-428.5 [151] -700 [152] -550	-1220 [151] -1540 [152] -1398	-1706 [151]* -2112 [152] -1970	61	-1215	-1674.5	-279	10	-442	-1219	-1672	49	-1227.5	-1695.5	-256.5	10
5	-348.5	-1187	-1580.5	52	-1191.5	-1595.5	-302	17.7	-344.405	-1196.5	-1619.5	25.5	-1201.5	-1626.5	-292	16
10	-284	-1177.5	-1557	35	-1179	-1564.5	-324.5	19.3	-327.5	-1184.5	-1598	2.5	-1189	-1617	-327.5	16.6
20	-269.5	-1166	-1538.5	23.5	-1171.5	-1549.5	-345.5	21.6	-299	-1171.5	-1591	-16	-1178.5	-1607	-352.5	18.4
40	-261.4	-1157	-1524.5	-9.5	-1153	-1524	-391.5	23.3	-286.5	-1164	-1593.5	-30	-1172.5	-1610	-389	19.3

Values are versus Ag/$AgNO_3$. [151] values obtained in THF from Reference[151]. [152] Values obtained in DMF from reference[152]. *Estimated value from ΔE_{23} in DMF[152]

Bibliography

(1) Wang, P.; Zakeeruddin, S. M.; Moser, J. E.; Gratzel, M. *J. Phys. Chem. B* **2003**, *107*, 13280.

(2) De Souza, R. F.; Padilha, J. C.; Gon??alves, R. S.; Dupont, J. *Electrochem. commun.* **2003**, *5*, 728.

(3) Lewandowski, A.; Galiński, M. In *Journal of Physics and Chemistry of Solids*; 2004; Vol. 65, 281–286.

(4) Buzzeo, M. C.; Hardacre, C.; Compton, R. G. *Anal. Chem.* **2004**, *76*, 4583.

(5) Wang, Y.; Zaghib, K.; Guerfi, A.; Bazito, F. F. C.; Torresi, R. M.; Dahn, J. R. *Electrochim. Acta* **2007**, *52*, 6346.

(6) Silvester, D. S. *Analyst* **2011**, *136*, 4871.

(7) Hasanzadeh, M.; Shadjou, N.; Eskandani, M.; Guardia, M. D. La. *TrAC Trends Anal. Chem.* **2012**, *41*, 58.

(8) Greaves, T. L.; Drummond, C. J. *Chem. Rev.* **2015**, *115*, 11379.

(9) Pârvulescu, V. I.; Hardacre, C. *Chem. Rev.* **2007**, *107*, 2615.

(10) Zhang, S.; Sun, N.; He, X.; Lu, X.; Zhang, X. *J. Phys. Chem. Ref. Data* **2006**, *35*, 1475.

(11) Hunt, P. a. *J. Phys. Chem. B* **2007**, *111*, 4844.

(12) Hapiot, P.; Lagrost, C. *Chemical Reviews*. 2008, 2238–2264.

(13) Noda, A.; Hayamizu, K.; Watanabe, M. *J. Phys. Chem. B* **2001**, *105*, 4603.

(14) Kalugin, O. N.; Voroshylova, I. V.; Riabchunova, A. V.; Lukinova, E. V.; Chaban, V. V. *Electrochim. Acta* **2013**, *105*, 188.

(15) Shi, J.; Shi, F.; Song, N.; Liu, J. X.; Yang, X. K.; Jia, Y. J.; Xiao, Z. W.; Du, P. *J. Power Sources* **2014**, *259*, 50.

(16) Hayes, R.; Warr, G. G.; Atkin, R. *Chem. Rev.* **2015**, *115*, 6357.

(17) Pádua, A. a H.; Costa Gomes, M. F.; Canongia Lopes, J. N. a. *Acc. Chem. Res.* **2007**, *40*, 1087.

(18) Triolo, A.; Russina, O.; Bleif, H.-J.; Di Cola, E. *J. Phys. Chem. B* **2007**, *111*, 4641.

(19) Dyson, P. J.; Khalaila, I.; Luettgen, S.; McIndoe, J. S.; Zhao, D. *Chem. Commun. (Camb).* **2004**, 2204.

(20) Dorbritz, S.; Ruth, W.; Kragl, U. *Adv. Synth. Catal.* **2005**, *347*, 1273.

(21) Bini, R.; Bortolini, O.; Chiappe, C.; Pieraccini, D.; Siciliano, T. *J. Phys. Chem. B* **2007**, *111*, 598.

(22) Gozzo, F. C.; Santos, L. S.; Augusti, R.; Consorti, C. S.; Dupont, J.; Eberlin, M. N. *Chem. - A Eur. J.* **2004**, *10*, 6187.

(23) Kennedy, D. F.; Drummondt, C. J. *J. Phys. Chem. B* **2009**, *113*, 5690.

(24) Puttick, S.; Davis, A. L.; Butler, K.; Lambert, L.; El harfi, J.; Irvine, D. J.; Whittaker, A. K.; Thurecht, K. J.; Licence, P. *Chem. Sci.* **2011**, *2*, 1810.

(25) Xiao, D.; Hines, L. G.; Bartsch, R. A.; Quitevis, E. L. *J. Phys. Chem. B* **2009**, *113*, 4544.

(26) Ivanov, M. Y.; Veber, S. L.; Prikhod'ko, S. A.; Adonin, N. Y.; Bagryanskaya, E. G.; Fedin, M. V. *J. Phys. Chem. B* **2015**, *119*, 13440.

(27) Shimizu, K.; Costa Gomes, M. F.; P??dua, A. A. H.; Rebelo, L. P. N.; Canongia Lopes, J. N. *J. Mol. Struct. THEOCHEM* **2010**, *946*, 70.

(28) Jiang, W.; Wang, Y.; Voth, G. A. *J. Phys. Chem. B* **2007**, *111*, 4812.

(29) Avent, A. G.; Chaloner, P. A.; Day, M. P.; Seddon, K. R.; Welton, T. *J. Chem. Soc. Dalt. Trans.* **1994**, 3405.

(30) Dupont, J.; Suarez, P.; De Souza RF; Burrow, R.; Kintzinger, J. *Chemistry* **2000**, *6*, 2377.

(31) Consorti, C. S.; Suarez, P. A. Z.; De Souza, R. F.; Burrow, R. A.; Farrar, D. H.; Lough, A. J.; Loh, W.; Da Suva, L. H. M.; Dupont, J. *J. Phys. Chem. B* **2005**, *109*, 4341.

(32) Remsing, R. C.; Liu, Z.; Sergeyev, I.; Moyna, G. *J. Phys. Chem. B* **2008**, *112*, 7363.

(33) Feng, Q.; Wang, H.; Zhang, S.; Wang, J. *Colloids Surfaces A Physicochem. Eng. Asp.* **2010**, *367*, 7.

(34) Zheng, Y.-Z.; Wang, N.-N.; Luo, J.-J.; Zhou, Y.; Yu, Z.-W. *Phys.*

Chem. Chem. Phys. **2013**, *15*, 18055.

(35) Li, W.; Zhang, Z.; Zhang, J.; Han, B.; Wang, B.; Hou, M.; Xie, Y. *Fluid Phase Equilib.* **2006**, *248*, 211.

(36) Schroder, U.; Wadhawan, J. D.; Compton, R. G.; Marken, F.; Suarez, P. A. Z.; Consorti, C. S.; Souza, F. De.; Dupont, J. *New J. Chem.* **2000**, *24*, 1009.

(37) Zhao, C.; Bond, A. M.; Lu, X. *Anal. Chem.* **2012**, *84*, 2784.

(38) Stark, A.; Behrend, P.; Braun, O.; Müller, A.; Ranke, J.; Ondruschka, B.; Jastorff, B. *Green Chem.* **2008**, *10*, 1152.

(39) Dash, P.; Scott, R. W. J. *Chem. Commun. (Camb).* **2009**, 812.

(40) Zhao, C.; Bond, A. M.; Compton, R. G.; O'Mahony, A. M.; Rogers, E. I. *Anal. Chem.* **2010**, *82*, 3856.

(41) Xiao, L.; Johnson, K. E. *J. Electrochem. Soc.* **2003**, *150*, E307.

(42) Li, Z.; Du, Z.; Gu, Y.; Zhu, L.; Zhang, X.; Deng, Y. *Electrochem. commun.* **2006**, *8*, 1270.

(43) Villagrán, C.; Banks, C. E.; Hardacre, C.; Compton, R. G. *Anal. Chem.* **2004**, *76*, 1998.

(44) Hapiot, P.; Lagrost, C. *Chem. Rev.* **2008**, *108*, 2238.

(45) Lagrost, C.; Carrié; Vaultier, M.; Hapiot, P. *J. Phys. Chem. A* **2003**, *107*, 745.

(46) Fontaine, O.; Lagrost, C.; Ghilane, J.; Martin, P.; Trippé, G.; Fave, C.; Lacroix, J. C.; Hapiot, P.; Randriamahazaka, H. N. *J. Electroanal. Chem.* **2009**, *632*, 88.

(47) Zhang, J.; Bond, A. M. *Anal. Chem.* **2003**, *75*, 2694.

(48) Xiao, L.; Dickinson, E. J. F.; Wildgoose, G. G.; Compton, R. G. *Electroanalysis* **2010**, *22*, 269.

(49) Matsumiya, M.; Terazono, M.; Tokuraku, K. *Electrochim. Acta* **2006**, *51*, 1178.

(50) Tachikawa, N.; Katayama, Y.; Miura, T. *J. Electrochem. Soc.* **2007**, *154*, F211.

(51) Pan, Y.; Cleland, W. E.; Hussey, C. L. *J. Electrochem. Soc.* **2012**, *159*, F125.

(52) Lagrost, C.; Preda, L.; Volanschi, E.; Hapiot, P. *J. Electroanal. Chem.* **2005**, *585*, 1.

(53) Taylor, A. W.; Puttick, S.; Licence, P. *J. Am. Chem. Soc.* **2012**, *134*, 15636.

(54) Rogers, E. I.; Silvester, D. S.; Poole, D. L.; Aldous, L.; Hardacre, C.; Compton, R. G. *J. Phys. Chem. C* **2008**, *112*, 2729.

(55) Long, J. S.; Silvester, D. S.; Barnes, A. S.; Rees, N. V.; Aldous, L.; Hardacre, C.; Compton, R. G. *J. Phys. Chem. C* **2008**, *112*, 6993.

(56) Clegg, A. D.; Rees, N. V; Klymenko, O. V; Coles, B. A.; Compton, R. G. *J. Am. Chem. Soc.* **2004**, *126*, 6185.

(57) Kim, D. Y.; Yang, J. C.; Kim, H. W.; Swain, G. M. *Electrochim. Acta* **2013**, *94*, 49.

(58) Buzzeo, M. C.; Klymenko, O. V.; Wadhawan, J. D.; Hardacre, C.; Seddon, K. R.; Compton, R. G. *J. Phys. Chem. A* **2003**, *107*, 8872.

(59) Zigah, D.; Wang, A.; Lagrost, C.; Hapiot, P. *J. Phys. Chem. B* **2009**, *113*, 2019.

(60) Wang, Y.; Rogers, E. I.; Belding, S. R.; Compton, R. G. *J. Electroanal. Chem.* **2010**, *648*, 134.

(61) Bentley, C. L.; Bond, A. M.; Hollenkamp, A. F.; Mahon, P. J.; Zhang, J. *Anal. Chem.* **2013**, *85*, 2239.

(62) Brooks, C. a; Doherty, A. P. *J. Phys. Chem. B* **2005**, *109*, 6276.

(63) Abdul-Rahim, O.; Simonov, A. N.; Rüther, T.; Boas, J. F.; Torriero, A. J.; Collins, D. J.; Perlmutter, P.; Bond, A. M. *Anal. Chem.* **2013**, *85*, 6113.

(64) Xiong, L.; Fletcher, A. M.; Davies, S. G.; Norman, S. E.; Hardacre, C.; Compton, R. G. *Chem. Commun.* **2012**, *48*, 5784.

(65) Nikitina, V. A.; Nazmutdinov, R. R.; Tsirlina, G. A. *J. Phys. Chem. B* **2011**, *115*, 668.

(66) Nikitina, V. A.; Gruber, F.; Jansen, M.; Tsirlina, G. A. *Electrochim. Acta* **2013**, *103*, 243.

(67) Macías-Ruvalcaba, N. a; Evans, D. H. *J. Phys. Chem. B* **2005**, *109*, 14642.

(68) Evans, D. H.; Hu, K. *J. Chem. Soc. Faraday Trans.* **1996**, *92*, 3983.

(69) Lehmann, M. W.; Singh, P.; Evans, D. H. *J. Electroanal. Chem.* **2003**, *549*, 137.

(70) Adams, C. J.; Da Costa, R. C.; Edge, R.; Evans, D. H.; Hood, M. F. *J. Org. Chem.* **2010**, *75*, 1168.

(71) Chung, Y. C.; Tu, Y. J.; Lu, S. H.; Hsu, W. C.; Chiu, K. Y.; Su, Y. O. *Org. Lett.* **2011**, *13*, 2826.

(72) Sauer, A.; Wasgestian, F.; Nickel, U. *Bull. Chem. Soc. Jpn.* **1989**, *62*, 2688.

(73) Hernández-Muñoz, L. S.; González, F. J.; González, I.; Goulart, M. O. F.; Abreu, F. C. De; Ribeiro, A. S.; Ribeiro, R. T.; Longo, R. L.; Navarro, M.; Frontana, C. *Electrochim. Acta* **2010**, *55*, 8325.

(74) Tian, D.; Jin, B. *Electrochim. Acta* **2011**, *56*, 9144.

(75) Fry, A. J. *J. Electroanal. Chem.* **2003**, *546*, 35.

(76) Minami, Y.; Fry, A. J. In *A Unifying View of Computational Electrochemistry.*; AIP Conference Proceedings., 2007, 481–486.

(77) Syroeshkin, M. A.; Mendkovich, A. S.; Mikhal'chenko, L. V.; Gul'tyai, V. P. *Russ. Chem. Bull.* **2010**, *58*, 1688.

(78) Jaeger, C. D.; Bard, A. J. *J. Am. Chem. Soc.* **1979**, *101*, 1690.

(79) Yasuda, A.; Seto, J. *J. Electroanal. Chem. Interfacial Electrochem.* **1988**, *247*, 193.

(80) Acker, D. S.; Hertler, W. R. *J. Am. Chem. Soc.* **1962**, *84*, 3370.

(81) Jeanmaire, D. L.; Van Duyne, R. P. *J. Am. Chem. Soc.* **1976**, *98*, 4029.

(82) Khoo, S. B.; Foley, J. F.; Korzeniewski, C.; Pons, S.; Marcott, C. *J. Electroanal. Chem.* **1987**, *233*, 223.

(83) Flowers, P. A.; Mamantov, G. *Anal. Chem.* **1989**, *61*, 190.

(84) Lipin, G.; Xiangqin, L. *Chinese J. Anal. Chem.* **1999**, *27*, 300.

(85) Rongfeng, Z.; Evans, D. H. *J. Electroanal. Chem.* **1995**, *385*, 201.

(86) Haufler, R. E.; Conceicao, J.; Chibante, L. P. F.; Chai, Y.; Byrne, N. E.; Flanagan, S.; Haley, M. M.; O'Brien, S. C.; Pan, C.; et al., . *J. Phys. Chem.* **1990**, *94*, 8634.

(87) Allemand, P. M.; Koch, A.; Wudl, F.; Rubin, Y.; Diederich, F.; Alvarez, M. M.; Anz, S. J.; Whetten, R. L. *J. Am. Chem. Soc.* **1991**, *113*, 1050.

(88) Dubois, D.; Kadish, K. M.; Flanagan, S.; Haufler, R. E.; Chibante, L. P. F.; Wilson, L. J. *J. Am. Chem. Soc.* **1991**, *113*, 4364.

(89) Reed, C. A.; Bolskar, R. D. *Chem. Rev.* **2000**, *100*, 1075.

(90) Dubois, D.; Kadish, K. M.; Flanagan, S.; Wilson, L. J. *J. Am. Chem. Soc.* **1991**, *113*, 7773.

(91) Xie, Q.; Perez-Cordero, E.; Echegoyen, L. *J. Am. Chem. Soc.* **1992**, *114*, 3978.

(92) Ohsawa, Y.; Saji, T. *J. Chem. Soc. Chem. Commun.* **1992**, 781.

(93) Dubois, D.; Moninot, G.; Kutner, W.; Jones, M. T.; Kadish, K. M. *J. Phys. Chem.* **1992**, *96*, 7137.

(94) Noviandri, I.; Bolskar, R. D.; Lay, P. a; Reed, C. a. *J. Phys. Chem. B* **1997**, *101*, 6350.

(95) Noviandri, I.; Brown, K. N.; Fleming, D. S.; Gulyas, P. T.; Lay, P. a; Masters, a F.; Phillips, L. *J. Phys. Chem. B* **1999**, *103*, 6713.

(96) Stinchcombe, J.; Penicaud, A.; Bhyrappa, P.; Boyd, P. D. W.; Reed, C. A. *J. Am. Chem. Soc.* **1993**, *115*, 5212.

(97) Bhyrappa, P.; Paul, P.; Stinchcombe, J.; Boyd, P. D. W.; Reed, C. A. *J. Am. Chem. Soc.* **1993**, *115*, 11004.

(98) Sun, Y.; Reed, C. A. *Chem. Commun.* **1997**, 747.

(99) Baumgarten, M.; Gherghel, L. *Appl. Magn. Reson.* **1996**, *11*, 171.

(100) Greaney, M. A.; Gorun, S. M. *J. Phys. Chem.* **1991**, *95*, 7142.

(101) Heath, G. A.; McGrady, J. E.; Martin, R. L. *J. Chem. Soc., Chem. Commun.* **1992**, 1272.

(102) Kato, T.; Kodama, T.; Oyama, M.; Okazaki, S.; Shida, T.; Nakagawa, T.; Matsui, Y.; Suzuki, S.; Shiromaru, H.; Yamauchi, K.; Achiba, Y. *Chem. Phys. Lett.* **1991**, *186*, 35.

(103) Lawson, D. R.; Feldheim, D. L.; Foss, C. A.; Dorhoug, P. K.; Elliott, C. M. Office of Naval Research, **1992,** *71,* 627-838.

(104) Khaled, M. M.; Carlin, R. T.; Trulove, P. C.; Eaton, G. R.; Eaton, S. S. *J. Am. Chem. Soc.* **1994**, *116*, 3465.

(105) Trulove, P. C.; Carlin, R. T.; Eaton, G. R.; Eaton, S. S. *J. Am. Chem. Soc.* **1995**, *117*, 6265.

(106) Duffy, N. W.; Bond, A. M. *Electrochem. commun.* **2006**, *8*, 892.

(107) Ueda, H.; Nishiyama, K.; Yoshimoto, S. *Electrochem. Commun.* **2014**, *43*, 102.

(108) Damlin, P.; Kvarnström, C.; Ivaska, a. *J. Electroanal. Chem.* **2006**, *590*, 190.

(109) Kadish, K. M.; Franzen, M. M.; Han, B. C.; Araullo-McAdams, C.; Sazou, D. *Jounal Am. Chem. Soc.* **1991**, *113*, 512.

(110) Kadish, K. M.; Franzen, M. M.; Han, B. C.; Araullo-McAdams, C.; Sazou, D. *Inorg. Chem.* **1992**, *31*, 4399.

(111) Lexa, D.; Momenteau, M.; Mispelter, J.; Saveant, J. M. *Inorg. Chem.* **1989**, *28*, 30.

(112) Stolzenberg, A. M.; Glazer, P. A.; Foxman, B. M. *Inorg. Chem.* **1986**, *25*, 983.

(113) Connick, P. A.; Macor, K. A. *Inorg. Chem.* **1991**, *30*, 4654.

(114) Kadish, K. M.; Sazou, D.; Liu, Y. M.; Saoiabi, A.; Ferhat, M.; Guilard, R. *Inorg. Chem.* **1988**, *27*, 1198.

(115) Czernuszewicz, R. S.; Macor, K. A.; Li, X. Y.; Kincaid, J. R.; Spiro,

T. G. *J. Am. Chem. Soc.* **1989**, *111*, 3860.

(116) Fuhrhop, J. H.; Mauzerall, D. *J. Am. Chem. Soc.* **1969**, *91*, 4174.

(117) Stolzenberg, A. M.; Stershic, M. T. *Inorg. Chem.* **1988**, *27*, 1614.

(118) Scheidt, W. R.; Buentello, K. E.; Ehlinger, N.; Cinquantini, A.; Fontani, M.; Laschi, F. *Inorganica Chim. Acta* **2008**, *361*, 1722.

(119) Scheidt, W. R.; Cheng, B.; Haller, K. J.; Mislankar, A.; Rae, A. D.; Reddy, K. V.; Song, H.; Orosz, R. D.; Reed, C. A. *J. Am. Chem. Soc.* **1993**, *115*, 1181.

(120) Fajer, J.; Borg, D. C.; Forman, A.; Dolphin, D.; Felton, R. H. *J. Am. Chem. Soc.* **1970**, *92*, 3451.

(121) Nahor, G. S.; Neta, P.; Hambright, P.; Robinson, L. R.; Harriman, A. *J. Phys. Chem.* **1990**, *94*, 6659.

(122) Lexa, D.; Momenteau, M.; Mispelter, J.; Saveant, J. *Inorg. Chem.* **1989**, *28*, 30.

(123) Kadish, K. M.; Franzen, M. M.; Han, B. C.; Araullo-McAdams, C.; Sazou, D. *J. Am. Chem. Soc.* **1991**, *113*, 512.

(124) Chang, C. K.; Ebina, F. *J. Chem. Soc., Chem. Commun.* **1981**, 778.

(125) Stephenson, N. A; Bell, A. T. *J. Am. Chem. Soc.* **2005**, *127*, 8635.

(126) Stephenson, N. A; Bell, A. T. *Inorg. Chem.* **2006**, *45*, 2758.

(127) Stephenson, N. A.; Bell, A. T. *Inorg. Chem.* **2007**, *46*, 2278.

(128) Anxolabehere, E.; Chottard, G.; Lexa, D. *New J. Chem*. 1994, 18, 889–899.

(129) Stephenson, N. A.; Bell, A. T. *J. Am. Chem. Soc.* **2005**, *127*, 8635.

(130) Song, B.; Yu, B. S. *Bull. Korean Chem. Soc.* **2003**, *24*, 981.

(131) Ma, H. L.; Jin, W. J.; Xi, L.; Dong, Z. J. *Spectrochim. Acta. A.* **2009**, *74*, 502.

(132) Ali, M.; Kumar, V.; Baker, S. N.; Baker, G. A.; Pandey, S. *Phys. Chem. Chem. Phys.* **2010**, *12*, 1886.

(133) Schmeisser, M.; van Eldik, R. *Inorg. Chem.* **2009**, *48*, 7466.

(134) Compton, D. L.; Laszlo, J. A. *J. Electroanal. Chem.* **2002**, *520*, 71.

(135) Tutunea, F.; Atifi, A.; Ryan, M. D. *J. Electroanal. Chem.* **2015**, *744*, 17.

(136) Schmeisser, M.; Illner, P.; Puchta, R.; Zahl, A.; Van Eldik, R. *Chem. - A Eur. J.* **2012**, *18*, 10969.

(137) Keesey, R. L.; Ryan, M. D. *Anal. Chem.* **1999**, *71*, 1744.

(138) Seto, K.; Nakayama, T.; Uno, B. *J. Phys. Chem. B* **2013**, *117*, 10834.

(139) Roy, L. E.; Jakubikova, E.; Batista, E. R. *Assoc. Dir. Theory, Simulation, Comput.* **2009**, 72.

(140) Talipov, M. R.; Boddeda, A.; Timerghazin, Q. K.; Rathore, R. *J. Phys. Chem. C. Nanomater. Interfaces* **2014**, *118*, 21400.

(141) Fry, A. J. *J. Org. Chem.* **2013**, *78*, 2111.

(142) Fry, A. J. *J. Org. Chem.* **2013**, *78*, 5476.

(143) Fry, A. J. *Electrochem. commun.* **2005**, *7*, 602.

(144) Bernales, V. S.; Marenich, A. V.; Contreras, R.; Cramer, C. J.; Truhlar, D. G. *J. Phys. Chem. B* **2012**, *116*, 9122.

(145) Isegawa, M.; Neese, F.; Pantazis, D. A. *J. Chem. Theory Comput.* **2016**, *12*, 2272.

(146) Merli, D.; Protti, S.; Petracca, P.; Fagnoni, M.; Profumo, A. *Electroanalysis* **2013**, *25*, 1453.

(147) Chen, N.; Beavers, C. M.; Mulet-Gas, M.; Rodríguez-Fortea, A.; Munoz, E. J.; Li, Y.-Y.; Olmstead, M. M.; Balch, A. L.; Poblet, J. M.; Echegoyen, L. *J. Am. Chem. Soc.* **2012**, *134*, 7851.

(148) Stolzenberg, A. M.; Stershic, M. T. *J. Am. Chem. Soc.* **1988**, *110*, 6391.

(149) Tutunea, F.; Ryan, M. D. *J. Electroanal. Chem.* **2012**, *670*, 16.

(150) Wei, Z.; Ryan, M. D. *Inorg. Chem.* **2010**, *49*, 6948.

(151) Bottomley, L. a.; Kadish, K. M. *Inorg. Chem.* **1981**, *20*, 1348.

(152) Kadish, K. M.; Larson, G.; Lexa, D.; Momenteau, M. *J. Am. Chem. Soc.* **1975**, *97*, 282.

(153) Mashiko, T.; Reed, C. A.; Haller, K. J.; Scheidt, W. R. *Inorg. Chem.* **1984**, *23*, 3192.

(154) Landrum, J. T.; Hatano, K.; Scheidt, W. R.; Reed, C. A. *J. Am. Chem. Soc.* **1980**, *102*, 6729.

(155) Grinstaff, M. W.; Hill, M. G.; Birnbaum, E. R.; Schaefer, W. P.; Labinger, J. A.; Gray, H. B. *Inorg. Chem.* **1995**, *34*, 4896.

(156) Quezada, D.; Honores, J.; García, M.; Armijo, F.; Isaacs, M. *New J. Chem.* **2014**, *38*, 3606.

(157) Sun, L.; Ramesha, G. K.; Kamat, P. V.; Brennecke, J. F. *Langmuir* **2014**, *30* (21), 6302.

(158) Niu, D.; Wang, H.; Li, H.; Wu, Z.; Zhang, X. *Electrochim. Acta* **2015**, *158*, 138.

(159) Rosen, B. A.; Salehi-Khojin, A.; Thorson, M. R.; Zhu, W.; Whipple, D. T.; Kenis, P. J. A.; Masel, R. I. *Science.* **2011**, *334*, 643.